

## Preface

### **Special Issue on Up-to-Date Problems in Modern Railways and Optimization in Engineering Structures**

The current issue is the fourth part of the Special Issue series in Acta Polytechnica Hungarica, the scientific journal of Óbuda University. In the first three issues altogether, 47 papers are available. The authors come from two continents, Europe and Asia – including nearly ten different countries. The published topics cover a wide range of railway and structure optimization. The topics published belong to the following disciplines, among others: civil engineering, mechanical engineering, and informatics.

Modern railways must address increased capacity, reduced environmental impact, and improved safety measures. Railways must develop innovative solutions to address these constraints as populations grow and urbanization continues. Engineering structure optimization is critical for resource efficiency and infrastructure longevity. Techniques such as optimizing bridge design and building construction can result in cost-effective, resilient, and sustainable structures. Innovative technologies like artificial intelligence and data analytics are critical for optimizing rail networks, predictive maintenance, and passenger safety. Transportation efficiency, safety, and environmental sustainability can be improved by focusing on these critical aspects.

We extend our appreciation to all the authors for contributing to the Special Issue and sharing their research findings with Acta Polytechnica Hungarica.

The Special Issue Series cannot be organized without the help of Anikó Szakál and Prof. Péter Baranyi. A huge thank for their help and support.

It is planned to continue the first four parts of the Special Issue in the future, i.e., further numbers are under preparation in the Acta Polytechnica Hungarica journal.

*Dragan Marinković, Dmytro Kurhan, Mykola Sysyn,  
Majid Movahedi Rad and Szabolcs Fischer*

*Guest Editors*

# Robust Optimization of the Steel Single Story Frame

**Paweł Zabojszcza<sup>1</sup>, Urszula Radoń<sup>2</sup>, Piotr Tautowski<sup>3</sup>**

<sup>1</sup>Kielce University of Technology, Faculty of Civil Engineering and Architecture, al. Tysiąclecia Państwa Polskiego 7, 25-314 Kielce, Poland, pawelzab@tu.kielce.pl

<sup>2</sup>Kielce University of Technology, Faculty of Civil Engineering and Architecture, al. Tysiąclecia Państwa Polskiego 7, 25-314 Kielce, Poland, zmbur@tu.kielce.pl

<sup>3</sup>Institute of Fundamental Technological Research Polish Academy of Sciences, Department of Information and Computational Science, ul. Pawińskiego 5B, 02-106 Warsaw, Poland, ptauzow@ippt.pan.pl

---

*Abstract: In contemporary design practices, building structures are expected to not only meet safety requirements but also be optimized. However, optimal designs can be highly sensitive to random variations in model parameters and external actions. Solutions that appear effective under nominal conditions may prove inadequate when parameter randomness is considered. To address this challenge, the concept of robust optimization has been introduced, which extends deterministic optimization formulations to incorporate the random variability of parameter values. In this study, we demonstrate the applicability of robust optimization in the design of building structures using a simple orthogonal frame as an example. The static-strength analysis is conducted based on the displacement method, utilizing second-order theory. To assess the safety level of the steel frame, a preliminary evaluation is performed by determining the reliability index and failure probability using the Monte Carlo Method. Robust optimization is then employed, leveraging the second-order response surface. Experimental designs are generated following an optimal Latin hypercube plan. The proposal of a mathematical-numerical algorithm for solving the optimization problem while considering the random nature of design parameters constitutes the innovative aspect of this research.*

*Keywords: reliability; robust optimization; second order theory; displacement method*

---

## 1 Introduction

The design of complex structures places a dual responsibility on engineers: ensuring building safety while simultaneously minimizing construction costs and structural weight. This trend has led to an increasing interest in optimization methods to

achieve efficient material utilization, making optimization an indispensable tool for rational structural design. While optimization modules are commonly incorporated in design approaches based on the Finite Element Method, they are typically employed in a deterministic manner. In this traditional approach, the random nature of design parameters is considered by incorporating partial safety factors into the optimization formulation. These factors, defined by relevant design standards (codes) [N1-N3], are often calibrated to suit a broad range of design tasks. However, this approach frequently yields overly conservative solutions, as the partial safety factors do not directly account for the random variations in design variables. Consequently, optimal structures may not achieve the desired level of reliability. If ensuring structural safety is a primary design requirement, it is worth considering a reliability-based design optimization (RBDO) formulation [1-7]. RBDO-based design constraints are formulated using probabilities of failure, which represent the likelihood of exceeding specific permissible states related to load capacity or allowable displacement. These permissible states are incorporated into the formulation through relevant limit functions in reliability analysis, commonly known as 'performance functions.'

Random fluctuations in structural response degrade its quality, leading to deviations from intended functionality and increased maintenance costs (e.g., inspections, maintenance, and repairs). An effectively designed building should minimize such costs, ensure proper functioning, and be less sensitive to the random nature of design parameters. To meet the required level of quality, design methods and procedures have been developed, collectively referred to as 'robust design' [8-10]. This methodology aims to design structures, devices, and production processes that maintain high functionality within a system. The objective is to find solutions that are as resistant as possible to variations in design parameters. Limiting or eliminating the variability of input parameters can reduce variance in quantities characterizing the structural state, such as displacements and stress. However, implementing such procedures often incurs unacceptable costs. A more effective approach is to reduce parameter variability without altering the variance of the structure's input parameters. This approach is known as robust optimization.

Robust optimization provides solutions that are less sensitive to model parameters that are challenging to control. This paper focuses on highlighting this significant aspect of optimal design for bar structures using robust optimization. The analysis centers on an orthogonal steel frame, with specific emphasis on columns subjected to high axial forces. The analysis incorporates the second-order theory, and the preliminary assessment of the steel frame's safety level involves determining the reliability index and failure probability using the Monte Carlo Method. Robust optimization is performed using a second-order response surface, which effectively mitigates the impact of uncontrollable model parameters. The second-order method accounts for non-linearity and interactions between variables in the model, enabling the identification of optimal solutions with a reduced need for experimental analysis. Reliable results are generated using an optimal Latin cubes plan for

conducting experiments, ensuring even and balanced sampling of the parameter space. This approach accelerates the analysis process while maintaining result reliability. The proposal of a mathematical-numerical algorithm for optimization that accounts for the random nature of design parameters contributes to the innovative nature of this research.

## 2 Materials and Methods

### 2.1 Displacement Method and Second-Order Beam Theory

To reduce computation time, we employed explicit forms of the performance function and constraints. The calculations are based on the classical displacement method and the second-order theory. This method involves several simplifying assumptions, including assuming small curvatures of the member axis in the current configuration, assuming flat cross-sections (known as Bernoulli's geometric hypothesis), assuming longitudinal non-deformability, assuming a linear-elastic physical law, and assuming material continuity, homogeneity, and isotropy. However, the second-order theory does not account for the principles of stiffness (small displacements) and superposition. The degrees of freedom consist of translational and rotational displacements of nodes. By imposing constraints on unknown displacements, the level of geometric indeterminacy can be determined, resulting in the derivation of additional equilibrium equations known as canonical equations. The right-side vector in the system of canonical equations represents the reactions of constraints determined by the external load.

These formulas establish a relationship between the forces and displacements associated with the local system of a given member. Our analysis focuses on a perfectly elastic prismatic rod with a length of  $l$  and a bending stiffness of  $EJ$  (see Figure 1). This rod serves as an illustration of the behavior of the columns in the frame, where significant axial force is considered alongside bending. Transformation formulas are derived through analytical solutions to the relevant boundary problem.

To perform the computations, it is necessary to derive a differential equation representing the equilibrium of forces on two planes perpendicular to the axis, located at distances  $x$  and  $x + dx$  from the origin of the coordinate system. Figure 2 depicts a cut section of the member with a length of  $dx$  in a deformed configuration, subjected to external load and two systems of cross-sectional forces that represent the interaction with the remaining portions of the member.

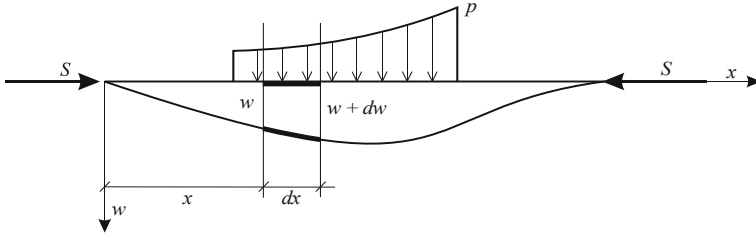


Figure 1

Rod in deformed configuration

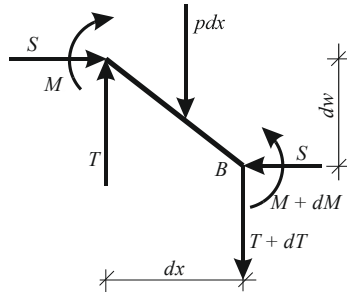


Figure 2

Section of the rod  $dx$  long

The section of the rod must be in equilibrium, so the equilibrium must be met:

$$\begin{cases} \sum W = -T + T + dT + p dx = 0 \\ \sum M_B = -M + M + dM - T dx - S dw + p dx \cdot \frac{dx}{2} = 0 \end{cases} \quad (1)$$

The quantity  $dx$  in the equation  $\frac{p dx^2}{2}$  is infinitesimally small, so we can skip it.

$$\begin{cases} \frac{dT}{dx} + p = 0 \\ \frac{dM}{dx} - T - S \frac{dw}{dx} = 0 \rightarrow T = \frac{dM}{dx} - S \frac{dw}{dx} \end{cases} \quad (2)$$

$$\begin{cases} \frac{dT}{dx} = -p \\ \frac{dT}{dx} = \frac{d^2 M}{dx^2} - S \frac{d^2 w}{dx^2} \end{cases} \quad (3)$$

$$\frac{d^2 M}{dx^2} - S \frac{d^2 w}{dx^2} = -p \quad (4)$$

$$M = -EJ \frac{d^2 w}{dx^2} \quad (5)$$

$$\frac{d^2 M}{dx^2} = -EJ \frac{d^4 w}{dx^4} \quad (6)$$

$$-EJ \frac{d^4 w}{dx^4} - S \frac{d^2 w}{dx^2} = \frac{-p}{(-1)} \quad (7)$$

$$EJ \frac{d^4 w}{dx^4} + S \frac{d^2 w}{dx^2} = p \quad (8)$$

Transforming into the dimensionless space, we can write:  $\xi = \frac{x}{l}$

$$\frac{EJ}{l^4} \cdot \frac{d^4 w}{d\xi^4} + \frac{S}{l^2} \cdot \frac{d^2 w}{d\xi^2} = \frac{p}{\frac{l^4}{EJ}} \quad (9)$$

$$\frac{d^4 w}{d\xi^4} + \frac{Sl^2}{EJ} \cdot \frac{d^2 w}{d\xi^2} = \frac{pl^4}{EJ} \quad (10)$$

$$\sigma^2 = \frac{Sl^2}{EJ}, \text{ dimensionless parameter } \sigma^2$$

$$w^{IV} + \sigma^2 w^{II} = 0 \quad (11)$$

The solution of the homogeneous differential equation is an exponential function:

$$w = e^{k\xi} \quad (12)$$

where:  $k$  – the coefficient that we determine by substituting into the equation (11) the corresponding derivatives:

$$k^4 e^{k\xi} + \sigma^2 k^2 e^{k\xi} = 0 \quad (13)$$

$$(k^2 + \sigma^2)k^2 e^{k\xi} = 0 \quad (14)$$

$$\begin{array}{ccc} k^2 = 0 & \text{or} & k^2 + \sigma^2 = 0 \\ \downarrow & & \downarrow \end{array} \quad (15)$$

$$k_1 = k_2 = 0 \quad k_3 = i\sigma \quad k_4 = -i\sigma$$

The general integral of the equation (11) is therefore a function

$$w_0 = \tilde{C}_1 + \tilde{C}_2 \sigma \xi + \tilde{C}_3 e^{i\sigma \xi} + \tilde{C}_4 e^{-i\sigma \xi} \quad (16)$$

After using the Euler formula

$$e^{\pm i\alpha} = \cos \alpha \pm i \sin \alpha \quad \alpha \in R \quad (17)$$

Get:

$$w_0 = C_1 + C_2 \sigma \xi + C_3 \cos \sigma \xi + C_4 \sin \sigma \xi$$

$$w_0^I = C_2 \sigma - C_3 \sigma \sin \sigma \xi + C_4 \sigma \cos \sigma \xi$$

$$w_0^{II} = -C_3 \sigma^2 \cos \sigma \xi - C_4 \sigma^2 \sin \sigma \xi \quad (18)$$

$$w_0^{III} = C_3 \sigma^3 \sin \sigma \xi - C_4 \sigma^3 \cos \sigma \xi$$

$$w_0^{IV} = C_3 \sigma^4 \cos \sigma \xi + C_4 \sigma^4 \sin \sigma \xi$$

The cross-sectional forces: the bending moment and the transverse force after switching to a dimensionless variable  $\xi = \frac{x}{l}$  will be as follows:

$$T = -\frac{EJ}{l^3} (w^{III} + \sigma^2 w^I) = -\frac{EJ}{l^3} \sigma^3 C_2$$

$$M = -\frac{EJ}{l^2} w'' = \frac{EJ}{l^2} \sigma^2 (C_3 \cos \sigma \xi + C_4 \sin \sigma \xi) \quad (19)$$

The integration constants present in the above formulas depend on the way the member is supported. For a fixed rod with support on both ends, as shown in Figure 3, the following boundary conditions can be written:

$$\begin{cases} w(0) = w_i \\ w'(0) = l\varphi_i \\ w(l) = w_j \\ w'(l) = l\varphi_j \end{cases} \quad \begin{cases} C_1 + C_3 = w_i \\ C_2\sigma + C_4\sigma = l\varphi_i \\ C_1 + C_2\sigma + C_3 \cos \sigma + C_4 \sin \sigma = w_j \\ C_2\sigma - C_3\sigma \sin \sigma + C_4\sigma \cos \sigma = l\varphi_j \end{cases} \quad (20)$$

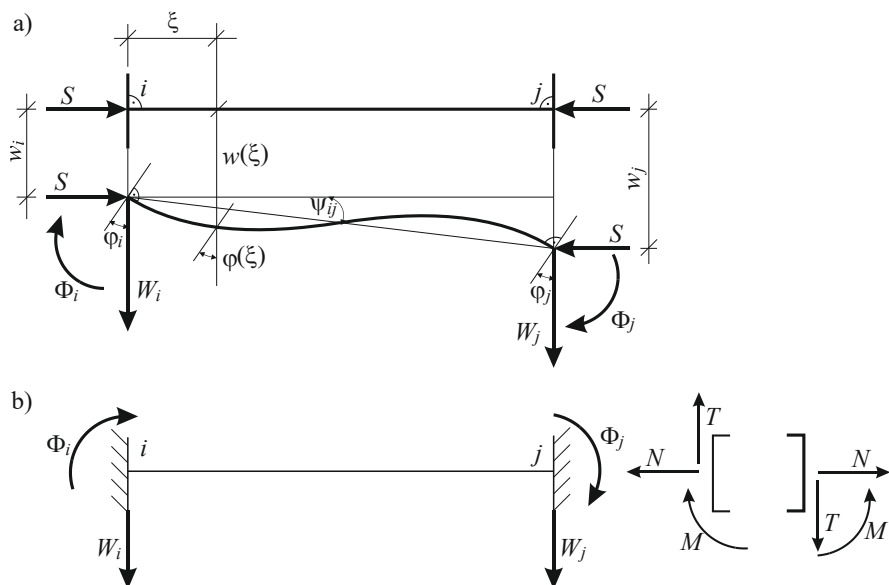


Figure 3

Fixed rod fixed on both sides

$$\Phi_i = M(0); \quad \Phi_j = -M(1); \quad W_i = -T(0); \quad W_j = T(1)$$

$$\Phi_i = \frac{EJ}{l^2} \sigma^2 C_3; \quad \Phi_j = -\frac{EJ}{l^2} \sigma^2 (C_3 \cos \sigma + C_4 \sin \sigma) \quad (21)$$

After some rearrangement, we obtain:

$$\Phi_i = \frac{EJ}{l} (\alpha\varphi_i + \beta\varphi_j - \vartheta\psi_{ij})$$

$$\Phi_j = \frac{EJ}{l} (\beta\varphi_i + \alpha\varphi_j - \vartheta\psi_{ij})$$

$$W_i = \frac{EJ}{l^2} (\vartheta\varphi_i + \vartheta\varphi_j - \delta\psi_{ij}) \quad (22)$$

$$W_j = -\frac{EJ}{l^2}(\vartheta\varphi_i + \vartheta\varphi_j - \delta\psi_{ij})$$

The coefficients  $\alpha$ ,  $\beta$ ,  $\delta$ ,  $\vartheta$  are not numbers, but the complex trigonometric functions of the parameter  $\sigma$ .

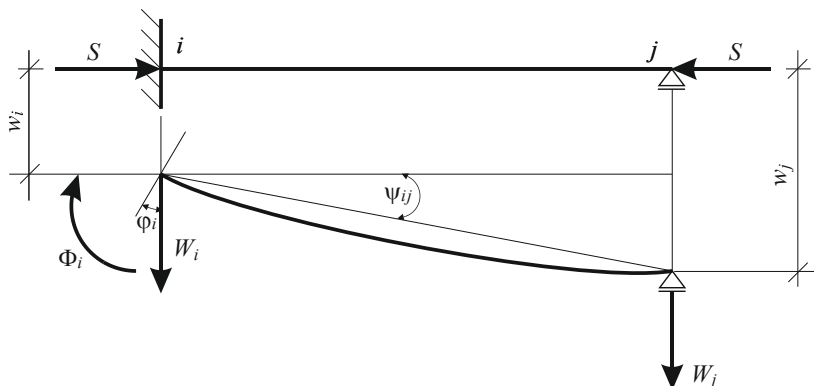


Figure 4

Rod fixed at one end and freely supported at the other

For a rod of the type fixed-joint (Figure 4), on the simply supported side (right), the bending moment is equal to zero  $\Phi_j = 0$

$$\Phi_j = 0 \Rightarrow \beta\varphi_i + \alpha\varphi_j - \vartheta\psi_{ij} = 0$$

$$\Phi_i = \frac{EJ}{l} \left[ \alpha\varphi_i + \beta \left( -\frac{\beta}{\alpha}\varphi_i + \frac{\vartheta}{\alpha}\psi_{ij} \right) - \vartheta\psi_{ij} \right] = \frac{EJ}{l} \left[ \underbrace{\left( \alpha - \frac{\beta^2}{\alpha} \right)}_{\alpha_1} \varphi_i - \underbrace{\left( \vartheta - \frac{\beta\vartheta}{\alpha} \right)}_{\alpha_1} \psi_{ij} \right]$$

$$W_i = \frac{EJ}{l^2} \left[ \vartheta\varphi_i + \vartheta \left( -\frac{\beta}{\alpha}\varphi_i + \frac{\vartheta}{\alpha}\psi_{ij} \right) - \delta\psi_{ij} \right] = \frac{EJ}{l^2} \left[ \underbrace{\left( \vartheta - \frac{\vartheta\beta}{\alpha} \right)}_{\alpha_1} \varphi_i - \underbrace{\left( \delta - \frac{\vartheta^2}{\alpha} \right)}_{\delta_1} \psi_{ij} \right]$$

$$W_i = \frac{EJ}{l^2} (\alpha_1\varphi_i - \delta_1\psi_{ij})$$

$$W_j = -\frac{EJ}{l^2} (\alpha_1\varphi_i - \delta_1\psi_{ij})$$

## 2.2 The Reliability Assessment using Monte Carlo Method

According to the codes [N4], the assessment of structural reliability is based on the concept of limit states, and their verification is conducted using a semi-probabilistic method with the use of partial safety factors. The purpose of these factors is to ensure the desired level of structural reliability. Approximate methods such as FORM [11-15] and SORM [16-18], as well as simulation techniques such as Monte

Carlo [19-23] and Importance Sampling [24-26], are extensions of the semi-probabilistic limit state method. The probabilistic approach allows for a more accurate and realistic modeling of structural materials, geometric parameters, and loads. In the present study, the Monte Carlo method was employed to determine the probability of failure.

The classic Monte Carlo simulation method involves generating realizations of the random vector  $\mathbf{X}$  according to the joint probability distribution density function  $f(\mathbf{x})$ . In the next step, for each realization of the random vector  $\mathbf{X}$ , the performance function is computed. The ratio of the number of 'hits' in the failure area to the total number of simulations provides an estimator of the probability of failure (see Figure 5). The above idea can be expressed by defining the characteristic function of the failure area set as:

$$X_{\Omega_f}(\mathbf{x}) = \begin{cases} 1 & \text{if } \mathbf{x} \in \Omega_f \\ 0 & \text{if } \mathbf{x} \notin \Omega_f \end{cases} \quad (24)$$

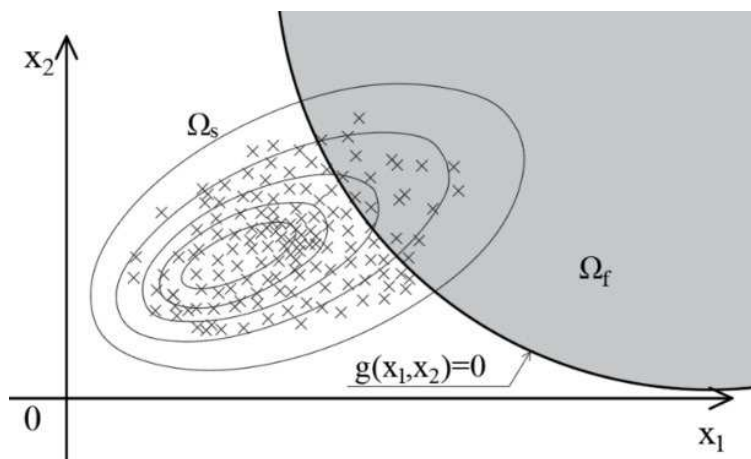


Figure 5  
Idea of Monte Carlo method

$X_{\Omega_f}(\mathbf{x})$  is therefore a random variable with a two-point distribution:

$$P[X_{\Omega_f}(\mathbf{X})=1]=P_f \quad P[X_{\Omega_f}(\mathbf{X})=0]=1-P_f \quad (25)$$

where:  $P_f = P[\mathbf{X} \in \Omega_f]$

$$Var[X_{\Omega_f}(\mathbf{X})] = E\left[\left(X_{\Omega_f}(\mathbf{X})\right)^2\right] - \left(E[X_{\Omega_f}(\mathbf{X})]\right)^2 = P_f - P_f^2 = P_f(1 - P_f) \quad (26)$$

In the Monte Carlo method, an estimator of the mean value of the characteristic function of the set of the form:

$$\tilde{X}_{\Omega_f}^0 = \frac{1}{K} \sum_{k=1}^K X_{\Omega_f}(\mathbf{X}_k) = \tilde{P}_f \quad (27)$$

where:  $\mathbf{X}_k$  - independent random vectors with a probability distribution defined by the density function  $f_x(\mathbf{x})$ ,  $K$  - the number of simulations.

The mean value and variance of the estimator are given as:

$$\begin{aligned} \tilde{P}_f^0 &= E[\tilde{P}_f] = \frac{1}{K} \sum_{k=1}^K X_{\Omega_f}^0(\mathbf{X}_k) = \frac{1}{K} K \cdot P_f = P_f \\ \sigma_{\tilde{P}_f}^2 &= Var[\tilde{P}_f] = \frac{1}{K^2} \sum_{k=1}^K Var[X_{\Omega_f}(\mathbf{X}_k)] = \frac{1}{K^2} K \cdot P_f(1 - P_f) = \frac{1}{K} P_f(1 - P_f) \end{aligned} \quad (28)$$

The coefficient of variation of the estimator is of the form:

$$v_{\tilde{P}_f} = \frac{\sigma_{\tilde{P}_f}}{P_f^0} = \sqrt{\frac{1 - P_f}{K \cdot P_f}} \quad (29)$$

The formula above indicates that in order to obtain a coefficient of variation of the estimator of 0.1 along with the expected probability of failure, which typically ranges from  $10^{-7}$  to  $10^{-4}$ , for real structures, it requires conducting  $K = 10^9 - 10^6$  simulations.

## 2.3 The Robust Optimization

Robust optimization is a non-deterministic optimization method that takes into account the random nature of parameters, which leads to scattering of the response. It typically enhances the reliability of the structure. In robust optimization, the objective function commonly includes the variance of the selected structural response quantity. Constraints can be deterministic or expressed through statistical moments. The optimal structure achieved through robust optimization is more resilient to fluctuations in parameter values. Unlike other types of optimization (e.g., reliability optimization), the precise determination of probability distribution types is not crucial. The values of the first statistical moments of the structural response primarily depend on the first moments of random variables. In the absence of adequate data, a uniform or normal distribution of variables is often assumed.

The goal of robust optimization is to minimize both the mean value and the variation (standard deviation) of the target function. Consequently, the task of robust optimization can be formulated as follows:

$$\text{Find values for variables: } \mathbf{X}_d, \boldsymbol{\mu}_x \quad (30)$$

$$\text{Minimizing: } \{E[f(\mathbf{X}_d, \mathbf{X}, \mathbf{P})], \sigma[f(\mathbf{X}_d, \mathbf{X}, \mathbf{P})]\} \quad (31)$$

Subjected to:

$$E[g_i(\mathbf{X}_p, \mathbf{X}, \mathbf{P})] - \tilde{\beta}_i \sigma[g_i(\mathbf{X}_p, \mathbf{X}, \mathbf{P})] \geq 0, \quad i=1, \dots, k_g, \quad (32)$$

$$\sigma [c_k(\mathbf{X}_d, \mathbf{X}, \mathbf{P})] \leq \sigma_k^u, \quad k=1, \dots, k_c, \quad (33)$$

$$X_{d_j}^l \leq X_{d_j} \leq X_{d_j}^u, \quad j = 1, \dots, n_d, \quad (34)$$

$$\mu_{x_r}^l \leq \mu_{x_r} \leq \mu_{x_r}^u, \quad r = 1, \dots, n_x, \quad (35)$$

where:  $f$  – objective function,  $\mathbf{X}_d$  – vector of deterministic design variables,  $\mathbf{X}, \mathbf{P}$  – vectors of random variables with expected values  $\boldsymbol{\mu}_x$  and  $\boldsymbol{\mu}_p$  respectively,  $g_i$  – constraint functions,  $c_k$  – functions whose standard deviations cannot exceed the permissible values  $\sigma_k^u$ ,  $\tilde{\beta}_i > 0$  – the coefficients corresponding to the constraints,  $g_i \geq 0$  represents the safety margins.

The vectors of random variables have been distinguished due to their different nature. Random variables  $\mathbf{X}$  can be defined as random design variables because their expected values  $\boldsymbol{\mu}_x$  change during the optimization process (where  $\boldsymbol{\mu}_x$  represents the design variable). This leads to a shift in the probability density function  $f_X(\mathbf{x})$ . On the other hand, the probability distribution of the vector  $\mathbf{P}$  remains unchanged during optimization, making these variables pure random parameters.

The concept of robustness is illustrated in Figure 6. The objective is to ensure that at the optimal point, the mean values of the constraint function  $g_i, i = 1, \dots, k_g$ , are greater than or equal to their corresponding standard deviations. The natural consequence of robust optimization is an increase in the reliability of the structure.

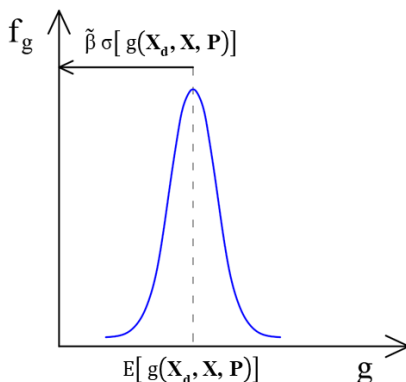


Figure 6

The concept of robust optimization limitations

In the above formulation, we are dealing with a multi-objective optimization problem: the mean value of  $E[f(\mathbf{X}_d, \mathbf{X}, \mathbf{P})]$  and the standard deviation of  $\sigma[f(\mathbf{X}_d, \mathbf{X}, \mathbf{P})]$ .

A widely used approach for identifying points in the Pareto set is scalarization of the multi-objective optimization problem, where a linear combination of the objectives is used as the objective function. By adjusting the coefficients (weights) assigned to each component of the vector, one can obtain points in the Pareto set.

The values of these points are also influenced by the designer's preferences, which focus on minimizing both the average value and variance. Therefore, the task can be reformulated as the following scalar optimization problem:

$$\text{Find values for variables: } \mathbf{X}_d, \boldsymbol{\mu}_x \quad (36)$$

$$\text{Minimizing: } \tilde{F} = \frac{1-\gamma}{\mu^*} E[f(\mathbf{X}_d, \mathbf{X}, \mathbf{P})] + \frac{\gamma}{\sigma^*} \sigma[f(\mathbf{X}_d, \mathbf{X}, \mathbf{P})] \quad (37)$$

subjected to:

$$E[g_i(\mathbf{X}_d, \mathbf{X}, \mathbf{P})] - \tilde{\beta}_i \sigma[g_i(\mathbf{X}_d, \mathbf{X}, \mathbf{P})] \geq 0, \quad i=1, \dots, k_g, \quad (38)$$

$$\sigma[c_k(\mathbf{X}_d, \mathbf{X}, \mathbf{P})] \leq \sigma_k^u, \quad k=1, \dots, k_c, \quad (39)$$

$$X_{d_j}^l \leq X_{d_j} \leq X_{d_j}^u, \quad j=1, \dots, n_d, \quad (40)$$

$$\mu_{x_r}^l \leq \mu_{x_r} \leq \mu_{x_r}^u, \quad r=1, \dots, n_x, \quad (41)$$

The weighting factor  $\gamma \in [0, 1]$  in the formula determines the meaning of each criterion, while  $\mu^*$  and  $\sigma^*$  are normalizing constants. Assuming  $\gamma = 0$ , the optimization problem is transformed into a simple task of minimizing the mean value, while for  $\gamma = 1$  to the task of minimizing the variance of the target function in the other words increasing structural robustness.

In the algorithm of robust optimization, we can distinguish 7 stages:

- 1) Definition of the permissible and choice of weighting factor  $\gamma$ .
- 2) Generating N implementation of the vector of design variables, which are evenly distributed in the current permissible area, according to the plan of optimal Latin Hypercubes.
- 3) Determination of statistical moments of the objective function and the constraint function for each of the N realizations of the vector  $\{\mathbf{X}_d, \boldsymbol{\mu}_x\}$ .
- 4) Structure of the response surface, e.g. by kriging, directly for individual statistical moments:  $\hat{\mu}_f, \hat{\sigma}_f, \hat{\mu}_{g_i}, \hat{\sigma}_{g_i}, \hat{\sigma}_{c_k}$ .
- 5) Solving the task of deterministic optimization

$$\text{Find the values of the variables: } \mathbf{X}_d, \boldsymbol{\mu}_x \quad (42)$$

$$\text{Minimizing: } \tilde{f}^{\text{DRS}} = \frac{1-\gamma}{\mu^*} \hat{\mu}_f(\mathbf{X}_d, \boldsymbol{\mu}_x) + \frac{\gamma}{\sigma^*} \hat{\sigma}_f(\mathbf{X}_d, \boldsymbol{\mu}_x) \quad (43)$$

Subjected to:

$$\hat{\mu}_{g_i}(\mathbf{X}_d, \boldsymbol{\mu}_x) - \tilde{\beta}_i \hat{\sigma}_{g_i}(\mathbf{X}_d, \boldsymbol{\mu}_x) \geq 0, \quad i=1, \dots, k_g, \quad (44)$$

$$\hat{\sigma}_{c_k}(\mathbf{X}_d, \boldsymbol{\mu}_x) \leq \sigma_k^u, \quad k=1, \dots, k_c, \quad (45)$$

$$\widehat{X}_{d_j}^l \leq \widehat{X}_{d_j} \leq \widehat{X}_{d_j}^u, \quad j=1, \dots, n_d, \quad (46)$$

$$\hat{\mu}_{x_r}^l \leq \mu_{x_r} \leq \hat{\mu}_{x_r}^u, \quad r=1, \dots, n_x, \quad (47)$$

where:  $\widehat{X}_d^l$ ,  $\widehat{X}_d^u$ ,  $\hat{\mu}_{x_r}^l$ ,  $\hat{\mu}_{x_r}^u$  - the current boundaries of the permissible area,  $\mu^*$  and  $\sigma^*$  - the normalization factors determined on the basis of the extreme values of the relevant moments obtained in point 3.

- 6) Check the terminate convergence condition.
- 7) Moving the permissible area over the optimal point determined in step 5. Reduction of the permissible area and return to 2.

### 2.3.1 Determination of the Response Surface by Polynomial Approximation

A crucial component of the algorithm employed in robust optimization is an efficient method for estimating the mean values and deviations of objective functions and constraints. To achieve this, various techniques have been utilized to approximate implicit functions of design variables using metamodels, also known as response surfaces. These surfaces are constructed by fitting suitable approximating functions to a set of experimental data points (Li et al. [26], Tang, Xu [27], Vining, Myers [28], Yeniay et al. [29]).

To approximate the response function, a commonly used method is to employ a low-degree polynomial. The purpose of the polynomial is not to precisely describe the entire response surface of the structure, but rather to provide the closest possible approximation near the limit state.

If the response of the structure is confined to a narrow region, it is possible to approximate the response surface using a linear function of independent random variables, which corresponds to a polynomial of the first-degree. Such a model is referred to as a first-order model and can be represented as:

$$\hat{y}(\mathbf{x}) = B_0 + \sum_{i=1}^n B_i x_i + \varepsilon \quad (48)$$

where:  $B_i$ ,  $i = 0, 1, \dots, n$  - dimension of the boundary state surface, - design variables,  $x_i \varepsilon$  - error taking into account the scatter of  $y_i$  values.

In cases where there is interaction between the realizations of random variables  $x_i$ , the first-order model can be extended to include second-order interaction terms, which take into account the curvature of the surface (taking into account the curvature of the surface) (Box, Wilson [30]):

$$\hat{y}(\mathbf{x}) = B_0 + \sum_{i=1}^n B_i x_i + \sum_{i=1}^n B_{ii} x_i^2 + \sum_{i < j}^n \sum_{j=2}^n B_{ij} x_i x_j + \varepsilon \quad (49)$$

In the strategy described in the paper, response surfaces are constructed not for the target function  $f$  or the constraint functions  $g_i$  or  $c_k$ , directly, but for their statistical moments. The approximate surfaces of the mean value and the standard deviation of these respective functions are taken into consideration. Typically, these surfaces are represented in polynomial form:

$$\hat{y}_\mu(\mathbf{z}) = b_0^\mu + \sum_{i=1}^{n_{dX}} b_i^\mu z_i + \sum_{i=1}^{n_{dX}} b_{ii}^\mu z_i^2 + \sum_{i=1}^{n_{dX}} \sum_{j=2, j>i}^{n_{dX}} b_{ij}^\mu z_i z_j \quad (50)$$

$$\hat{y}_\sigma(\mathbf{z}) = b_0^\sigma + \sum_{i=1}^{n_{dX}} b_i^\sigma z_i + \sum_{i=1}^{n_{dX}} b_{ii}^\sigma z_i^2 + \sum_{i=1}^{n_{dX}} \sum_{j=2, j>i}^{n_{dX}} b_{ij}^\sigma z_i z_j \quad (51)$$

where:  $\hat{y}_\mu$  – approximation of the mean value of the function ( $f$ ,  $g_i$  or  $c_k$ );  $\hat{y}_\sigma$  – approximation of the standard deviation of the function ( $\hat{y}_\sigma f$ ,  $g_i$  or  $c_k$ );  $z_i$ ,  $i=1, \dots, n_{dX}$  – design variables ( $X_d$  and  $\mu_x$ );  $n_{dX} = n_d + n_x$  – number of design variables.

### 3 Numerical Example

In order to illustrate the advantages of robust optimization, a steel single-storey frame with dimensions  $L=600\text{cm}$  and  $B=550\text{cm}$  (Figure 7) was analyzed. Both the bolt and the columns of the frame were modeled with steel square tubes with dimensions  $D = 39\text{cm}$  and  $d = 33\text{cm}$ , Young's module  $E = 210\text{GPa}$ , Poisson coefficient  $\nu = 0.3$ , yield strength  $f_y=235\text{MPa}$ . The structure was loaded with two forces with values,  $S = 1200\text{kN}$  and  $P = 120\text{kN}$ .

#### Static Analysis

According to the method of displacement, only horizontal displacement of the bolt is possible. Therefore, adopting the basic scheme of the displacement method, an additional bond blocking the movement was introduced. The reaction  $R$  in the bond was determined from the equilibrium equation of  $\sum X$  floor 1-2 of the frame (Figure 8).

$$\sum X = 0$$

$$P + R - W_1 - W_2 = 0 \quad (52)$$

$$R = W_1 + W_2 - P = 0$$

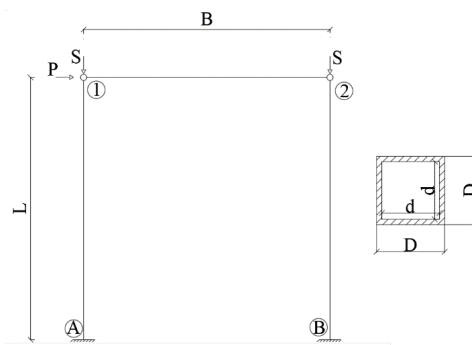


Figure 7

Geometry and cross-section of the steel single-storey frame

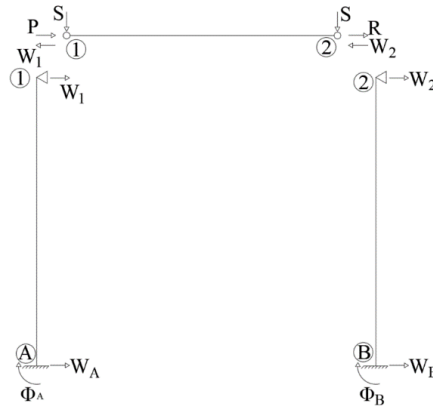


Figure 8

Basic scheme of the frame according to the method of displacement

The values of the parameter  $\sigma$  on both columns are the same ( $\sigma = \sqrt{\frac{SL^2}{EI}}$ ). In the case of a unit displacement  $\Delta$ , the angles of rotation of the columns 1-A and 2-B are equal to  $\Psi_{1A} = \Psi_{1B} = \frac{1}{L}$ . Using the transformation formulas, the equilibrium equation can be written:

$$2\delta_I(\sigma) \cdot \Delta = \frac{P \cdot L^3}{EI} \quad (53)$$

The horizontal displacement of the frame bolt is:

$$\Delta = \frac{P \cdot L^3}{2EI\delta_I(\sigma)} \quad (54)$$

$$M = \frac{EI}{L^2} (-\alpha_I(\sigma)) \frac{PL^3}{2EI\delta_I(\sigma)} = -\frac{PL}{2\sigma} \operatorname{tg} \sigma \quad (55)$$

### Reliability Analysis

The reliability analysis of the structure was carried out using the Monte Carlo method (random sample size:  $10^6$ ). The geometrical characteristics of the cross-sections of the members were adopted as random variables ( $D$  – the external dimension of the cross-section,  $d$  – the internal dimension of the cross-section). The random variables are described in Table 1. Random variables are not correlated. The initial mass of the modeled structure is  $M = 5935.36$  kg. The value of the coefficient of variation was set at 2% for the external dimension  $D$  and 1% for the internal dimension  $d$  of the cross-section.

The example assumes two boundary functions describing the serviceability limit state SGU and the ultimate limit state SGN, respectively.

Table 1  
Description of random variables

Random variables $x_i$	Average values [cm]	Standard deviation [cm]	Coefficient of variation [%]
D	39	0.78	2
d	33	0.33	1

$$f_{SGU} = \Delta_{max} - \Delta \quad (56)$$

where:  $\Delta$  – horizontal displacement of the frame bolt,  $\Delta_{max}$  – maximum horizontal displacement equal to  $L/150=4$  cm.

$$f_{SGN} = 0.87 \cdot W_y \cdot f_y - M \quad (57)$$

where:  $W_y$  – the section modulus.

The reliability index for SGU and SGN were  $\beta^{SGU} = 2.29$  and  $\beta^{SGN} = 3.82$ , respectively.

### Deterministic Optimization

In the next step, we look for optimal cross-section dimensions, using the classic deterministic optimization algorithm.

The objective function is the mass of the structure:

$$f_C = \text{minimum} (\rho \cdot A \sum_{i=1}^3 L_i) = \text{min} (Mass) \quad (58)$$

where:  $L_i$  – length of the  $i^{\text{th}}$  member,  $A$  – cross-sectional area,  $\rho$  – volumetric density of steel.

Simple bounds are described in Table 2. They are the upper and lower limits of the searched design variables.

Table 2  
Simple bounds of design variables

Design variable	Lower limit [cm]	Upper limit [cm]
D	36.66	41.34
d	32.34	33.66

Simple bounds were imposed on the basis of literature [31, 32, N5, N6]. For this case 2% tolerance of the cross-sectional dimensions of the pipe was assumed. Inequality limitations are formulated as conditions for not exceeding the permissible displacement of the horizontal bolt of the frame and not exceeding 87% of the load capacity for bending:

$$f_{SGU} = \Delta_{max} - \Delta = 4 - \Delta \quad (59)$$

$$f_{SGN} = 0.87 \cdot W_y \cdot f_y - M \quad (60)$$

The resulting cross-sectional dimensions are summarized in Table 3. The value of the objective function was 3862.916 kg.

Table 3  
Values of design variables obtained in deterministic optimization

Design variable	Optimal value [cm]
D	37.61
d	33.66

The probability of failure and the reliability index were also verified. For SGU and SGN functions, respectively:  $p^{SGU} = 0.495$ ,  $\beta^{SGU} = 0.011$ ,  $p^{SGN} = 0.065$ ,  $\beta^{SGN} = 1.51$ .

### Robust Optimization

The objective function is mass of the structure, but assuming that it takes into account the weighting factor  $\gamma$  determining the meaning of each of the criteria. Design variables are the expected values of the external and internal dimensions of the cross-section:  $\mu_D$ ,  $\mu_d$ . The value of the coefficient of variation was set at 2% and 1%.

The task of robust optimization takes the form of:

$$\text{Find the values of the variables: } \mu_D, \mu_d \quad (61)$$

$$\text{Minimizing: } f_C = \frac{1-\gamma}{\eta^*} E [Mass] + \frac{\gamma}{\sigma^*} \sigma [Mass] \quad (62)$$

Subjected to:

$$E[4 - \Delta] - \widehat{\beta}^{SGU} \cdot \sigma[4 - \Delta] \geq 0 \quad (63)$$

$$E[0.87 \cdot W_y \cdot f_y - M] - \widehat{\beta}^{SGN} \cdot \sigma[0.87 \cdot W_y \cdot f_y - M] \geq 0 \quad (64)$$

$$36.66 \leq \mu_D \leq 41.34 \quad (65)$$

$$32.34 \leq \mu_d \leq 33.66 \quad (66)$$

where:  $\gamma \in [0, 1]$  – weighting factor determines the importance of each of the criteria,  $\eta^*$ ,  $\sigma^*$  – normalizing constants,

Robust optimization was performed using the second-order response surface. Experiments are generated according to the plan of optimal Latin cubes. The parameters:  $\gamma = 0.5$ ,  $\widehat{\beta}^{SGU} = 2.0$ ,  $\widehat{\beta}^{SGN} = 3.0$ .

The values of the design variables obtained as a result of robust optimization are summarized in Table 4. The weight of the structure in this case was 5150.32 kg.

Table 4  
Mean values of random variables obtained in robust optimization

Random variable	Optimal value [cm]
D	38.03
d	32.34

The probability of failure and reliability index were verified for SGU and SGN functions, respectively:  $p^{SGU} = 0.04452$ ,  $\beta^{SGU} = 1.700$ ,  $p^{SGN} = 0.00035$ ,  $\beta^{SGN} = 3.390$ .

### Impact of the $\gamma$ Weighting Factor on Optimization Results

The weighting factor  $\gamma \in [0, 1]$  determines the importance of each of the criteria of the objective function. If  $\gamma = 0$ , the optimization problem is transformed into a regular average value minimization task, while for  $\gamma = 1$  into a variance value minimization task. The influence of the weighting factor on the values of the optimized design variables is presented on Figure 9.

The higher the weight of the average value, the more optimal the structure should be. And when weights of the standard deviation is increased, the robustness of the structure is increasing, but optimality is reduced.

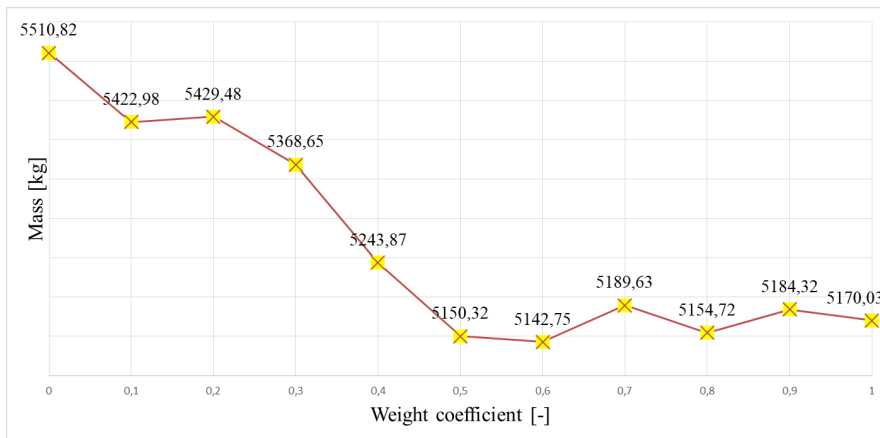


Figure 9  
Mass of optimal structure depending on the weight of the average value

### Conclusions

An indispensable element of rational structural design should include both deterministic optimization and robust optimization. Through robust optimization, we obtain designs that are slightly less optimal in terms of weight but significantly safer, as indicated by the reliability indices. Optimal structures are sensitive to imperfections in design parameters. Optimal solutions located near the limit state surface can easily become infeasible if parameter values deviate even slightly from

the assumed nominal values. Incorporating the uncertainty of design parameters in the formulation of robust optimization effectively addresses this issue by providing the designer with control over the level of structural safety. By controlling the value of the weighting factor, we can consciously decide whether to prioritize minimizing the average value or the variance of the target function.

Furthermore, it is recommended to integrate robust optimization as a standard practice in structural design processes. This approach allows engineers to account for the random nature of design parameters and provides a more realistic and accurate representation of the structure's behavior under uncertain conditions. By considering both the mean value and variance of the target function, designers can achieve designs that are not only efficient but also resilient to parameter variations.

Future research efforts should focus on refining the methodologies and techniques used in robust optimization, such as improving the accuracy of response surface models and exploring advanced optimization algorithms. Additionally, investigations into the impact of different probability distribution assumptions and the development of techniques for handling correlated random variables would further enhance the robustness and reliability of structural designs.

In conclusion, incorporating robust optimization into the design process enhances the overall safety and performance of structures, ensuring their functionality and minimizing the risks associated with parameter uncertainties. By embracing robust optimization as a standard approach, engineers can achieve designs that strike a balance between efficiency and resilience, meeting the demands of modern structural engineering.

## References

- [1] N. Kuschel, R. Rackwitz: Optimal design under time-variant reliability constraints, *Struct. Saf.*, Vol. 22, No. 2, 2000, pp. 113-128, DOI: 10.1016/S0167-4730(99)00043-0
- [2] H. Streicher, R. Rackwitz: Reliability-oriented optimization for time-invariant problems with optimization algorithm JOINT 5, research report, Technical Report Project 28159, 2001
- [3] H. Streicher, R. Rackwitz: Structural optimization - a one level approach, S. Jendo, K. Doliński, M. Kleiber (eds.), *AMAS Workshop on Reliability-Based Design and Optimization - RBO'02*, 2002
- [4] N. Kuschel, R. Rackwitz: Two basic problems in reliability-based structural optimization, *Math. Methods Oper. Res.*, Vol. 46, No. 3, 1997, pp. 309-333, DOI: 10.1007/BF01194859
- [5] B. D. Youn, K. K. Choi: A new response surface methodology for reliability-based design optimization, *Comput. Struct.*, Vol. 82, No. 2-3, 2004, pp. 241-256, DOI: 10.1016/j.compstruc.2003.09.002.

- [6] M. Habashneh, M. Movahedi Rad, Reliability based geometrically nonlinear bi-directional evolutionary structural optimization of elasto-plastic material. *Sci Rep* 12, Vol. 5989, 2022, DOI: 10.1038/s41598-022-09612-z
- [7] M. Movahedi Rad, M. Habashneh, J. Lógó, Elasto-Plastic limit analysis of reliability based geometrically nonlinear bi-directional evolutionary topology optimization, *Structures*, Vol. 34, 2021, pp. 1720-1733, DOI:10.1016/j.istruc.2021.08.105.z
- [8] I. Doltsinis, Z. Kang: Robust design of non-linear structures using optimization methods, *Comput. Methods Appl. Mech. Eng.*, Vol. 194, No. 12–16, 2005, pp. 1179–1795, DOI: 10.1016/j.cma.2004.02.027
- [9] W. Chen, W. Fu, S. B. Biggers and R. A. Latour: An affordable approach for robust design of thick laminated composite structure, *Optim. Eng.*, Vol. 1, No. 3, 2000, pp. 305–322, DOI: 10.1023/A:1010078107194
- [10] P. Zabojszcza, U. Radoń and P. Tazowski: Robust optimization of a single-layer lattice dome, *Modern Trends in Research on Steel, Aluminium and Composite Structures*, 2021, DOI: 10.1201/9781003132134
- [11] R. Rackwitz, B. Fiessler: Structural reliability under combined random load sequences, *Comput. Struct.*, Vol. 9, No. 5, 1978, pp. 489–494
- [12] A. M. Hasofer, N. Lind: Exact and Invariant Second-Moment Code Format, *J Eng Mech Div-ASCE*, Vol. 100, No. 1, 1974, pp. 111–121
- [13] W. Mochocki, U. Radoń: Analysis of Basic Failure Scenarios of a Truss Tower in a Probabilistic Approach, *Appl. Sci.*, Vol. 9, 2662, 2019, DOI: 10.3390/app9132662
- [14] K. Kubicka, P. Obara, U. Radoń and W. Szaniec: Assessment of steel truss fire safety in terms of the system reliability analysis, Vol. 19, No 2, 2019, pp. 417 – 427, DOI: 10.1016/j.acme.2018.12.002
- [15] A. Dudzik: Reliability Assessment of Steel-Aluminium Lattice Tower, *IOP Conf. Ser. Mater. Sci. Eng.*, Vol. 245, pp. 1–9, 2017, DOI: 10.1088/1757-899X/245/3/032072
- [16] M. Hohenbichler, S. Gollwitzer, W. Kruse and R. Rackwitz: New light on first and second order reliability methods, *Struct. Saf.*, No. 4, 1987, pp. 267-284
- [17] A. Der Kiureghian, M. De Stefano: Efficient algorithm for second-order reliability analysis, *J. Eng. Mech.*, Vol. 117, No. 12, 1991, pp. 2904–2923
- [18] A. Dudzik and U. Radoń: The evaluation of algorithms for determination of the reliability index, *Arch. Civ. Eng.*, Vol. LXI, No. 3, 2015, pp. 133–147, DOI: 10.1515/ace-2015-0030

- [19] L. Rossi, M. H. M. Winands and C. Butenweg: Monte Carlo Tree Search as an intelligent search tool in structural design problems, *Eng. Comput.*, 2021, DOI: 10.1007/s00366-021-01338-2
- [20] B. Potrzyszcz-Sut: Reliability analysis of shell truss structure by hybrid Monte Carlo method, *Journal of Theoretical and Applied Mechanics*, No. 58, 2020, pp. 469–482, DOI: 10.15632/jtam-pl/118886
- [21] A. Dudzik and B. Potrzyszcz-Sut: Hybrid Approach to the First Order Reliability Method in the Reliability Analysis of a Spatial Structure, *Appl. Sci.-BASEL*, Vol. 11, No. 2:648, 2021, DOI: 10.3390/app11020648
- [22] U. Radoń, P. Zabojszcza: The impact of node location imperfections on the reliability of single-layer steel domes, *Appl. Sci.* 2019, 9(13), 2742; <https://doi.org/10.3390/app9132742>
- [23] U. Radoń, P. Zabojszcza: Stability analysis of the single-layer dome in probabilistic description by the Monte Carlo method, *J. Theor. Appl. Mech.*, Vol. 58, No. 2, 2020, pp. 425–436, DOI: 10.15632/jtam-pl/118950
- [24] K. Doliński: Importance Sampling Techniques in Reliability Calculation, Vol. 37, IPPT PAN, Warszawa, 1988
- [25] M. Fujita, R. Rackwitz: Updating first and second order reliability estimates by importance sampling, *Jpn. Soc. Civ. Eng.*, Vol. 392, No. I-9, 1988, pp. 53–59
- [26] Y. Q. Li, Z. S. Cui, X. Y. Ruan, D. J. Zhang: CAE-based six sigma robust optimization for deep-drawing sheet metal process, *The International Journal of Advanced Manufacturing Technology*, Vol. 30, 2006, pp. 631 – 637
- [27] L. C. Tang, K. Xu, A unified approach for dual response surface optimization, *Journal of Quality Technology*, Vol. 34, 2002, pp. 437 – 447
- [28] G. G. Vining, R. H. Myers: Combining Taguchi and response surface philosophies: a dual response approach, *Journal of Quality Technology*, Vol. 22, 1990, pp. 38–45
- [29] O. Yeniay, R. Unal, A. R. Lepsch: Using dual response surfaces to reduce variability in launch vehicle design: A case study, *Reliability Engineering and System Safety*, Vol. 91, 2006, pp. 407– 412
- [30] G.E.P. Box, K.B. Wilson: On the Experimental Attainment of Optimum Conditions (with discussion), *Journal of the Royal Statistical Society Series B* 13, 1951, pp. 1–45
- [31] E. Urbańska-Galewska: Tolerances in steel structures connected to screws, *Monograph*, Vol. 59, Gdańsk University of Technology Publishing House, Gdańsk, 2005

- [32] E. Urbańska-Galewska: Tolerances in the construction of steel bar structures, Monograph, Vol. 52, Gdańsk University of Technology Publishing House, Gdańsk, 2004

**List of standards**

- N 1. EN 1993-1-1. Eurocode 3: Design of steel structures – Part 1–1: General rules and rules for buildings.
- N 2. EN 1991-1-3. Eurocode 1: Actions on structures – Part 1–3: General actions – Snow loads.
- N 3. EN 1991-1-4. Eurocode 1: Actions on structures – Part 1–4: General actions – Wind actions.
- N 4. EN 1990: 2002. Eurocode – Basis for structural design.
- N 5. PN-EN 10210-2. Hot finished steel structural hollow sections – Part 2: Tolerances, dimensions and sectional properties.
- N 6. PN-EN 1090-2. Execution of steel structures and aluminium structures. Part 2: Technical requirements for steel structures.

# Dynamic Analysis of Geosynthetic-reinforced Pile-supported Embankment for a High-Speed Rail

**Rashad Alsirawan, Edina Koch**

Széchenyi István University. Egyetem tér 1, H-9026 Győr, Hungary  
alsirawan.rashad@sze.hu, koche@sze.hu

---

*Abstract: Geosynthetic-Reinforced-Pile-Supported (GRPS) embankments are a trustworthy option ideal to support the railways over soft soils. They are widely used for the time-bound infrastructure projects. The majority of earlier research concentrated on the analysis of the GRPS embankments under static loads while the studies on the behavior of these constructions under dynamic loads are scarce. The fundamental purpose of this study has been to better comprehend the dynamic behavior of GRPS embankments in terms of stresses and settlements distribution via 3D modeling employing the finite element method (FEM). The advanced constitutive model of Hardening soil with small-strain stiffness was utilized to simulate the behavior of the soils under dynamic loads and the train load was modeled according to the recommendations of LM71 Eurocode. The results indicate to the contribution of the piles and geosynthetic reinforcement in the decrease of the settlements. The behavior of settlements and stresses under static and dynamic loads is similar. The load efficiency of the piles decreases during the passage of the train remarkably. The train speed affects obviously on the behavior of the GRPS embankment*

*Keywords: GRPS embankment; 3D modeling; stresses and settlements distribution; dynamic loads; load efficiency*

---

## 1 Introduction

Rail transport is among the most ecologically responsible solutions of transportation in the world since it relies heavily on electric haulage [1]. Generally, the geosynthetic reinforcement with piles is considered an ideal solution to support the embankments of high-speed railways over soft soil layers [2]. This technology contributes to substantially reduce embankment settlement, construction time, and cost [3].

The behavior of Geosynthetic-Reinforced Pile-Supported (GRPS) embankments under static loading is investigated extensively. The mechanism of load transfer in the GRPS embankments is described as a combination of different phenomena:

the soil arching due to the difference between stiffness of piles and surrounding soft soil, tensioned membrane effect of the geosynthetic, frictional behavior of soil-geosynthetic interface and the soft soil support. Different researchers have investigated the behavior of GRPS embankments and suggested many analytical methods of design (Terzaghi [4], Low *et al.* [5], Russell & Pierpoint [6], Abusharar *et al.* [7], BS 8006 [8], EBGEO [9], CUR226 [10], Pham [11]).

In regards of cyclic loading, the literature review is much more limited, however the behavior of the GRPS embankment under this type of loading is crucial owing to the real representation of the problem. Heitz *et al.* [12] indicated that numerous factors reduce the soil arching and, as a result, the load efficiency ( $E$  is the ratio of load applied over the pile head to the total load). Based on a small-scale model of a GRPS embankment exposed to cyclic loading. These factors include pile configuration, layers of geosynthetic, number of cycles, and loading frequency. Yu *et al.* [13] compared the difference in the behavior of piled embankment under static and traffic loads, the results indicate that the soil arching phenomenon has disappeared after 300 cycles and the vertical stress carried by the soft soil increases with the cycle numbers. Han and Bhandari [14] developed a 2D discrete element model (DEM) of a GRPS embankment and discovered that the stress concentration ratio (SCR is the ratio of the stress over the pile head to the stress over the soft soil in a unit cell) and the geogrid tension increase as the embankment height, geogrid stiffness, and pile elastic modulus increase under cyclic loads.

Han *et al.* [15] created a laboratory model and the model tests was followed by FE analysis. The findings indicate that the dynamic load has an obvious influence on the soil arching if the embankment height is not enough. Moreover, the geogrid presence contributes in more stability of the soil arch if the ratio of embankment height to pile spacing is more than 1.4. Zhuang *et al.* [16] investigated the behavior of piled embankment using FE method and Mohr–Coulomb to model the embankment soil. The results indicated that the applied vertical stress over the pile cap increases with the increase of cyclic loading to a certain point of time and then decreases due to the reduction of the soil arching. The vertical stress increases also with the decrease of the vehicle speed. The researchers stated that the complicated dynamic soil behavior of the embankment cannot be represented adequately due to the adoption of the simple constitutive model Mohr-Coulomb. To investigate the behavior of the GRPS embankment, Houda *et al.* [17] performed several 3D small-scale model tests under low frequency cyclic load. The investigation revealed a settlement accumulation, particularly in the first ten cycles, where 50 % settlement accumulation occurred. Furthermore, applying the cycles increases load efficiency. After 20–30 cycles, a value of roughly 1, in which practically the full load is transferred to the pile heads, is obtained and thereafter remains stable.

Zhuang *et al.* [18] investigated a range of 3D finite element (FE) models of GRPS embankment under cyclic load. The parametric study revealed that settlements increase with vehicle wheel load and speed, whereas the soil arching is reduced

with larger vehicle load and speed. 3D numerical simulations of GRPS embankment were conducted in the Pham et al. [19] study. The analysis results indicated that the SCR decreases with the number of cycles due to the reduction of the soil arching, the vehicle speed contributes to quick dissipation of the soil arching. Additionally, the cumulative settlements increase as the vehicle speed and embankment height rise. The researchers also discovered that the influence of the number of geosynthetic layers could be negligible. Wang et al. [20] observed through the 3D dynamic analysis that the pile stiffness and the fixed end piles can reduce the stresses in the soft subsoil. Aqoub et al. [21], based on experimental analysis, observed an improvement of the GRPS embankment behavior related to the load efficiency and settlement under cyclic loading with the increase of geosynthetic layer numbers. It was noticeable that approximately 50% of the embankment surface settlement occurred during the first 100 cycles. On the other hand, the researchers found also that the geosynthetic tension increases during different cyclic loading stages, however, remains nearly constant in every stage.

The static and dynamic performance of GRPS embankment was investigated Bi et al. [22] numerically, the researchers observed that the SCR decreases under long-term traffic loads and the stiffness of the soft soil has a main role in undermining the performance of soil arching. They observed also that the differential settlements increase with the cycles number to finally be in a stable state. Zhuang et al. [23] evaluated the GRPS embankment under cyclic loading and unloading through the FE analysis. The parametric study demonstrates that the higher vehicle speed and the wheel load and the lower the geosynthetic stiffness, the load efficiency lower. Patel et al. [24] analyzed the dynamic response of GRPS embankment and found that for an embankment height to pile spacing ratio ( $a$ ) of less than or equal to 4.5, geosynthetic stiffness of 3000 kN/m is adequate to achieve high SCR, as well as to decrease the differential settlements under dynamic loads and different heights of the embankment. If  $a$  is more than 4.5 then the SDR increases with the geosynthetic stiffness. Fang et al. [25] provided a dual-beam model to simulate the pavement and geosynthetic in order to assess the dynamic behavior of the GRPS embankment. The findings indicate that the moving load position has an influence on the GRPS embankment's stress and deflection distribution. Deflection and stress increase as the speed of the moving load increases. By increasing pile stiffness and geosynthetic modulus, the effect of moving load speed on the GRPS embankment can be decreased, these two parameters contribute to improve the stability of the GRPS embankments. Duan et al. [26] discussed the redistribution of the dynamic stress under moving train load due to the soil arching phenomenon in the embankment body and the contribution of geogrid in this process. 3D simulations are employed in the study to better elucidate the dynamics of GRPS embankments under a single cycle of high-speed train. Proper constitutive models are utilised to simulate the behavior of the bearing soil, soft soil and embankment fill based on the recommendations of Shahraki et al. [27] to better representation of their behavior. Results highlight the influence of using piles and the geosynthetic reinforcements to sustain the

embankment, and the behavior of the vertical stresses and settlements in the embankment body. The indices of describe the behavior of the GRPS embankment are different as shown in the literature, this paper adopts the load efficiency, the geosynthetic tension, and the settlements to find out the influences of the embankment height, cover ratio, and train speed on the aforesaid indices.

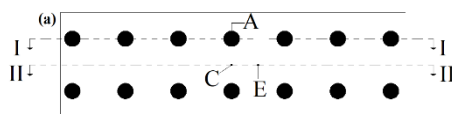
## 2 Finite Element Modelling

### 2.1 Description of GRPS Embankment Model

The technology employed to support embankments consists of (i) a network of vertical elements (piles), which are commonly slender and cylindrical in shape. The installation method (driving, boring, etc...) and mesh pattern (square, triangle, rectangle, etc...) of the piles are adopted based on soil conditions and both geometry and nature of applied loads. The installation of piles is regarded as the first stage of construction. (ii) a load transfer platform (LTP), this platform typically composed of a granular soil and one horizontal layer or more of geosynthetic reinforcement, and this is the second stage of construction. The last stage is the construction of the embankment body [28].

GRPS embankment is constructed atop a simple geological profile consisting of a 10-m soft soil layer resting on a stiff soil of gravel. The groundwater level is located directly at the soft soil layer surface. The 13.0 m wide embankment with a height of 2.6 m and slope angle of 1:1.15 is supported by a network of piles and one layer of geogrid as illustrated in Figure.1.

At the top of the embankment, a clustered ballast layer with a thickness of 0.35 m capped by transverse sleepers to support the railway track. In a square pattern, circular-cross-section piles with a diameter of 0.6 m and pile spacing of 2.0 m are installed. This network of piles penetrates the gravel's stiff layer. The geogrid layer with a stiffness of 5000 kN/m is located 0.1 m above the pile heads. The following points are utilized to display the outputs of the numerical analysis. Points B and D are located on the ballast surface. Points A, C, and E are located on the embankment's base level, as indicated in Figure 1. Longitudinally, Points D, C, and E are 2 meters from the boundaries, whereas Points B and A are 3 meters away.



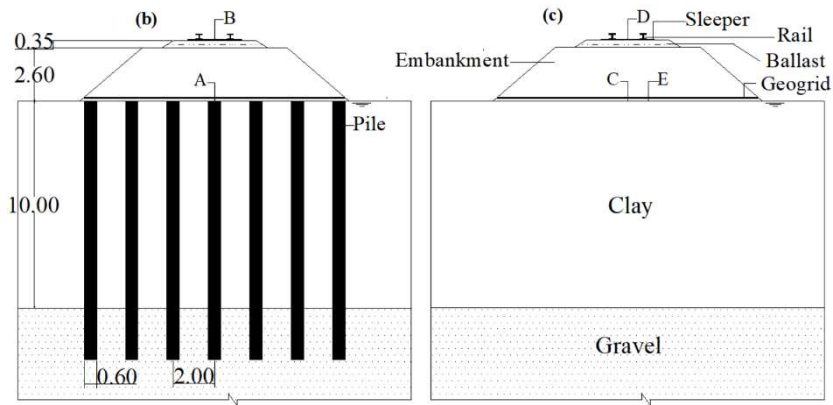
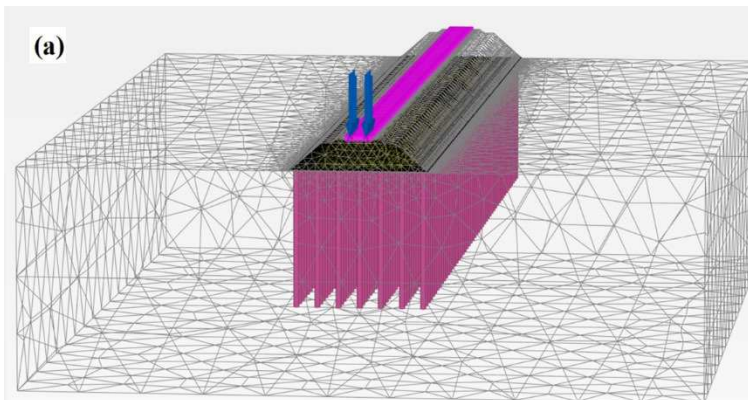


Figure 1

GRPS embankment profile (a) Plan view at the embankment base plane; (b) section I-I; (c) section II-II

## 2.2 3D Modelling of the Problem

To simulate the dynamic behavior of the GRPS embankment under the moving load which represents the high-speed train, a model of 96 m length and 45 m width was created in Plaxis 3D CONNECT Edition V20 program. The absorbent boundaries and Standard fixities were employed to minimize the reflections of the waves at the boundaries. The finite element mesh of the GRPS embankment is shown in Figure 2.



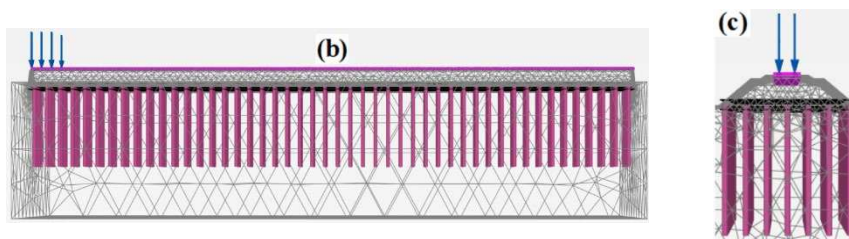


Figure 2

(a) Numerical model of GRPS embankment; (b) Side view; (c) Front view

The rails, rail fastening systems, and sleepers, all of which lay on the ballast layer and the underlying subgrade represent the typical components of the railway track [29]. The rails and sleepers are modeled as beam elements. The properties of UIC 60 rail [30] are adopted in the simulation, and the distance between the two rails is 1.5 m. The properties of concrete sleeper type B70 [30] are adopted by supplying the area moment of inertia, the model included 121 sleepers with a center-to-center distance of 60 cm. The properties of rail and sleepers are listed in Table 1.

Table 1  
The properties of UIC60 rail and B70 sleeper

Basic parameters	Characters and units	UIC60 rail	B70 sleeper
Cross-sectional area	$a$ (m <sup>3</sup> )	0,0077	0.0513
Unit weight	$\gamma$ (kN/m <sup>3</sup> )	78	25
Young's modulus	E (MPa)	200000	36000
Inertia moments	I2 (m <sup>4</sup> )	0,00000513	0.00024
	I3 (m <sup>4</sup> )	0,00003	0.0253

The LM71 Eurocode load model was used to simulate the moving train, which includes eight dynamic point loads of 125 kN vertical force with a constant distance of 1.6 m. Each point load has its own dynamic multiplier in Plaxis 3D, which is characterized as a time-shear force signal. The “Beams on the elastic foundation” theory can be used to determine the shear forces in the rails. The shear force signal is multiplied by the dynamic point load (125 kN) in each time step, if the moving train's acceleration is negligible and the distance between the dynamic point loads is constant, the time step is deemed constant. In our case study, the train with speed of 250 km/h passes 1.6 m in 0.023 sec., the time frame during which the dynamic load may be deemed fixed is represented by the earlier period. In this model of 96 m long, the total time between the first and the last load is 1.38 sec., an extra 1.12 sec. was provided to dissipate the majority of the waves created by the moving train to obtain full dynamic time of 2.5 sec. All of the point loads have their values for each time step. As a result, the point loads are continually triggered and reach their maximum levels when the moving train passes over them.

### 2.2.1 Material Parameters

Benz [31] proposed the generalized Hardening Soil model with Small-strain stiffness (HSS) through the development of the Hardening Soil (HS) model, this model takes the small strain characteristics of soil at high stiffness into consideration. The HSS model exhibits typical hysteretic behavior under cyclic loading. Based on that, this model is used to simulate the behavior of embankment soil, soft soil, and the bearing layer soil [27]. Several authors have utilized the HSS model to simulate the soil behavior under dynamic loading in different geosynthetic reinforced earth (GRE) structures. They found that the results are consistent with the field measurements [32]. The ballast is modeled with Mohr–Coulomb (MC) model [27]. The properties of the different soils are listed in Tables 2 and 3.

The piles are represented by embedded beam elements with a unit weight of 24 kN/m<sup>3</sup>, a Young's Modulus of 20 GPa, and a Poisson's ratio of 0.20. The biaxial geogrid, on the other hand, is represented as an elastoplastic material.

Table 2  
The properties of embankment fill, soft soil, and gravel

Basic parameters	Embankment fill	Soft soil	Gravel
Saturated unit weight: $\gamma_{sat}$ (kN/m <sup>3</sup> )	20.0	15.0	20.0
Unsaturated unit weight: $\gamma_{unsat}$ (kN/m <sup>3</sup> )	18.0	12.0	19.0
Internal friction angle: $\phi$ (°)	35.0	25.0	38.0
Dilatancy angle: $\Psi$ (°)	5.0	0.0	8.0
Cohesion: c (kPa)	5.0	5.0	1.0
Reference secant stiffness: $E_{50}^{ref}$ (kN/m <sup>2</sup> )	36000	1500	48000
Reference tangent stiffness: $E_{tend}^{ref}$ (kN/m <sup>2</sup> )	36000	750	48000
Reference unloading /reloading stiffness: $E_{ur}^{ref}$ (kN/m <sup>2</sup> )	108000	6000	144000
Exponential power: m (-)	0.5	0.7	0.5
Reference shear modulus at small strain: $G_0^{ref}$ (kN/m <sup>2</sup> )	100800	15000	114400
Reference strain threshold: $\gamma_{0.7}$	0,00014	0.00026	0.00012
Coefficient of earth pressure at rest: $K_0^{nc}$ (-)	0.419	0.5775	0.384
Unloading/reloading Poisson's ratio: $\nu_{ur}$ (-)	0.2	0.2	0.2

Failure ratio: $R_f$ (-)	0.9	0.9	0.9
Permeability: $k$ (m/day)	1.0	5.55E-4	1.00

Table 3  
The properties of ballast soil

<b>Ballast</b>	$\gamma_{sat} = \gamma_{unsat} = 25$ kN/m <sup>3</sup>	$\phi = 40^\circ$	$\Psi = 0^\circ$	$c = 10$ kPa
	$E = 100000$ kPa	$\nu = 0.2$	$k = 1.0$ m/day	

### 3 Results and Discussion

The reference case is created in order to investigate the behavior of the GRPS embankment under a single cycle of high-speed train. It is composed of a 2.6 m embankment supported by a network of piles and one layer of geogrid as indicated previously in section (2.1). A loading cycle is produced by a train speed of 250 km/h.

The first part of this study introduces the following:

- A comparison between the GRPS embankment and the conventional embankment with the behavior of settlements.
- A comparison of the behavior of vertical stresses and settlements under the static (embankment weight) and dynamic loads.
- The behavior of vertical wave velocity at two points (C, D).

A parametric analysis is conducted in the second part to examine the effect of the height of the embankment, cover ratio, and train speed on the behavior of the GRPS embankment in terms of the load efficiency (point A), the geosynthetic tension (point E), and the settlements at the ballast surface, (points D and B). The parametric analysis focuses on the time of the train operation. This time changes with the variation of the embankment height and moving train speed. For example, for different speeds ( $v_1 = 80$  km/h,  $v_2 = 160$  km/h,  $v_3 = 250$  km/h), Plaxis 3D outputs demonstrate different time of the maximum load over the pile head ( $t_1 = 0.36$  sec.,  $t_2 = 0.23$  sec.,  $t_3 = 0.16$  sec.) respectively.

#### 3.1 Assessment of the Pile and Geogrid Influence on an Embankment Subjected to Moving Train Load

The embankment supported by a network of piles and one layer of geogrid was compared to the case of the unsupported (conventional) embankment to assess the function of the pile and geogrid in the dynamic response of the embankment erected over soft soil. Figure 3 depicts the embankment failure scenarios of the

entire geometry in two cases (A) unsupported embankment and (B) GRPS embankment.

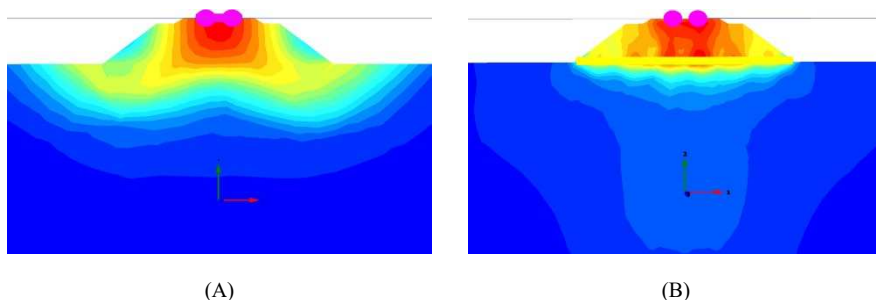


Figure 3

Failure scenario of (a) unsupported embankment, (b) GRPS embankment

For a more explanation, the piles serve to transfer the majority of the load to the bearing soil layer, reducing the load on the soft soil and, as a result, the vertical settlements of the railway structure. Furthermore, the geogrid reinforcement contributes to strengthen the embankment by increasing compressive strength, which reduces the effect of dynamic loads on the railway structure. Figure 4 shows the maximum vertical settlement behavior at the ballast surface (point D) in the two scenarios during the train's passage ( $t=0.16$  sec.). The use of piles and geogrid aids in reducing the vertical settlement to a reasonable level.

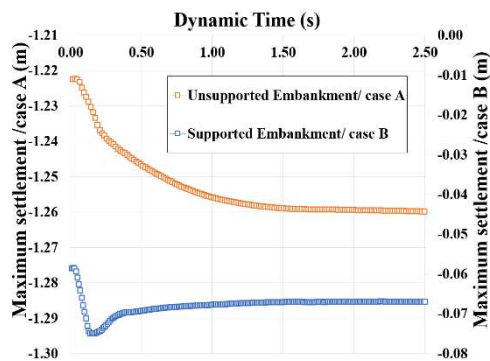


Figure 4

Vertical settlements of (a) unsupported embankment, (b) GRPS embankment

### 3.2 Stress Distribution in the GRPS Embankment

The stress distribution along the embankment body over the pile head (point A) and in the midway between four piles (point E) is investigated. The investigation was conducted under the static and dynamic loads.

At the ballast surface, the vertical stress over the pile axis equal to 0 kPa under static load, the amplitude of the vertical stress increases with the depth progressively to attain the maximum value over the pile head. Regarding the dynamic load, the vertical stress commences with 210 kPa owing the train load, this value reduces with depth before increasing again near the embankment base and attain the maximum value over the pile head as illustrated in Figure 5.

On the other side, the stress distribution behaves differently over the midpoint between the piles; the vertical stress increases to a specified depth, then starts to decrease due to the formation of the soil arch, and subsequently increases again to a small extent due to the weight of the soil under the arch. It is noteworthy that the vertical stress distribution under the static and dynamic loads is similar. As illustrated in Figure 5, the soil arch height in this reference case is 0.83 m, representing the phase of vertical stress reduction in the structure.

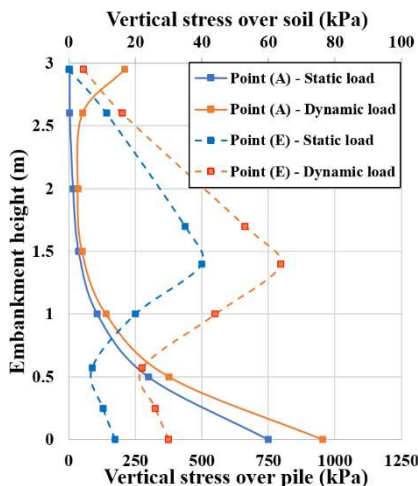


Figure 5

Vertical stress distributions in the GRPS embankment body

### 3.3 Vertical Settlement Distribution in the GRPS Embankment

The settlements as a function of the embankment height are illustrated in Figure 6 through points (B, D) on a vertical profile. The settlement distributions were investigated the static and dynamic loads.

The maximum settlements decrease with the depth over the pile and soil as illustrated in Figure 6. It is noticeable also that the differential settlements under the dynamic loading is larger than those under the static loading.

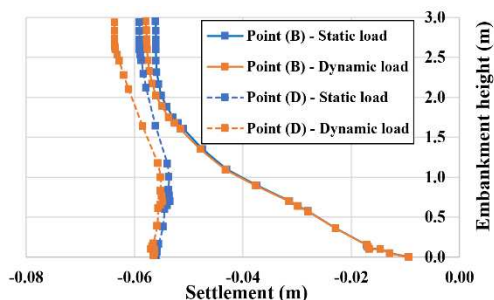


Figure 6

Vertical settlement distribution along the GRPS embankment height

The results show that the maximum value of the differential settlement between the points (B, D) is 0.0047 m. The intersection point of the two curves (oranges or blues) represents the critical height, in this reference case, the authors determined that the critical height is more than 2.95 m. The critical height represents the height from the pile head level to the plane of equal settlements in the embankment body. In other words, the differential settlements can be negligible over this plane.

### 3.4 Vertical Velocity in the GRPS Embankment

Figure 7 shows the vertical velocity at points (D, C). The peak of the observed amplitude at the ballast surface culminates during the train's passage. The vertical velocity begins to attenuates progressively after the train's passage, on the other hand, the amplitude of the vertical velocity decreases with the depth as illustrated in Figure 7. It is noticeable the low value of the velocity at point (C), this is attributed to the involvement of piles and geogrid in improving the ability of the soft soil to attenuate the velocity in this medium.

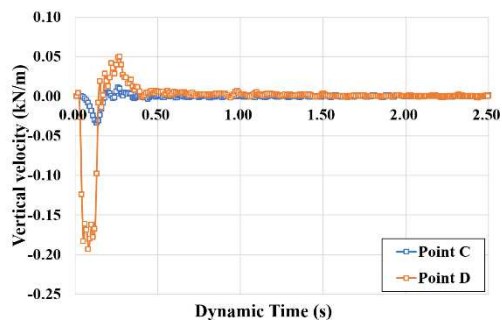


Figure 7

Vertical velocity of different depths

## 3.5 Parametric Study

### 3.5.1 Influence of GRPS Embankment Height (H)

To consider the influence of the embankment height, the applied load over the pile head and the load efficiency are investigated during the passage of the train. Figure 8 demonstrates that the applied load increases to a large extent under the dynamic loading before decreasing after the train passes. At the same time, despite receiving an additional load, it is clear that load efficiency reduces dramatically. This may be read as the inability of the soil arch to transfer a considerable portion of the dynamic load to the pile, which is reflected in more settlements of the soft soil. The load efficiency increases again under the pure load of the self-weight of the embankment.

Figure 8 further illustrates that the load efficiency increases with the higher embankment under static and dynamic loading. Moreover, the magnitude of the dynamic load transferred to the pile head increases as the embankment height decreases.

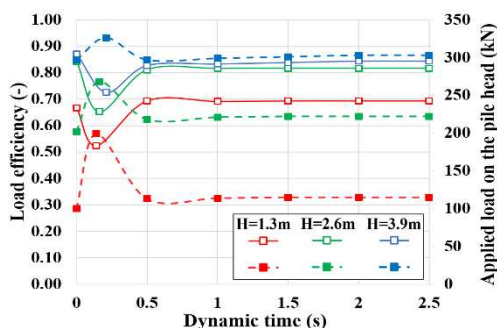


Figure 8

The load efficiency in the dynamic time for different embankment heights (Dashed curve represents the vertical load on the pile head, solid curve represents the load efficiency)

Figure 9 shows the geosynthetic tension for different embankment heights. As shown in the Figure, for a given dynamic time the geosynthetic tension increases when the height increases. It is obvious that the tension increases significantly for the low embankment ( $H=1.3$  m) with a tendency to be constant progressively after the passage of train.

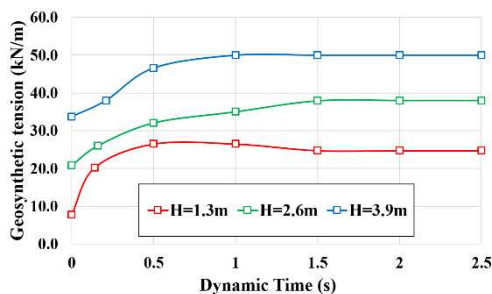


Figure 9

The tension in the geosynthetic for different embankment heights

Figure 10 illustrates the variance in maximum and differential settlements at point D and points (D, B) on the ballast surface respectively. Due to the increased self-weight of the embankment, the maximum vertical settlement (columns) of point D increases with the embankment height during the train passage. On the other side, the differential settlements (lines) decrease as the embankment height increases progressively as explained in section (3.3). As can be seen, the differential settlements for the different presumed embankment heights cannot be neglected.

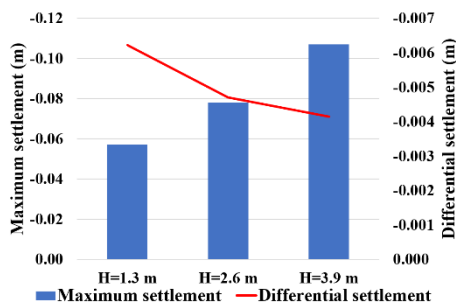


Figure 10

The maximum and differential settlements at the ballast surface for different embankment heights

### 3.5.2 Influence of Cover Ratio (a)

The effect of the cover ratio variation in the dynamic time domain has been investigated. For this purpose, three diameters of the pile are used (0.6 m, 0.8 m, 1.0 m). The cover ratio can be governed by adjusting the pile diameter or by enlarging the pile cap. In this reference case, the cover ratio is controlled by the pile diameter. The results are depicted in Figure 11. As can be noticed, increasing the cover ratio lower the load efficiency. The influence of the cover ratio is more noticeable under the static load than dynamic load.

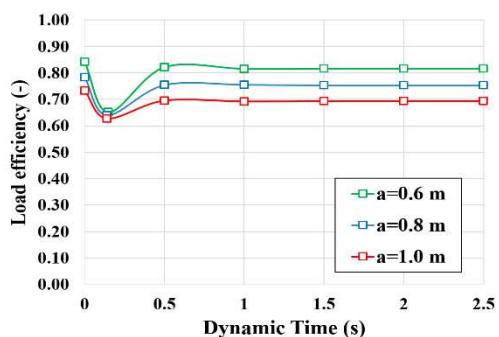


Figure 11

The load efficiency in the dynamic time for different cover ratios

This phenomenon can be explained as follows, with larger pile diameter, the pile's skin friction area expands. Consequently, the negative skin friction generated by the stresses over the soft soil along the upper part of the pile increases. Conversely, the load applied on the pile's head decreases. The axial forces distribution along the pile shaft is illustrated in Figure 12.

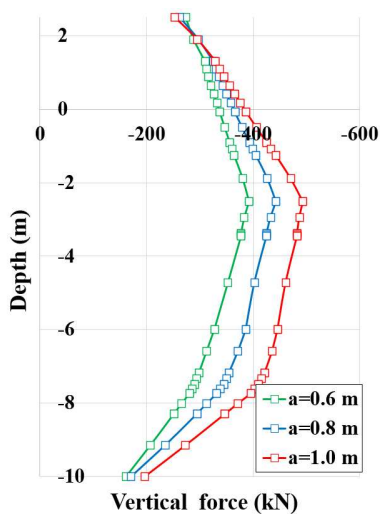


Figure 12

The axial forces distribution for different pile diameters

The utilize of large-diameter piles contributes to boost the stability of the soil arch; in consequence, the magnitude of load transfer through the soil arch improves while that transferred to the pile via geosynthetic reinforcement to the piles diminish.

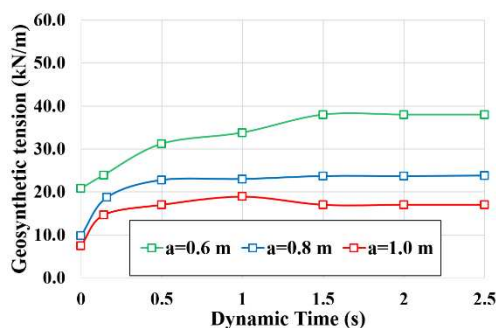


Figure 13

The tension in the geosynthetic for different cover ratios

Based on that, the increase of the cover ratio reduces the tension in the geosynthetic which in turn tends to be stable after the train passage as shown in Figure 13. It was noticeable in this study that the maximum tension in the geosynthetic occurs at the edge of the pile.

Figure 14 depicts the maximum and differential settlements at the ballast layer surface for various pile diameters. It can be seen that settlements decrease as the cover ratio increases. The reason for this is that the soil arch develops with the increased cross-sectional area of the pile, which contributes to restrict the amount of stress applied to the soft soil.

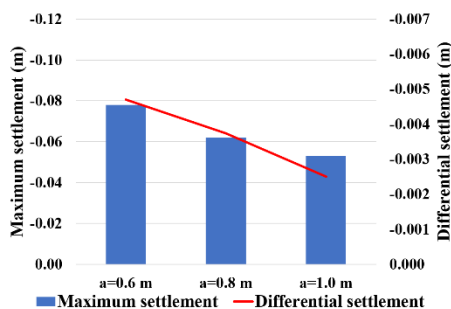


Figure 14

The maximum and differential settlements at the ballast surface for different cover ratios

### 3.5.3 Influence of Train Speed (v)

The influence of moving train speed on load efficiency is discussed in this section in which compares the findings of three different speeds, e.g. 80, 160, and 250 km/h at the corresponding times ( $t$ ) = 0.36, 0.23, and 0.16 sec., respectively, as shown in Figure 15. The higher train speeds reduce the vertical stress transferred to the pile heads. This might be because the amplitude and frequency of the

dynamic load increased with speed [33]. These results are compatible with those of Pham *et al.* [19]. The researchers found that the SCR is closer to equal to 1.0 with high speeds after limited number of cycles, in other words, the soil arching reduction is faster with the higher speeds.

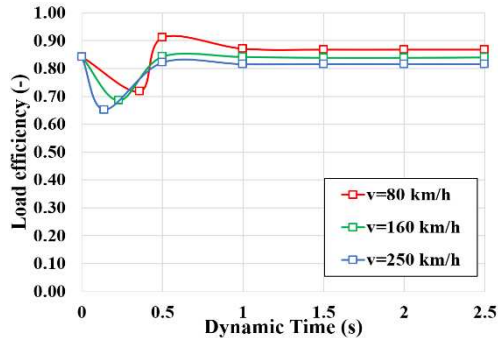


Figure 15

The load efficiency in the dynamic time for different train speeds

The use of a geogrid contributes to regulate the vibration in the soil during the train passage. Referring to the effect of the train speed on the geosynthetic tension. Figure 16 shows that the geosynthetic tension of 80 km/h speed is the highest under the dynamic loading. Conversely, it is noticeable that the tension increases with speed at the end of the dynamic time (static loading). The Figure 16 shows also that the different behavior of the geosynthetic tension with the various speeds.

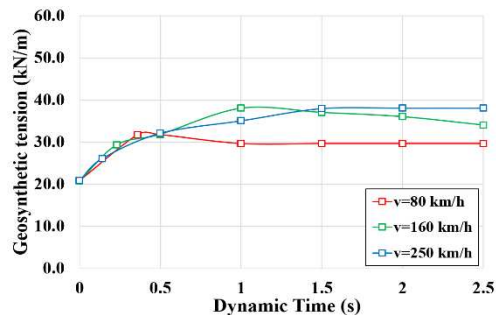


Figure 16

The tension in the geosynthetic for different train speeds

Figure 17 refers to the effect of the train speeds on the maximum and differential settlements. It is visible from the preceding results that the load efficiency reduces with speed, and as a consequence, the vertical stresses applied to soft soil rise. Figure 17 depicts the development of the settlements at the ballast surface; the maximum settlements increase with the high speeds. At the same time, the differential settlements decrease as demonstrated by Meena *et al.* [34].

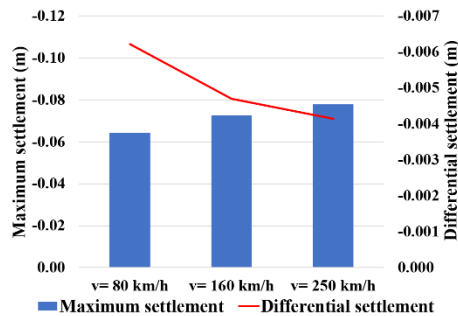


Figure 17

The maximum and differential settlements at the ballast surface for different train speeds

## Conclusions

In this study, the authors used 3D numerical method to investigate the behavior of a GRPS embankment during a single high-speed train cycle. To simulate the behavior of bearing soil, soft soil, and embankment fill, the Hardening soil model with small-strain stiffness was utilized. The dynamic load which represents the moving train was modeled using the LM71 Eurocode recommendations. The following conclusions are obtained:

- The piles and geogrid reinforcement contribute significantly to support the railway track through the reduction of the vertical settlements to a reasonable level.
- The distribution of the vertical stresses in the embankment body is similar under the static and dynamic loading. So is the case for the distribution of the vertical settlements.
- The vertical velocity of the waves decreases with the depth remarkably due to the involvement of piles and geogrid in improving the ability of the soft soil to attenuate this velocity.
- The magnitude of the dynamic load transferred to the pile head decreases as the embankment height increases. An increase in the embankment height results in an increase in the load efficiency and the maximum settlement and a decrease in the differential settlement at the ballast surface.
- The increase of the cover ratio by the cross-sectional area of the pile lower the load efficiency due to the increase of the negative skin friction generated by the stresses over the soft soil along the upper part of the pile. The higher cover ratios improve the stability of the railway track due to the reduction of the maximum and differential settlements.
- Given the different train speeds, the higher train speeds reduce the load efficiency, and as a consequence, the maximum settlements increase at the ballast surface. While the results related to the differential settlements indicate that these settlements decrease with the faster the train speeds.

## References

- [1] Sz. Fischer, Investigation of the Horizontal Track Geometry regarding Geogrid Reinforcement under Ballast, *Acta Polytechnica Hungarica*, Vol. 19, No. 3, 2022, pp. 89-101
- [2] L. Briançon, B. Simon, Pile-supported embankment over soft soil for a high-speed line, *Geosynthetics International*, Vol. 24, No. 3, 2017, pp. 293-305
- [3] P. Ariyaratne, D. S. Liyanapathirana, Review of existing design methods for geosynthetic-reinforced pile-supported embankments, *Soils and Foundations*, Vol. 55, No. 1, 2015, pp. 17-34
- [4] K. Terzaghi, *Theoretical soil mechanics*, Soils and Foundations, 1943, New York: John Wiley and Sons
- [5] B. Low, S. Tang, Arching in piled embankments, *Journal of Geotechnical Engineering*, Vol. 120, No. 11, 1994, pp. 1917-1938
- [6] D. Russell, N. Pierpoint, An assessment of design methods for piled embankments, *Ground Engineering*, Vol. 30, No. 11, 1997, pp. 39-44
- [7] S. Abusharar, J. Zheng, B. Chen, J. Yin, A simplified method for analysis of a piled embankment reinforced with geosynthetics, *Geotextiles and Geomembranes*, Vol. 27, No. 1, 2008, pp. 39-52
- [8] BS8006, *Code of Practice for Strengthened Reinforced Soils and Other Fills*, London, UK, 2010
- [9] EBGEO, *Recommendations for design and analysis of earth structures using Geosynthetic Reinforcements*, German geotechnical society, 2011
- [10] Dutch standard CUR226, *Design guideline basal reinforced piled embankments*, CRC press, 2016
- [11] T. Pham, Analysis of geosynthetic-reinforced pile-supported embankment with soil-structure interaction models, *Computers and Geotechnics*, Vol. 121, 2020, pp. 1-17
- [12] C. Heitz, J. Lüking, H. G. Kempfert, *Geosynthetic Reinforced and Pile supported Embankments under Static and Cyclic Loading*, 4<sup>th</sup> European Geosynthetics Conference, Edinburgh, UK, 2008
- [13] C. Yu, L. Pan, B. Qian, J. Cai, *The Behavior of Piled Embankments under Embankment Loads and Traffic Loads*, Second International Conference on Transportation Engineering, 2009, Chengdu, China, pp. 1566-1571
- [14] J. Han, A. Bhandari, *Evaluation of Geogrid-Reinforced Pile-Supported Embankments under Cyclic Loading using Discrete Element Method*, Proceedings of the US-China Workshop on Ground Improvement Technologies, 2009, Orlando, Florida, United States, pp. 73-82

- [15] G. Han, Q. Gong, S. Zhou, Soil Arching in a Piled Embankment under Dynamic Load, *International Journal of Geomechanics*, Vol. 15, No. 6, 2015, pp. 04014094-1 to 7
- [16] Y. Zhuang, S. Li, Three-dimensional finite element analysis of arching in a piled embankment under traffic loading, *Arabian Journal of Geosciences*, Vol. 8, No. 10, 2015, pp. 7751-7762
- [17] M. Houda, O. Jenck, F. Emeriault, Physical evidence of the effect of vertical cyclic loading on soil improvement by rigid piles: a small-scale laboratory experiment using Digital Image Correlation, *Acta Geotechnica*, Vol. 11, No. 2, 2016, pp. 325-346
- [18] Y. Zhuang, K. Wang, Finite element analysis on the dynamic behavior of soil arching effect in piled embankment, *Transportation Geotechnics*, Vol. 14, 2018, pp. 8-21
- [19] H. V. Pham, D. Dias, A. Dudchenko, 3D modeling of geosynthetic-reinforced pile-supported embankment under cyclic loading, *Geosynthetics International*, Vol. 27, No. 2, 2018, pp. 8-21
- [20] D. Wang, M. Sanchez, J. L. Briaud, Numerical study on the effect of rigid inclusions on existing railroads, *Int J Numer Anal Methods Geomech*, Vol. 43, No. 18, 2019, pp. 2772-2796
- [21] K. Aqoub, M. Mohamed, T. Sheehan, Analysis of unreinforced and reinforced shallow piled embankments under cyclic loading, *Geosynthetics International*, Vol. 27, No. 2, 2019, pp. 182-199
- [22] Z. Bi, Q. Gong, J. Huang, Long-Term Stability of High-Speed Railway Geosynthetic Reinforced Pile-Supported Embankment Subjected to Traffic Loading Considering Arching Effect, *Transportation Research Board*, Vol. 2674, No. 7, 2020, pp. 596-607
- [23] Y. Zhuang, X. Cui, S. Zhang, G. Dai, X. Zhao, The load transfer mechanism in reinforced piled embankment under cyclic loading and unloading, *European Journal of Environmental and Civil Engineering*, Vol. 26, No. 4, 2020, pp. 1364-1378
- [24] R. M. Patel, B. R. Jayalekshmi, R. Shivashankar, Stress Distribution in Basal Geogrid Reinforced Pile-Supported Embankments Under Seismic Loads, *Transportation Infrastructure Geotechnology*, Vol. 8, No. 3, 2021, pp. 516-541
- [25] H. Fang, J. J. Zheng, Y. Liu, R. Y. Hou, Z. R. Jia, Analytical solutions of the dynamic response of a dual-beam model for a geosynthetic reinforced pile-supported embankment under moving load, *Computers and Geotechnics*, Vol. 142, 2022

- 
- [26] X. Duan, Y. Wu, X. Bian, J. Jiang, Dynamic Behaviors of Piled Embankment Under High-Speed Train Loads, *Advances in Transportation Geotechnics IV*, Vol. 166, 2022, pp. 1041-1047
- [27] M. Shahraiki, M. Sadaghiani, K. J. Witt, Th. Meier, 3D Modelling of Train Induced Moving Loads on an Embankment, *Plaxis Bulletin*, Autumn issue, 2014, pp. 10-15
- [28] R. Alsirawan, Review of Geosynthetic-Reinforced Pile-Supported (GRPS) embankments- parametric study and design methods, *Acta Technica Jaurinensis*, Vol. 14, No. 1, 2021, pp. 36-59
- [29] Sz. Fischer, Geogrid reinforcement of ballasted railway superstructure for stabilization of the railway track geometry – A case study, *Geotextiles and Geomembranes*, In press, 2022
- [30] E. Koch, Finite element analysis of bridge transition zone for investigating the effect of moving loads. 17<sup>th</sup> European Conference on Soil Mechanics and Geotechnical Engineering, Reykjavik, Iceland, 2022
- [31] T. Benz, Small-strain stiffness of soils and its numerical consequences, PhD Thesis, 2007, University of Stuttgart
- [32] A. Herold, P. A. Von Wolfersdorff, The Use of Hardening Soil Model with Small-Strain Stiffness for Serviceability Limit State Analyses of GRE Structures, *Proceedings of GeoAfrica 1*, 2009, Cape Town, South Africa
- [33] Y. M. Zhang, B. Liang, Dynamic response of expressway subgrade under geometric irregularity conditions, *Journal of Lanzhou Railway University*, Vol. 20, No. 4, 2001, pp. 66-69
- [34] N. K. Meena, S. Nimbalkar, B. Fatahi, G. Yang, Effects of soil arching on behavior of pile-supported railway embankment:2D FEM approach, *Computers and Geotechnics*, Vol. 123, 2020

# The Analysis of High-Speed Railway Seismic-induced Track Geometric Irregularity

**Guolong Li<sup>1</sup>, Fei Yang<sup>1</sup>, Mangmang Gao<sup>1</sup>, Wentao Sun<sup>2</sup>, and Xiangyu Qu<sup>3,\*</sup>**

<sup>1</sup> Infrastructure Inspection Research Institute, China Academy of Railway Sciences Corporation Limited, 100081 Beijing, China, liguolong@rails.cn; yf2009@rails.cn; gaomang@rails.cn

<sup>2</sup> Railway Science & Technology Research & Development Center, China Academy of Railway Sciences Corporation Limited, 100081 Beijing, China, sunwt@rails.cn

<sup>3</sup> Institute of Sound and Vibration Research, University of Southampton, SO17 1BJ, Southampton, UK, xq2n20@soton.ac.uk

---

*Abstract: The high-speed railway in China passes through various seismic zones. As the track geometric irregularity is a critical aspect impacting train operation safety and train-induced vibration, it is meaningful to investigate the influence of earthquakes on the seismic-induced track geometric irregularity of high-speed railways. To determine the impact of earthquakes on track conditions, a complete study was conducted using various earthquake magnitude levels (3.0 to 7.0), varied limiting train speeds, and different track structural types (ballasted and ballastless track). The track quality index, long-wave irregularities, 10 m chord measurement, and vehicle vibration are analysed to suggest the change of track geometric irregularity and its influence after the earthquake. At the same time, the vehicle-track analysis model is used to calculate the difference in vehicle vibration under different seismic-induced track conditions. The vehicle acceleration, the rate of wheel load reduction, derailment coefficient indicators are investigated. These results imply that earthquakes have an impact on high-speed railways, causing track geometric irregularities to shift, which may contribute to increased vibration while trains are running. Compared to the ballasted track, whose normal speed is 250 km/h, the ballastless track, whose nominal speed is 350 km/h, was affected by the earthquake less. According to data, earthquakes have an influence on long waves greater than 1 m. While small and moderate earthquakes have a minor effect on railway safety, they do have an effect on train operating comfort because vehicle vibration is amplified as a result of the seismic-induced track geometric irregularity being worse.*

*Keywords: High-speed railway; track geometric irregularity; seismic-induced response; train vibration; track quality index*

---

# 1 Introduction

In recent years, the development of high-speed railways (HSR) has made significant progress in some regions such as East Asia, Europe, and Africa. More HSRs are being built in hilly areas and coastal seismic fault belts with significant seismic intensity [1], such as in western China and Japan. Due to this situation, the probability of high-speed railways interfering with earthquakes has also grown significantly. In natural disasters that endanger railway safety, earthquakes are difficult to forecast. Destructive earthquakes not only inflict direct damage to railway infrastructure, but can produce a variety of secondary catastrophes and even result in accidents such as high-speed train derailment and overturning. Therefore, the effect of earthquakes on high-speed rail systems has garnered increased attention.

Destructive earthquakes not only inflict direct damage to railway infrastructure, but can produce a variety of secondary catastrophes and even result in accidents such as high-speed train derailment and overturning [2, 3]. Thus, there is considerable interest in the damage to the railway structure caused by earthquakes, and various studies are being undertaken in this field. Seismic-induced track damage and deformation may be classified into two types: failure of track structural stability, e.g., track irregularities [4, 5], and failure of track underlying structures such as embankments [6, 7] and bridges [8]. Because bridges are the critical components of railway systems, the seismic response of bridges has attracted considerable research, including different bridge types: long-span bridges, [9], steel truss girder bridges [10], cable-stayed bridges [11]. Also, some numerical [12, 13] and analytical [14, 15] train-track-bridge models are established to investigate the dynamic seismic-induced response of the track structure.

Although certain extremely severe earthquakes might cause damage to the railway structure, the majority of earthquakes are less severe. It can be found that the earthquake will not cause damage to the track's subgrade or bridge construction, but it will impair the track's stability, irregularity, and residual stress and deformation [16]. These irregularities grow may lead to extra train vibration. Track irregularity is one of the main factors for the vibration of railway vehicles. If the roughness of the track is severer after the earthquake, the train vibration and the wheel-rail force induced by the track irregularity will grow with the increase of the speed of the vehicle, which cannot be ignored. The earthquakes and track irregularities are often combined considered. Stochastic analysis model is built for investigating the dynamic track response [17]. The influence of train speed and seismic wave propagation velocity on the random vibration characteristics of the bridge and train are discussed by using the pseudo-excitation method [18]. However, the above studies mainly focused on the track irregularities influence when the earthquake occurred. Actually, the earthquake could induce more severer track irregularities. The seismic-induced geometric irregularity of rail

alignment is investigated. The amplitude for seismic-induced track irregularity significantly increases with the increase of earthquake intensity [19]. Additionally, the power spectral density curve of track geometry irregularity is considered and studied when transverse random earthquakes occur [20, 21]. The effects of track irregularity and seismic stresses on the dynamic response of the vehicle system demonstrated that track irregularity may greatly enhance the vehicle system's dynamic response [22]. Using both measured U.S. earthquake data and a finite element model, the frequency-domain distribution of earthquake-induced track irregularities was investigated [23]. However, the majority of these conclusions are based on model analysis and earthquake database library. Inadequate validation of track irregularities test data affected by the earthquake. The analysis of high-speed railway seismic-induced track geometric irregularity based on in-situ measurement data needs further explanation.

This paper measures and analyses the impact of track irregularities on several railway lines in China when subjected to seismic activity. Additionally, choose several typical irregularities from the measured data and do additional analysis using the vehicle-track coupling model. The impact of the track on the vibration of the vehicle is described when the track is affected by an earthquake and the track irregularity becomes severe. The in-situ measurement of track irregularities affected by the earthquake is introduced in Section 2. Then, the measurement data is statistically analysed in Section 3. Combined with a train-track model, the introduction of the model and calculation results are drawn in Section 4. The conclusion is shown in the end.

## **2 On-Site Measurement of Seismic-induced Geometric Irregularity**

In reaction to the earthquakes that occurred in China during the last decade, special attention has been devoted to the railway infrastructure around the epicentre. Sense,t track irregularities impair driving safety and cause vibrations, it is essential to consider the effect of earthquakes on track conditions. The geometry of the track was compared before and after the earthquake. Track Quality Index (TQI) variation and the amplitude of track irregularities were determined twice before and following the earthquake. The measurement data is shown below, including the train's limited speed 250 km/h ballasted track and 350 km/h ballastless track that was severely damaged by the earthquake in all tested cases.

Numerous in-situ measurements were performed including the track irregularity of longitudinal level, alignment level, gauge, cross-level, and twist on the ballastless track designed for 350 km/h HSR, and ballasted track designed for 250 km/h HSR.

The situation of the site is shown in Figure 1 (a). The deformation and track irregularity under earthquake effects can be observed in the photographs of the site and detected by the track geometry car shown in Figure 1 (b).

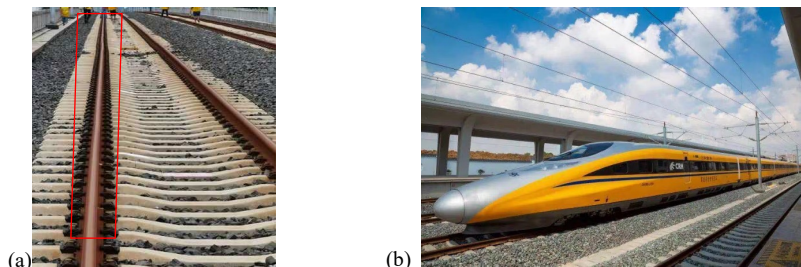


Figure 1

On-site measurement (a) Track geometry and (b) Track geometry car

The original data of the track longitudinal level, alignment, cross level and twist for ballastless track is shown in Figure 2. The red dashed box shows a distinct difference in the track geometric irregularity from the pre- and post-earthquake.

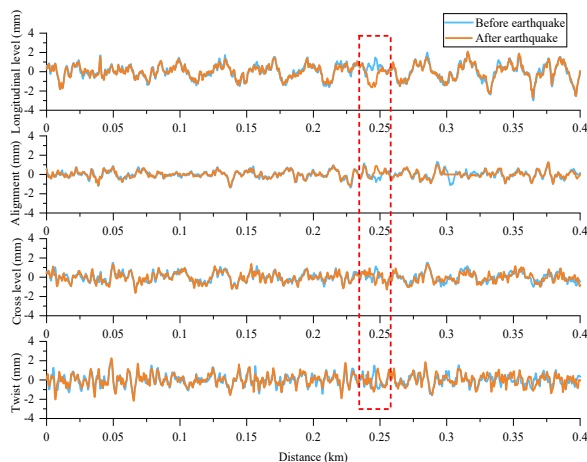


Figure 2

Original measurement data of track geometric irregularity.

The in-situ measurements data in Figure 2 indicated that the track geometric irregularity varies dramatically at the HSR beam junction locations. The earthquake caused the bridge piers to vibrate, which in turn caused the girders to vibrate and then lead to track deformation. Figure 3 illustrated the special sites where deformation is expected to occur marked in red dashed line.

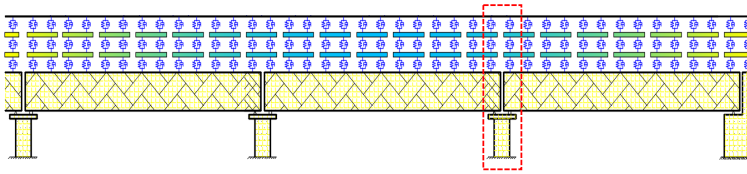


Figure 3  
Beam junction locations

## 2.1 Track Geometric Irregularity

The waveform of long wave (1-120 m) and medium wave (1-42 m) can be analysed based on in-situ track irregularities data. The long wave affects the low frequency of the vehicle and vehicle ride comfort. Therefore, the long waveform of the track irregularity was selected for analysis. The details of the waveform of three cases are shown in Figure 4. As can be observed, the track irregularity has altered significantly in many areas with the effects of the earthquake.

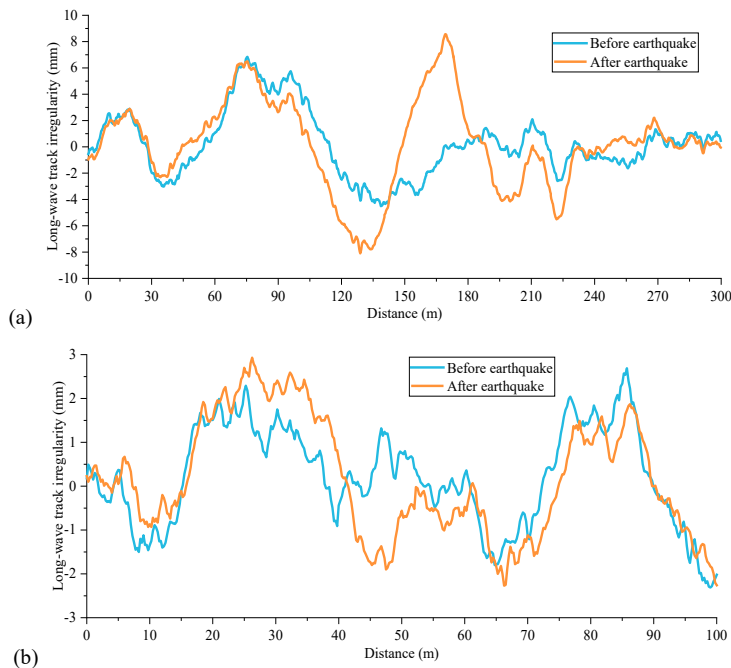


Figure 4  
Long-waveform longitudinal level in (a) 250 km/h HSR track (b) 350 km/h HSR track

Long-wave track irregularity values up to 7 mm in certain locations of the 250 km/h HSR track owing to seismic events. The considerable change spans around 100 m. For the ballastless 350 km/h HSR track, the difference is also up to around 2 mm, the span of this area is nearly 40 m. These results demonstrate that the earthquake had a major effect on the rail structure's long-wave irregularity. The track's long-wave irregularity will affect the low-frequency train-induced vibration.

## 2.2 10 m-chord Measurement Method

The medium wave affected train safety. In this paper, the 10 m chord measurement method, a suitable method to describe the medium wave of track geometric irregularity, is used to measure the track irregularity data. The Chord measurement method [24] is a typical method to measure the track irregularities. Based on measurement data for pre-earthquake and post-earthquake, the left and right longitudinal level and alignment difference is shown in Figure 5.

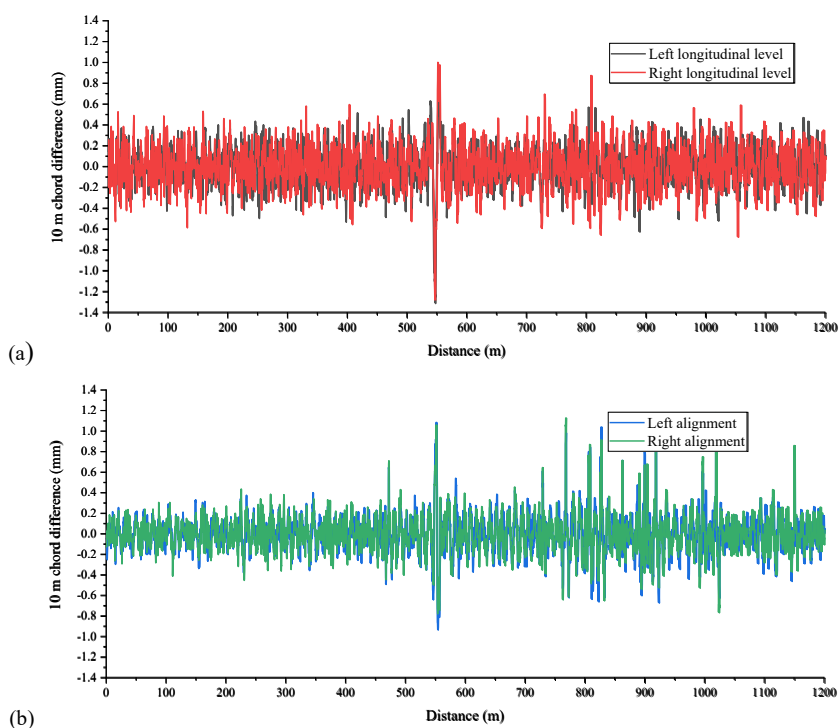


Figure 5

The difference of track irregularity based on 10m-chord method of 250 km/h HSR track including (a) longitudinal level and (b) alignment

According to the data in Figure 5, there is a significant disparity in longitudinal level and alignment. The longitudinal level has a maximum value of 1.4 mm. There is, however, no noticeable difference between the data for the left and right rails.

Figure 6 depicts the cumulative distribution of the difference between the output values of the 10 m-chord measurement before and after the earthquake at the ballasted track designed for 250 km/h HSR.

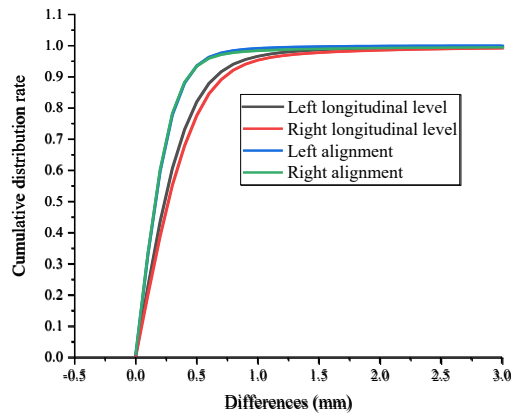


Figure 6

Cumulative distribution of the value difference of track irregularity

For 250 km/h high-speed railways, 95% of the cumulative distribution of the 10 m chordal measurements of track height before and after the earthquake is within 2 mm. Because the red and black lines, which indicate longitudinal level track irregularities, are lower than the blue and green lines, which show alignment track irregularities, particularly in the 0.5-1 mm difference range. As a result, the longitudinal level is more changeable than the track alignment, and the difference in track irregularities between the left and right rails is more noticeable.

### 2.3 Track Quality Index

Track Quality Index (TQI) [25] is a comprehensive index and assessment system that uses quantitative statistics to characterise the track's overall quality. It is the total of the standard deviations of the track irregularity in the vertical and horizontal direction, gauge, and twist irregularities elements. This number is directly connected to the overall track irregularity state, which shows the degree of dispersion of the track state in the 200 m segment. The larger the value, the more uneven and irregular the track is. It can be denoted as

$$\overline{\text{TQI}} = \sum_{i=1}^7 \sqrt{\frac{1}{n} \sum_{j=1}^n (X_{ij} - \bar{X}_i)^2} \quad (1)$$

where  $X_{ij}$  means the magnitude of each geometric deviation in 200 m range of track. There are 7 standard deviations of items involved in evaluating track irregularities including the left longitudinal level, right longitudinal level, left alignment, right alignment, the track gauge, cross level and twist.  $n$  is the number of sampling points in 200 m range.  $\bar{X}_i$  is the mean value of each project describing the track irregularities. It can be denoted as

$$\bar{X}_i = \frac{1}{n} \sum_{j=1}^n X_{ij} \quad (2)$$

In this part, three cases reflecting the track irregularity difference are chosen based on the measured track deformation degree data after the earthquake. The significant TQI changes measured data of 250 km/h and 350 km/h HSR track is chosen. A value is recorded every 200 metres, and the most visible gap of 10 kilometres is picked and shown in Figure 7.

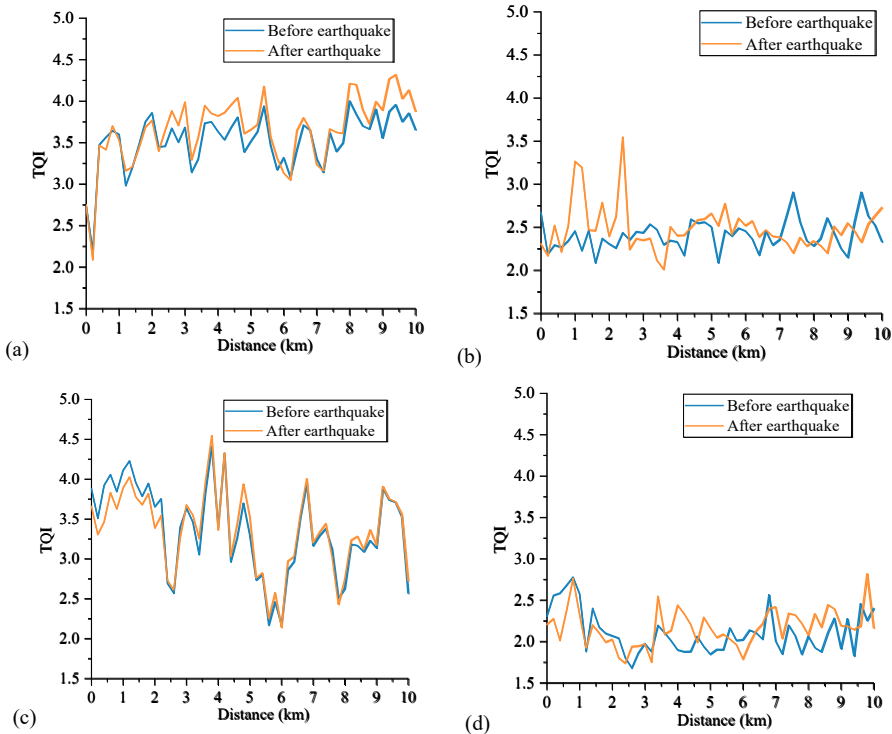


Figure 7

TQI difference influenced by the earthquake in (a) severe case from 350 km/h HSR ballastless track (b) severe case from 250 km/h HSR ballasted track (c) slight case from 350 km/h HSR ballastless track and (d) slight case from 250 km/h HSR ballasted track

It can be known that after the earthquake, although the TQI values have changed in selected regions, the difference is not statistically significant when observed in raw data. Sense, TQI is a comprehensive index for evaluating track conditions, it incorporates not only track height irregularity but also horizontal irregularity, gauge, and so forth. As a result, the general status of the track does not alter much after the earthquake.

The percentage of the seven components of the TQI evaluation indicators is shown in Figure 8. It includes the standard deviation for longitudinal level, alignment, track gauge, cross-level, and twist for ballasted and ballastless track that was severely and slightly impacted by the earthquake.

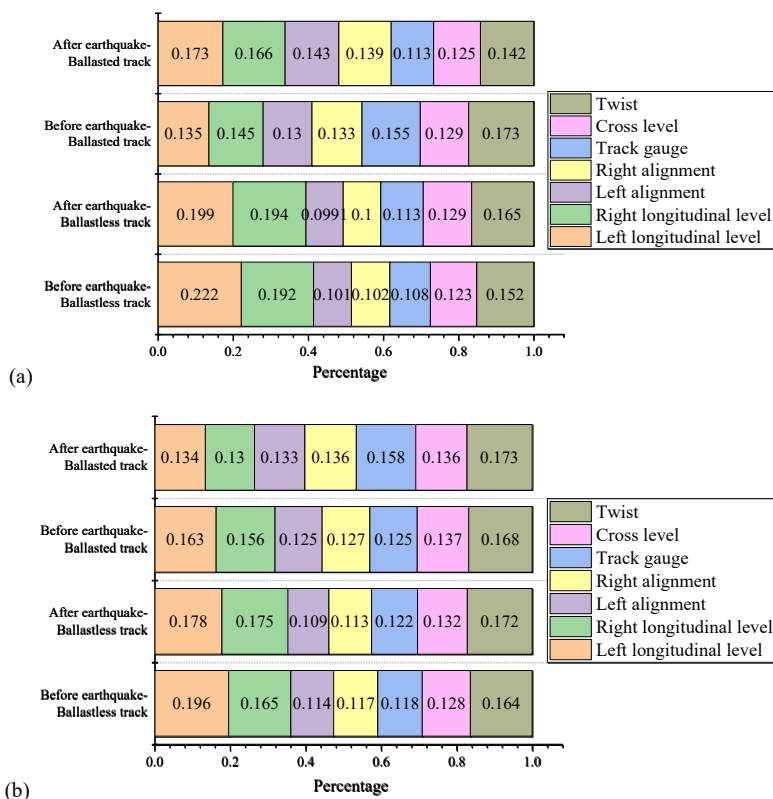


Figure 8

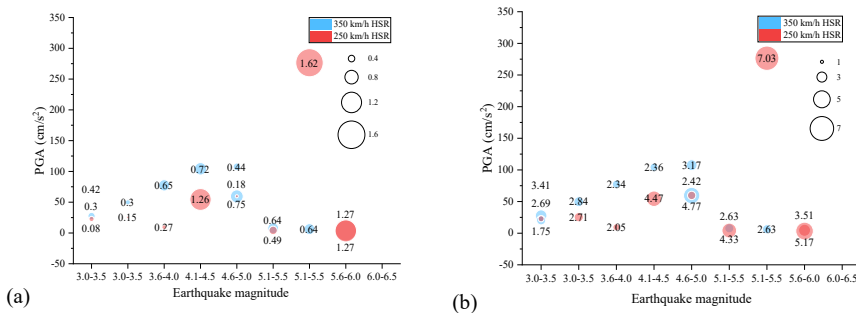
The percentage of 7 indicators from TQI evaluating the track influenced by the earthquake (a) severe case and (b) slight case

It can be seen that longitudinal level and twist account for a reasonably substantial amount of the overall TQI value when it comes to the contribution of each sub-factor to TQI values. Alignment track irregularities have a negligible impact on the TQI value. Less than track gauge and cross-level. The ballasted track exhibits

a comparatively high shift in longitudinal level and the gauge during seismic activity as compared to the ballastless track. In the case that the track is influenced by the earthquake significantly, due to seismic influences, the standard deviation of the longitudinal level is lower for the ballastless track, while the percentage rises for the ballasted track. Twist standard deviation demonstrates the inverse pattern. Therefore, the longitudinal level of track irregularities is the indicator most affected by the earthquake.

### 3 Analysis of Seismic-induced Geometric Irregularity of Track

Based on over 30 observations of the effect of earthquakes on track geometry during the last decade, the statistical results of TQI difference maximum value, long-waveform variations in the vertical direction, 10m-chord measurement value, and vehicle vertical acceleration are analysed. All statistical data of the earthquake is shown in Figure 9. This figure contains TQI difference maximum value, long-wave vertical differences, 95% cumulative value of 10 m-chard measurements and vehicle acceleration measured data of all the cases at 250 km/h HSR whose track form is mainly ballasted track (red) and 350 km/h HSR track whose track form is mainly ballastless track (blue). Different train speeds may cause different train-induced vibrations. The location of each bubble means the corresponding earthquake magnitude and peak ground acceleration (PGA, unit:  $\text{cm/s}^2$ ) of each earthquake case. The size of each bubble means the evaluated value.



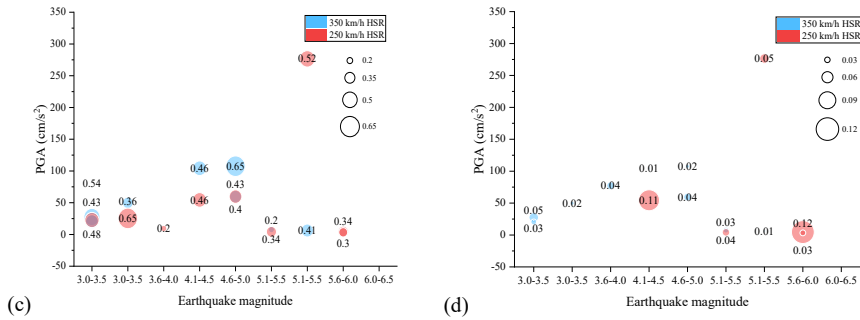


Figure 9

Statistical value of track irregularities (a) TQI difference max value (b) long wave vertical differences (unit: mm) (c) 95% cumulative value of 10 m chard measurement (unit: mm) (d) vehicle acceleration (unit:  $m/s^2$ ).

The  $x$  axis is the earthquake magnitude scale,  $y$  axis is PGA values, which are critical for describing the effect and damage caused by earthquakes on infrastructure. In China, it can be determined by

$$PGA = C_0 + C_1 M + C_2 \lg R + C_3 T \quad (3)$$

where  $C_n$  is the factor,  $M$  represents earthquake magnitude,  $R$  means Epicentre distance.  $T$  is horizontal earthquake vector. More details can be found in [26].

Focus on the maximum difference value between TQI before the earthquake and after the earthquake, the value is located approximately in the range of 0-1.6. The value is greater for the ballasted track, indicating that the form of the ballasted track changes dramatically as a result of the earthquake. The long-wave irregularity and vehicle acceleration values follow the same rule, whose range is around 1-7 mm and 0-0.12  $m/s^2$  respectively. 95% cumulative value of 10 m chard measurement is in the range of 0.2-0.65 mm. It can be found that the larger the PGA value, the larger the 95% cumulative value of the 10 m chard measurement. According to data, TQI's different maximum values for 350 km/h tracks are less than 1, whereas some 250 km/h HSR tracks exceed 1. Similarly, the 350 km/h HSR track caused a change in vehicle vibration of less than 0.05  $m/s^2$  after the earthquake, but some of the 250 km/h HSR tracks induced a vehicle vibration change of more than 0.1  $m/s^2$  following the earthquake. Based on the monitoring and analysis of over 30 ballasted and ballastless tracks influenced by the seismic dynamics, it can be shown that earthquakes impair track geometric irregularities and further influence the safety and comfort of the train.

## 4 Vehicle-Track Analysis Model

### 4.1 Vehicle Model

The vehicle is modelled as a multibody system with 35 degrees of freedom (DOF). The vehicle is made up of one car body, two bogie frames, and four wheels. Each component has five DOFs, which include lateral movement, vertical movement, roll, pitch, and yaw. The sketch of the vehicle model is shown in Figure 10.

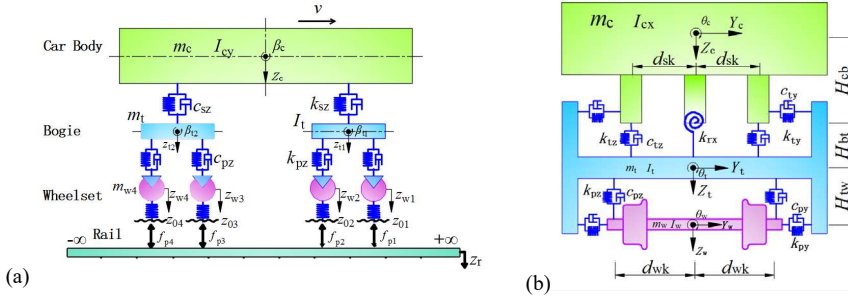


Figure 10

Vehicle dynamic analysis model (a) Side view of vehicle model (b) Front view of vehicle model

Kelvin springs, which are composed of a spring and a damping element, could be used to replicate the first and second suspensions, which can connect different multibody.

The model of the rail subsystem is constructed using two-layer nodes that correspond to the top and lower layers. The rail is a continuous Euler beam supported at discrete nodes by an elastic spring. The bottom node corresponds to the fastener position, and the spring-damper element between the upper and lower nodes corresponds to the elastic constraint imposed by the rubber pad under the rail.

### 4.2 Vehicle-Track Coupling Equation

The dynamic simulation analysis system is composed of the vehicle, track, which are connected by wheel-rail force. At all times, the system's vibration should adhere to force balance and deformation compatibility. The system's motion equation is as follows:

$$[M]\{\ddot{x}\} + [C]\{\dot{x}\} + [K]\{x\} = \{P\} \quad (4)$$

where  $[M]$ ,  $[C]$ , and  $[K]$  represent the mass, damping and stiffness matrix of the whole vehicle-track coupling model respectively. Thus, Eq. (4) can be written as

$$\begin{bmatrix} M_c & & \\ & M_r & \\ & & M_b \end{bmatrix} \begin{bmatrix} \ddot{x}_c \\ \ddot{x}_r \\ \ddot{x}_b \end{bmatrix} + \begin{bmatrix} C_{cc} & C_{cc} & \\ C_{rc} & C_{rr} & C_{rb} \\ & C_{br} & C_{bb} \end{bmatrix} \begin{bmatrix} \dot{x}_c \\ \dot{x}_r \\ \dot{x}_b \end{bmatrix} + \begin{bmatrix} K_{cc} & K_{cc} & \\ K_{rc} & K_{rr} & K_{rb} \\ & K_{br} & K_{bb} \end{bmatrix} \begin{bmatrix} x_c \\ x_r \\ x_b \end{bmatrix} = \begin{bmatrix} P_c \\ P_r \\ P_b \end{bmatrix} \quad (5)$$

The subscript  $c$  means car,  $r$  means rail, and  $b$  means ballast.

The details of the train and track parameters are shown in Ref. [27]. These values are expected to stabilise after the earthquake. The rail pad has a vertical static stiffness of 60 MN/m and a vertical damping of 75 kNs/m. The rail pad has a lateral static stiffness of 20 MN/m and a horizontal damping of 60 kNs/m.

The wheel-rail interaction force is simulated by Hertz nonlinear elastic contact theory. This theory can be adopted in the normal direction of wheel-rail contact. The vertical wheel-rail interaction force is denoted as

$$N_z(t) = \left[ \frac{1}{G} \delta Z(t) \right]^{3/2} \quad (6)$$

where  $G$  is the wheel-rail contact constant factor, whose unit is  $\text{m/N}^{2/3}$ .  $\delta Z(t)$  is the elastic compression deformation between wheel and rail whose unit is m.

Kalker linear creep theory [28] is used to calculate the longitudinal, lateral, and rotational creep forces between wheel and rail.

$$\begin{cases} F_x = -f_{11}\xi_x \\ F_y = -f_{22}\xi_y - f_{23}\xi_\phi \\ M_z = f_{23}\xi_y - f_{33}\xi_\phi \end{cases} \quad (7)$$

where  $f_{ij}$  is the Kalker creep coefficient.  $\xi$  is creepage.

The Shen-Hedrick-Elkins theory [29] is utilised to perform nonlinear adjustments on the longitudinal and lateral creep slip forces between the wheel and rail.

The Newmark- $\beta$  technique approach is used to solve the dynamic equations of the train, track, and under-track structure once they have been determined. Multiple iterations are required because the interaction between the subsystems at each time step is reliant on the system's response at that moment in time. The conditions of equilibrium of forces were used to calculate the interaction between the subsystems. As a consequence, the displacement difference between two successive iterations of the vehicle, rail, and under-rail structure at each time step meets the convergence condition's accuracy criterion. The highest precision in displacement is 0.1  $\mu\text{m}$ .

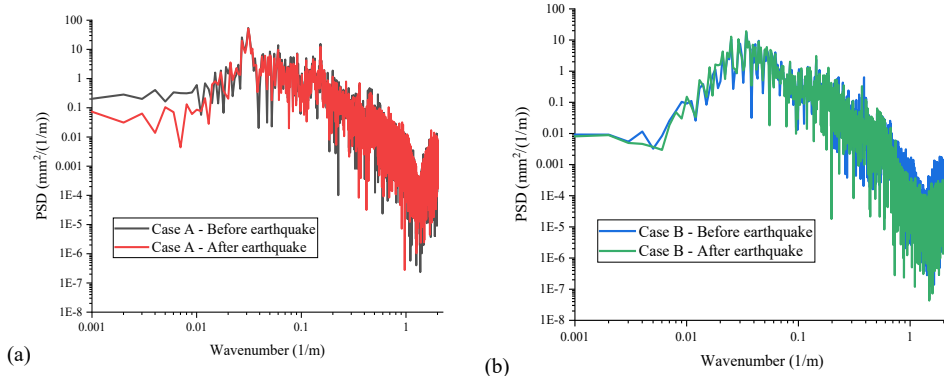
### 4.3 Calculation Results

Four scenarios are selected to investigate the impact of seismic-induced track irregularity. It is said to include two types of tracks, ballastless track, and ballasted track, as well as two levels of earthquake-affected track irregularities. The term 'severely' refers to the fact that the track irregularities alter much after the earthquake. The term 'slightly' refers to the track irregularities not altered notably as a result of the earthquake. Four cases information is summarised in Table 1.

Table 1  
Case summary

Case number	Track type	Track affected by earthquake
Case A	Ballastless track	Severely
Case B	Ballastless track	Slightly
Case C	Ballasted track	Severely
Case D	Ballasted track	Slightly

The power spectrum density of track longitudinal level is shown in Figure 11. From the PSD plot, it can be seen that the earthquakes have an influence on long waves from track irregularities greater than 10 m. For ballasted track, there is also a difference zone at wavenumber 0.1-0.3 (1/m) range which corresponding to the wavelength range 3-10 m.



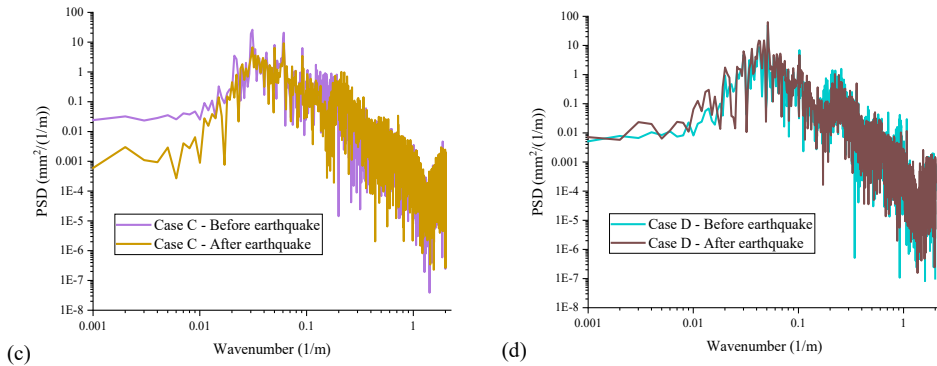


Figure 11

PSD of track irregularity longitudinal level from (a) Case A, (b) Case B, (c) Case C and (d) Case D.

The vehicle vibration, the rate of wheel load reduction, and derailment coefficient in time domain are shown in Figure 12. It can be known that within the green dashed line, the track geometric irregularity generated by the earthquake results in a more apparent deviation.

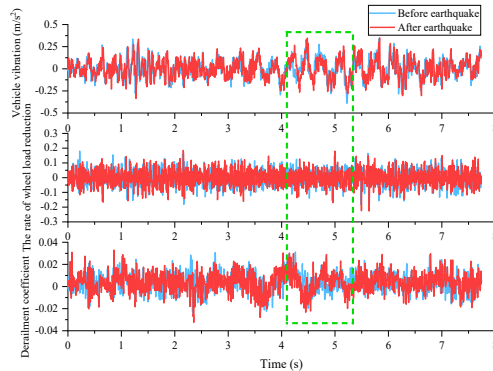


Figure 12

Vehicle vibration, the rate of wheel load reduction, and derailment coefficient in time domain.

### 4.3.1 Vehicle Acceleration

Focus on the vehicle acceleration, the maximum value and root mean square (RMS) value of acceleration in time domain is shown in Figure 13 corresponding to four cases introduced in Table 1.

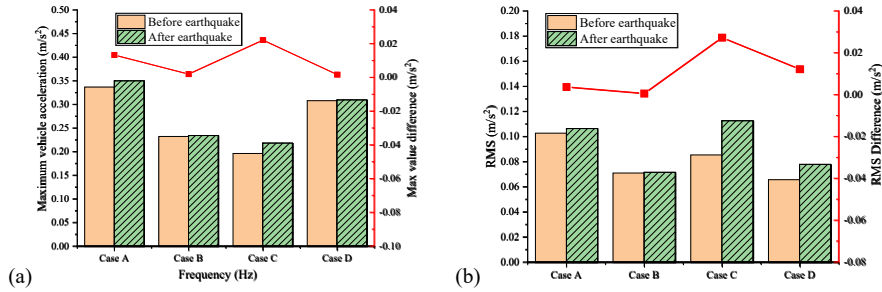


Figure 13

The vehicle acceleration value and differences (a) maximum value and (b) RMS value

The RMS value is calculated based on:

$$X_{\text{rms}} = \sqrt{\frac{\sum_{i=1}^N X_i^2}{N}} = \sqrt{\frac{X_1^2 + X_2^2 + \dots + X_N^2}{N}} \quad (8)$$

where  $X_i$  means the data sample and  $N$  is the number of sampling point.

From Figure 13, it is shown that there is a considerable rise in the maximum value of vehicle vibration for conditions that are badly affected by the earthquake, and the difference in the maximum value of vehicle vibration for circumstances that are slightly impacted by the earthquake is not significant. Focus on the RMS value of vehicle acceleration increase based on seismic-induced track geometric irregularities increased, the ballasted track can lead to more vibration increase compared with the ballastless track.

All the results presented above assume that after the earthquake, the track irregularity is altered while the track parameters remain unchanged. In this section, the RMS values of the vehicle are investigated when the track's vertical parameters are modified after the earthquake. Case C after the earthquake is selected as the reference case, and the RMS values of the vehicle are summarized in Table 2.

Table 2  
RMS value under different track parameters

Parameters: changed item	RMS value (m/s <sup>2</sup> )
Vertical stiffness: 48 MN/m (increase 20%)	0.115
Vertical stiffness: 72 MN/m (decrease 20%)	0.111
Vertical damping: 60 kNs/m (increase 20%)	0.116
Vertical damping: 90 kNs/m (decrease 20%)	0.111

From the results, it is evident that reducing the vertical stiffness and damping of the track after the earthquake leads to an increased response of the train (Case C exhibits an RMS value of the vehicle as  $0.1125 \text{ m/s}^2$ ).

### 4.3.2 The Rate of Wheel Load Reduction

The rate of wheel load reduction is an indicator to evaluate the train's safety. It can be calculated by:

$$P = \frac{\Delta P}{P_0} = \frac{P_2 - P_1}{P_2 + P_1} \quad (9)$$

where  $P$  is the rate of wheel load reduction  $\Delta P$  is lowering load side wheels' heavy load reduction.  $P_0$  is the average wheel weight.  $P_1$  signifies the wheelset's decreasing wheel side, while  $P_2$  denotes the wheelset's growing wheel side. The safety standard from Chinese standard is less than 0.65 for first limit related to vehicle operation security and less than 0.60 for second limit, which is related to safety allowance. The maximum value of the rate of wheel load reduction and the power spectrum density value of the rate of wheel load reduction before and after the seismic dynamic response is introduced in Figure 14.

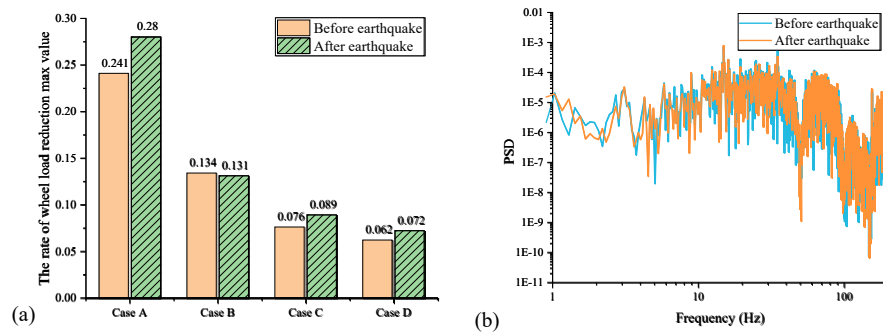


Figure 14

The rate of wheel load reduction (a) maximum value for one wheelset and (b) PSD value for case A

It can be known that for the ballastless track, the rate of wheel load reduction rises when the track is substantially affected by earthquakes and remains relatively constant when the track is not disturbed. When the ballasted track is also extensively affected by the earthquake, the rate of wheel load reduction rises, although not as much as on the ballastless track. Therefore, focusing on Case A, the PSD value is investigated. There is a significant difference in the 20-40 Hz frequency band. The rate of wheel load reduction above 50 Hz does not change significantly due to the track geometric irregularity caused by the earthquake.

### 4.3.3 Derailment Coefficient

The derailment coefficient is defined as the  $Q/P$  ratio of the lateral force  $Q$  to the vertical force  $P$  operating on the wheel at any given time. It can be denoted as

$$\frac{Q}{P} = \frac{\tan \alpha - \mu}{1 + \mu \tan \alpha} \quad (10)$$

where  $Q$  means the lateral force act on the wheel,  $P$  means the vertical force act on the wheel.  $\mu$  means the friction coefficient,  $\alpha$  means the maximum flange contact angle. For rail safety considerations, the Chinese standard specifies that this indicator be smaller than 0.8.

The maximum value and Case A PSD value of derailment coefficient is shown in Figure 15.

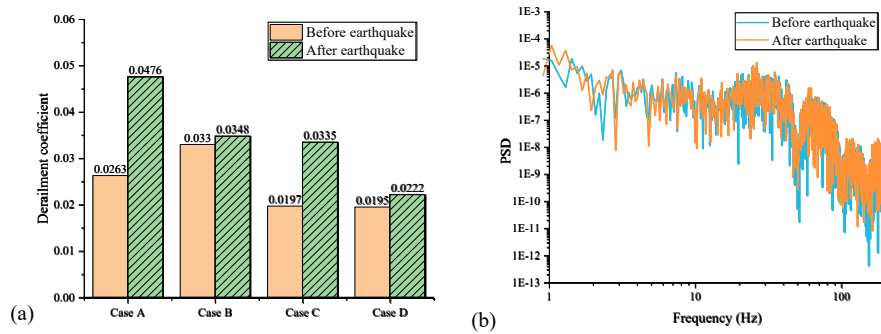


Figure 15

The derailment coefficient (a) maximum value and (b) PSD of Case A

From Figure 15, it can be seen that Case A has the highest derailment coefficient, followed by Case C. After the earthquake, the derailment coefficients for Cases B and D remain almost unchanged. The maximum value differences of derailment coefficient are from Case A, thus, the PSD value analysis from Case A is investigated. The main trend PSD of Case A is similar before and after the earthquake. There are some not very significant differences at 30 Hz and 150 Hz.

Although the derailment coefficient and rate of wheel load reduction have increased somewhat in maximum value as a result of the earthquake, they remain within the specification's normal range. This demonstrates that minor and moderate earthquakes have little effect on train operation safety.

### Conclusion

The seismic-influenced track states of HSR were evaluated, as was the effect of earthquakes of various magnitudes level (3.0-7.0), different lines, and varied track types (ballasted and ballastless). Additionally, the impact of various earthquake-induced track irregularities on vehicle vibration are estimated and investigated

using the vehicle-track dynamic analysis model. Some conclusions can be summarised.

According to measurements and statistical analysis of the track state on-site after the earthquake in China, the earthquake had varying degrees of influence on the HSR track. The long-wave irregularity, 95% cumulative value of 10 m-chord measurements, and track quality index vehicle acceleration measured data are seen as the parameters for evaluating the seismic-induced track geometric irregularity. These parameters suggest that high-speed railways are affected by earthquakes which can produce a certain amount of track irregularities changes.

The statistical conclusions of TQI differences value, long-waveform vertical waveform, 10 m-chord measurement value, and vehicle vertical acceleration are analysed based on over 30 measurement sites of the influence of earthquakes on track geometry during the previous decade. For a ballast track with a nominal speed of 250 km/h, the TQI variation can reach a maximum of 1.6 and the track geometric irregularity variation of 1.4 mm obtained by 10 m chord measurement, both of which are greater than for a ballastless track with a nominal speed of 350 km/h, whose TQI variation value is up to 0.75, and track irregularity variation based on 10 m-chord method is around 1mm.

A train-track coupling model is built to calculate the train running safety and comfort under different track geometric irregularities. The ballasted track can induce higher train vibration. The maximum value from calculation results is around  $0.45 \text{ m/s}^2$ . The rate of wheel load reduction and derailment coefficient is higher for the ballastless track, whose value is up to 0.28 and 0.0476 respectively, compared with that indicator for the ballasted track. However, all of these indicators meet the requirement.

### **Acknowledgement**

This research was funded by China State Railway Group Corporation Limited science foundation (No. P2021T013) and China Academy of Railway Sciences Corporation Limited science foundation (No.2021YJ250). The supports are gratefully acknowledged.

### **References**

- [1] A. Vijayakumar, H. Qian, The High-Speed Railway Bridges Under Vehicle Moving Load And Near Fault Seismic Ground Motions – Review, *Journal of Building Materials and Structures*, 8(2), 2021, pp. 115-127
- [2] X. Xiao, L. Ling, X. Jin, A study of the derailment mechanism of a high speed train due to an earthquake, *Vehicle System Dynamics*, 50(3), 2012, pp. 449-470
- [3] X. Wu, S. Liang, M. Chi, An investigation of rocking derailment of railway vehicles under the earthquake excitation, *Engineering Failure Analysis*, 117 2020

- 
- [4] Y. C. Cheng, C. T. Hsu, Derailment safety analysis for a tilting railway vehicle moving on irregular tracks shaken by an earthquake, *Proceedings of the Institution of Mechanical Engineers, Part F: Journal of Rail and Rapid Transit*, 230(3), 2014, pp. 625-642
- [5] Z. Lai, X. Kang, L. Jiang, W. Zhou, Y. Feng, Y. Zhang, J. Yu, L. Nie, M. Bayat, Earthquake Influence on the Rail Irregularity on High-Speed Railway Bridge, *Shock and Vibration*, 2020 2020, pp. 1-16
- [6] Y. Lin, G. Yang, Dynamic behavior of railway embankment slope subjected to seismic excitation, *Natural Hazards*, 69(1), 2013, pp. 219-235
- [7] S. H. Ju, H. C. Li, Dynamic interaction analysis of trains moving on embankments during earthquakes, *Journal of Sound and Vibration*, 330(22), 2011, pp. 5322-5332
- [8] X. Kang, L. Jiang, Y. Bai, C. C. Caprani, Seismic damage evaluation of high-speed railway bridge components under different intensities of earthquake excitations, *Engineering Structures*, 152 2017, pp. 116-128
- [9] X. Gao, P. Duan, H. Qian, Dynamic response analysis of long-span continuous bridge considering the effect of train speeds and earthquakes, *International Journal of Structural Stability and Dynamics*, 20(06), 2020, 2040013
- [10] Y. Feng, L. Jiang, W. Zhou, J. Han, Y. Zhang, L. Nie, Z. Tan, X. Liu, Experimental investigation on shear steel bars in CRTS II slab ballastless track under low-cyclic reciprocating load, *Construction and Building Materials*, 255 2020
- [11] C. Yang, X. Cai, Seismic Response of a Cable-Stayed Bridge considering Non-uniform Excitation Effect: Model Design and Shake Table Testing, *KSCCE Journal of Civil Engineering*, 26(1), 2021, pp. 286-297
- [12] X. He, M. Kawatani, T. Hayashikawa, T. Matsumoto, Numerical analysis on seismic response of Shinkansen bridge-train interaction system under moderate earthquakes, *Earthquake Engineering and Engineering Vibration*, 10(1), 2011, pp. 85-97
- [13] X. T. Du, Y. L. Xu, H. Xia, Dynamic interaction of bridge-train system under non-uniform seismic ground motion, *Earthquake Engineering & Structural Dynamics*, 41(1), 2012, pp. 139-157
- [14] Y. B. Yang, Y. S. Wu, Dynamic stability of trains moving over bridges shaken by earthquakes, *Journal of Sound and vibration*, 258(1), 2002, pp. 65-94
- [15] M. Tanabe, N. Matsumoto, H. Wakui, M. Sogabe, H. Okuda, Y. Tanabe, A simple and efficient numerical method for dynamic interaction analysis of a high-speed train and railway structure during an earthquake, *Journal of Computational and Nonlinear Dynamics*, 3(4), 2008

- 
- [16] L. Jiang, J. Yu, W. Zhou, W. Yan, Z. Lai, Y. Feng, Applicability analysis of high-speed railway system under the action of near-fault ground motion, *Soil Dynamics and Earthquake Engineering*, 139 2020
- [17] L. Xu, W. Zhai, Stochastic analysis model for vehicle-track coupled systems subject to earthquakes and track random irregularities, *Journal of Sound and Vibration*, 407 2017, pp. 209-225
- [18] Z. Zeng, Y. Zhao, W. Xu, Z. Yu, L. Chen, P. Lou, Random vibration analysis of train-bridge under track irregularities and traveling seismic waves using train-slab track-bridge interaction model, *Journal of Sound and Vibration*, 342 2015, pp. 22-43
- [19] J. Yu, L. Jiang, W. Zhou, X. Liu, Z. Lai, Seismic-Induced Geometric Irregularity of Rail Alignment under Transverse Random Earthquake, *Journal of Earthquake Engineering*, 2022, pp. 1-22
- [20] J. Yu, L. Jiang, W. Zhou, J. Lu, T. Zhong, K. Peng, Study on the influence of trains on the seismic response of high-speed railway structure under lateral uncertain earthquakes, *Bulletin of Earthquake Engineering*, 19(7), 2021, pp. 2971-2992
- [21] J. Yu, L. Jiang, W. Zhou, X. Liu, Z. Lai, Evolutionary power spectrum density of earthquake-induced rail geometric irregularities, *Structure and Infrastructure Engineering*, 2022, pp. 1-16
- [22] D. Mu, S. G. Gwon, D. H. Choi, Dynamic responses of a cable-stayed bridge under a high speed train with random track irregularities and a vertical seismic load, *International Journal of Steel Structures*, 16(4), 2016, pp. 1339-1354
- [23] J. Yu, L. Jiang, W. Zhou, Study of the target earthquake-induced track irregularity spectrum under transverse random earthquakes, *International Journal of Structural Stability and Dynamics*, 22(16), 2022, 2250190
- [24] L. Ma, H. Ouyang, C. Sun, R. Zhao, L. Wang, A curved 2.5D model for simulating dynamic responses of coupled track-tunnel-soil system in curved section due to moving loads, *Journal of Sound and Vibration*, 451 2019, pp. 1-31
- [25] A. E. Fazio, J. Corbin, Track quality index for high speed track, *Journal of transportation engineering*, 112(1), 1986, pp. 46-61
- [26] J. Zhuang, J. Peng, X. Zhu, W. Huang, Scenario-Based Risk Assessment of Earthquake Disaster Using Slope Displacement, PGA, and Population Density in the Guyuan Region, China, *ISPRS International Journal of Geo-Information*, 8(2), 2019
- [27] S. Ma, L. Gao, X. Liu, J. Lin, Deep Learning for Track Quality Evaluation of High-Speed Railway Based on Vehicle-Body Vibration Prediction, *IEEE Access*, 7 2019, pp. 185099-185107

- [28] J. J. Kalker, On the rolling contact of two elastic bodies in the presence of dry friction, Delft University, The Netherland, 1967
- [29] Z. Shen, J. Hedrick, J. Elkins, A comparison of alternative creep force models for rail vehicle dynamic analysis, *Vehicle System Dynamics*, 12(1-3), 1983, pp. 79-83

# Investigation of Rail Welded Joint Stresses, by using a Narrow Gap Welding Method, in Ballasted Railway Tracks

**Milad Alizadeh Galdiani, Seyed Ali Mosayebi and Mohamad Ali Mohit**

Department of Railway Engineering, Iran University of Science and Technology, University St., Hengam St., Resalat Sq., 13114-16846 Tehran, Islamic Republic of Iran, milad\_alizadeh@alumni.iust.ac.ir, mosayebi@iust.ac.ir, mohit@inha.edu

---

*Abstract: In the modern railway superstructure construction and maintenance, particularly where higher speeds are required, the rail sections may be welded together to form Continuous Welded Rail (CWR). There are various methods for welding the rails, such as thermite welding, flash-butt welding, gas-pressure welding, enclosed-arc welding, etc. Narrow Gap Welding is another way of welding the rail joints and because of the lower implementation costs, easier, quicker process and acceptable performance, it is usually used over other methods in maintenance operations. Since this method is newer than others, there is lack of knowledge concerning the standard process of narrow gap welding and the factors that affect the final quality. In the narrow gap welding, two different welding electrodes are used for the welding process. One electrode, with higher stiffness, is used for the rail head and the other electrode, with lower stiffness, is used for the rail web and foot. In this research, the relationship between these different welding electrodes and the amount of stress in rail joint was investigated via experiments and modeling, by a finite element method. The results indicate that the number of stresses, in the junction of rail head and web, was reduced by 37%, when the electrode with higher stiffness was used for the whole rail head, plus 1 cm of rail web. Field investigations demonstrated that the performance of rail welds was acceptable.*

*Keywords: railway superstructure; rail joint; welding electrodes; narrow gap welding; finite element method*

---

## 1 Introduction

In railway tracks, the use of fishplates and bolts was common to connect the rail sections, before the advent of producing longer rail sections and using welding technology, for the connection of rails in joints [1]. In this method, the rail sections are connected only through the rail web using bolts, nuts and fishplates on both sides of the rail web [2] [3]. This system has numerous disadvantages, such as:

- Creating very large dynamic forces in rail joints when the train passes through the track
- Weakening the railway structure
- Reducing the service life of the track elements including rails, sleepers and the fastening system
- Increasing the cost of maintenance and repair operations by 25%
- Increasing the cost of the maintenance and repair operations for the railway track and rolling stock
- Defects, such as crushing of the end of the rails in joints and failures due to the inherent fatigue
- Generation of excessive noise while the vehicle is passing on the track
- Deterioration of the desired track geometry in a short time [2, 4, 5]

As the speed and the axel loads of the rolling stock increase, the destructive effects of the expansion joints become more important [6] [7]. In order to reduce the negative effects of the expansion joints in railway tracks, there are two solutions: 1- using longer rails and thus reducing the number of expansion joints required to connect rail sections to each other and 2- using the welding techniques to connect the rails to each other (In this way, the expansion joints are completely welded to form CWR tracks) [8-11]. Therefore, welding the rails in joints is done to achieve these goals: increasing the continuous length of the rail and thus reducing the number of joints, fishplates and bolts; overcoming the weakness of the track due to the expansion joints; saving money by reducing the volume of repair and maintenance operations; increasing the service life of the track; and so on [12] [13]. There are different methods of welding the rails in joints in Iranian railways including thermite welding, electric welding, gas pressure welding, electric arc welding and narrow gap welding. Thermite welding is a set of processes in which the filler material is made of molten metal created by a highly exothermic chemical reaction [14-16]. The chemical reaction or thermite usually takes place between the oxide of a metal (iron or copper) and aluminum powder at a high temperature. A rapidly ignited powder is used as a detonator to provide the heat needed to start the reaction [1]. Two examples of the chemical reactions in this type of welding are as given in the following Eq. (1) and (2):



This type of welding is more like casting and there is a mold around the two components that must be welded together [15]. The molten metal produced by this chemical reaction is directed to this mold and is hardened inside the welding mold due to cooling [12]. In this welding method, there is no need for energy supply systems such as electricity generators and the welding process can be carried out anywhere [12]. The main disadvantages of this method are:

- 1) The welding process generates gaseous pollutants (hydrogen) and also slag.
- 2) Sometimes the high temperature of the process causes distortion and relatively large deformations at the welding joint [17-19].

Electric welding along with thermite welding is a common method to remove rail joints by welding the rail sections. One of the advantages of electric welding compared to thermite welding is performing the welding process without adding extra material, which has a great impact on the strength of the rail and its service life [13]. Electric welding is done in two different methods in railways. In the first method, the rail sections are welded to the required lengths and then a crane is used to transport them to the site for installation. In the second method, welding operations are carried out by modern fixed and mobile welding machines [20].

Gas pressure welding is another method to build a CWR track. Special equipment is needed to weld the rails in this method and the welding process take more time than the previous methods. This method also requires trained technicians and the welding quality is higher [13].

Narrow gap welding is a relatively newer method than other rail welding methods. In the narrow gap welding method, according to the results of research from 1975 to 2000, the quality of rail at welded joints has improved compared to the original metal [13] [21]. The quality of this type of welding is greatly improved by using the appropriate electrode, designing and optimizing suitable alloys, and using water or air cooling shoes to control the rate of temperature during the welding process. The quality of the narrow gap welding is directly related to the skill and experience of the welding technicians and the welders [13] [21]. Besides, it is very important to provide precise instructions for the whole process which have to be observed, since the slightest change in the correct narrow gap welding process will cause a defect in the welded joint. This factor prolongs the time needed to carry out the narrow gap welding process compared to other rail welding methods, and also causes human errors [8, 13, 22]. Although the narrow gap welding method is currently used in the most railways under construction and has been accepted as a welding method, so far there are no comprehensive and complete instructions for the implementation of this method. In this research, while the existing criteria for narrow gap welding are investigated, the optimal pattern of the electrodes is defined by a finite element method.

## 2 Narrow Gap Welding

Within the railway industry, the narrow gap welding method is utilized for the construction of CWR tracks and also, for repair and maintenance operations. This method is widely used due to its advantages than other methods of welding namely, lower costs compared to other welding methods and also fulfilling the structural

standards needed for railway operations based on the loading and velocity of the rolling stock [23]. As mentioned before, this method requires skilled welding teams, precise welding process and strict regulations and instructions [8, 13, 21, 22].

There are some materials used to perform narrow gap welding including electrodes and retaining molds. The electrodes used in this method must be selected such that they can accommodate to the original rail properties [1]. The elasticity as well as the abrasion resistance of the weld must be proportional to the reference metal and this is possible by selecting the appropriate electrode. Tensile strength parameter should be considered in selecting the appropriate electrode for the rail web and foot, and abrasion resistance along with tensile strength should be considered in selecting the appropriate electrode for the rail head. Welding of rail joints by narrow gap method is done inside a chamber including rails and retaining molds [13]. These molds are made of cast copper whose dimensional characteristics are proportional to the type of electrode, type of rail and operating temperature. The retaining molds must be thermally conductive; therefore, the molds are made of copper. In addition, the molds control the tension of the rail and welding. The molds have several separate sections for the rail web and foot. The retaining molds must be carefully maintained, as they can lose their original geometry, over time [4, 8, 13, 22, 24].

The narrow gap welding method has two steps. The first step is preparation, which its purpose is to prepare the rails and joints for welding. This step must be done carefully and it has to be controlled multiple times. Prior to welding, the rails at the joint must be free of defects like cracks and crushed heads, and if these defects are already occurred, the rails must be ground and cut with the related machines [22]. In the tracks with Vossloh-fastening system, to carry out the welding, only the screws of the near sleepers can be opened. Because when the screws are opened, the dust is infiltrated into the dowels. In order to perform a clean weld, the cross section of the rail at the joint must be completely polished and free of any greasy or impure materials. In this regard, the rail and weld materials are completely connected by using a continuous electric arc between the rail and the electrode, and consequently a perfect weld is created [13]. One of the most important factors in performing a desirable weld by narrow gap method is adjusting the rail joint. The rail ends at the joint should be aligned vertically and horizontally so that the foot, web and head of both rails are in the same direction [8, 21, 25].

The second step is welding the rails. After adjusting the rail joint, the rails at both sides of the joint, are heated to a distance of 100 mm, which is called, preheating [1, 12, 13]. When the rail reaches a certain temperature, the welding process begins. The special mold for the rail foot is fixed at the certain position, before starting the welding process. Then the lowest part of the rail is welded. As mentioned before, accuracy and skill in performing welding are very important in its quality. The electrode used in this step is exerted for both the foot and web [25]. In this research, the mechanical properties of ESAB OK 74.78 electrode are considered for the web and foot. Welding of rail foot is carried on until the beginning of rail web section. At this stage, the special web mold is installed in the desired position and

welding process continues. When the web section welding is completed, the head of the joint is welded immediately and without interruption [22]. As previously described, the electrode used in the head of the joint has different materials than the foot and web section. This electrode must have abrasion resistance [25]. In this research, the mechanical specifications of ESAB OK 83.28 electrode have been considered for the head. Following the end of the welding process, the molds are separated and the original rail and the welded joint are leveled using the grinding machine. The last step in narrow gap welding is the post-heating operation [21] [22]. In the post-heating operation, the parts are heated to a certain temperature after welding and then cooled at a gentle rate. This prevents unwanted compressive and tensile stresses from welding process [25].

As illustrated earlier, two different electrodes are used for welding the rail sections in the narrow gap welding method. The electrode used for welding the rail head must resist against abrasion. The properties of the electrodes used in this research are demonstrated in Table 1.

Table 1  
The properties of the electrodes in the narrow gap welding

Category	Yield Stress (MPa)
ESAB OK 74.78	600
ESAB OK 83.28	650

One of the most important steps in the narrow gap welding is determining the position where the different electrode must be used for welding the rail head. According to Fig. 1 there are three options for this position. Determining this position will affect the construction, maintenance and repair costs of the railway tracks, since the electrode used for the rail head is more expensive. Also, each of the three patterns “a”, “b” or “c” is effective in finding the stresses created in the weld section. Although experiential observations demonstrate that the best pattern is option “b”, but there are less scientific investigations in this issue [21, 22, 25]. Therefore, in this research, three models based on the Fig. 1 are created in the ABAQUS software to analyze the produced stresses in the welded joint due to the loading of rolling stock.

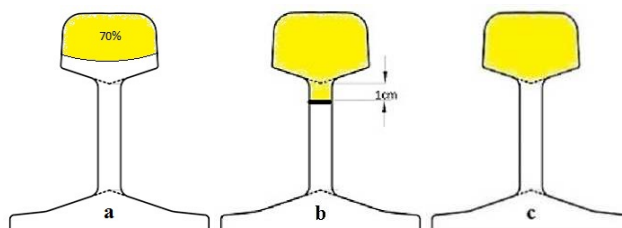


Figure 1

The yellow area shows the special electrode with abrasion resistance: a- 70% of the rail head, b- rail head and 1cm of web, c- the whole rail head area

### 3 Railway Loadings

The railway structure is subject to various forces. Since there is direct connection between the rail and the wheel, and the first component which is bearing the loads of rolling stock is the rail; all of loads are transferred by the rail to other components [26-30]. So, analyzing the various rail stresses, is the first step, in designing the railway track [8, 31-36].

One way to classify the forces applied to the rail is based on the direction of the force, which is divided into three categories of vertical, lateral (horizontal force and perpendicular to the track) and longitudinal forces (horizontal force and in the track direction) [37] [38]. These forces are shown in the Fig. 2.

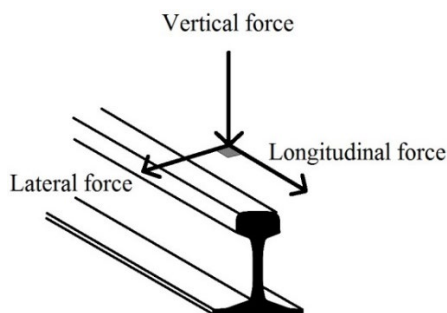


Figure 2  
Different forces introduced by a wheel on a rail

Another method classifies the forces applied to the railway track into two categories of static and dynamic forces[39]. Static forces are mainly due to the weight of the railway vehicles, but it should be noted that since the rolling stock is passing over the rail and due to the existence of geometric and structural defects in the rails and in the railway vehicles, the nature of the vertical and lateral forces on the rail is dynamic [8, 40-47].

In this paper, the vertical and lateral forces are considered based on the railway track systems in Iran, and the longitudinal forces are ignored. The lateral forces on the rail are calculated based on the model calibrated by Sadeghi (2008) which is appropriate for the Iranian railway network [48]. The advantage of this model is that it is based upon the two parameters of velocity and the radius curve in the track. In this equation the curve radius is considered an infinite number since it has been presumed that the joint is located in the direct track and not in the curve[49, 51, 53]. This equation has been shown in the Eq. (3):

$$H = \left(\frac{1}{R}\right)(0.028V^2 + 7.62V + 4742.1) + V(1.34 \times 10^{-4}V + 0.036) + 22.43 \quad (3)$$

H: Lateral load (kN)

V: Velocity (Km/h)

R: Radius curve (m)

The axle load of 22.5 tons is considered as the vertical force, which is the common axle load in the Iran's railway network. Therefore, the single wheel vertical static force is 11.25 tons. In order to consider the dynamic impacts of the railway vehicles, a dimensionless dynamic impact factor is multiplied by the vertical force.

The train wheels motion and the shocks caused by the movement of wheels on the uneven surface of rails are two main reasons for the dynamic nature of railway loading. There are various methods to calculate dynamic loads in the literature and it is performed by considering a dimensionless dynamic loading coefficient. In this research, Eq. (4), which is offered by AREMA, has been used to calculate the dynamic coefficient[49].

$$\varphi = 1 + 5.21 \frac{V}{D} \quad (4)$$

V: Velocity (Km/h)

D: Wheel diameter (mm)

In Iranian railway network the passenger and freight trains are running simultaneously from the tracks which means that the tracks are designed to carry the loads coming from both passenger and freight trains[48]. The loading pattern on the railway track is considered as a mixture of axle load from wagons and locomotive. The axle load of wagons and locomotives of passenger trains are 12 and 22.5 tons respectively[48]. The axle load of freight trains is considered as 22.5 tons. Hence, the designation axle load in the railway tracks in Iran railway network is 22.5 tons. According to the Iranian Railways system, the train speed is 120 km/h and the wheel diameter for wagons and locomotive is 1000 and 1200 mm respectively. Consequently, the values of dynamic coefficients are 1.62 and 1.52, for wagon and locomotive respectively [51] [53]. A standard UIC 60 rail profile and concrete sleepers are assumed for the modeling. The distance between sleepers is considered 600 mm. It has been presumed that the joint is located in the direct track and not in the curve. Also, there is no longitudinal or lateral slope in the track. It has to be mentioned that the gravitational forces are simulated in the model due to the weight of the materials. After determining the vertical and lateral forces introduced on the rail, these forces are applied to the weld section in the model to analyze the weld and rail stresses at the joint.

## 4 Modelling of Railway Track

The modeling of a railway track and the welded joint has been performed based on finite element method (ABAQUS software). There are eight steps for creating a model of a railway structure. In the first step (part step), the geometry of the different components of railway structure is drawn. According to the common railway systems of the Iran's railway network, a UIC 60 rail profile and simple concrete sleepers are used in the model (Table 2).

Table 2  
The properties of the rail in the finite element model

<b>Rail geometric properties</b>				
<b>Rail type</b>	<b>Head width (mm)</b>	<b>Height (mm)</b>	<b>Base width (mm)</b>	<b>Web thickness (mm)</b>
60E1 (UIC60)	72	172	150	16.5

<b>Rail mechanical properties</b>							
<b>Rail type</b>	<b>Rail steel hardness (MPa)</b>	<b>Yield stress (MPa)</b>	<b>Ultimate stress (MPa)</b>	<b>Allowable elongation (mm)</b>	<b>Poisson's ratio</b>	<b>Elastic modulus (GPa)</b>	<b>Specific mass (Kg/m<sup>3</sup>)</b>
60E1 (UIC60)	900	580	1000	10	0.3	200	7854

Also, the joint between the two rail sections that is supposed to be filled with welding electrodes, is drawn separately. The width of the joint is considered as 10 mm. The joint is drawn in three different cases based on the patterns shown in Fig. 1. In the second step (property step), all the specifications and mechanical properties of the materials, including electrodes, rail and concrete sleepers, are assigned to the materials based on the standards and the relevant regulations (Table 3).

Table 3  
The properties of the materials in the finite element model

<b>Sleeper (B70) properties</b>			
<b>Sleeper type</b>	<b>Fc (MPa)</b>	<b>Ft (MPa)</b>	<b>Section dimension (cm<sup>2</sup>)</b>
Pre stressed B70	50	5	20 * 20

<b>Electrode properties</b>				
<b>Electrode type</b>	<b>Yield stress</b>	<b>Tensile strength</b>	<b>Elongation</b>	<b>Welding current</b>
ESAB OK 74.78	600 MPa	650 MPa	24%	DC+, AC
ESAB OK 83.28	650 MPa	-----	24%	DC+, AC

In the assembly step, all components of the track structure are put together according to Fig. 3, and in the fourth step, the type of analysis is determined which is semi-dynamic. An essential aspect of the assembly process is to ensure that each component of the railway track is accurately positioned at the appropriate angle to facilitate reasonable interactions between elements such as the rail to sleeper and sleeper to ballast etc. In addition to the precise positioning of the railway track components during assembly step, it is also crucial that their dimensions are accurately defined to enable direct connections between them. This is particularly important in subsequent steps, such as the meshing process, where the components need to be securely interconnected to form a stable and functional railway track in the model. Also, the type of interaction between the materials is determined in the next step (interaction step), which means that the contact of the surface of the components including rail to sleeper and sleeper to ballast is defined in this step. The loading is assigned according to the Iran's railway network which has been discussed in the previous section. Boundary conditions are also considered in the load step, with proportional stiffness to simulate the ballast and subgrade layers under the sleepers [50].

Table 4  
The properties of the ballast and sub-ballast in the finite element model

Item	$E_b$ (MPa)	$\Phi$ (°)	Stiffness (KN/mm)
Ballast	250	20	25.53
Sub-ballast	150	35	25.53

To calculate the stiffness in the ballast, sub-ballast and subgrade, the ballast pyramid model has been used.[48, 52, 54]. In this research, stiffness of the ballast, sub-ballast and subgrade is calculated as 25.53 KN/mm which detail of the layers has been shown in Table 4. This stiffness is considered as the total stiffness under the sleeper and is implemented in the model.

The stress measurements are specifically focused on the part of the rail that lies between the sleepers. Referring to Fig. 3, it is observed that the blue section represents the welding point, while the orange section represents the rail's cross-section where the analysis is conducted. Mesh step is one of the most important parts of modeling and this module is for creating finite element meshes. In the mesh step the nodes, number of nodes and size of the elements of the track are defined. The nodes of the elements of the different components must have the necessary coordination with each other. The size of each component should be defined so that the number of elements is appropriate, which means that the number of elements will increase. This will increase the precision, but it should not cause any numerical errors.

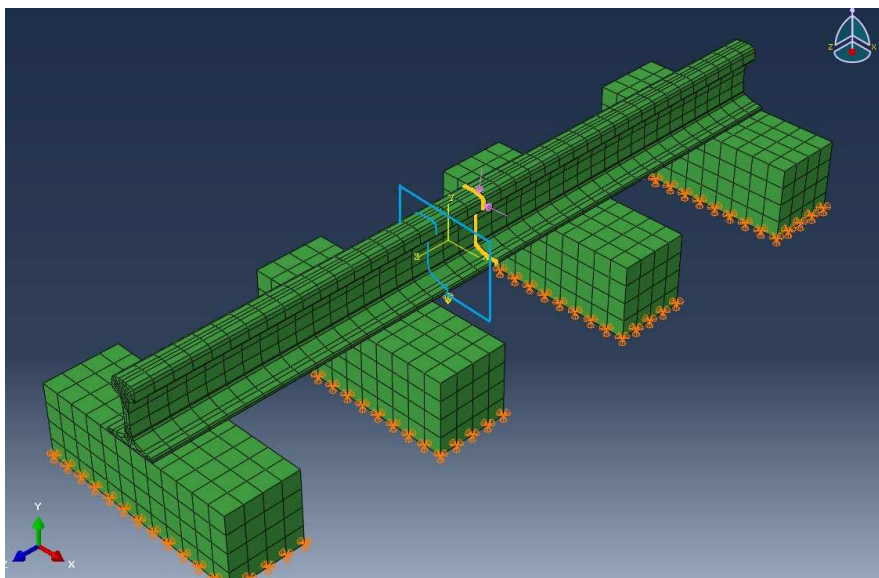


Figure 3  
Finite element model

To ensure greater accuracy in the interaction between components and reduce the computational load, it is necessary for the size of the elements in the rail foot to be consistent with the size of the sleeper's upper surface. By maintaining the same dimensions, a more precise representation of the component interaction can be achieved, while simultaneously minimizing the volume of calculations required. Finally, according to the existing system, the analysis operation is performed and the results are extracted to be analyzed. As mentioned before, the model is created in three different cases for all the three patterns “a”, “b” and “c” according to Fig. 1; so, the analysis of the stresses in the rail and the welded joint, is performed three times.

## 5 Results and Discussion

### 5.1 Finite Element Analysis and Loading

The results of stress distribution in the welded joint and rail cross sections are shown in the Figures 5-7, based on the model created for the three different patterns “a”, “b” and “c”. The figures demonstrate two cross sections: one cross section exactly at the welded joint location; and the other cross section at the rail close to the welded joint.

The bending stresses caused by the vertical and lateral forces are calculated in 3 critical points at the rail, including rail head, the junction of rail head and web and the junction of rail web and foot in which there is stress concentration. The measured stresses are shown in Table 5.

Table 5  
The measured stresses at 3 stress concentration zones in the rail

Measured point	Stress (MPa)		
	Pattern (a)	Pattern (b)	Pattern (c)
Rail head	153.48	169.30	155.06
Junction of rail head and web	142.41	142.40	142.41
Junction of rail web and foot	79.11	94.94	50.63

Since the stress concentration occurs at the junction of the rail head and web and also at the end of the rail foot, the stress value in these points has been investigated in the three patterns “a”, “b” and “c”. The results in the welded joint cross section for the patterns “a”, “b” and “c”; indicated that the maximum stress at the junction of the rail head and web occurred at the pattern “c” where the whole rail head has been welded by the abrasion resistant electrode. The lowest stress at the junction of the rail head and web in the welded cross section occurred at the pattern “b”, where the whole head and 1 cm of the web have been welded by the abrasion resistant electrode. The results demonstrated that the stress value decreased by 37% from pattern “c” to pattern “b” at the mentioned position. The stress value at the junction of the rail head and web for the pattern “a”, is similar to the pattern “c” according to Fig. 4 and Fig. 6. The results of stress analysis in the rail foot indicated that the pattern “c” achieved the best performance compared to other patterns. The maximum stress value in the pattern “c” for the rail foot decreased by 28% in comparison with stress value at the patterns “a” and “b”.

Regarding the results of modeling and the stress distribution at the rail cross section close to the welded joint, a negligible difference between the stress values of three patterns has been observed at the junction of the rail head and web. However, in the rail foot, the maximum stress value in pattern “c”, decreased by 21% compared to patterns “a”, and “b”, and the pattern “c” performed more properly than other patterns.

To validate the model, a comprehensive analysis was performed by comparing its outputs with previous studies. Specifically, the stress levels in the rail were evaluated and compared with those calculated in prior research based on relevant leaflets and standards. The results indicated that the stress values predicted by the

model fell within a similar range as those obtained from previous studies, thus, confirming the model's accuracy and reliability in assessing rail stresses. [48, 49, 51, 53, 55].

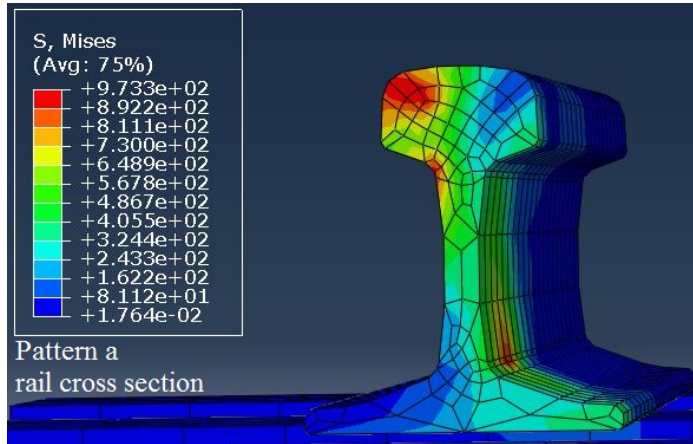


Figure 4  
Stress distribution in the pattern "a"

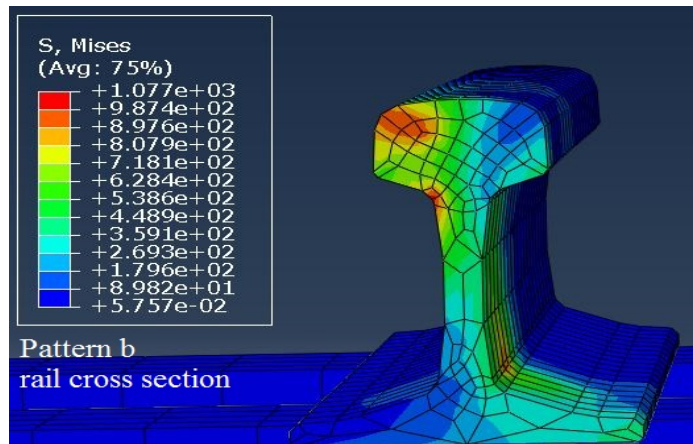


Figure 5  
Stress distribution in the pattern "b"

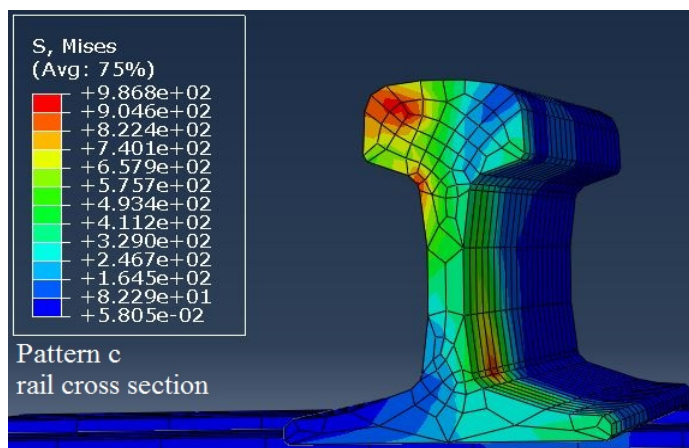


Figure 6

Stress distribution in the pattern "c"

## 5.2 Field Investigations

Based on the results of finite element modeling and the stress distribution in three patterns "a", "b" and "c" for a welded joint by narrow gap welding method, it is recommended to use pattern "b" as the most effective way of using electrodes in the narrow gap welding in Iran's railway network. The welding process of rail sections in Iran has been conducted by narrow gap welding method and using pattern "b" is shown in Fig. 7 (a).

The ultrasonic and portable hardness tests have been used to evaluate the performance of welded joints after the welding process. The outcome of the tests showed that the performance of welded joints was acceptable and the welding process has been done according to the recommended instructions. The procedure of ultrasonic test is demonstrated in Fig. 7 (b).

Although the narrow gap welding method is a new innovative way for rail joint welding, in its primary prototypes have had an acceptable performance and based on statistics and limited tests in railway track, it has been proven that it can be used on a large scale in the railway industry. An important aspect to highlight is the relatively new adoption of the narrow gap welding method within Iran's railway industry. Due to the limited knowledge and confidence surrounding its implementation, this welding technique has been utilized in only a few selected projects thus far. Consequently, there is a scarcity of information pertaining to the narrow gap welding method, necessitating further studies and research in the coming years. As the industry progresses, it is expected that increasing attention will be directed towards exploring and refining the potential of the narrow gap welding method, for railway applications in Iran.



Figure 7

(a) Welding process by narrow gap welding method (b) The ultrasonic test for rail welds

## Conclusions

In the modern railway systems, the rail sections are welded together to form a Continuous Welded Rail (CWR) track. According to the predicted increase in train speed and axle loads, the use of CWR tracks could increase the safety and comfort of trains. There are different methods for welding the rails. Meanwhile, Narrow Gap Welding, is a common method in the construction and maintenance of railways, which has advantages, such as availability and lower costs. In the Narrow Gap Welding process, two types of electrodes are used with different stiffness; one electrode with abrasion resistance is used for the rail head and the other for the rail web and foot. In the current research a ESAB OK 74.78 electrode is considered for the rail web and foot, and an ESAB OK 83.28 electrode for the rail head. Due to the limitations of this welding method, the procedure concerning the use of the harder electrode in the rail head is less discussed. In this study, three different patterns for welding the rail head with harder electrode are investigated and modeled, based on a Finite Element Method (FEM). In the pattern “a”, 70% of the rail head is welded by the harder electrode, in the pattern “b”, the whole rail head plus 1 cm of the rail web is welded by the harder electrode and in the pattern “c”, the whole rail head is welded by the harder electrode. The results of modeling and stress distribution in the mentioned patterns, indicated that in the welded joint, the stress value at the junction of the rail head and web in the pattern “b” is 37% less than the stress value at the same point in the patterns “a”, and “c”. Also in the rail foot, the maximum stress value in the pattern “c” is 70% of the maximum stress value of other patterns. According to the modeling results and analysis of existing stresses, it is recommended to use pattern “b”, in the Narrow Gap Welding method.

## References

- [1] Esveld, C.: *Modern Railway Track, 2nd Edition*. MRT Productions, 2012.

- [2] Zerbst, U. et al.: Introduction to the damage tolerance behaviour of railway rails – a review. *Eng Fract Mech*, **76** (17), 2009, p. 2563–2601.
- [3] Németh, A., Fischer, S.: Investigation of the glued insulated rail joints applied to CWR tracks. *Facta Universitatis, Series: Mechanical Engineering*, **19** (4), 2021, p. 681–704.
- [4] Profillidis, P.V.A.: *Railway Management and Engineering*. Ashgate Publishing Limited, 2014.
- [5] Kuang, K.S.C. et al.: Acoustic emission source location and noise cancellation for crack detection in rail head. *Smart Struct Syst*, **18** (5), 2016, p. 1063–1085.
- [6] Xu, L. et al.: On effects of rail fastener failure on vehicle/track interactions. *Structural Engineering and Mechanics*, **63** (5), 2017, p. 659–667.
- [7] Németh, D. et al.: *Investigation of the Track Gauge in Straight Sections, Considering Hungarian Railway Lines*. 2022.
- [8] Kerr, A.D.: *Fundamentals of Railway Track Engineering*. Simmons-Boardman Books, Incorporated, 2003.
- [9] Zakeri, J.A. et al.: Field Investigations on the Effects of Track Lateral Supports on the Ballasted Railway Lateral Resistance. *Periodica Polytechnica Civil Engineering*, **64** (3 SE-Research Article), 2020, p. 640–646.
- [10] Mosayebi, S.-A. et al.: Investigations on Vehicle Interaction with CWR Tracks Considering Some Aspects of Rail Support Modulus. *Periodica Polytechnica Civil Engineering*, **62** (2 SE-Research Article), 2018, p. 444–450.
- [11] Zakeri, J.A. et al.: New Definition of Neutral Temperature in Continuous Welded Railway Track Curves. *Periodica Polytechnica Civil Engineering*, **62** (1 SE-Research Article), 2018, p. 143–147.
- [12] Mundrey, J.S.: *Railway Track Engineering*. McGraw-Hill Education (India) Pvt Limited, 2009.
- [13] Chandra, S., Agarwal, M.M.: *Railway Engineering*. Oxford University Press India, 2013.
- [14] Josefson, B.L. et al.: Residual stresses in thermite welded rails: significance of additional forging. *Welding in the World*, **64** (7), 2020, p. 1195–1212.
- [15] Steenbergen, M.J.M.M., van Bezooijen, R.W.: *12 - Rail welds*. (Editors: R. Lewis and U. B. T.-W. I. H. Olofsson). Woodhead Publishing, 2009, p. 377–408.

- [16] Fischer, S. et al.: Investigation of Heat-Affected Zones of Thermite Rail Weldings. *Facta Universitatis Series Mechanical Engineering*, 2020.
- [17] Liu, Z. et al.: Dynamic finite element modeling and fatigue damage analysis of thermite welds. *Fatigue Fract Eng Mater Struct*, **43**, 2019, p. 119–136.
- [18] Lu, C. et al.: Fatigue prediction of rail welded joints. *Int J Fatigue*, **113**, 2018, p. 78–87.
- [19] Barna, V. et al.: Investigation of the Effects of Thermit Welding on the Mechanical Properties of the Rails. *Acta Polytechnica Hungarica*, **19**, 2022, p. 37–49.
- [20] Bajic, D. et al.: Welding of rails with new technology of arc welding. *Metalurgija -Sisak then Zagreb-*, **52**, 2013, p. 399–402.
- [21] Gong, L. et al.: Effect on Hardness and Microstructures of Rail Joint with Ultra-Narrow Gap Arc Welding by Post Weld Heat Treatment. *Key Eng Mater*, **737**, 2017, p. 90–94.
- [22] Ando, S., Okubo, M.: Narrow gap automatic gas shielded arc welding of high carbon steel. *Welding International*, **11** (8), 1997, p. 621–627.
- [23] Josefson, B.L., Ringsberg, J.: Assessment of uncertainties in life prediction of fatigue crack initiation and propagation in welded rails. *Int J Fatigue*, **31**, 2009, p. 1413–1421.
- [24] Yan, M. et al.: Effect of welding defects on mechanical properties of welded joints subjected to temperature. *Steel and Composite Structures*, **40** (2), 2021, p. 193–202.
- [25] Gong, L. et al.: Effect of Alloying Composition on Microstructure and Mechanical Properties of Ultranarrow Gap Welded Joints of U71Mn Rail Steel. *Advances in Materials Science and Engineering*, **2021**, 2021, p. 11 pages.
- [26] Domingo, L.M. et al.: Experimental modal analysis of transverse-cracked rails- influence of the cracks on the real track behavior. *Structural Engineering and Mechanics*, **52** (5), 2014, p. 1019–1032.
- [27] Mosayebi, S.A. et al.: Vehicle/track dynamic interaction considering developed railway substructure models. *Structural Engineering and Mechanics*, **61**, 2017, p. 775–784.
- [28] Fischer, S.: Investigation of the Horizontal Track Geometry regarding Geogrid Reinforcement under Ballast. *Acta Polytechnica Hungarica*, **19**, 2022, p. 89–101.
- [29] Li, X. et al.: Simulation of wheel-rail impact load and sleeper-ballast contact pressure in railway crossings using a Green's function approach. *Journal of Sound Vibration*, **463**, 2019, p. 114949.

- [30] Remennikov, A.M., Kaewunruen, S.: A review of loading conditions for railway track structures due to train and track vertical interaction. *Struct Control Health Monit*, **15** (2), 2008, p. 207–234.
- [31] Ranjha, S. et al.: Finite element prediction of the stress state of a rail underhead radius under high axle load conditions. **19**, 2016, p. 11–16.
- [32] Sábitz, L., Kolonits, F.: Finite element and analytical computation of flash temperature. *Periodica Polytechnica Civil Engineering*, **58** (3 SE-Research Article), 2014, p. 267–278.
- [33] Ma, N. et al.: Investigation of welding residual stress in flash-butt joint of U71Mn rail steel by numerical simulation and experiment. *Mater Des*, **88**, 2015, p. 1296–1309.
- [34] Yang, Y. et al.: Research on static and dynamic behaviors of PC track beam for straddle monorail transit system. *Steel and Composite Structures*, **31** (5), 2019, p. 437–452.
- [35] Skrypyk, R. et al.: Long-term rail profile damage in a railway crossing: Field measurements and numerical simulations. *Wear*, **472–473**, 2021, p. 203331.
- [36] Cai, W. et al.: Dynamic stress analysis of rail joint with height difference defect using finite element method. *Eng Fail Anal*, **14** (8), 2007, p. 1488–1499.
- [37] Bonnett, C.F.: *Practical Railway Engineering*. Imperial College Press, 2005.
- [38] Dersch, M. et al.: Investigation into the effect of lateral and longitudinal loads on railroad spike stress magnitude and location using finite element analysis. *Eng Fail Anal*, **104**, 2019.
- [39] Zhang, K. et al.: Effect of lateral differential settlement of high-speed railway subgrade on dynamic response of vehicle-track coupling systems. *Structural Engineering and Mechanics*, **80** (5), 2021, p. 491–501.
- [40] Shi, X. et al.: An integrated fatigue assessment approach of rail welds using dynamic 3D FE simulation and strain monitoring technique. *Eng Fail Anal*, **120**, 2021, p. 105080.
- [41] Steenbergen, M.J.M.M., Esveld, C.: Relation between the geometry of rail welds and the dynamic wheel - rail response: Numerical simulations for measured welds. *Proc Inst Mech Eng F J Rail Rapid Transit*, **220** (4), 2006, p. 409–423.
- [42] Li, S. et al.: Dynamic deflection monitoring of high-speed railway bridges with the optimal inclinometer sensor placement. *Smart Struct Syst*, **26** (5), 2020, p. 591–603.

- [43] Wang, H. et al.: Identification of moving train loads on railway bridge based on strain monitoring. *Smart Struct Syst*, **23** (3), 2019, p. 263–278.
- [44] Cai, Z., Raymond, G.P.: Modelling the dynamic response of railway track to wheel/rail impact loading. *Structural Engineering and Mechanics*, **2** (1), 1994, p. 95–112.
- [45] Salehi, I. et al.: Multi-axial fatigue analysis of aluminothermic rail welds under high axle load conditions. *Int J Fatigue*, **33**, 2011, p. 1324–1336.
- [46] Kou, L.: A Review of Research on Detection and Evaluation of the Rail Surface Defects. *Acta Polytechnica Hungarica*, **19**, 2022.
- [47] Edwards, J.R. et al.: Quantification of rail transit wheel loads and development of improved dynamic and impact loading factors for design. *Proc Inst Mech Eng F J Rail Rapid Transit*, **232** (10), 2018, p. 2406–2417.
- [48] Sadeghi, J.: *Fundamentals of analysis and design of railway ballasted track*. Tehran, Iran.: IUST publication Service, 2008.
- [49] American Railway Engineering and Maintenance of Way Association: Manual for Railway Engineering. *Volume 1, Chapter 1, "Roadway and Ballast"*, 2010.
- [50] Hu, Q. et al.: Bayesian ballast damage detection utilizing a modified evolutionary algorithm. *Smart Struct Syst*, **21** (4), 2018, p. 435–448.
- [51] Management and Planning Organization Office of Deputy for Technical Affairs of Iran: Supervision of Railway Track Construction, Leaflet No. 355. 2006.
- [52] Doyle, N.F., Australia. Bureau of Transport Economics.: *Railway track design : a review of current practice*. Australian Government Pub. Service, 1980.
- [53] Management and planning organization of Iran: Technical and general specification of Ballasted Railway, Leaflet No 301. 2005.
- [54] Mosayebi, S.A. et al.: Some aspects of support stiffness effects on dynamic ballasted railway tracks. *Periodica Polytechnica Civil Engineering*, **60** (3), 2016, p. 427–436.
- [55] Gedney, B.L., Rizos, D.C.: Combining welding-induced residual stress with thermal and mechanical stress in continuous welded rail. *Results in Engineering*, **16**, 2022, p. 100777.

# Weight Optimization of Tower Structures with Continuous Variables using Jaya Algorithm

**Maksym Grzywiński**

Czestochowa University of Technology, Faculty of Civil Engineering  
69 Dabrowskiego Str., 42200 Czestochowa, Poland  
maksym.grzywinski@pcz.pl

---

*Abstract: A popular metaheuristic algorithm named Jaya is preferred to solve the problem of finding the minimum weight of tower structures. Joints coordinates of free nodes and the area of bar elements are constrained using the lower and upper bounds of these design variables for shape and size optimization, respectively. The constraints used in this study are the Euler buckling, allowable stress, and displacement. The presented algorithm is tested with two classic benchmark problems: the spatial truss tower with 39-bar and the transmission tower with 272-bar. The Jaya algorithm is coded in MATLAB environment and implemented into the linear finite element solver.*

*Keywords: weight optimization; tower structures; shape and size optimization; continuous optimization; Jaya algorithm*

---

## 1 Introduction

The feasible optimal design of structures is an interesting topic to engineers in practice. The minimal cost and the optimal geometry of the construction are the basic purposes of the engineers when designing the structure by taking into account the constrained objective function. We are interested in designing structures with high reliability. Many optimal algorithms for this aim were tested, including innovative algorithms and classical methods.

Until now, many meta-heuristic methods have been presented for the structural optimization problems. Some of the most popular optimization algorithms are GA: Genetic Algorithm, SA: Simulated Annealing, PSO: Particle Swarm Optimization, HS: Harmony Search and ACO: Ant Colony Optimization.

In the recent years, JA: Jaya Algorithm was presented as a new metaheuristic technique and it has a very simple form and does not use more specific parameters. Many studies were made by using this algorithm. The optimization of cables size in cable-stayed bridge with Jaya algorithm was used by Atmaca et al. [1], optimum

design of steel grillage was presented by Dede [3], braced dome structures with natural frequency constraints was studied by Grzywiński et al. [4]. Grzywiński et al. [5] studied four benchmark problems (trusses 2D ten-bar, 3D thirty-seven-bar, 3D seventy-two-bar and 2D two-hundred-bar by TLBO (Teaching-learning based optimization) algorithm. The optimization of spatial truss tower (25-bar, 39-bar, 72-bar, and 160-bar) based on Rao algorithm was analyzed by Grzywiński [6].

## 2 Jaya Optimization Algorithm

As a popular optimization method the Jaya was firstly presented by Rao [11, 12, 14]. The meaning of this new algorithm is the “victory” in the Sanskrit language. The basic rules of this method are to close the best solution and stay away from the worst solution in a population consist of the potential solutions for an optimization problem. The main properties of this algorithms is that it does not has a special parameter to carry out the optimization process. Like the other population-based algorithms, Jaya need a population size (Pn) and the use a generation number (Gn). The general equation for Jaya is given in Eq. (1).

$$P_{k,l,i}^{new} = P_{k,l,i} + r_{1,k,i}(P_{k,b,i} - |P_{k,l,i}|) - r_{2,k,i}(P_{k,w,i} - |P_{k,l,i}|) \quad (1)$$

Let  $P_{k,l,i}$  it shows the  $k^{\text{th}}$  design variable for the  $l^{\text{th}}$  design of the population at the beginning of the  $i^{\text{th}}$  iteration. Where  $P_{k,l,i}^{new}$  is the updated design variable, and  $r_{1,k,it}$ ,  $r_{2,k,it}$  are random numbers which can be change from “0” to “1”.

The Jaya algorithm has of following steps:

- 1) first are define the size of the population (Pn) and the termination criterion,
- 2) next program generates the initial population randomly,
- 3) algorithm finds the best and worst solutions in the population,
- 4) after method looking for a new solution in accordance with the equation (1)
- 5) if the updated solution is better than the old one, the updated solution is used for the next iteration
- 6) if the termination criterion is satisfied, stop the optimization (else go to step 2).

### 3 Optimization of Tower Structures Problems

Formulation of design optimization includes the weight minimization of tower structures subjected to displacement, stress and buckling constraints. The design variables and the objective function are given as below;

$$\text{obtain} \quad A = [A_1, A_2, \dots, A_{ng}] \quad (2)$$

$$\text{to optimize} \quad W(A, x) = \sum_{k=1}^{ng} A_k \sum_{i=1}^{mk} \rho_i L_i x_i \quad (3)$$

where  $W(A, x)$  is the total structural weight;  $A_k$  is vector of the size optimization (cross-section area) and  $x_i$  are joint coordinates of the free nodes as shape optimization, respectively;  $\rho_i$  and  $L_i$  is the density and length of bar elements.  $ng$  and  $mk$  are the number of groups and the number of bar elements in each groups, respectively.

The structural constraints used in this study are;

$$\text{for tensile members,} \quad \sigma_k \leq \sigma_k^t \quad k = 1, 2, \dots, ntm \quad (4)$$

$$\text{for compressive members,} \quad \sigma_k \leq \sigma_k^c \quad k = 1, 2, \dots, ncm \quad (5)$$

where  $\sigma_k$  is the calculated stress,  $\sigma_k^t$  and  $\sigma_k^c$  is the allowable tensile and the compressive stresses, respectively. “ntm” and the “ncm” are the number of tensile member and the number of compressive member, respectively.

$$\sigma_k \leq \sigma_k^b \quad k = 1, 2, \dots, ncm \quad (6)$$

where  $\sigma_k^b$  is the Euler buckling and it is given as:

$$\sigma_k^b = \frac{K \cdot E \cdot A_k}{L_k^2} \quad k = 1, 2, \dots, ncm \quad (7)$$

where  $E$  is the elasticity property of the material, and  $K$  is a constant. The constraint for the displacement is given below.

$$|d_i| \leq d_{max} \quad i = 1, 2, \dots, nn \quad (8)$$

where  $d_i$  is the nodal displacement,  $d_{max}$  is allowable displacement,  $nn$  and  $nm$  are number of nodes and number of bar elements, respectively.

$$A_{min} \leq A_k \leq A_{max} \quad k = 1, 2, \dots, nm \quad (9)$$

$$x_{min} \leq x_i \leq x_{max} \quad i = 1, 2, \dots, nn \quad (10)$$

To obtain best solution without the violations a penalty function is transformed another form to include the effect of the constraints. Using this function, it will be hoped that the optimization problem will find a feasible global solution. Thus, the penalized objective function (Fp) is obtained as given in Eq. 11.

$$Fp = W(A, x)[1 + Cp] \quad (11)$$

The penalized objective function including the nodal violates and member stress violates given as:

$$Cp = \sum_{i=1}^{nn} c_i + \sum_{k=1}^{ng} c_k \quad (12)$$

$$c_i = \frac{|d_i|}{d_{max}} \quad (13)$$

$$c_k = \frac{|\sigma_k|}{\sigma_{max}} \quad (14)$$

## 4 Testing of the Jaya Algorithm

The 272-bar transmission truss tower with 28 continuous design variables and 39-bar spatial truss tower with 11 continuous design variables were tested to show the performance of the Jaya algorithm. These structural example were taken from literature. The present the efficiency and the performance of the proposed algorithm the best feasible global solution obtained from this study were compared with the previous studies in the tables includes final design variables. In this study twenty independent runs were carried out to show the robustness of the Jaya algorithms. The Jaya algorithm, optimization tools and a standard linear elastic finite element solver were coded in the MATLAB programming by the author of this paper.

### 4.1 The First Numerical Example: 39-bar Truss

The first structural example is 39-bar spatial tower given in Figure 1a with the sizing and shape optimization. This tower structure was before designed by Shojaee et al. [13], Dede & Ayvaz [2], and Ho-Huu et al. [7]. Input data for this example was given in Table 1 and the elements connectivity and nodal coordinates were presented in Table 2. Among the total free nodes of the structure, the top and bottom nodes have fixed position, and the other middle nodes' coordinates are taken as design variables. At the end of the optimization process, final feasible shape obtained using proposed algorithm is given in Figure 1b. To compare the results with those given in previous studies, the optimal design variables were listed in Table 3.

The population size and number of iterations is set to 40 and 200, respectively. The Jaya algorithm found the best design after 7640 analyses and actually obtained an optimum design with the 133.51 kg. In Figure 2 is presented the converge history for the best result, and Figure 3 is shown results of 20 independent runs.

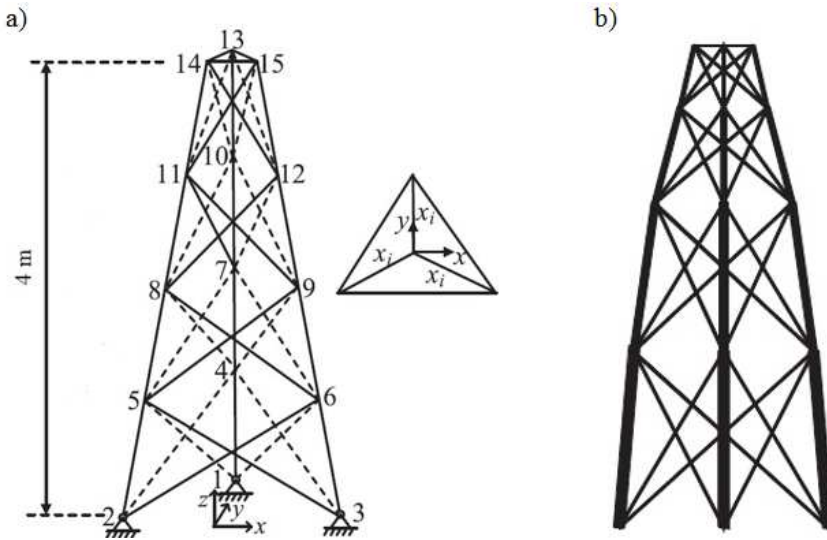


Figure 1

The first example: 39-truss spatial truss tower: a) before optimization, b) after optimization

Table 1

Material data and the constraints for the 39-bar spatial truss tower

Properties / constraints	Unit	Value / notes
Modulus of elasticity	E (GPa)	210
Material density	$\rho$ (kg/m <sup>3</sup> )	7800
Stress constraints	$\sigma$ (MPa)	240 for tension -240 for compression
Displacement constraints	$\delta$ (cm)	0.4 for Y directions (nodes 13-15)
Nodal forces	F (kN)	$\pm 10$ for Y directions (nodes 13-15)
Euler buckling	$\sigma_e$ (MPa)	$\sigma_e \leq \frac{K_e E A_e}{L_e^2}$

Table 2

Initial data for the 39-bar spatial truss tower

Shape variables				Size variables	
joint	x (m)	y (m)	z (m)	cross-area	node-node
1	0.000	1.000	0.000	A1	(1-4), (2-5), (3-6)
2	-0.866	-0.500	0.000	A2	(4-7), (5-8), (6-9)
3	0.866	-0.500	0.000	A3	(7-10), (8-11), (9-12)
13	0.000	0.280	4.000	A4	(10-13), (11-14), (12-15)
14	-0.242	-0.140	4.000	A5	the remaining elements
15	0.242	-0.140	4.000		

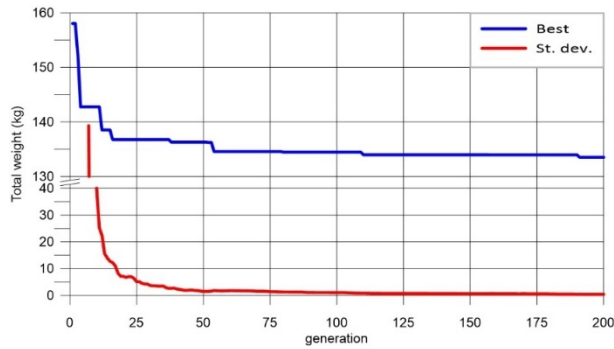


Figure 2

Convergence history of 39-bar spatial truss tower

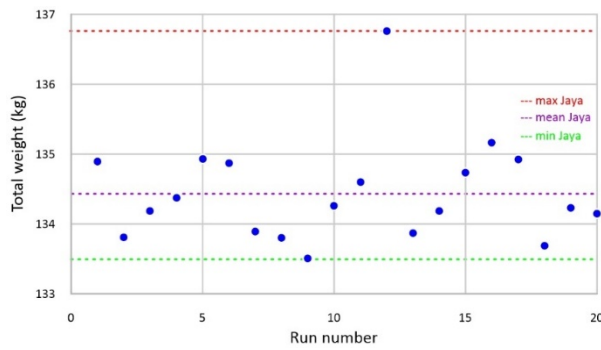


Figure 3

Results of the twenty runs for the 39-bar spatial truss tower

Table 3  
Optimal results for the 39-bar spatial truss tower

Design variables	Group members	DPSO-MMA [13]	TLBO [2]	D-ICDE [7]	JA This study
1	A1 (cm <sup>2</sup> )	10.01	11.9650	13.0	11.9900
2	A2 (cm <sup>2</sup> )	9.91	11.1457	12.9	9.7811
3	A3 (cm <sup>2</sup> )	8.56	7.8762	9.0	6.9870
4	A4 (cm <sup>2</sup> )	3.92	2.7013	2.7	2.0264
5	A5 (cm <sup>2</sup> )	3.44	2.4058	1.6	1.7309
6	Y4 (m)	0.6683	0.8996	0.9232	0.8694
7	Z4 (m)	1.9000	1.3507	0.5380	1.1972
8	Y7 (m)	0.4732	0.6917	0.7958	0.6774
9	Z7 (m)	2.8734	2.3122	2.1637	2.4966
10	Y10 (m)	0.3002	0.4825	0.5105	0.4697
11	Z10 (m)	3.4415	3.3031	3.4134	3.3985

	W (kg)	176.834	154.13	140.35	133.51
	MFE	N/A	7560	1140	7640

W: weight; MFE: maximum function evaluations.

### 4.2 The Second Numerical Example: 272-bar Truss

The second structural example is size optimization of the 272-bar transmission tower shown in Figure 4. This tower structure was previously designed by Kaveh & Massoudi [8], Kaveh & Zaeerza [9], and Kaveh et al. [10].

The Young’s modulus is 200 GPa and the allowable stresses for all members is  $\pm 275$  MPa. The more information about model: nodal coordinates, topology and member grouping find in Kaveh & Massoudi [8]. The transmission tower is grouped into 28 continuous design variables. The limit for the design variables of cross-sectional areas are  $10 \text{ cm}^2$  and  $160 \text{ cm}^2$  for the lower bounds and upper bounds, respectively. The tower has many different loading cases. The details for these cases are given in Table 4. The structural constraints in the case of displacements are limited 20 mm in z-direction and 100 mm both x- and y-direction for the joints 1, 2, 11, 20, 29.

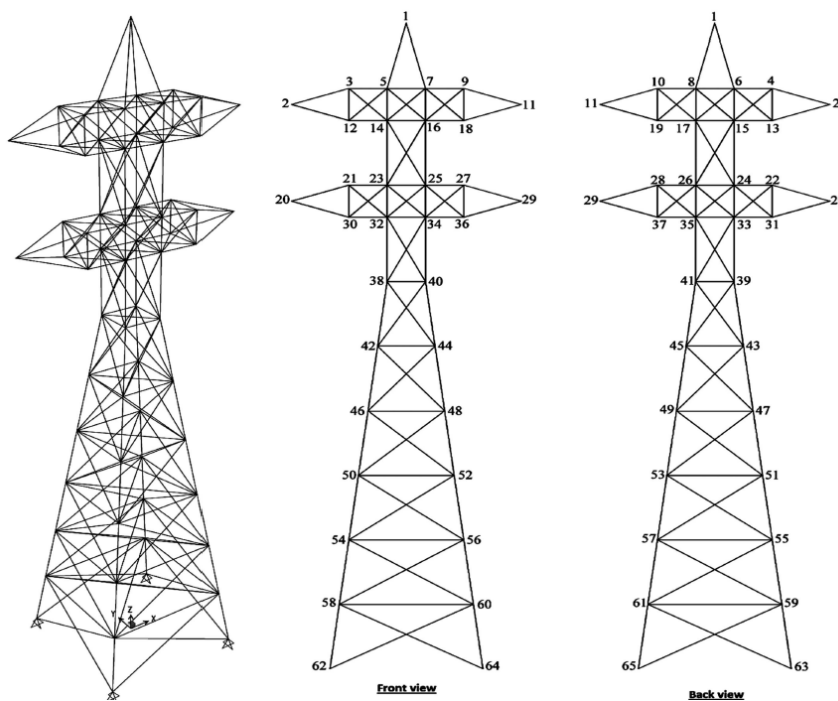


Figure 4  
The second example: the 272-bar transmission tower

Table 4  
Load cases for the 272-bar transmission tower

Load case	Force direction	Nodes					
		1	2	11	20	29	other free
1	F <sub>x</sub> (kN)	20	20	20	20	20	5
	F <sub>y</sub> (kN)	20	20	20	20	20	5
	F <sub>z</sub> (kN)	-40	-40	-40	-40	-40	0
2	F <sub>x</sub> (kN)	0	20	20	20	20	5
	F <sub>y</sub> (kN)	0	3)	20	20	20	5
	F <sub>z</sub> (kN)	0	-40	-40	-40	-40	0
3	F <sub>x</sub> (kN)	20	0	20	20	20	5
	F <sub>y</sub> (kN)	20	0	20	20	20	5
	F <sub>z</sub> (kN)	-40	0	-40	-40	-40	0
4	F <sub>x</sub> (kN)	20	20	20	0	20	5
	F <sub>y</sub> (kN)	20	20	20	0	20	5
	F <sub>z</sub> (kN)	-40	-40	-40	0	-40	0
5	F <sub>x</sub> (kN)	20	0	0	0	0	5
	F <sub>y</sub> (kN)	20	0	0	0	0	5
	F <sub>z</sub> (kN)	-40	0	0	0	0	0
6	F <sub>x</sub> (kN)	0	20	0	0	0	5
	F <sub>y</sub> (kN)	0	30	0	0	0	5
	F <sub>z</sub> (kN)	0	-40	0	0	0	0
7	F <sub>x</sub> (kN)	0	0	0	20	0	5
	F <sub>y</sub> (kN)	0	0	0	20	0	5
	F <sub>z</sub> (kN)	0	0	0	-40	0	0
8	F <sub>x</sub> (kN)	0	0	20	20	20	5
	F <sub>y</sub> (kN)	0	0	20	20	20	5
	F <sub>z</sub> (kN)	0	0	-40	-40	-40	0
9	F <sub>x</sub> (kN)	0	20	20	0	20	5
	F <sub>y</sub> (kN)	0	20	20	0	20	5
	F <sub>z</sub> (kN)	0	-40	-40	0	-40	0
10	F <sub>x</sub> (kN)	0	0	20	0	20	5
	F <sub>y</sub> (kN)	0	0	20	0	20	5
	F <sub>z</sub> (kN)	0	0	-40	0	-40	0
11	F <sub>x</sub> (kN)	0	0	0	20	20	5
	F <sub>y</sub> (kN)	0	0	0	20	20	5
	F <sub>z</sub> (kN)	0	0	0	-40	-40	0
12	F <sub>x</sub> (kN)	0	0	20	20	0	5
	F <sub>y</sub> (kN)	0	0	20	20	0	5
	F <sub>z</sub> (kN)	0	0	-40	-40	0	0

The optimum volume of the 272-bar transmission tower found by Jaya algorithm is shown in Table 5. The optimization result is the same as in the PGO algorithm. Jaya algorithm find optimal volume after 23100 analyses. In Figure 5 is presented the converge history for the best result  $1.1681 \text{ m}^3$ , and Figure 6 is shown results of 20 independent runs.

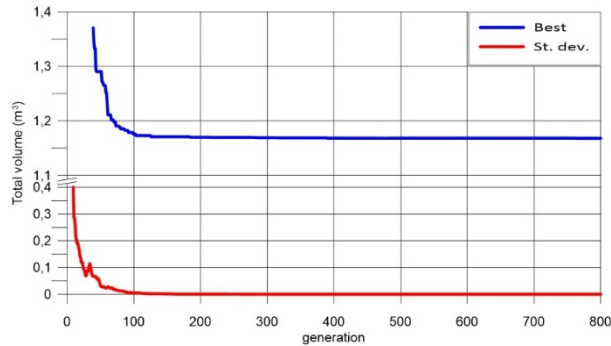


Figure 5

Convergence history for the 272-bar transmission tower

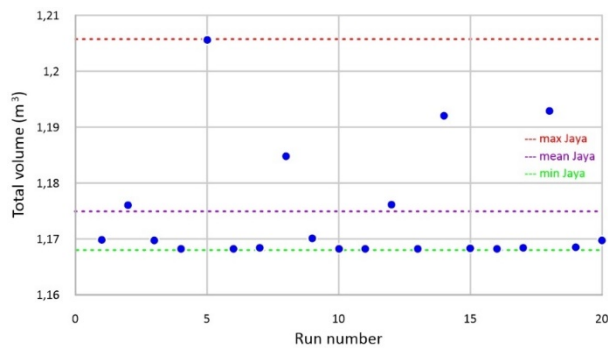


Figure 6

Results of the independent runs for the 272-bar transmission tower

## Conclusions

In this article, a proposed popular optimization method named Jaya is preferred for the optimization of structural example which are the 39-bar, and 272-bar truss spatial towers. The validity of the JA is demonstrated by using these tower structures. By taking into account three different structural constraints which are the displacement, allowable stress, and Euler's buckling. The original Jaya algorithm is tested for the constrained single objective problem.

The Jaya algorithm doesn't use any special parameters to carry out the optimization process. By the help of this properties, the Jaya algorithms is a popular optimization

algorithm. When compared the feasible optimal solutions obtained from this study using Jaya algorithm with those given in previous studies, it can be clearly stated that the Jaya algorithm can be effectively used in the design of spatial tower structures.

Table 5  
Best results for the 272-bar transmission tower

Group members	SSOA [9]	PGO [10]	JA This study	Group members	SSOA [9]	PGO [10]	JA This study
A1 (cm <sup>2</sup> )	10.00	10.00	10.00	A15 (cm <sup>2</sup> )	93.20	91.19	91.77
A2 (cm <sup>2</sup> )	12.40	12.17	12.34	A16 (cm <sup>2</sup> )	10.00	10.00	10.00
A3 (cm <sup>2</sup> )	24.92	24.45	24.83	A17 (cm <sup>2</sup> )	10.00	10.00	10.00
A4 (cm <sup>2</sup> )	10.17	10.00	10.01	A18 (cm <sup>2</sup> )	10.02	10.00	10.00
A5 (cm <sup>2</sup> )	96.18	95.80	95.51	A19 (cm <sup>2</sup> )	83.90	91.19	91.77
A6 (cm <sup>2</sup> )	10.00	10.00	10.00	A20 (cm <sup>2</sup> )	10.01	10.00	10.00
A7 (cm <sup>2</sup> )	120.64	122.59	123.63	A21 (cm <sup>2</sup> )	10.00	10.00	10.00
A8 (cm <sup>2</sup> )	10.01	10.01	10.00	A22 (cm <sup>2</sup> )	10.03	10.00	10.00
A9 (cm <sup>2</sup> )	10.00	10.00	10.06	A23 (cm <sup>2</sup> )	79.82	85.41	80.29
A10 (cm <sup>2</sup> )	10.00	10.00	10.00	A24 (cm <sup>2</sup> )	10.00	10.00	10.00
A11 (cm <sup>2</sup> )	102.17	106.15	102.09	A25 (cm <sup>2</sup> )	10.00	10.00	10.00
A12 (cm <sup>2</sup> )	10.00	10.00	10.00	A26 (cm <sup>2</sup> )	10.00	10.00	10.00
A13 (cm <sup>2</sup> )	10.00	10.00	10.00	A27 (cm <sup>2</sup> )	75.04	76.57	74.57
A14 (cm <sup>2</sup> )	10.00	10.00	10.00	A28 (cm <sup>2</sup> )	10.00	10.00	10.00
				V(m <sup>3</sup> )	1.1682	1.1681	1.1681
				MFE	14020	23920	23100

### Conflicts of Interest

The author declares no conflict of interest.

### References

- [1] B. Atmaca, T. Dede, and M. Grzywiński. Optimization of cables size and prestressing force for a single pylon cable stayed bridge with Jaya algorithm”, *Steel and Composite Structures*, 34(6), 2020, pp. 853-862
- [2] T. Dede, and Y. Ayvaz. Combined size and shape optimization of structures with a new meta-heuristic algorithm, *Applied Soft Computing*, 28, 2015, pp. 250–258
- [3] T. Dede. Jaya algorithm to solve single objective size optimization problem for steel grillage structures, *Steel and Composite Structures*, 26(2), 2018, pp. 163–170
- [4] M. Grzywiński, T. Dede, and Y.I. Ozdemir. Optimization of the braced dome structures by using Jaya algorithm with frequency constraints. *Steel and Composite Structures*, 30(1), 2019, pp. 47-55

- 
- [5] M. Grzywiński, J. Selejdak, and T. Dede. Shape and size optimization of trusses with dynamic constraints using a metaheuristic algorithm, *Steel and Composite Structures*, 33(5), 2019, pp. 747-753
- [6] M. Grzywiński. Optimization of spatial truss towers based on Rao algorithms. *Structural Engineering and Mechanics*, 81(3), 2022, pp. 367-378
- [7] V. Ho-Huu, T. Nguyen-Thoi, M.H. Nguyen-Thoi, and L. Le-Anh. An improved constrained differential evolution using discrete variables (D-ICDE) for layout optimization of truss structures. *Expert Systems with Applications*, 42(20), 2015, pp. 7057-7069
- [8] A. Kaveh, and M.S. Massoudi. Multi-objective optimization of structures using charged system search. *Scientia Iranica, Transactions A: Civil Engineering*, 21(6), 2014, pp. 1845-1860
- [9] A. Kaveh, and A. Zaerreza. Shuffled shepherd optimization method: a new meta-heuristic algorithm. *Engineering Computations.*, 37(7), 2020, pp. 2357-2389
- [10] A. Kaveh, H. Akbari, and S.M. Hosseini. Plasma generation optimization: a new physically-based metaheuristic algorithm for solving constrained optimization problems. *Engineering Computations.*, 38(4), 2021, pp. 1554-1606
- [11] R.V. Rao. Jaya: A simple and new optimization algorithm for solving constrained and unconstrained optimization problems, *International Journal of Industrial Engineering Computations*, 7(1), 2016, pp. 19–34
- [12] R.V. Rao. *Jaya: An advanced optimization algorithm and its engineering applications*. Springer International Publishing, Switzerland, 2019
- [13] S. Shojae, M. Arjomand, and M. Khatibinia. A hybrid algorithm for sizing and layout optimization of truss structures combining discrete PSO and convex approximation”, *Int. J. Optim. Civil Eng*, 3(1), 2013, pp. 57-83
- [14] <https://sites.google.com/site/jayaalgorithm>

# Numerical Study of the Effect of the Shape and Area of Shallow Foundations on the Bearing Capacity of Sandy Soils

**Ammar Alnmr, Rashad Alsirawan**

Széchenyi István University. Egyetem tér 1, H-9026 Győr, Hungary  
alnmr.ammar@hallgato.sze.hu, alsirawan.rashad@sze.hu

---

*Abstract: The settlement and bearing capacity of shallow foundation models with different shapes and areas on cohesionless subsoil under the applied vertical load are presented in this study. Different shapes of foundations with rectangular, square, strip, plus horizontal cross-sectional shapes are numerically studied after the validation on the laboratory model has been conducted and the constitutive soil model that simulates the behaviour of sandy soil has been chosen. The result of the validation showed that the HS model is the most suitable for the simulation of stress-deformation behaviour of sand. The effect of the shape and area are clearly visible and greatly affects the bearing capacity of the soil. The study generally compared Vesic's, Hansen's and German's bearing capacity equations and showed that Vesic's and Hansen's bearing capacity equations are best suited to the bearing capacity computed from numerical analysis by Plaxis3D. Finally, as a development of Hansen's bearing capacity equation, a new equation of plus shape foundation bearing capacity has been determined.*

*Keywords: bearing capacity; sand (cohesionless soil); shallow foundations; foundation shape*

---

## 1 Introduction

The settlement and bearing capacity of the soil are influenced by the size, shape, and depth of the foundations as well as the loads, the physical and mechanical properties and reinforcement of the soils ([1]; [2]; [3]). Generally, foundations are classified into shallow and deep foundations. Shallow foundations are those that transfer structural loads to the soil layers at a relatively shallow depth. According to Terzaghi [4], a shallow foundation is one that is laid at a depth  $D_f$  that does not exceed the foundation's width  $B$ , or  $D_f/B \leq 1$ . Studies conducted later on have indicated that  $D_f/B$  for shallow foundations can be as high as 3 to 4 ([1]; [2]).

Shallow foundations are a very commonly used type of foundation system. Several bearing capacity equations proposed by different authors and adopted in

different codes are available to calculate the ultimate bearing capacity of soil at foundation levels. However, different methods of evaluating bearing capacity yield different results. Subsequently, one should estimate the bearing capacity and settlement of this type of foundation on a sound basis and as close to reality as possible, which will enhance the selection, design and construction of the foundation of the structure.

Shallow foundations can be built in a variety of shapes, but the most popular and extensively utilized are circular, square, and strip foundations. However, the only thing that differentiates them from one another is their horizontal cross-sections. Extensive research has been carried out on the effect of foundation shapes on settlement and soil bearing capacity ([5]; [6]; [7]; [8]; [9]; [10]; [11]; [12]; [13]; [14]; [15]; [16]). However, they do not account for the size of the foundation, and only a few studies, such as ([17]; [18]; [19]) that focus on plus-shaped foundations, came to the conclusion that multi-edge foundations might perform better than square-shape foundations. Nonetheless, the majority of these studies on multi-edge foundations were conducted on small experimental models. Therefore, to solve these issues, and for a more realistic study of the bearing capacity of shallow foundations [20], numerical modelling using PLAXIS 3D is used to model several areas (Full scale) and shapes of foundations.

Studying the effect of the foundation shape on the bearing capacity of the foundation soil and its settlement by laboratory or field methods requires conducting a very large number of laboratory experiments. Given the difficulty of conducting these experiments, their high cost and the multiple sources of inaccuracy in the results, including achieving the same initial state in all experiments, as well as, the great effort and time required, the finite element method was used to calculate the numerical bearing capacity and the variables were studied more extensively.

The aim of this research is to study the soil bearing capacity and determine the best empirical equation of bearing capacity where the comparisons between the numerical bearing capacity, the Hansen, Vesic and German empirical equation of bearing capacity are carried out.

## **2 Research Materials and Methodology**

The analytical method was used to achieve the objectives of this research, according to the following stages:

## 2.1 Laboratory Experiments

Sufficient laboratory experiments were conducted according to ASTM to determine the specifications of the sand used in the study. All laboratory experiments were carried out in the laboratory of soil mechanics and foundations at the Faculty of Civil Engineering - Tishreen University.

The granular gradient curve is shown in Fig. 1. It was found that the coefficient of uniformity ( $C_u$ ) was 3.4 and the coefficient of curvature ( $C_z$ ) was 0.95, so it was classified as SP (Poorly Graded Sand) according to the Unified Soil Classification System (USCS). Table 1 shows the results of laboratory experiments of sand at relative density 60%.

Table 1  
The results of laboratory experiments of sand at relative density 60%

Parameter	Value	Parameter	Value
$e_{max}$	0.656	G (-)	2.65
$e_{min}$	0.402	$E_{oed}$ (kN/m <sup>2</sup> )	40000
$\gamma_{unsat}$ (kN/m <sup>3</sup> )	17.6 kN/m <sup>3</sup>	$\phi$ (°)	34
$\gamma_{sat}$ (kN/m <sup>3</sup> )	21	c (kN/m <sup>2</sup> )	1.1

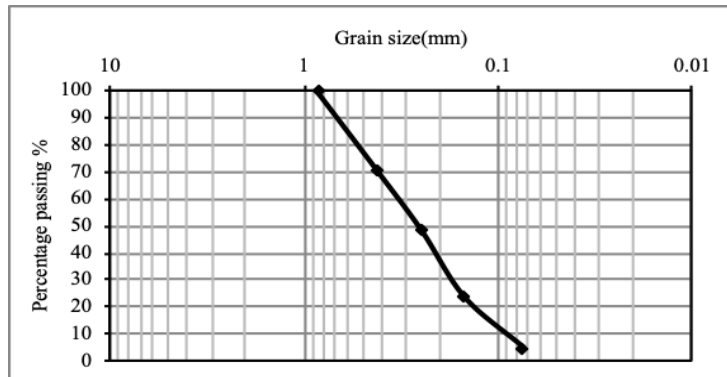


Figure 1  
The granular gradient curve of sand

## 2.2 Determination of the Constitutive Model

The validation of the numerical model in the finite element method is considered vital through the comparison of a numerical model results and measurements. The validation procedures should take into consideration the appropriate constitutive model, geometric simplifications, and other sources of inconsistencies to obtain a satisfactory representative numerical model [21].

### 2.2.1 Laboratory Model

To select the constitutive model, a laboratory model was built (Fig. 2) consisting of a metal cylindrical mould with dimensions of 280 mm (diameter) x 230 mm (height) filled with sand at a relative density of 60%, and from a circular metal foundation with dimensions: 50 mm (D) x 17 mm (thick), placed on the aforementioned sandy soil. The foundation was carried with a vertical load and the corresponding settlement was recorded. The dimensions of the mould were sufficient, where the diameter of the mould is 5.6 times the diameter of the circular foundation, and the height of the mould is 4.6 times the diameter of the foundation, which are sufficient dimensions so that the deformations do not reach the side borders of the mould and therefore have no effect on the results.



Figure 2  
laboratory model

### 2.2.2 Modelling the Laboratory Model using Plaxis 3D

The same dimensions of the laboratory model were used to determine the geometric dimensions of the numerical model, (FE-Model), where a three-dimensional model (3D-Model) was used, similar to the laboratory model, as the sides of the model allowed only vertical settlement, and the bottom of the model was fixed. The foundation had a circular shape (D=50 mm) and the foundation has been considered a rigid equivalent to a uniformly distributed settlement imposed on the soil surface. For reasons of symmetry, only a quarter of the model was modelled. Fig. 3 shows the numerical model used in calibration for the laboratory model.

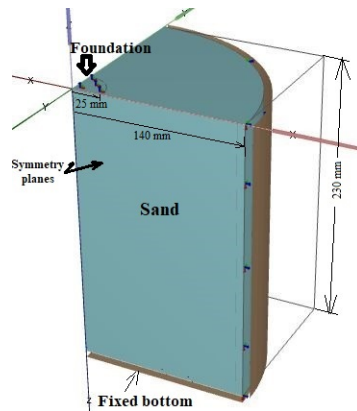


Figure 3

Numerical model used to validate the laboratory model

Two constitutive models were used in simulating the laboratory model, the Hardening soil model (HS) being one of the advanced models and the Mohr-Coulomb model (MC) being one of the most common and widely used models. Table.2 and Table.3 show the parameters of each model that are derived from laboratory experiments on the sand used in this study.

Table 2

Soil parameters used (MC- Model)

Parameter	Value	Parameter	Value
$\gamma_{unsat}$ (kN/m <sup>3</sup> )	17.6	$\varphi$ (°)	34
$\gamma_{sat}$ (kN/m <sup>3</sup> )	21	c (kN/m <sup>2</sup> )	1.1
$E_{ref}$ (kN/m <sup>2</sup> )	29500	$\Psi$ (°)	3

Table 3

Soil parameters used (MC- Model)

Parameter	Value	Parameter	Value
$\gamma_{unsat}$ (kN/m <sup>3</sup> )	17.6	C (kN/m <sup>2</sup> )	1.1
$\gamma_{sat}$ (kN/m <sup>3</sup> )	21	$\varphi$ (°)	34
$E_{50}^{ref}$ (kN/m <sup>2</sup> )	29500	$\psi$ (°)	3
$E_{oed}^{ref}$ (kN/m <sup>2</sup> )	40000	$\nu_{ur}$ (-)	0.2
$E_{ur}^{ref}$ (kN/m <sup>2</sup> )	120000	m (-)	0.53

Fig. 4 shows a comparison between the results of the numerical model and the results of the laboratory model, using the constitutive models mentioned earlier.

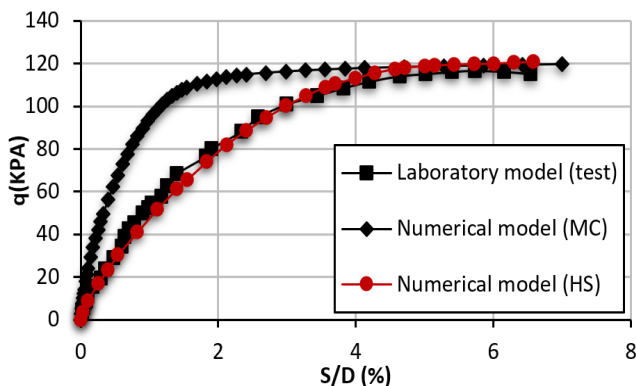


Figure 4

Comparison between the results of the numerical model and the results of the laboratory model

Where  $q$  is the applied stress on circular foundation,  $S/D$  is the nondimensional relative settlement and  $S$  is the corresponding settlement. If the settlement ( $S$ ) is expressed in a nondimensional relative settlement of  $S/D$ , the load-settlement response is not affected by the scale effect [22].

In Fig. 4 a great convergence can be seen between the results of the laboratory experiments and the modelling using (HS-Model), This is consistent with the findings of [23]. It is also noted that (HS-Model) simulates soil behavior more accurately than (MC-Model) until reaching collapse. Therefore, HS is the adopted constitutive model in this research.

### 3 Results and Discussion

After it is verified that the constitutive model of the FEM model reflects the stress-strain behaviour with acceptable accuracy, compared to the results of the laboratory model, the numerical study is conducted in light of the research objectives through a parametric study of different shapes and areas of shallow foundations to determine the optimal relationship of the bearing capacity of sandy soil.

In this study, the effect of the foundation area and shape on the soil bearing capacity is examined. The shapes chosen for the areas 9-50-144-625 m<sup>2</sup> are displayed in Tables 4-5-6-7. With the use of the HS model, which simulates the behavior of the employed sandy soil, foundations are modelled on Plaxis 3D as fully solid foundations. The equivalent dimensions  $L1$ ,  $B1$  represent the

dimensions of a rectangular foundation with the same area of the plus foundation, as shown in Fig. 5, where these dimensions were used to determine the bearing capacity using the empirical equations of Vesic, Hansen, and the German code as these relationships are not applicable for irregular or multi-edge foundations [16].

Table 4  
shapes related to area 9 m<sup>2</sup>

shape of foundation	Symbol	Area (A) [m <sup>2</sup> ]	Dimensions [m]	Equivalent width B1[m]	Equivalent length L1[m]	L1/B1
Circular	C1	9	D=3.385	3.385	3.385	1
Square	S1	9	L=3 B=3	3	3	1
Rectangle l/B=2	R1-2	9	L=4.24 B=2.12	2.12	4.24	2
Rectangle l/B=3	R1-3	9	L=5.196 B=1.732	1.732	5.196	3
Rectangle l/B=5	R1-5	9	L=6.71 B=1.342	1.342	6.71	5
Plus sign shape +	P1-0.2	9	b=2.236 a=0.4472	2.9	3.1	1.1
Plus sign shape +	P1-0.35	9	b=1.937 a=0.678	2.733	3.292	1.2
Plus sign shape +	P1-0.5	9	b=1.732 a=0.866	2.6	3.464	1.33
Plus sign shape +	P1-0.75	9	b=1.5 a=1.125	2.4	3.75	1.563
Plus sign shape +	P1-1	9	b=1.342 a=1.342	2.23	4.03	1.8
Plus sign shape +	P1-2	9	b=1 a=2	1.8	5	2.78

Table 5  
shapes related to area 50 m<sup>2</sup>

shape of foundation	Symbol	Area (A) [m <sup>2</sup> ]	Dimensions [m]	Equivalent width B1[m]	Equivalent length L1[m]	L1/B1
Circular	C2	50.26	D=8	8	8	1
Square	S2	50.26	L=7.09 B=7.09	7.09	7.09	1
Rectangle l/B=2	R2-2	50.26	L=10.03 B=5.01	5.01	10.03	2
Rectangle l/B=3	R2-3	50.26	L=12.28 B=4.09	4.09	12.28	3
Rectangle	R2-5	50.26	L=15.85	3.17	15.85	5

l/B=5			B=3.17			
Plus sign shape +	P2-0.2	50.26	b=5.284 a=1.057	6.76	7.435	1.1
Plus sign shape +	P2-0.35	50.26	b=4.576 a=1.602	6.46	7.78	1.2
Plus sign shape +	P2-0.5	50.26	b=4.09 a=2.047	6.145	8.18	1.33
Plus sign shape +	P2-0.75	50.26	b=3.545 a=2.659	5.67	8.862	1.563
Plus sign shape +	P2-1	50.26	b=3.171 a=3.171	5.29	9.5	1.8
Plus sign shape +	P2-2	50.26	b=2.363 a=4.727	4.25	11.82	2.78

Table 6  
shapes related to area 144 m<sup>2</sup>

shape of foundation	Symbol	Area (A) [m <sup>2</sup> ]	Dimensions [m]	Equivalent width B1[m]	Equivalent length L1[m]	L1/B1
Circular	C3	144	D=13.54	13.54	13.54	1
Square	S3	144	L=12 B=12	12	12	1
Rectangle l/B=2	R3-2	144	L=16.98 B=8.48	8.48	16.98	2
Rectangle l/B=3	R3-3	144	L=20.79 B=6.93	6.93	20.79	3
Rectangle l/B=5	R3-5	144	L=26.8 B=5.37	5.37	26.8	5
Plus sign shape +	P3-0.2	144	b=8.94 a=1.79	11.5	12.52	1.1
Plus sign shape +	P3-0.35	144	b=7.746 a=2.711	10.94	13.168	1.2
Plus sign shape +	P3-0.5	144	b=6.93 a=3.46	10.37	13.86	1.33
Plus sign shape +	P3-0.75	144	b=6 a=4.5	9.6	15	1.563
Plus sign shape +	P3-1	144	b=5.39 a=5.37	8.93	16.12	1.8
Plus sign shape +	P3-2	144	b=4 a=8	7.2	20	2.78

Table 7  
 shapes related to area 625 m<sup>2</sup>

shape of foundation	Symbol	Area (A) [m <sup>2</sup> ]	Dimensions [m]	Equivalent width B[m]	Equivalent length L[m]	L/B
Circular	C4	625	D=28.21	28.21	28.21	1
Square	S4	625	L=25 B=25	25	25	1
Rectangle l/B=2	R4-2	625	L=35.36 B=17.67	17.67	35.36	2
Rectangle l/B=3	R4-3	625	L=43.3 B=14.4	14.4	43.3	3
Rectangle l/B=5	R4-5	625	L=55.9 B=11.2	11.2	55.9	5
Plus sign shape +	P4-0.2	625	b=18.633 a=3.727	23.96	26.09	1.1
Plus sign shape +	P4-0.35	625	b=16.137 a=5.648	22.782	27.434	1.2
Plus sign shape +	P4-0.5	625	b=14.434 a=7.22	21.664	28.85	1.33
Plus sign shape +	P4-0.75	625	b=12.5 a=9.375	20	31.25	1.563
Plus sign shape +	P4-1	625	b=11.18 a=11.18	18.63	33.54	1.8
Plus sign shape +	P4-2	625	b=8.33 a=16.66	14.98	41.713	2.78

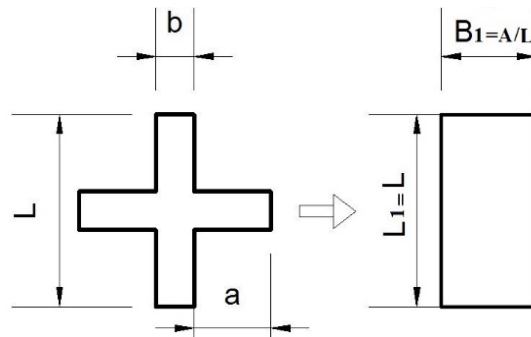


Figure 5

Symbols and equivalent dimensions of the Plus Foundation

### 3.1 Comparison of the Numerical and Empirical Equations of Ultimate Bearing Capacity

#### 3.1.1 Square, Circle and Rectangular Foundations

As can be seen from Figures 6, 7, 8, and 9 for areas 9, 50, 144, 625 m<sup>2</sup> respectively, the Vesic equation achieves the best fit for square and circle shapes while the Hansen equation achieves the best fit for rectangular shapes. The reason being that Vesic uses in his equation the same  $N_c$  and  $N_q$  terms of the Hansen relation but  $N_\gamma$  is different.

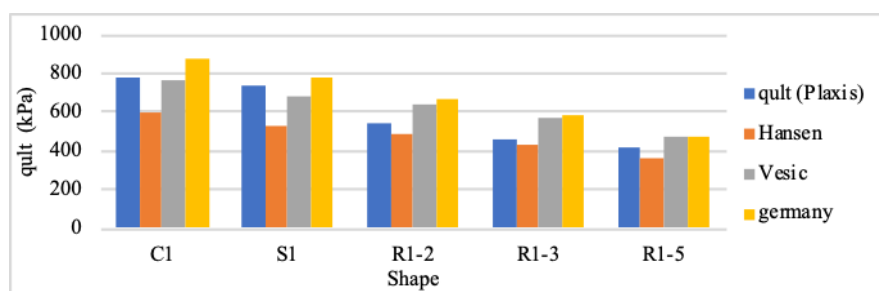


Figure 6

Comparison of Plaxis' calculation of bearing capacity and an empirical equation of bearing capacity for a 9-m<sup>2</sup> area

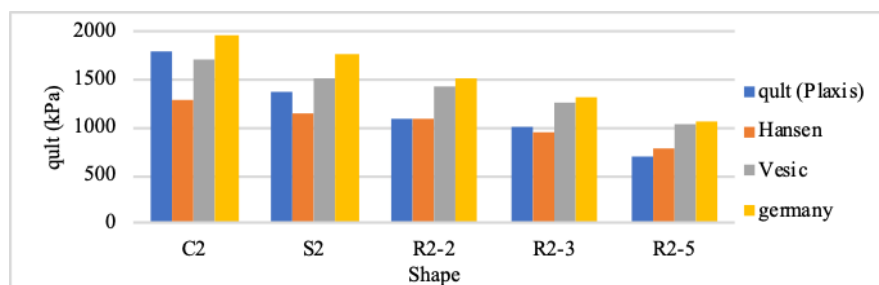


Figure 7

Comparison of Plaxis' calculation of bearing capacity and an empirical equation of bearing capacity for a 50-m<sup>2</sup> area

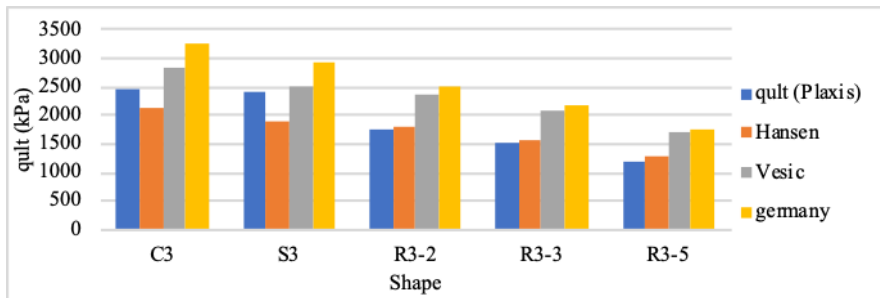


Figure 8

Comparison of Plaxis' calculation of bearing capacity and an empirical equation of bearing capacity for a 144-m<sup>2</sup> area

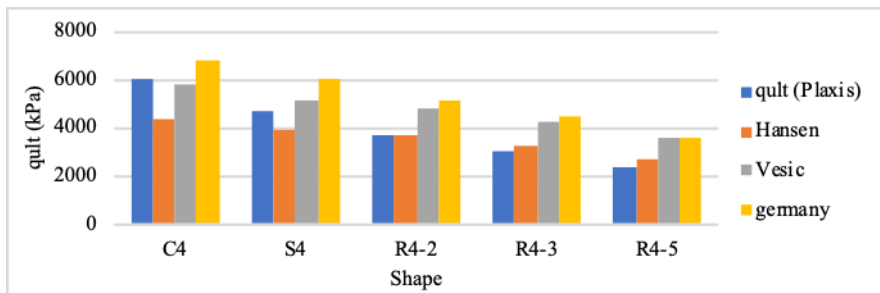


Figure 9

Comparison of Plaxis' calculation of bearing capacity and an empirical equation of bearing capacity for a 625-m<sup>2</sup> area

### 3.1.2 Plus Shape Foundations

The relationships between the ultimate bearing capacity ( $q_{ult}$ ) and  $a/b$  where the dimensions  $a$  and  $b$  are clarified in figure 5. It is noted that the best value of  $a/b$  is about 0.5 (Fig. 10). This is consistent with the laboratory study of Ghazavi and Mirzaeifar [17], because at this value the best blocking occurs and the soil between edges behaves as if it was part of the foundation and moves down upon loading as a single unit.

Figures 11, 12, 13 and 14 show a comparison between the numerical results and empirical equations of ultimate bearing capacity of different areas 9, 50, 144 and 625m<sup>2</sup> respectively for plus shape foundations using the equivalent dimension of a rectangular foundation where  $L$  is the length of the enveloped square shape of the plus shape foundation and  $B1=A/L$  where  $A$  is the Area of the plus shape foundation as shown in Fig. 5.

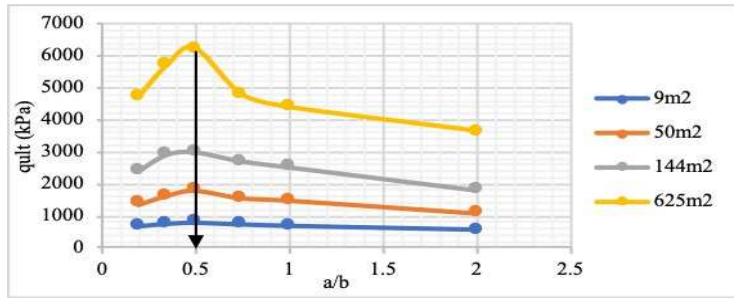


Figure 10

The relationships between ultimate bearing capacity (qult) and a/b

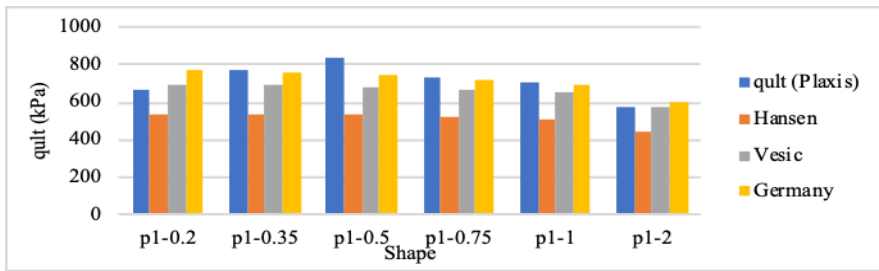


Figure 11

Comparison of Plaxis' calculation of bearing capacity and an empirical equations of bearing capacity for a 9-m<sup>2</sup> area of plus foundation

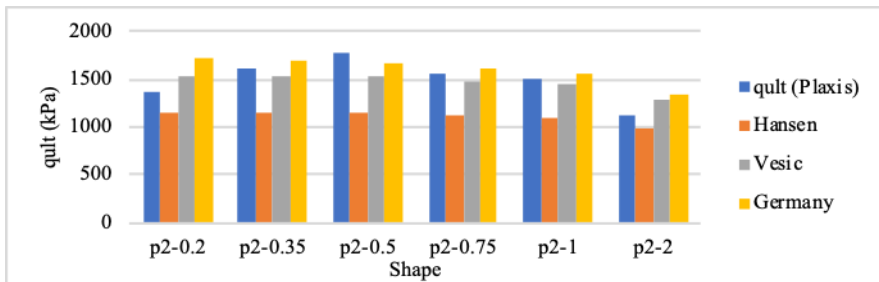


Figure 12

Comparison of Plaxis' calculation of bearing capacity and empirical equations of bearing capacity for a 50-m<sup>2</sup> area of plus foundation

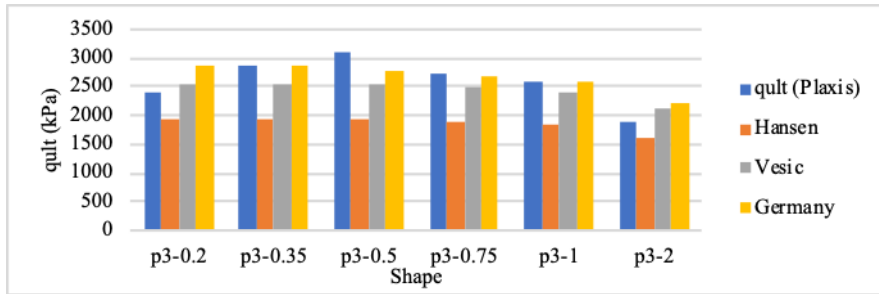


Figure 13

Comparison of Plaxis' calculation of bearing capacity and empirical equations of bearing capacity for a 144-m<sup>2</sup> area of plus foundation

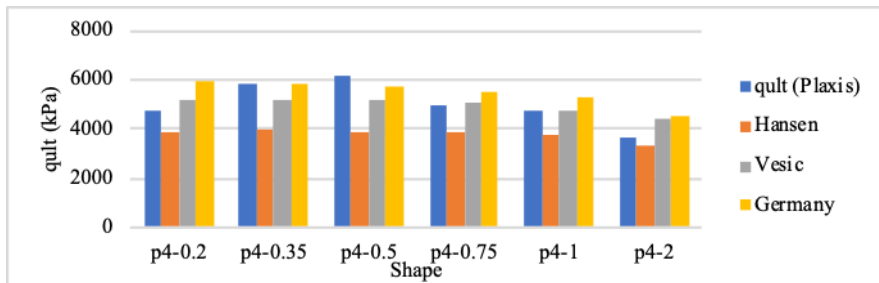


Figure 14

Comparison of Plaxis' calculation of bearing capacity and empirical equations of bearing capacity for a 625-m<sup>2</sup> area of plus foundation

It is noted from Figures 11, 12, 13 and 14 that the Vesic equation fits the numerical bearing capacity in most cases especially when  $a/b > 0.5$  but they do not take the effect of blocking well when  $a/b \leq 0.5$ . To solve this issue the Hansen equation is chosen since it gives the best results when it is multiplied by the blocking coefficient which is determined using the solver feature in Excel. Equation (1) is the new equation of bearing capacity of the plus shape foundation that is modified from (Chazavi and Hadiani [19]) equation.

$$q_{ult.Plus} = q_{ult.Hansen} \times e^{\left( \frac{1.8 \times 10^{-6} \left( \frac{B_1}{L_1} \right)^{7.3}}{4.6 \times 10^{-7} + \left( \frac{B_1}{L_1} \right)^{24.2}} \right)^{0.21}} \quad (1)$$

Where  $q_{ult.Hansen}$  : is the ultimate bearing capacity calculated by the Hansen equation using the equivalent dimension of the rectangular foundation as clarified in Fig. 5. Figures 15, 16, 17 and 18 show a comparison between numerical, empirical equations and modified equations (1) of the ultimate bearing capacity of different areas 9, 50, 144 and 625 m<sup>2</sup> respectively.

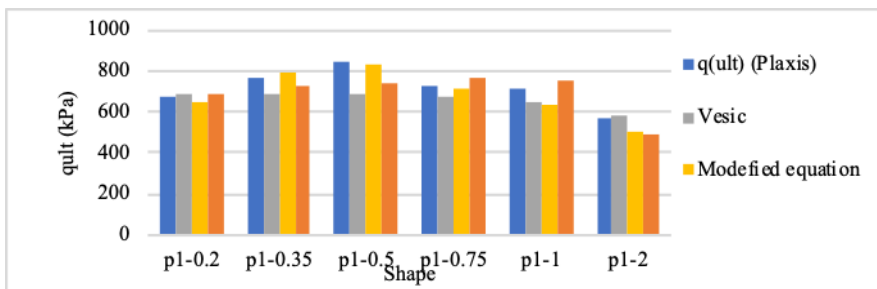


Figure 15

Comparison of numerical bearing capacity, empirical equations, and a modified equation for a 9-m<sup>2</sup> area

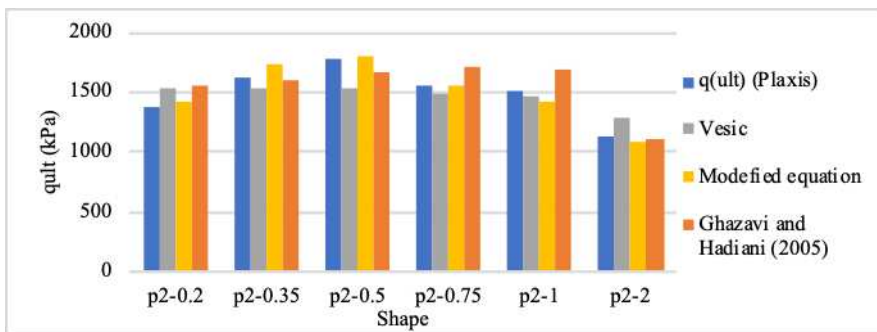


Figure 16

Comparison of numerical bearing capacity, empirical equations, and a modified equation for a 50-m<sup>2</sup> area

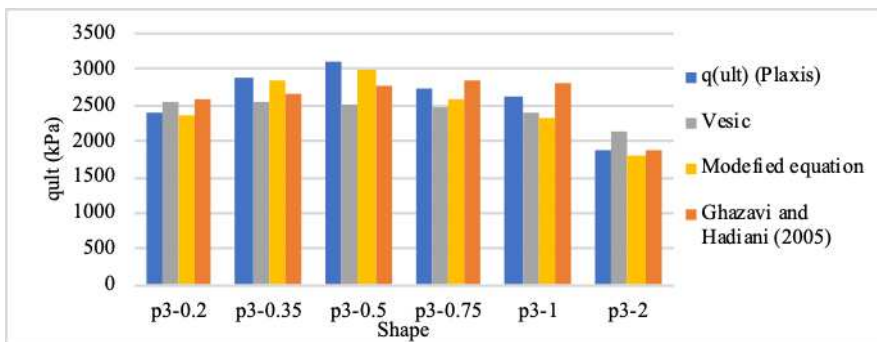


Figure 17

Comparison of numerical bearing capacity, empirical equations, and a modified equation for a 144-m<sup>2</sup> area

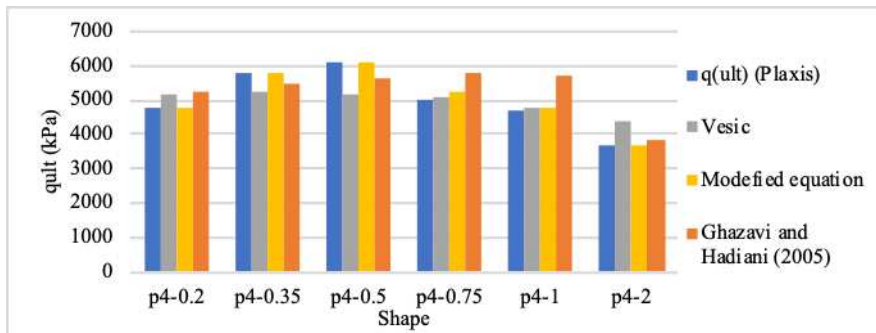


Figure 18

Comparison of numerical bearing capacity, empirical equations, and a modified equation for a 625-m<sup>2</sup> area

It is clear from Figures 15, 16, 17 and 18 that the modified equation achieves the best consistency with numerical results for different areas of the plus shape foundation.

It is worth mentioning that the plus shape foundation at  $a/b=0.5$  achieves the highest bearing capacity compared to other shapes that have the same area, as is shown in Fig. 19, which depicts the stress-settlement curves for foundations with an area of 144 m<sup>2</sup>. Fig. 20 shows the improvement percentages in bearing capacity at  $a/b=0.5$  in comparison to square shape foundations. The percentage increases with an increase in the area of the foundation; for example, with the area of 50m<sup>2</sup> the ultimate bearing capacity increases by 25%.

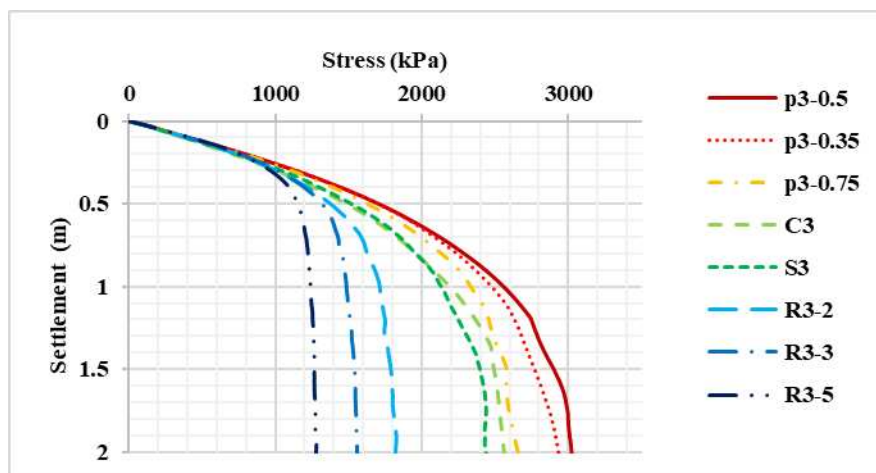


Figure 19

Stress-settlement relationship curves

From these curves in Fig. 19, we can deduce that the shear bearing capacity is the highest for the plus shape foundation at the ratio  $a/b = 0.5$ , whereas the shear bearing capacity is the least for the strip foundation.

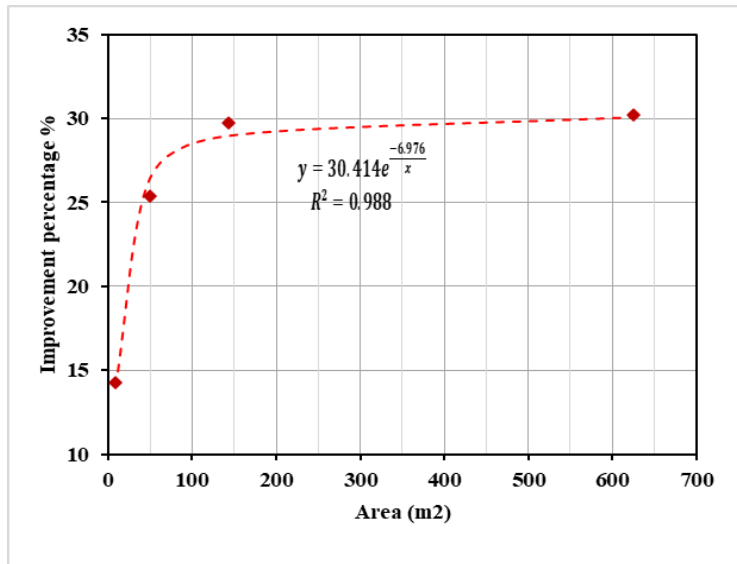


Figure 20

Improvement percentages in bearing capacity at  $a/b=0.5$  as comparison with square shape foundation

## Conclusions

According to the outcomes of the numerical analysis performed using the Plaxis 3D software, which uses the finite element method FEM for various foundation shapes and with various areas of foundation on sandy soil, the following conclusions were made:

- The Hansen equation provides the closest value to the numerical analysis of rectangular shapes, while the Vesic equation is the best fitting for circular and square foundations for all areas.
- The plus foundation outperforms square and circular foundations in terms of performance and provides the best shear bearing capacity at the ratio  $a/b = 0.5$ .
- Finding the blocking coefficient led to the development of a new equation (Equation 1) for the bearing capacity of plus foundations.
- The improvement percentages in bearing capacity at  $a/b=0.5$  in comparison to the square shape foundation increase from 15% to 30% with an increase in the area of the foundation from 9 m<sup>2</sup> to 625 m<sup>2</sup>, respectively.

The following recommendations may be taken into account for further research on the topic:

- ✓ Studying new foundation shapes, such as H, T and U-shaped foundations.
- ✓ Investigating how the bearing capacity of sand is affected by alterations in the elastic modulus and internal friction angle.
- ✓ Investigating the bearing capacity effects of foundation depth, soil layering, load inclination, decentralization, land surface slope, foundation base inclination, and groundwater presence.

## References

- [1] B. M. Das, *Shallow foundations: Bearing capacity and settlement, third edition*. USA: CRC Press, 2017
- [2] B. M. Das, *Principles of foundation engineering. 8<sup>th</sup> edition*. Global Engineering, 2016
- [3] S. Fischer, "Geogrid reinforcement of ballasted railway superstructure for stabilization of the railway track geometry – A case study," *Geotext. Geomembranes*, Vol. 50, No. 5, Oct. 2022, pp. 1036-1051
- [4] K. Terzaghi, *Theoretical Soil Mechanics*. New York: John Wiley & Sons, Inc., 1943
- [5] B. M. Fellenius and A. Altaee, "Stress and settlement of footings in sand," *Geotech. Spec. Publ.*, Vol. 2, No. 40, 1994, pp. 1760-1773
- [6] R. Nova and L. Montrasio, "Settlements of shallow foundations on sand," *Géotechnique*, Vol. 41, No. 2, 1991, pp. 243-256
- [7] F. Zhu, J. I. Clark, and R. Phillips, "Scale Effect of Strip and Circular Footings Resting on Dense Sand," *J. Geotech. Geoenvironmental Eng.*, Vol. 127, No. 7, Jul. 2001, pp. 613-621
- [8] A. B. Cerato and A. J. Lutenecker, "Scale Effects of Shallow Foundation Bearing Capacity on Granular Material," *J. Geotech. Geoenvironmental Eng.*, Vol. 133, No. 10, Oct. 2007, pp. 1192-1202
- [9] J. Kumar and V. N. Khatri, "Effect of Footing Width on Bearing Capacity Factor  $N_\gamma$  for Smooth Strip Footings," *J. Geotech. Geoenvironmental Eng.*, Vol. 134, No. 9, Sep. 2008, pp. 1299-1310
- [10] M. Jahanandish, M. Veiskarami, and A. Ghahramani, "Effect of stress level on the bearing capacity factor,  $N_\gamma$ , by the ZEL method," *Korean Soc. Civ. Eng. (KSCE Journal)*, Vol. 14, No. 5, 2010, pp. 709-723
- [11] B. J. Nareeman, "A study on the scale effect on bearing capacity and settlement of shallow foundations," *Int. J. Eng. Technol.*, Vol. 2, No. 3, 2012, pp. 480-488
- [12] I. L. Boiko and M. Alhassan, "Effect of Vertical Cross-Sectional Shape of

- Foundation on Settlement and Bearing Capacity of Soils,” *Procedia Eng.*, Vol. 57, Jan. 2013, pp. 207-212
- [13] N. Kaya and M. Ornek, “Experimental and numerical studies of T-shaped footings,” *Acta Geotech. Slov.*, Vol. 10, No. 1, 2013, pp. 43-58
- [14] A. Shafaghat, H. Khabbaz, S. Moravej, and A. Shafaghat, “Effect of footing shape on bearing capacity and settlement of closely spaced footings on sandy soil,” *Int. J. Geotech. Geol. Eng.*, Vol. 12, No. 11, 2018, pp. 676-680
- [15] S. Nazeer and R. K. Dutta, “Bearing capacity of E-shaped footing on layered sand,” *J. Achiev. Mater. Manuf. Eng.*, Vol. 105, No. 2, 2021, pp. 49-60
- [16] K. . Stone, S. Kozman, T. Newson, and Z. Guan, “An investigation of the bearing capacity of irregular shaped (Triangular) footings,” in *Proceeding of the 6th international offshore site investigation and geotechnics conference: Confronting new challenges and sharing knowledge, 11-13 September 2007, London, UK, 2007*, pp. 491-696
- [17] B. Davarci, M. Ornek, and Y. Turedi, “ANALYSES OF MULTI-EDGE FOOTINGS RESTED ON LOOSE AND DENSE SAND,” *Period. Polytech. Civ. Eng.*, Vol. 58, No. 4, Oct. 2014, pp. 355-370
- [18] M. Ghazavi and H. Mirzaeifar, “Bearing capacity of multi-edge shallow foundations on geogrid-reinforced sand,” in *Proceedings of the 4<sup>th</sup> International Conference on Geotechnical Engineering and Soil Mechanics*, 2010, pp. 1-9
- [19] M. Ghazavi and N. Hadiani, “Bearing capacity of multi-edge foundations,” MS thesis, university of Technology, Tehran (Iran): Department of civil engineering, 2005
- [20] G. R. Dodagoudar and N. Aarthi, “Three-Dimensional Finite-Element Analysis of Pressure-Settlement Response of Sand Compaction Pile-Treated Cohesionless Deposits,” *Int. J. Geomech.*, Vol. 21, No. 4, 2021, pp. 1-10
- [21] R. Alsirawan and E. Koch, “The finite element modeling of rigid inclusion-supported embankment,” *Pollack Period.*, Vol. 17, No. 2, May 2022, pp. 86-91
- [22] Q. Chen and M. Abu-Farsakh, “Numerical analysis to study the scale effect of shallow foundation on reinforced soils,” in *Geo-Frontiers 2011: Advances in Geotechnical Engineering*, Reston, VA: ASCE: Geotechnical Special Publication 221, edited by J. Han, and D. E. Alzamora, 2011, pp. 595-604
- [23] A. Alnmr, “Material Models to Study the Effect of Fines in Sandy Soils Based on Experimental and Numerical Results,” *Acta Tech. Jaurinensis*, Vol. 14, No. 4, 2021, pp. 651-680

# Decision Support System for Managing Marshalling Yard Deviations

**Nikola Vitković<sup>1</sup>, Dragan Marinković<sup>1,3</sup>, Sergiu-Dan Stan<sup>2</sup>,  
Miloš Simonović<sup>1</sup>, Aleksandar Miltenović<sup>1</sup>, Miša Tomić<sup>1</sup>,  
Milica Barać<sup>1</sup>**

<sup>1</sup> University of Niš, Faculty of Mechanical Engineering, Aleksandra Medvedeva 14, 18000 Niš, Serbia, e-mail: nikola.vitkovic@masfak.ni.ac.rs, dragan.marinkovic@masfak.ni.ac.rs, milos.simonovic@masfak.ni.ac.rs, aleksandar.miltenovic@masfak.ni.ac.rs, misa.tomic@masfak.ni.ac.rs, milica.barac@masfak.ni.ac.rs

<sup>2</sup> Technical University of Cluj-Napoca, Strada Memorandumului 28, Cluj-Napoca 400114, Romania, e-mail: Sergiu.Stan@mdm.utcluj.ro

<sup>3</sup> Technische Universität Berlin, Department of Structural Mechanics and Analysis, Strasse des 17. Juni 135, 10623 Berlin, Germany, e-mail: dragan.marinkovic@tu-berlin.de

---

*Abstract: The presented studies, research and innovation focus in marshalling yards is on providing adequate responses on standard timings or deviations from the normal timetable. To address the possible deviations in the marshalling yard daily operation, the decision support system called SMART Real Time Management System (RTMY) is developed and introduced in this study. In general, Smart RTMY should give real-time responses to deviations, and decrease the time for making an adequate decision by providing a decision support system with optimal solutions based on selected criteria and optimization objectives. The system is based on the optimization function, which calculates the numerical (influence) value for each wagon in the marshalling yard, and on the developed expert system. The application of SMART RTMY in its current state is verified through the developed web application used by experts from universities and railways. This system should bring a novel solution to the marshalling yard classification and deviation response systems, thus providing a powerful software tool for marshalling yard dispatchers and operators.*

*Keywords: decision support system; software; marshalling yard; expert system*

---

# 1 Introduction

Marshalling Yard (MY) is a complex system with many processes that should be properly executed. The main processes in marshalling yard are: Pre-notification of incoming and outgoing trains, Arriving and checking incoming trains, Disaggregating/aggregating trains; Wagon shunting within the yard; Throwing wagons using the hump and/or the locomotive; Checking and departure outgoing trains; Wagon maintenance. These are standard processes and part of the standard and usual daily data flow [1-5]. The common processes are automated on satisfaction level with various IT applications [2]. Besides the developed applications, numerous research solutions address the problems with marshalling yard operations, and all of them are focused on keeping the operations active and removing bottlenecks. In general, the complex problem of managing the marshalling yard can be divided into smaller problems and partially addressed [6]. Considering sorting algorithms the existing literature already covers numerous types, which can be divided into three main categories [7]. The first consists of simple heuristics or rule-based sorting schemes, which can be easily applied in practice. The rule-based sorting schemes can further be divided into sequential (meant to rearrange wagons within a single train) and simultaneous sorting schemes (rearranging multiple input trains into other outgoing trains). The second category of algorithms are the exact methods that try to calculate an optimal solution, similar to the one presented in this research. Lastly, there is a third category of complex deterministic heuristics that tries to solve the sorting problem, by finding a good instead of an optimal solution. These methods are used in most classification activities, but each marshalling yard has some specific properties that should be considered. In general, for the classification of arriving trains all cars should eventually be rolled to the siding that has been assigned to the train they're supposed to depart with. There is usually a problem with capacity of these tracks, so experienced dispatcher or train operator should conduct actions to use mixing tracks for wagon classification properly. The studies [8, 9] presents a solution for these operations by introducing image discrimination theory and different online planning strategies tested using stochastics and deterministic approaches. The first tested strategy assigns tracks to trains on a first-come-first-served basis, while the second strategy uses time limits to determine when tracks should be assigned to departing trains. The research [10] investigates the influence of inbound traffic volume variation and schedule flexibility on classification yard performance. Simulation experiments using YardSYM, a discrete-event simulation model developed for hump classification yard analysis, quantify the interaction of these factors through different yard performance metrics. Simulation results suggest increasing schedule flexibility causes classification yard performance to decline while increasing volume variability has a less pronounced effect.

Expert systems are decision making systems that provide semantic solutions to different problems and are defined by rules and facts. They are a means to share and distribute knowledge [11], acquired directly or indirectly from domain experts of

different scientific areas. They not only aid users lacking specific know-how but also provide support and guidance [12], if not even substitutes, for human experts. Therefore, the power of an expert system should be its ability to mimic the human decision process [13]. An example of this kind of system is a solution for the output recommendations with an increased workload of the Baladjar station, presented in [14]. An expert system based on structured technology is introduced and applied to address this issue. Structural technologies are a set of technological techniques that allow you to control the properties of the structure of the station. With these methods, it is possible to bring the structural properties of the station closer to the optimum in any mode of operation. However, studies have shown that introducing "elastic technologies" in practice can increase stations' capacity only in the short-term. For greater efficiency in this direction, it is more advisable to use the technique of structural technologies together with the gradual optimization of the track development of the station.

Regarding the presented studies, research and innovation activities focus on providing adequate responses on standard timings or on deviations from the standard timetable. Special attention is given to deviations from decision making processes in marshalling yards. Different types of deviations are presented in [6, 15, 16] and can be summarised as the following: Deviations of the incoming train – later (delay) or earlier than timetable plan; Deviations of the outgoing train - later (delay) or earlier than timetable plan; Deviations in personal resources – lack of train driver or other staff for operations in MY; Deviations in individual wagons modification; Unexpected repair or breakage of sections of rail line; Unexpected repair or breakage of wagons; Deviations or incorrect weight of incoming trains or wagons; Priorities in cases of congested infrastructure or other priority policies; Extraordinary requests; Not defined deviations. All deviations can be grouped related to four factors: time, the present state of infrastructure, personal resources, and additional cargo operators' demands. The main factor is time, which is why the first two above deviations are also one of the consequences of all other deviations. Each deviation has causes, consequences of deviations, decisions that need to be realized, and consequences of selected decisions.

To address the possible deviations in the marshalling yard daily operation, the SMART Real Time Management System (RTMY), i.e., decision support system is developed and introduced in this study. In general, Smart RTMY should give real time responses to deviations, and decrease the time for making an adequate decision by providing support system with optimal solutions based on selected criteria and optimization objectives. This means the system is based on past experience (past interactions) and includes additional yard operational parameters (static and dynamic – content-based systems). Furthermore, the proposed solution is based on the optimization function, which calculates the numerical (influence) value for each wagon in the marshalling yard and the developed set of expert system rules. The expert system represents a hybrid decision support system because it includes rules and calculated influence factor to propose solutions. Therefore, SMART

RTMY should bring novel solution to the marshalling yard classification and deviation response systems, thus providing a powerful software tool for marshalling yard dispatchers and operators.

## 2 The Overall System Architecture

Smart RTMY is a decision support system represented by the developed web application (<https://tehnogenijalci.rs/smartvis/>). The web application is open and free to use. However, the application is still in the testing phase, and responses from different experts are required to improve it in future work. It is composed of visualization and an optimization module. The other developed modules are supporters (security, data exchange and transformation modules) or providers (e.g. data input module). The visual representation module displays the current status of the marshalling yard to the user, based on manually entered data acquired from a specific marshalling yard. In addition, this module will also display the future state of the marshalling yard based on input data and the optimal marshalling process planning results. The optimization or marshalling process planning module implements an expert system based on the optimization function and expert knowledge acquired from the Popovac (Serbia) marshalling yard.

The developed expert system is a Decision Support System or Decision Making System that provides instructional data to the marshalling yard dispatcher or operator. To properly define the functional and technical requirements of the SMART RTMY, Unified Modeling Language (UML) is used [17]. UML diagrams are created for all specific marshalling yard and software requirements and used to develop software modules. There are nine selected types of deviations in decision making processes in marshalling yards, and they can be described as use cases in UML. They are modelled and presented in Fig. 1. To properly model deviations and data included in marshalling yard management systems, additional parameters are defined as static (yard connections, layout data, operative times, equipment) and dynamic (data flow, restrictions and deviation) and presented in [18]. This is standard data already applied in marshalling yard operations. Finally, the data and object model were created and used as the basis for making the Decision support system application. The data model is expressed through a developed relational database, and the object model was developed using MVC (Model – View - Controller) pattern [19]. The database structure was defined with separate tables for trains, wagons, sidings, timetables, traffic directions, and users [18]. Database defines the structure of a Marshalling yard data model on which the object model depends, and it includes all requirements and limitations restricting the use of freight transport in the marshalling yard and freight transport that will be processed in the marshalling yard.

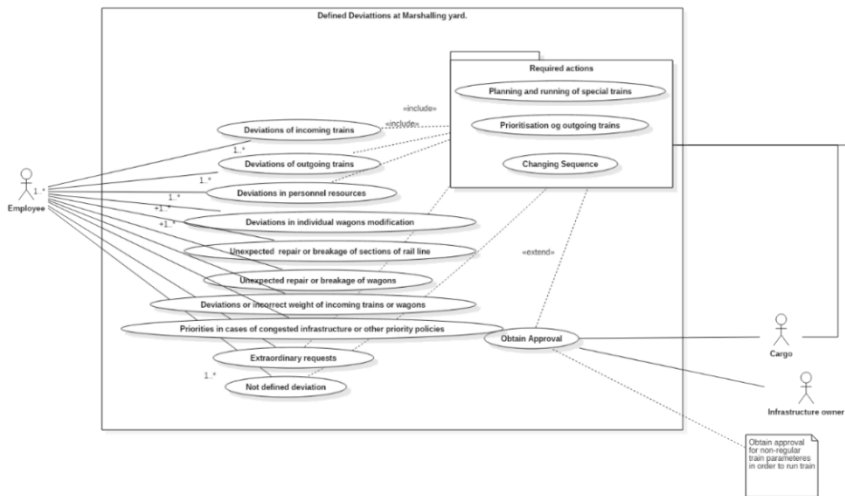


Figure 1

Use case diagram of defined types of deviations in the marshalling yard

The defined composition of the database, allows input and processing of all the described deviations and inputs or outputs. In addition, static and actual data from marshalling yard Popovac, Serbia was inserted into the database for further manipulation and processing.

To conclude, the Smart RTMY system uses the following:

- Material: Marshalling yard data from Popovac, Serbia; Expert knowledge gained from university and marshalling yard staff;
- Methods: Numerical Optimization; Expert system based on rules and facts; Relational database for data manipulation; MVC framework for application development

### 3 The Methodology

Smart RTMY complex structure enables a complete overview of the marshalling yard infrastructure and adequate real-time response by applying its developed modules. The visualization module can display status of the marshalling yard to the user, based on data entered manually or the possibility of showing data acquired automatically from a railway information system in the future upgrade. In addition, it displays the current snapshot of the marshalling yard infrastructure (warehouse, repairing station). Based on the security level, visual representation is differently formed for different users, e.g., dispatchers or marshalling yard operators [18].

The visualization module receives data from the database as static and optimized data (from the optimization module) and shows it to the user. It also enables data manipulation by using web app forms dedicated to yard elements (e.g., wagons, sidings, trains). Every modification of the data is reflected in recreating the data process, which creates a distinct visual representation of yard elements and inserts changes to the database. Furthermore, the database regularly makes replications using automatic DBMS service due to the possible errors in yard elements classification, which can be reverted to the previous verified state.

The module was developed using the following technologies: Front End – JQuery (standard, generally known JavaScript library) and D3.js (Data-Driven Documents); Back End – Currently, cakePHP is used as the main platform framework. It is important to mention that application works in a closed environment due to the railway regulations, but with the possibility to share data over secured connections.

The optimization module is created to control the classification of the trains (wagons) in the marshalling yard, and its overall composition is presented in Fig. 2. The diagram(s) are created by using adapted Structured Analysis and Design Technique - SADT [20]. Data analysis includes (P1) a static and dynamic dataset.

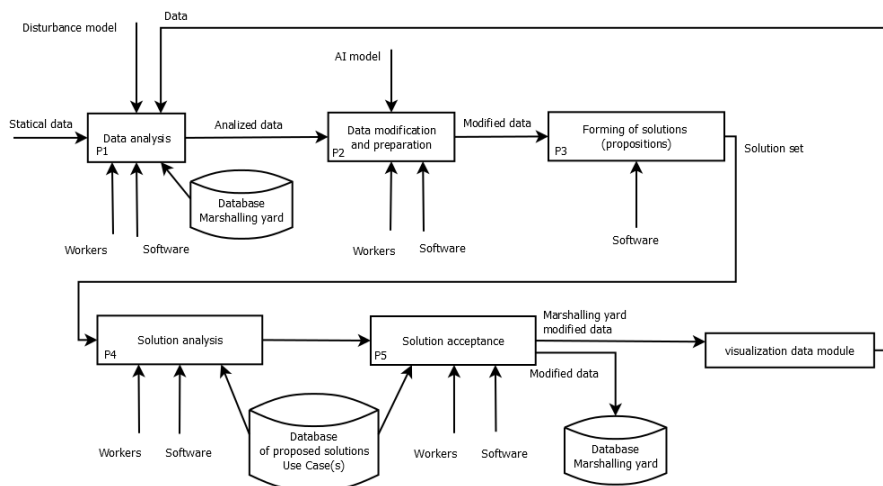


Figure 2

Optimization module of the Decision support system

The disturbance model presented in the scheme is currently under development, but its behaviour should be controlled like in the workflow systems, i.e., these should represent workflow interruptions. Furthermore, the disturbance model should encompass interruptions not defined in the system as deviations, i.e., unknown deviations. The decision system contains software solutions and manual progress monitoring (marshalling yard experts), defined in a scheme by "Data Modification

and Preparation" – P2, "Forming of solutions" – P3, "Solution analysis" – P4. P2 includes an intelligent system that controls the input dataset processing. The P2 process outputs data in a numeric-readable form (arrays, matrices) and process P3 creates human-readable data (presented in Fig. 3c) in a state of the solutions, which goes to P4 for the final verification (software can make wrong conclusions). In the process of "Solution(s) acceptance" – P5, solutions are finalized, modified marshalling classification is stored in the database for the next iteration, and new data is sent to the visualization module for display.

In the developed application, deviations are defined as:

- D1 - Train & Infrastructure, which includes Time deviation for incoming and outgoing trains and Wagon Malfunction (Fig. 3a)
- D2 - People (characterized by a shortage of people): Machine operator, Worker, Support worker. (Fig. 3b)
- D3 – Other generally refers to marshalling yard out of service (Fig. 3c)

Figure 3 consists of three screenshots of the Smart RTMY web application interface for entering deviations. Each screenshot shows the 'smart' logo and navigation menus for 'Infrastructure', 'Visualization', and 'Deviations/Recommendations'.  
 (a) **Train & Infrastructure deviation form**: The 'Train & Infrastructure' tab is active. It features radio buttons for 'No deviations', 'Time Deviation for Incoming Train' (selected), 'Wagon malfunction', and 'Time deviation of outgoing train'. Below these is a text input field with the placeholder 'insert value for delay (in minutes for time, or wagon description for wagon)' and the value '120'. To the right is a table with columns 'Mark deviation' and 'Source'.  
 (b) **People deviation form**: The 'People' tab is active. It features radio buttons for 'Machine operator' (selected), 'Worker', and 'Support Worker'. Below is a text input field with the placeholder 'Enter number of people:'.  
 (c) **Others deviation form with filled deviation – out of service**: The 'Other' tab is active. It contains a text area with the instruction 'Describe deviation and include deviation sources separated by dot-comma. Example: Marshalling yard out of service;from(in hours);to(hours);Y-m-d' and the example 'Marshalling yard out of service;12;17;2019-09-23'. The text area contains the filled example: 'Marshalling yard out of service;12;17;2019-09-23'.

Figure 3

Web forms (Smart RTMY) for entering marshalling yard deviations

To control the data flow based on the defined deviations and to find the optimal solutions, decision support system application (SMART RTMY) based on the developed expert system is applied. The Expert system is based on the marshalling yard dispatcher and operators' experience and it is included as a set of rules and facts. The optimization function (calculated influence factor) is part of the expert system as a numbering tool that presents the current influence on the specific wagon and/or train to the marshalling yard classification. The two elements of the expert system can be separated and work independently. Currently, the expert system is

developed by using an if-then set of rules and predefined parametric sentences (similar to parametric queries in relational databases) that simulate standard operator's responses, but it will be transferred to the experta package (<https://experta.readthedocs.io/>) in the future versions. The developed system contains standard rules for operating wagons and their classification, used for many years in the marshalling yards. The expert system is good up to a point, or up to a number of rules and their capabilities to respond to the marshalling yard requirements. The expert system should provide correct answers for the D2 and D3 deviations because these two are standard, and responses are uniform and straightforward. It is more complicated for deviation D1, which includes trains and wagons. Rules can be set, but sometimes it is required to optimize wagon classification and to properly distribute wagons to an adequate siding (outgoing train, for the service, etc.). The logical/mathematical model is defined and described in the following section to respond to this possible complex situation.

Wagons are defined as matrices elements in Wagons matrix ( $W_M [S \times N]$ ) – Sidings are rows, and positions are columns. Wagons dimensions are standard, and for the marshalling yard infrastructure definition, it is enough to know the starting position of each wagon, and its dimension. Another defined matrix is positional wagon matrix ( $P_{WM} [S \times N]$ ) which relates to each wagon in  $W_M$  and it defines wagons dimension and position which relates to siding length, and all values are transformed between  $[-1:1]$ . Siding length is defined as 100%. Each wagon length defines a percentage of that length, which is reflected to real numbers, up to 1. These matrices represent a current snapshot of the marshalling yard infrastructure and wagon distribution, i.e. if a wagon is re-positioned, the positional matrix is changed. If wagon leaves the station, it can be (is) deleted from both matrices. One note, timetable influence on the matrix is defined by adding virtual or physical incoming (-1) and outgoing sidings for outgoing trains (1). This feature of the proposed classification enables "bubble" sorting for wagons before they hit the yard, allowing proper reaction for train time deviation.

We introduce the new category called temporary trains with influence factor between -1 and 1 – They are virtual trains positioned on each siding, and its vector  $T_{WM}$  contains rows from  $W_M$  matrix, i.e., individual siding. When temporary train reflects incoming or outgoing trains, then we changed category, or influence on -1 (not yet in the station), or 1 (in the station, scheduled for departure). Each siding is influenced by the marshalling yard rules, which can be changed. The influence factor on each is defined according to the current timetable for the marshalling yard and sidings definition (incoming, outgoing, mixed, or service). These values defines the marshalling yard operator or dispatcher. To add a time variable temporary train factors are multiplied with the time factors from the timetable. This factor is from  $[-1:1]$ , and it reflects the time schedule of trains coming  $[-1:0]$  or scheduled for departure  $[0:1]$  the station. Factor for temporary trains already in the station, e.g., on classification yards, are set to values defined for the train they belong to or the trains they will be added.

To form a Decision support system, the function (1) which defines the wagon influence on the station operation is expressed by space matrices and vectors for trains and timetable:

$$\begin{aligned}
 W_M &= [W_{1,1} \cdots W_{1,n} \vdots \vdots W_{s,1} \cdots W_{s,n}]; \\
 P_{WM} &= [P_{1,1} \cdots P_{1,n} \vdots \vdots P_{s,1} \cdots P_{s,n}]; \\
 T_{WM} &= [T_{1,1} \cdots T_s]; C_T = [C_{1,1} \cdots C_s] \\
 W_{Pi,j} &= \prod_{j=1,n}^{i=1,s} W_{Mi,j} \times P_{WMi,j}; T_{Ci,j} = \prod_{i=1,s} T_{WMi} \times C_{Ti}; \\
 W_I &= \prod_{j=1,n}^{i=1,s} W_{Pi,j} \times T_{Ci} \tag{1}
 \end{aligned}$$

This operation returns the value from [-1:1] for each wagon in the matrix. Therefore, the reaction importance for each wagon is presented to the user. For example, if some wagon needs to be re-positioned to the outgoing or mixed siding because of the timetable schedule, he will get a high influence factor. Multiple wagons can have an influencing factor close to or equal to one. Still, for each wagon in the expert system, a description is introduced and attached to the influence factor by using the following function (2):

$$W_{EI} = \prod_{j=1,n}^{i=1,s} W_{Ii,j} \times E_{xi,j} \tag{2}$$

Ex is a matrix (3) of wagon properties already described in the system, based on an already known timetable for the marshalling yard and the yard infrastructure. The matrix Ex also includes wagons in a timetable, which are defined for future arrival, which is essential if we want to create a temporary train in the virtual incoming siding.

$$\begin{aligned}
 E_x &= [E_{1,1} \cdots E_{1,n} \vdots \vdots E_{s,1} \cdots E_{s,n}]; E_{i,j} = \\
 &\quad \text{Time scheduled: Time format} \\
 &\quad [ \text{Temporary train id : Integer} \quad ] \\
 &\quad \text{Wagon operational status: 0 or 1, ...} \tag{3}
 \end{aligned}$$

Finally, the influence matrix for all existing wagons is formed and applied in the expert system, which gives the marshalling yard operator possible actions based on the defined deviations in the application. The rules and facts define the expert system, but one important addition is created. This addition refers to the set of parametric sentences with parameters like train number, wagon id, and incoming time, which can be replaced by the actual values based on the expert system recommendation. When the expert system creates suggestions/recommendations, it uses the parametric sentences and changes the values of parameters with the recommended ones, as presented in included examples. The optimization model (influence factors) is one of the inputs for the expert decision on wagon classification. It is essential to mention that this part of the system is currently under development, so most of the rules are now defined in the PHP as a set of if-then

statements and will be transferred to the "experta" python package. The python library *Experta* is used for building expert systems and is strongly inspired by CLIPS [21, 22], which means that different notations are used to describe rules implemented in the system. An expert system is written as a program capable of pairing up a set of facts with rules to those facts and executing some actions based on the matching rules. Facts are the basic unit of information of *Experta* (generally for any expert system). Rules have two components, LHS (left-hand-side) and RHS (right-hand-side). The LHS describes (using patterns) the conditions for executing the rule (or firing). The RHS is the set of actions to perform when the rule is fired. With expert systems like *experta*, the program flow should not be defined explicitly. The knowledge (Rules) and the data (Facts) are separated, and the Knowledge Engine is used to apply the knowledge to the data. The rules for static data are defined as is, meaning that these rules are defined descriptively, i.e., if a worker is not available for work, call another worker, or if nobody is available, then make different scheduling. For dynamic data, rules are made differently, and for example, the wagon data is currently defined as object notation:

- $W_i = (\text{wagon} = \{\text{wagon\_id} = \text{unique\_value}, \text{sidings\_id} = \text{unique\_value}, \text{train\_id} = \text{unique\_value}, \text{positional\_data} = \text{temporary\_value}, \text{calculated\_matrix} = W_{i,j}, \text{descriptive\_matrix} = WE_i, \dots\})$
- $T_i = (\text{train} = \{\text{train\_id} = \text{unique\_value}, \text{sidings\_id} = \text{unique\_value}, \text{wagons} = [\text{wagon\_id\_list}], \dots\})$
- $S_i = (\text{siding} = \{\text{siding\_id} = \text{unique\_value}, \text{siding\_type} = \text{unique\_value}, \dots\})$

The same notation is performed for the sidings and trains. Because temporary trains are introduced, each wagon is classified as part of a train, as a collection object. The wagon definition provides complete information for the wagon and it contains data from the relation database and calculated data. From the current defined Decision support system (not yet transferred to *experta*, but defined in the required form), the marshalling yard operator can analyze suggestions and analyze matrix pattern for every station wagon and the incoming or outgoing train.

To see how the Smart RTMY system works in its current state, two examples are presented, one for incoming train delay and one for interruption of yard working hours.

Example 1: Suppose we state the problem of incoming train (40600) one hour deviation (Fig. 3a). In that case, possible solutions based on the Smart RTMY can be:

Option 1: If train 40600 is going to be processed first, it means that processing and shunting of train 56921 can start at 15:28 and it can leave station with 53 minutes delay and leave the yard at 16:21. This mean that workers and shunting locomotive for next operation can start at 16:31.

Option 2: If train 56921 is going to leave station according to the plan, processing will be from 02:27 until 03:30 and processing for the train can start at 03:40 and will be finished at 05:38. This means that workers and shunting locomotive for next operation can start at 05:48.

Example 2: Suppose we state the problem of Marshalling yard out of service from 12 to 17 hours on a specific date. We first need to enter it into adequate web form (Fig. 3c), like: Marshalling yard out of service;12;17;2019-09-23. In that case, possible solutions based on the developed Smart RTMY can be:

Option 1: Train 56921 is going to be processed from 17:00 until 17:53. Train 45003 is going to be processed from 18:03 until 20:01. It can leave yard at 20:01. Train 44707 is going to be processed from 20:11 until 22:09. It can leave yard at 22:09.

Option 2: Train 56921 is going to be processed from 17:00 until 17:53. Train 44707 is going to be processed from 22:19 until 00:17. It can leave yard at 00:17. Train 45003 is going to be processed from 00:27 until 02:25. It can leave yard at 02:25.

Option 3: Train 45003 is going to be processed from 17:37 until 18:30. Train 56921 is going to be processed from 18:40 until 20:38. It can leave yard at 20:38. Train 44707 is going to be processed from 20:48 until 22:46. It can leave yard at 22:46.

Option 4: Train 45003 is going to be processed from 17:37 until 18:30. Train 44707 is going to be processed from 22:56 until 00:54. It can leave yard at 00:54. Train 56921 is going to be processed from 01:04 until 03:02. It can leave yard at 03:02.

Option 5: Train 44707 is going to be processed from 17:00 until 18:58. Train 56921 is going to be processed from 19:08 until 21:06. It can leave yard at 21:06. Train 45003 is going to be processed from 21:16 until 23:14. It can leave yard at 23:14.

### 3.1 Methodology Discussion

The presented solution defines novel approach for the marshalling yard deviation response, and it is based on the expert system application. The Smart RTMY is composed of two main parts, which can be completely individual and work independently. The first part is defined as a mathematical marshalling classification model that defines the influence factor for each wagon on the siding, including incoming and outgoing wagons. This exact value reflects the ones stated in the [7, 8], but with a different approach. The calculation is different because this research is focused on wagon influence factor, and mentioned studies on the position of the wagons on the yard. The second part represents expert system currently defined as if-then rules, and facts already prepared for import in the experta python package. In general, machine learning replaces expert systems in many fields. Still, in this case, the later represent a good approach because it can reflect marshalling yard operator experience, and the rules can be constantly upgraded. The system is currently in the testing phase, and the results are promising (found in the web

application). Future work on improving the expert system (e.g., implementing machine learning) should be conducted to make the system work with a significant confidence factor.

### **Conclusion**

The decision support system should provide the marshalling yard operator an overview picture of the current snapshot of the marshalling yard and provide information on possible actions which can be performed in the case of deviations, or even in other situations like the energy optimization described in [23, 24], or for wagon and track maintenance described in [25-27].

It is important to mention the possible benefits of Smart RTMY for the railway network structure of the Europe. The support for integration with railway information systems will be developed to provide the opportunity to obtain inbound and outbound traffic data automatically from external sources, but this requires a lot of additional effort and is planned for the future work. In developing support for integration with railway information systems the focus will be on data exchange following industry standards such as TAF TSI and RailML. Additional information may be collected depending on the data available from the railway information system, such as traffic information for the next 24 hours (or another defined period). With such data the information system could offer information about estimated waiting and marshalling time to railway officials planning freight transport.

### **Acknowledgement**

The paper presents the case that resulted from application of the research project Smart Automation of Rail Transport (Project reference – 730836), H2020, founded by European Union, and was financially supported by the Ministry of Science, Technological Development and Innovation of the Republic of Serbia (Contract No. 451-03-47/2023-01/ 200109).

### **References**

- [1] Gestrelus, ssS., Dahms, F., Bohlin, M.: Optimization of simultaneous train formation and car sorting at marshalling yards, Proc. 5<sup>th</sup> International Seminar on Railway Operations Modelling and Analysis RailCopenhagen, 2013
- [2] Khoshniyat, F.: Simulation of planning strategies for track allocation at marshalling yards, Masterarbeit, Master of Science Dissertation in Transport Systems, KTH Royal Institute of Technology, Stockholm, Sweden, 2012, 64 p.
- [3] Vukšić Popović, M., Tanasković, J., Starčević, Z., & Mededović, N. Analysis of coupling system failures on freight trains. *Acta Technica Jaurinensis*, 16(1), 2023, pp. 11-17, <https://doi.org/10.14513/actatechjaur.00687>

- [4] Šestáková, J., Pultznerová, A., & Mečár, M.: The maintenance of the railway superstructure and its influence on the track geometry of regional line. *Acta Technica Jaurinensis*, 15(3), 2022, pp. 162-173, <https://doi.org/10.14513/actatechjaur.00664>
- [5] sCsortos, G., Augusztinovicz, F., & Bocz, P.: Optimal operation of a rail lubrication device with respect to noise reduction and wheel/rail friction coefficient. *Acta Technica Jaurinensis*, 14(2), 2021, pp. 138-154, <https://doi.org/10.14513/actatechjaur.00592>
- [6] Adlbrecht, J. A., Hüttler, B., Zazgornik, J., Gronalt, M.: The train marshalling by a single shunting engine problem, *Transportation Research Part C: Emerging Technologies*, 58, 2015, pp. 56-72
- [7] Guo, C., Li, S.: Optimizing operation of delivering and fetching wagons at a railway station with mixed-shaped goods operation sites, *Plos one*, 17(1), 2022, e0263029. doi:<https://doi.org/10.1371/journal.pone.0263029>
- [8] Bohlin, M., Gestrelus, S., Khoshniyat, F.: Simulation of planning strategies for track allocation at marshalling yards, *WIT Transactions on Modelling and Simulation*, 55, 2013, pp. 465-475, doi:10.2495/CMEM130381
- [9] Shabelnikov, A. N., Liabakh, N. N., Gibner, Y. M., Saryan, A. S.: Automatic Adviser on Mobile Objects Status Identification and Classification, *Journal of Physics: Conference Series*, 1015(3), 2018, p. 032041, IOP Publishing. doi:10.1088/1742-6596/1015/3/032041
- [10] Tyler Dick, C.: Influence of mainline schedule flexibility and volume variability on railway classification yard performance, *Journal of Rail Transport Planning & Management*, 20, 2021, 100269, doi:<https://doi.org/10.1016/j.jrtpm.2021.100269>
- [11] Hendriks, P.: Why share knowledge? The influence of ICT on the motivation for knowledge sharing, *Knowledge and process management*, 6(2), 1999, pp. 91-100. doi:[https://doi.org/10.1002/\(SICI\)1099-1441\(199906\)6:2<91::AID-KPM54>3.0.CO;2-M](https://doi.org/10.1002/(SICI)1099-1441(199906)6:2<91::AID-KPM54>3.0.CO;2-M)
- [12] Saibene, A., Assale, M., Giltri, M.: Expert systems: Definitions, advantages and issues in medical field applications, *Expert Systems with Applications*, 177, 2021, 114900. doi:<https://doi.org/10.1016/j.eswa.2021.114900>
- [13] Pozna, C., Precup, R. E.: Applications of Signatures to Expert Systems Modelling, *Acta Polytechnica Hungarica*, 11, 2, 2014, pp. 21-39, DOI: 10.12700/APH.11.02.2014.02.2
- [14] Manafov, E.: Application of artificial intelligence techniques to reduce the loading of the marshalling yard, *Збірник наукових праць ДНУЗТ ім. акад. В. Лазаряна. Вип.*, 23, 2022, pp. 5-10, doi: 10.15802/tsst2022/261643
- [15] Galonske, N., Riebe, E., Toubol, A., Weismantel, S.: The ViWaS project: future-proof solutions for wagonload transport, *Transportation Research Procedia*, 14, 2016, pp. 2850-2859, doi: <https://doi.org/10.1016/j.trpro.2016.05.402>

- [16] Minbashi, N., Palmqvist, C. W., Bohlin, M., Kordnejad, B.: Statistical analysis of departure deviations from shunting yards: case study from Swedish railways, *Journal of Rail Transport Planning & Management*, 18, 2021, 100248, doi:<https://doi.org/10.1016/j.jrtpm.2021.100248>
- [17] Rumbaugh, R., Jacobson, I., Booch, G.: *The Unified Modeling Language Reference Manual*, Addison-Wesley, California, ISBN 0-201-30998-X, 1998
- [18] Vitković, N., Simonović, M., Miltenović, A., Trifunović, M., Software Module for the Visualization and Planning of Marshalling Yard Operations, *Machine Design*, 11(21), 2019, pp. 1821-1259, doi:[10.24867/MD.11.2019.1.29-32](https://doi.org/10.24867/MD.11.2019.1.29-32)
- [19] Pop, D. P., Altar, A.: Designing an MVC model for rapid web application development, *Procedia Engineering*, 69, 2014, pp. 1172-1179, doi:[10.1016/j.proeng.2014.03.106](https://doi.org/10.1016/j.proeng.2014.03.106)
- [20] Fathi-Karoui, M., Najeh-Lakhroua, M.: Modeling a Numerically Controlled Machine Tool For Integrated Supervision Design, *International Journal of Information Technology and Electrical Engineering*, 8(6), 2019, pp. 90-95
- [21] Wygant, R. M.: CLIPS—A powerful development and delivery expert system tool, *Computers & industrial engineering*, 17(1-4), 1989, pp. 546-549, doi:[https://doi.org/10.1016/0360-8352\(89\)90121-6](https://doi.org/10.1016/0360-8352(89)90121-6)
- [22] Atanasova, I.: Using CLIPS to Realize Quality of Life Expert System (QLIFEX), *FMNS*, 2015, pp. 98-103
- [23] Fischer, S., Szürke, S. K., Detection process of energy loss in electric railway vehicles, *Facta Universitatis, Series: Mechanical Engineering*, 21(1), 2023, pp. 081-089, doi:[10.22190/FUME221104046F](https://doi.org/10.22190/FUME221104046F)
- [24] Cao, Y., Stojičić, S., Milovančević, M.: Management Schemes Incorporating all Services for Optimum Railway System Energy Utilization Based on Level Set Calculation Method, *Acta Polytechnica Hungarica*, 19(1), 2022, pp. 9-20, doi: [10.12700/APH.19.6.2022.6.2](https://doi.org/10.12700/APH.19.6.2022.6.2)
- [25] Banić, M., Simonović, M., Stojanović, L., Rangelov, D., Miltenović, A., Perić, M.: Digital twin based lightweighting of robot unmanned ground vehicles, *Facta Universitatis, Series: Automatic Control and Robotics*, 21(3), 2022, pp. 187-199, doi:<https://doi.org/10.22190/FUACR221121015B>
- [26] Szalai, S., Eller, B., Juhász, E., Movahedi, M. R., Németh, A., Harrach, D., Baranyai, G., & Fischer, S. Investigation of deformations of ballasted railway track during collapse using the Digital Image Correlation Method (DICM), *Reports in Mechanical Engineering*, 3(1), 2022, pp. 168-191, <https://doi.org/10.31181/rme20016032022s>
- [27] Tomków, J., Sobota, K., Krajewski, S. Influence of tack welds distribution and welding sequence on the angular distortion of tig welded joint, *Facta Universitatis, Series: Mechanical Engineering*, 18(4), 2020, pp. 611-622, doi:[10.22190/FUME200520044T](https://doi.org/10.22190/FUME200520044T)

# A Study on Possibility of Application of Recent Self-Healing Methods for Self-Healing Concrete Railway Sleeper Manufacturing: A Review

Fei Yang<sup>1</sup>, Mohammad Siahkouhi<sup>2\*</sup>, Guixian Liu<sup>3</sup>

<sup>1</sup> Infrastructure Inspection Research Institute, China Academy of Railway Sciences Co., Ltd., Beijing 100081, China; yf2009@rails.cn

<sup>2</sup> Center for Infrastructure Engineering, Western Sydney University, Penrith, NSW 2751, Australia; m.siahkouhi@westernsydney.edu.au

<sup>3</sup> Infrastructure Inspection Research Institute, China Academy of Railway Sciences Co., Ltd., Beijing 100081, China; liuguixian@rails.cn

\* Corresponding author

---

*Abstract: Railway sleepers are under different types of dynamic, static, and impact loads. Due to a lack of a short span of track maintenance and inspection, damaged railway sleepers may not be detected and replaced after sudden damage. Cracks in concrete railway sleepers are almost inevitable and difficult to detect. According to the main role of sleepers to keep track of standard gauge and transfer loads to railway track interlayers, these damages may bring train derailment. Therefore, the application of self-healing methods can provide more lifespan time and compensate for some load capacity of damaged sleepers to extend their service life until they are inspected and removed from the track. Several self-healing methods have been proposed for large-scale beam shape structures, including autogenous and autonomous. But according to the special service condition of sleepers, most of these methods are not suitable for manufacturing railway sleepers. In this study, most of the available methods are reviewed and assessed based on the railway sleeper manufacturing process, service environment, loading condition, and lifespan. Finally, some prospective methods have been proposed to manufacture self-healing concrete railway sleepers such as the application of nanomaterials, vascular methods, and the LatConX system.*

*Keywords: Self-healing concrete; concrete railway sleeper; railway track*

---

## 1 Introduction

One of the main roles of railway sleepers is to transfer loads coming from passing trains to the track interlayers [1-3]. Moreover, sleepers keep standard track gauge to avoid extra rails lateral displacement that may result in train derailment [4, 5].

Therefore, railway sleepers are one the critical components of railway tracks. Normally, track inspection is based on million gross tons (MGT) in some specific periods of time, unless an emergency damage causes emergency maintenance action [6, 7]. Damaged sleepers are detected using several methods such as measuring machine, ultrasonic, visual inspection, etc. [6, 8]. Therefore, self-healing railway concrete sleeper may avoid sudden failure of sleeper and compensate some load capacity of damaged sleepers to save track until next maintenance operation. Equipping conventional sleeper with self-healing feature can increase the final cost a sleeper, but due to the healing process and avoiding the sleeper failure under operation it can compensate its higher cost [9].

## 1.1 Railway Concrete Sleeper Characteristics

Railway sleepers include timber, steel, concrete and composite sleepers [10, 11]. Concrete railway sleepers have been used extensively. Almost each year 20 million concrete sleepers are used in railway tracks construction [12]. These concrete railway sleepers are under static, quasi static, dynamic and impact loads that provide a complicated loading condition [13, 14]. Concrete sleepers have three main critical zones as positive bending moment zone in rail seats and negative bending moment zone in middle of sleeper in which railway damages have been mostly observed, as shown in Figure 1.

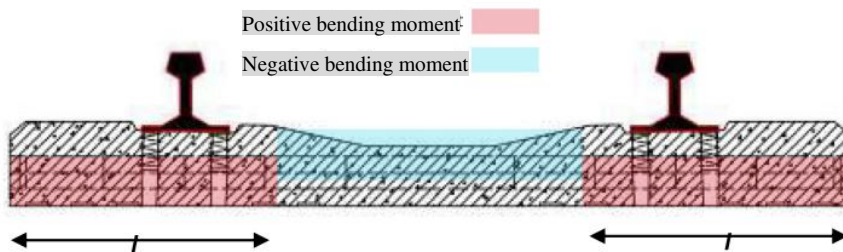


Figure 1  
Critical zones in concrete railway sleepers [6] with potential of damage

## 1.2 Self-Healing Concrete Methods Classification

Self-healing concrete is mostly utilized for concrete composites that can repair minor cracks without the need for external intervention. Autogenous healing and autonomous healing are two types of self-healing techniques. Autogenous healing in concrete refers to the hydration of unhydrated cement. Autonomous healing, on the other hand, requires a trigger to start the process [15, 16]. Autonomous healing, unlike autogenous healing, relies on embedded atypical designed additions rather than unhydrated cement to fix bigger cracks. Autonomous healing strategies have outperformed most autogenous healing methods in crack healing [17].

Most autogenous healing methods are confined to cracks with a width of less than 150  $\mu\text{m}$ .

### 1.2.1 Autogenous Self-Healing Methods

Table 1 lists some of the recent autogenous self-healing fracture repair techniques, including four categorizations as mineral powder, fibers, nanofillers and curing agents. Autogenous healing methods can heal crack up to 60%. The cracks mended by autogenously healing were observed in various diameters such as 0.05 mm to 0.87 mm, 5 to 10  $\mu\text{m}$ , 100  $\mu\text{m}$ , 200  $\mu\text{m}$ , 205  $\mu\text{m}$  and 300  $\mu\text{m}$  according to the analysis and investigation of different authors [18].

Table 1  
Overview of recent autogenous self-healing methods

Healing method	Sample dimensions	Healing materials	Crack width	Results	Ref.
Mineral powder	240 × 60 × 10 mm	Blast furnace slag and Limestone powder	60 $\mu\text{m}$	40%–60% healing for air cured specimen	[19]
	360 × 75 × 50 mm	Fly ash	< 100 $\mu\text{m}$	30 days of continuous moist curing was enough for specimens to achieve ultrasonic pulse velocity results higher than reference specimens.	[20]
	10 $\Phi$ x 20 cm	expansive agent, geo-materials (montmorillonite) and chemical agents	0.22 mm	The 0.22 mm crack of concrete was self-healed at 33 days.	[21]
Fibers	360 × 75 × 50 mm	Carbon fiber	60-80 $\mu\text{m}$	Final healing improvement ranged between 2.3% and 5%.	[22]
	85 × 85 × 30 mm	synthetic fiber (polyvinyl alcohol (PVA) and hybrid fiber reinforcing (polyethylene (PE) and steel code (SC)	<0.1 mm	Only after the crack width was sufficiently narrowed by sealing the very tiny cracks around the bridging fibers could	[23]

				mechanical property be recovered.	
	25 × 25 × 100 mm	steel-fiber	20 μm	As the healing period increases from 0 to 14 days, the healing ratio increases from 9.4% to 36% for most multiple micro-cracks widths smaller than 50 μm.	[24]
Nanofillers	360 × 75 × 50 mm	Carbon nano tube	40-50 μm	Healing processed between 2.3% and 5%.	[22]
Curing agents	160 × 40 × 15 mm	PVA fiber, Superabsorbent polymer (SAP) (hybrid)	104 μm	Hydration was continued by absorbed water and to precipitate CaCO <sub>3</sub> .	[25]
	100 mm × 200 mm cylinders	saturated lightweight aggregates (SLWA)	–	The 11.0 % mixture is slightly more hydrated than the 55/0.30 combination because the 11.0 percent mixture contains a minor amount of additional water in the LWA.	[26]
	70 × 70 × 280 mm	water-saturated lightweight aggregate and super-absorbent polymer	–	The findings show that internal curing and a shrinkage-reducing additive work together to reduce cracking potential significantly.	[27]

	150 × 150 ×150 mm	Polyethylene Glycol	–	Healing concrete meet the minimum strength requirement as 25 MPa and even with strength much above 25MPa.	[28]
--	----------------------	------------------------	---	---	------

### 1.2.2 Autonomous Self-Healing Methods

Table 2 shows recent research in autonomous self-healing methods. Autonomous methods can heal wider cracks up to 1.16 mm, especially in vascular technique that more healing agent is provided in damaged zone. In micro capsul performance, shell which carries healing agent has a significant role. Some shells or cargos are easier to break and release the epoxy due to crack and followed by healing agent flows into the cracks due to a capillary effect, which is the flow of a liquid through a confined space without the aid of external forces such as gravity.

Table 2  
Overview of recent autonomous self-healing methods

Healing method	Application method	Cargo	Crack width	results	Ref.
Electrodeposition technology	Electrolyte solutions + Direct current	ZnSO <sub>4</sub> and MgSO <sub>4</sub>	0.3 mm ± 0.05 m	In this method the fastest crack healing speed is during the first 5 days and the cracks are completely healed after 20 days	[29]
	Electrochemical deposition treatment processes	MgCl <sub>2</sub> solution in an electrolyte	100 μm to 200 μm	Magnesium ions formed at the mouth of a surface-opened crack and continued to the crack Interface.	[30]
Shape memory alloy embedded technology	NiTi and NiTiNb shape memory alloy (SMA)	–	0.5 mm	The main crack recovery began at 75 °C and reached 73–100% in the NiTi, 38.7–74.1% in the NiTiNb specimens.	[31]
	deformed shape memory alloy fibers, NiTi and NiTiNb	–	–	The NiTi fibers showed the maximum enhancement of 67% after heat treatment.	[32]

Capsule technology	horone diisocyanate (IPDI) microcapsules	Araffin wax, polyethylene wax, and nano silica	Micro cracks	Concrete containing microcapsules exposed to sulfate attack provided a shield in the pores after 14 days.	[33]
	epoxy resins microcapsules	St-DVB shell	Micro crack	The hardened epoxy bridged the cracks, as the dominant elements of C and O accounted for 95% of the mass in the surrounding cracks.	[34]
	dicyclopentadiene (DCPD) and sodium silicate	–	–	The modulus of elasticity of the concrete improved by 11% and 30% using sodium silicate, and the healing agent for DCPD microcapsules.	[35]
Vascular technology	polymeric healing agents	poly(methyl methacrylate) tubes	1.16 mm	Chloride resistance was increased in cracked concrete beams using mixed-in capsules (glass or PMMA) packed with a water-repellent chemical.	[36]
	Methyl methacrylate	hollow glass tubes	–	In samples containing released adhesive, flexural toughening was increased for the second loading event, while most of the non-adhesive controls showed a decrease in flexural toughening.	[37]
	Cyanoacrylate, Sodium silicate	Heat shrinkable tube	–	In a 3-point bending test, the results reveal that pressurizing the network increases the flow of healing agents to the point where they fill the majority of a 0.2 mm crack.	[38]
Microbial technology	Bacteria	porous expanded	0.15 mm	The cracks healed using mechanism bacterial concrete	[39]

		clay particles		which occurs due to metabolic conversion of calcium lactate to calcium carbonate.	
	Microbial induced carbonate precipitation (MICP)	recycled concrete aggregates (RCAs)	0.6 mm	The average crack healing ratio was 71 %, while the crack area healing ratio was 84 %.	[40]
	bacterial powder and calcium source	Mixture of sulfo aluminat cement, fly ash, and iron sand powder	–	The carrier made from low-alkali cementitious materials may protect the loaded spores for at least 516 days.	[41]

## 2 Recent Studies on Large Scale Self-Healing Beam Shaped Structures

Because the crack width and service circumstances of large scale structures differ from those of experimental samples, a specific approach for providing self-healing property is required. Based on the polyurethane encapsulation that is integrated in the matrix with eight concrete mixes, Huang et al. [42] investigated an autogenous approach for manufacturing self-healing concrete sleepers. In the laboratory, artificial and man-made cracks have been generated. Modal impact excitation, ultrasonic pulse velocity, and visual inspection were used to track crack healing. According to the findings, modal impact excitation is the least effective method for crack monitoring, especially when the cracks are small. In another study, fracture development promotes capsule rupture, release, and subsequent hardening of the polyurethane inside the crack, according to Tittelboom et al. [43]. The second method involves mixing superabsorbent polymers (SAPs) into the concrete. These SAPs absorb water that enters the crack, swell, and close it. They also cause ongoing hydration and calcium carbonate precipitation when they release their water content later. Smaller cracks are more likely to heal than larger cracks, as seen in Figure 2. Crack closing ratios of 40-80% were found for crack widths of 0-50  $\mu\text{m}$ , whereas ratios of 10-30% were obtained for crack widths of 200-250  $\mu\text{m}$ .

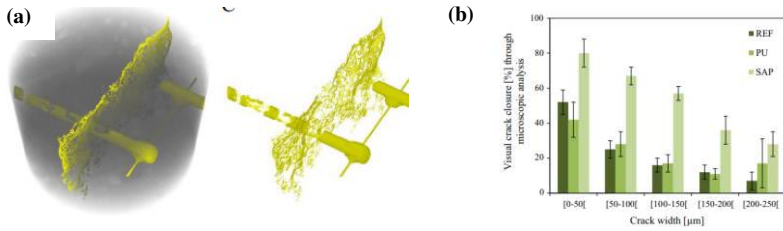


Figure 2

(a) Layout of long tube PU capsules, (b) Crack healing ratio [43]

Al-Tabbaa *et al.* [44] discussed a larger national effort to produce biomimetic cementitious infrastructure materials. In Fig. 15a, the daily average air temperature acquired from local meteorological stations is shown with the mean crack width recorded over the monitoring period. During the first four monitoring sessions, crack width readings consistently decreased between November 2015 and February 2016. The average normalised crack width is shown in Fig. 15b, along with daily rainfall totals. One of the most critical factors for successful autogenous self-healing is the presence of water.

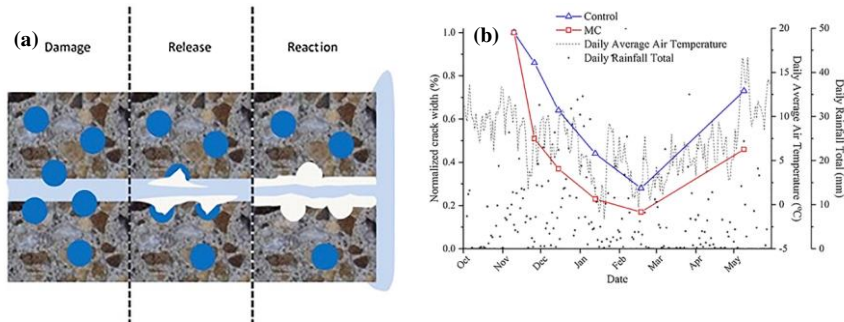


Figure 3

(a) A schematic of self-healing capsules, (b) crack width measurements throughout the 6-month period [44]

The long-term behavior of a new self-healing concrete material system was compared to that of regular reinforced concrete by Hazelwood *et al.* [45]. LatConX (LCX) is a revolutionary material system that combines reinforcing steel and shape memory polymer (SMP) tendons within a cementitious matrix. The tendons' shrinkage process is activated when a beam has been cast, cured, and loaded, providing a compressive force to the cementitious matrix. Long-term simulations demonstrate the LatConX system's potential effectiveness in minimizing fracture widths in reinforced concrete structural parts. However, when a polymer shrinkage stress of 100 MPa is used and 50% of the damage is healed, the results reveal that a 65% reduction is possible.

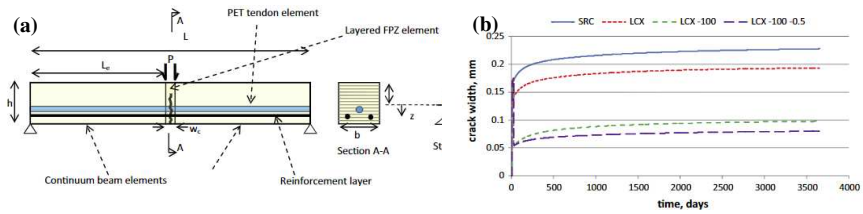


Figure 4

(a) A schematic of self-healing beam, (b) Long-term behavior simulations of LCX beam [45]

The fracture process in self-healing concrete with implanted brittle capsules was explored by Dai et al. [46]. The validated numerical model reveals that the ratio of capsule slenderness to concrete-capsule interface strength is a critical characteristic for a successful self-healing process since it allows complete control over when the capsule breaks. The longer the capsule is, the longer it will take to break. Furthermore, increasing the length of the capsules has been found to assist improve the overall fracture energy of the beam, even after it has been fully broken (Fig. 5).

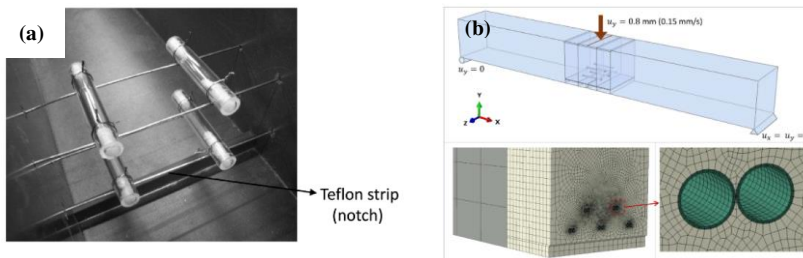


Figure 5

(a) An overview of tubes layout in the middle of beam, (b) schematic view of the healing tubes setup in numerical modeling [46]

Siahkouhi et al. [9] studied application of embedded different size PU tubes self-healing method to construct a self-healing railway sleeper. Final results showed that different size of PU tubes is needed in rail seat or middle of sleeper. Long tubes have a better performance in middle of sleeper and short tubes have a better performance in rail seat (Figure 6).

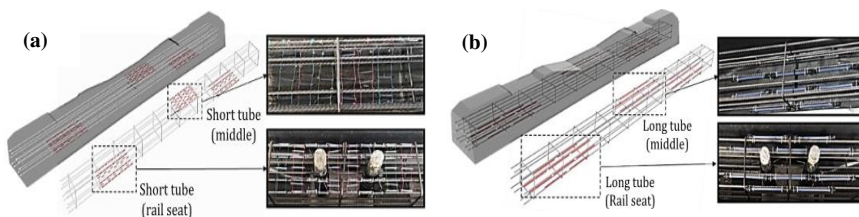


Figure 6

(a) short tubes at middle and rail seat, (b) long tubes at middle and rail seat of sleepers [9]

## **3 Compatibility of Self-Healing Methods for Sleeper Manufacturing**

### **3.1 Manufacturing Process**

In this section, differences between manufacturing of self-healing concrete and concrete railway sleepers are compared. Studying different methods through mix design, mixing and molding methods, and curing bring a bright overview of self-healing sleeper manufacturing.

#### **3.1.1 Mix Design**

By applying self-healing technology or incorporating the appropriate healing methods, concrete's ability to heal itself can be achieved and enhanced [47]. Typically, the conventional concrete mix design approach is used to calculate the self-healing concrete's mixing proportion [48]. However, some healing methods affects the concrete performance, for instance, rheological performance of fresh concrete decreases in presence of geo-materials with swelling characteristics or other small particle size materials such as micro and nano materials [49]. The mechanical properties of concrete may improve or degrade depending on the circumstance when mineral admixtures are employed as a partial replacement for cement, resulting in a small drop in cement content [50]. Concrete mechanical strength may suffer with the addition of capsules [51]. Water/cement (W/C) ratios of 0.3 to 0.37 are considered in concrete railway sleeper mix design, resulting in low flowability and slump tests of 7 to 9 cm [52]. A small change in the mix design for sleepers can make a major difference in flowability.

#### **3.1.2 Mixing and Molding Methods**

The features of freshly formed and cured cementitious composites are significantly influenced by the method, speed, and length of the mixing process, according to earlier studies [53]. The fluidity and strength of cementitious composites are decreased while the number of pores in the matrix is increased by faster and longer mixing durations [54]. So it's important to use the right mixing and dispersion techniques. The most typical method of mixing is to place materials in a mechanical mixer until they are homogeneous enough [55]. Self-healing components that are brittle should be inserted into cementitious composites by the end of mixing to prevent them from damaging during production [56]. Brittle self-healing materials may have reinforcing steel bars, metallic wires, or fibers which are added during fracture formation to delay premature failure and reduce crack width [57]. To prevent breaking, capsules need additional protection, especially while combining [58]. In particular, for micro and nanoparticles with large surface areas and fibrous fillers with high aspect ratios, uniform dispersion of healing materials is necessary

for significant self-healing capabilities [59]. Similar to conventional concrete, self-healing concrete can be molded. In order to obtain appropriate structural compaction, fresh concrete is frequently poured into molds in a number of layers, each of which is exposed to mechanical vibration [60]. Concrete railway sleeper consumes high amount of fresh concrete and has a high frequency vibration process. So in case of choosing self-healing method these parameters should be considered.

### 3.1.3 Curing

Water has been proven to be a critical component in improving self-healing performance in both autogenous and autonomous healing methods, and even high humidity is insufficient to ensure self-healing [34]. When pre-cracked mortars with mineral admixtures are dried in still water as opposed to flowing water, the permeability coefficient decreases more quickly and the crack width decreases more significantly. This is probably because flowing water eliminates calcium and hydroxide ions, reducing the pH and calcium ion concentration, both of which are necessary for the synthesis of healing products [61]. In terms of mechanical recovery, the water/air cycle curing method, followed by periodically renewed tap water, contributed to a superior self-healing performance of strain hardening cementitious composites [50]. Water curing compared with wet/dry cycles curing or wet curing, usually helps microbiological concrete in obtaining a greater fracture healing ratio [62]. Figure 7 shows how concrete railway sleepers are cured using steam and temperature. Maximum temperature increases to 90 °C for at least two days.

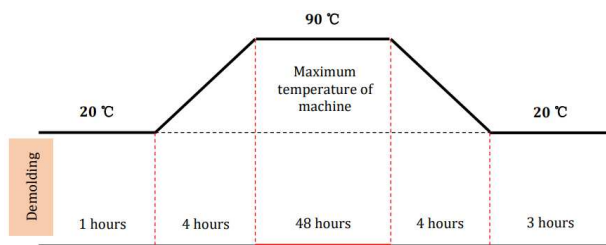


Figure 7  
concrete sleeper curing method [52]

## 3.2 Self-Healing Methods Discussion

Railway sleepers have been exposed to wear and weathering in a tough environment. Temperature, humidity, and other climatic conditions are highly variable in the region where sleepers are used, moreover, this structure is exposed to the sun without protection. As a result, this service condition precludes the use of several self-healing technologies, as shown in Table 3. Electrodeposition

technology, which involves conductors (conductive concrete), electricity, and electrolytes, is particularly well suited to repairing marine concrete structures. Concrete's self-healing tendency with SMA requires thermal stimulation, but that with capsules or vascular is usually activated by crack formation. However, both autogenous and autonomous healing processes are highly capable of fixing cracks that are in micrometers scale width. However, some methods may be suitable to manufacture self-healing sleepers which are discussed in the following sections.

Table 3

An overview of contradiction between self-healing methods and railway sleeper production

No.	Self-healing methods	Contradiction with railway sleeper manufacturing
1	mineral powder	These methods provide self-healing property by more hydration to close cracks, for sleepers this water cannot be provided externally, unless in rainy places. Furthermore, presence of nanomaterials may influence on concrete flowability, especially in case of sleeper concrete with low w/c. These methods mostly are used for microcracks but in case of sleepers their crack sometimes is opened in mm scale.
2	fibers	
3	nanofillers	
4	Curing agents	
5	mineral powder	
6	Electrodeposition technology	The existence of micro capsules may decrease mechanical performance of concrete. Moreover, they may damage during mixing and manufacturing concrete railway sleeper. Healing material captive in cargo inside of concrete should not be influenced by curing temperature of concrete sleepers. Bacteria is not suitable for concrete railway sleeper manufacturing as it has short lifespan and needs special growing environment.
7	Shape memory alloy embedded technology	
8	Capsule technology	
9	Vascular technolog	
10	Microbial technolog	

## 4 Future Prospective

### 4.1 Self-Healing Tubes

One of the method which can be used for self-healing concrete sleeper manufacturing is application of vascular methods such as long and short tubes that can provide enough amount of healing agent [63]. Sleepers are under dynamic loads that can enforce agents captive inside tubes to come out and cover crack zone due to a capillary effect which is the flow of a liquid through a confined space without the aid of external forces such as gravity.

## 4.2 Nano Materials

Application of nanomaterials such as carbon nano tubes (CNTs) can be an option to manufacture self-healing concrete sleeper [6], just in case that external water can be provided for sleepers. So this method is not suitable for a desert area. Moreover, convenient to heal microcracks in long time.

## 4.3 LatConX System

The system comprises cementitious beams with Unbonded pre-oriented polymer tendons. When hydration reaction starts due to the initial curing process, the crack is closed by thermally initiating the shrinking mechanism of the constrained polymer tendons [64].

### Conclusions

This study reviews the potential self-healing methods to manufacture a self-healing concrete railway sleeper. First, these methods are categorized and then they are compared with concrete railway sleeper manufacturing process, lifespan and loading condition. Autonomous self-healing methods are suitable for higher crack width than autogenous, but they depend on some inside triggers such as long and short tube PU encapsulation, micro capsules, LatConX system, bacteria etc. There are several parameters influence on application of self-healing methods to produce sleeper such as water that cannot be provided externally, unless in rainy places, presence of nanomaterials which may influence on concrete flowability, especially in case of sleeper concrete with low w/c, existence of micro capsules which decreases mechanical performance of concrete and they may damage during mixing and manufacturing, healing agents captive in cargo inside of concrete which should not be influenced by curing temperature, bacteria which has short lifespan and needs special growing environment. According to sleeper service condition, vascular method, LatConX system and application of nano materials can be suitable self-healing methods to manufacture self-healing sleeper. Although in a vascular method, high amount of healing agent should be supplied in fracture zone for crack healing.

### Acknowledgement

This paper has been supported by the Scientific research and development project of China Academy of Railway Sciences Corporation Limited (2020YJ117) .

### References

- [1] G. Jing, D. Yunchang, R. You, M. Siahkouhi, Comparison study of crack propagation in rubberized and conventional prestressed concrete sleepers using digital image correlation, Proceedings of the Institution of Mechanical Engineers, Part F: Journal of Rail and Rapid Transit (2021) 09544097211020595

- 
- [2] S. Fischer, D. Harangozó, D. Németh, B. Kocsis, M. Sysyn, D. Kurhan, A. Brautigam, Investigation of Heat-Affected Zones of Thermite Rail Weldings, *Facta Universitatis, Series: Mechanical Engineering* (2023)
- [3] J. Wang, M. Siahkouhi, F. Astaraki, S. Uuganbayar, G. Jing, M. Movahedi Rad, Modification of Concrete Railway Sleeper Mix Design, Using a Hybrid Application of Steel Fibers, *Acta Polytechnica Hungarica* 19(3) (2022) 119-130
- [4] G. Jing, M. Siahkouhi, K. Qian, S. Wang, Development of a field condition monitoring system in high speed railway turnout, *Measurement* 169 (2021) 108358
- [5] Z. Major, S. K. Ibrahim, M. M. Rad, A. Németh, D. Harrach, G. Herczeg, S. Szalai, S. Kocsis Szürke, D. Harangozó, M. Sysyn, Numerical Investigation of Pre-Stressed Reinforced Concrete Railway Sleeper for High-Speed Application, *Infrastructures* 8(3) (2023) 41
- [6] G. Jing, M. Siahkouhi, J. R. Edwards, M. S. Dersch, N. Hoult, Smart railway sleepers-a review of recent developments, challenges, and future prospects, *Construction and Building Materials* 271 (2021) 121533
- [7] L. Kou, M. Sysyn, J. Liu, Influence of Crossing Wear on Rolling Contact Fatigue Damage of Frog Rail, *Facta Universitatis, Series: Mechanical Engineering* (2022)
- [8] S. Szalai, B. Eller, E. Juhász, M. R. Movahedi, A. Németh, D. Harrach, G. Baranyai, S. Fischer, Investigation of deformations of ballasted railway track during collapse using the Digital Image Correlation Method (DICM), *Reports in Mechanical Engineering* 3(1) (2022) 168-191
- [9] M. Siahkouhi, X. Han, M. Wang, A. Manalo, G. Jing, Development and performance evaluation of self-healing concrete railway sleepers using different size PU tubes, *Engineering Structures* 283 (2023) 115920
- [10] M. Siahkouhi, X. Li, X. Han, G. Jing, Improving the Mechanical Performance of Timber Railway Sleepers with Carbon Fabric Reinforcement: An Experimental and Numerical Study, *Journal of Composites for Construction* 26(1) (2022) 04021064
- [11] C. Strzalka, M. Zehn, The influence of loading position in a priori high stress detection using mode superposition, *Reports in Mechanical Engineering* 1(1) (2020) 93-102
- [12] À. Palomo, A. Fernández-Jiménez, C. López Hombrados, J. L. Lleyda, Railway sleepers made of alkali activated fly ash concrete, (2007)
- [13] M. Esmaeili, M. Siahkouhi, Tire-derived aggregate layer performance in railway bridges as a novel impact absorber: Numerical and field study, *Structural Control and Health Monitoring* 26(10) (2019) e2444

- 
- [14] A. Németh, S. Fischer, Investigation of the glued insulated rail joints applied to CWR tracks, *Facta Universitatis, Series: Mechanical Engineering* 19(4) (2021) 681-704
- [15] K. Van Tittelboom, N. De Belie, Self-healing in cementitious materials—A review, *Materials* 6(6) (2013) 2182-2217
- [16] N. Ter Heide, Crack healing in hydrating concrete, *Delft University of Technology* 12 (2005) 82
- [17] W. Zhang, Q. Zheng, A. Ashour, B. Han, Self-healing cement concrete composites for resilient infrastructures: A review, *Composites Part B: Engineering* 189 (2020) 107892
- [18] S. Luhar, S. Gourav, A review paper on self healing concrete, *J. Civ. Eng. Res* 5(3) (2015) 53-58
- [19] S. Qian, J. Zhou, M. De Rooij, E. Schlangen, G. Ye, K. Van Breugel, Self-healing behavior of strain hardening cementitious composites incorporating local waste materials, *Cement and Concrete Composites* 31(9) (2009) 613-621
- [20] G. Yildirim, A. Alyousif, M. Şahmaran, M. Lachemi, Assessing the self-healing capability of cementitious composites under increasing sustained loading, *Advances in Cement Research* 27(10) (2015) 581-592
- [21] T.-H. Ahn, T. Kishi, Crack self-healing behavior of cementitious composites incorporating various mineral admixtures, *Journal of Advanced Concrete Technology* 8(2) (2010) 171-186
- [22] H. Siad, M. Lachemi, M. Sahmaran, H. A. Mesbah, K. A. Hossain, Advanced engineered cementitious composites with combined self-sensing and self-healing functionalities, *Construction and Building Materials* 176 (2018) 313-322
- [23] T. Nishiwaki, S. Kwon, D. Homma, M. Yamada, H. Mihashi, Self-healing capability of fiber-reinforced cementitious composites for recovery of watertightness and mechanical properties, *Materials* 7(3) (2014) 2141-2154
- [24] D. J. Kim, S. H. Kang, T.-H. Ahn, Mechanical characterization of high-performance steel-fiber reinforced cement composites with self-healing effect, *Materials* 7(1) (2014) 508-526
- [25] D. Snoeck, K. Van Tittelboom, S. Steuperaert, P. Dubruel, N. De Belie, Self-healing cementitious materials by the combination of microfibres and superabsorbent polymers, *Journal of Intelligent Material Systems and Structures* 25(1) (2014) 13-24
- [26] R. Henkensiefken, J. Castro, D. Bentz, T. Nantung, J. Weiss, Water absorption in internally cured mortar made with water-filled lightweight aggregate, *Cement and Concrete Research* 39(10) (2009) 883-892

- 
- [27] S. Zhutovsky, K. Kovler, A. Bentur, Effect of hybrid curing on cracking potential of high-performance concrete, *Cement and concrete research* 54 (2013) 36-42
- [28] V. T. B. BR, An Experimental Investigation of Self-Curing Concrete Incorporated with Light Weight Fine Aggregate and Polyethylene Glycol, *IJIRST–International Journal for Innovative Research in Science & Technology* 3(04) (2016) 116-122
- [29] H. Chu, L. Jiang, C. Xiong, L. You, N. Xu, Use of electrochemical method for repair of concrete cracks, *Construction and building materials* 73 (2014) 58-66
- [30] J.-K. Kim, J.-J. Yee, S.-H. Kee, Electrochemical Deposition Treatment (EDT) as a Comprehensive Rehabilitation Method for Corrosion-Induced Deterioration in Concrete with Various Severity Levels, *Sensors* 21(18) (2021) 6287
- [31] K.-J. Lee, J.-H. Lee, C.-Y. Jung, E. Choi, Crack-closing performance of NiTi and NiTiNb fibers in cement mortar beams using shape memory effects, *Composite Structures* 202 (2018) 710-718
- [32] D. J. Kim, H. A. Kim, Y.-S. Chung, E. Choi, Pullout resistance of deformed shape memory alloy fibers embedded in cement mortar, *Journal of Intelligent Material Systems and Structures* 27(2) (2016) 249-260
- [33] W. Du, R. Lin, Q. Liu, Investigation of isophorone diisocyanate microcapsules to improve self-healing properties and sulfate resistance of concrete, *Construction and Building Materials* 300 (2021) 124438
- [34] W. Li, Z. Jiang, Z. Yang, N. Zhao, W. Yuan, Self-healing efficiency of cementitious materials containing microcapsules filled with healing adhesive: Mechanical restoration and healing process monitored by water absorption, *PloS one* 8(11) (2013) e81616
- [35] J. Gilford III, M. M. Hassan, T. Rupnow, M. Barbato, A. Okeil, S. Asadi, Dicyclopentadiene and sodium silicate microencapsulation for self-healing of concrete, *Journal of Materials in Civil Engineering* 26(5) (2014) 886-896
- [36] M. Araújo, S. Chatrabhuti, S. Gurdebeke, N. Alderete, K. Van Tittelboom, J.-M. Raquez, V. Cnudde, S. Van Vlierberghe, N. De Belie, E. Gruyaert, Poly (methyl methacrylate) capsules as an alternative to the “proof-of-concept” glass capsules used in self-healing concrete, *Cement and Concrete Composites* 89 (2018) 260-271
- [37] C. Dry, Matrix cracking repair and filling using active and passive modes for smart timed release of chemicals from fibers into cement matrices, *Smart Materials and Structures* 3(2) (1994) 118
- [38] R. E. Davies, A. Jefferson, R. Lark, D. Gardner, A novel 2D vascular network in cementitious materials, (2015)
- [39] H. M. Jonkers, Bacteria-based self-healing concrete, *Heron*, 56 (1/2) (2011)
-

- [40] X. Wang, J. Xu, Z. Wang, W. Yao, Use of recycled concrete aggregates as carriers for self-healing of concrete cracks by bacteria with high urease activity, *Construction and Building Materials* 337 (2022) 127581
- [41] X. Zhang, Z. Jin, M. Li, C. Qian, Effects of carrier on the performance of bacteria-based self-healing concrete, *Construction and Building Materials* 305 (2021) 124771
- [42] X. Huang, S. Kaewunruen, Self-Healing and Highly-Damped Concrete for Applications as Railway Sleepers and Track Slabs, *Multidisciplinary Digital Publishing Institute Proceedings* 2(16) (2018) 1144
- [43] K. Van Tittelboom, J. Wang, M. Araújo, D. Snoeck, E. Gruyaert, B. Debbaut, H. Derluyn, V. Cnudde, E. Tsangouri, D. Van Hemelrijck, Comparison of different approaches for self-healing concrete in a large-scale lab test, *Construction and building materials* 107 (2016) 125-137
- [44] A. Al-Tabbaa, C. Litina, P. Giannaros, A. Kanellopoulos, L. Souza, First UK field application and performance of microcapsule-based self-healing concrete, *Construction and Building Materials* 208 (2019) 669-685
- [45] T. Hazelwood, A. D. Jefferson, R. J. Lark, D. R. Gardner, Numerical simulation of the long-term behaviour of a self-healing concrete beam vs standard reinforced concrete, *Engineering Structures* 102 (2015) 176-188
- [46] Z. Dai, E. Tsangouri, K. Van Tittelboom, X. Zhu, F. Gilabert, Understanding fracture mechanisms via validated virtual tests of encapsulation-based self-healing concrete beams, *Materials & Design* 213 (2022) 110299
- [47] M. Seifan, A. K. Samani, A. Berenjian, Bioconcrete: next generation of self-healing concrete, *Applied microbiology and biotechnology* 100(6) (2016) 2591-2602
- [48] A. Talaiekhosani, M. Z. Abd Majid, A review of self-healing concrete research development, *Journal of Environmental Treatment Techniques* 2(1) (2014) 1-11
- [49] S. Chuah, Z. Pan, J. G. Sanjayan, C. M. Wang, W. H. Duan, Nano reinforced cement and concrete composites and new perspective from graphene oxide, *Construction and Building materials* 73 (2014) 113-124
- [50] K. Sisomphon, O. Copuroglu, E. Koenders, Effect of exposure conditions on self healing behavior of strain hardening cementitious composites incorporating various cementitious materials, *Construction and Building Materials* 42 (2013) 217-224
- [51] A. Kanellopoulos, P. Giannaros, A. Al-Tabbaa, The effect of varying volume fraction of microcapsules on fresh, mechanical and self-healing properties of mortars, *Construction and Building Materials* 122 (2016) 577-593
- [52] J. Wang, M. Siahkouhi, F. Astaraki, S. Uganbayar, G. Jing, M. M. Rad, Modification of Concrete Railway Sleeper Mix Design, Using a Hybrid Application of Steel Fibers, *Acta Polytechnica Hungarica* 19(3) (2022)

- 
- [53] P. N. Hiremath, S. C. Yaragal, Influence of mixing method, speed and duration on the fresh and hardened properties of Reactive Powder Concrete, *Construction and Building Materials* 141 (2017) 271-288
- [54] J. Dils, G. De Schutter, V. Boel, Influence of mixing procedure and mixer type on fresh and hardened properties of concrete: a review, *Materials and structures* 45(11) (2012) 1673-1683
- [55] M. Şahmaran, S. B. Keskin, G. Ozerkan, I. O. Yaman, Self-healing of mechanically-loaded self consolidating concretes with high volumes of fly ash, *Cement and Concrete Composites* 30(10) (2008) 872-879
- [56] K. Van Tittelboom, N. De Belie, F. Lehmann, C. U. Grosse, Acoustic emission analysis for the quantification of autonomous crack healing in concrete, *Construction and Building Materials* 28(1) (2012) 333-341
- [57] B. Dong, G. Fang, W. Ding, Y. Liu, J. Zhang, N. Han, F. Xing, Self-healing features in cementitious material with urea–formaldehyde/epoxy microcapsules, *Construction and Building Materials* 106 (2016) 608-617
- [58] B. Hilloulin, K. Van Tittelboom, E. Gruyaert, N. De Belie, A. Loukili, Design of polymeric capsules for self-healing concrete, *Cement and Concrete Composites* 55 (2015) 298-307
- [59] M. Siahkouhi, G. Razaqpur, N. Hoult, M. H. Baghban, G. Jing, Utilization of carbon nanotubes (CNTs) in concrete for structural health monitoring (SHM) purposes: A review, *Construction and Building Materials* 309 (2021) 125137
- [60] A. Kanellopoulos, T. Qureshi, A. Al-Tabbaa, Glass encapsulated minerals for self-healing in cement based composites, *Construction and Building Materials* 98 (2015) 780-791
- [61] Z. Jiang, W. Li, Z. Yuan, Influence of mineral additives and environmental conditions on the self-healing capabilities of cementitious materials, *Cement and Concrete Composites* 57 (2015) 116-127
- [62] M. Luo, C.-x. Qian, R.-y. Li, Factors affecting crack repairing capacity of bacteria-based self-healing concrete, *Construction and building materials* 87 (2015) 1-7
- [63] K. Van Tittelboom, E. Tsangouri, D. Van Hemelrijck, N. De Belie, The efficiency of self-healing concrete using alternative manufacturing procedures and more realistic crack patterns, *Cement and concrete composites* 57 (2015) 142-152
- [64] A. Jefferson, C. Joseph, R. Lark, B. Isaacs, S. Dunn, B. Weager, A new system for crack closure of cementitious materials using shrinkable polymers, *Cement and Concrete Research* 40(5) (2010) 795-801

# Analytical Identification of Critical Section of Axle of Freight Wagon

**Milan Bižić, Dragan Petrović**

University of Kragujevac, Faculty of Mechanical and Civil Engineering in Kraljevo, Dositejeva 19, 36000 Kraljevo, Serbia  
bizic.m@mfkv.kg.ac.rs; petrovic.d@mfkv.kg.ac.rs

---

*Abstract: The paper deals with the analytical identification of the critical section of the axle of a freight wagon. The procedure for calculating the strength of railway axles in accordance with the European standard EN 13103 is shown. Based on this, a method for identifying the critical section of the axle was presented. The goal is to find the section or zone with the lowest dynamic safety factor. The proposed method was applied to a specific example of standard axle of freight wagon for an axle load of 22.5 tons. The obtained results have shown that the critical section is located in the zone of transition radius between the wheel-seat and the middle part of the axle. The obtained analytical results were verified by FEM calculation in the ANSYS software package. The results of the research presented in the paper may be interesting and should be considered for future design, optimization and standardization of axles of freight wagons.*

*Keywords: railway axle; freight wagon; critical section; EN 13103*

---

## 1 Introduction

The axles of railway vehicles are among the most responsible elements in the entire railway system. The quality of functioning and reliability of railway axles directly affects the safety and security on the railway. Failure of the railway axle in running very often leads to the derailment of a given railway vehicle and sometimes of a larger part or the whole train (one example is shown in Fig. 1) [1]. The consequences of these events are great direct and indirect material damage, and very often human casualties. Therefore, research on the problems of railway axles takes the one of the most important places in the railway engineering [2, 3].

Nowadays, there are many developed methods for analyzing and investigation the behavior of vital elements of railway vehicles and track [4-11]. Actual research on railway axles is primarily related to analyzing their behavior and characteristics as extremely dynamically loaded elements. Martínez-Casas et al. have investigated the numerical determination of the stresses of railway axles using the model of

interaction between the train and track [12]. In [13] and [14] Nikolov and Krishna Sudha *et al.* have studied the strength characteristics and design of locomotive axles. Xue *et al.* have analyzed the problem of assessing the reliability of axle of a freight wagon [15], while Dikmen *et al.* and Yasniy *et al.* have investigated the problem of estimating the lifetime of the railway axle [16, 17]. Given that railway axles belong to unsprung masses, the problem of reducing their weight is a constantly current topic. In [18] Han *et al.* have researched how to reduce the weight of axle of a city railway vehicle. Son *et al.* have studied the problems of designing a hollow railway axle [19]. In order to reduce unsprung masses, there are approaches to introduce new materials of wheels and axles. In this regard, Bruni *et al.* and Mistry *et al.* have studied the design of a railway axle made of composite material [20, 21].



Figure 1

Example of derailment of freight train caused by axle failure [1]

The aim of this paper is to establish an analytical method for identifying the critical section of the axle of a freight wagon. The main goal is to identify the cross-section of the axle with the lowest dynamic safety factor. In doing so, all relevant loads for axle calculation and its strength requirements are taken from the relevant international standard EN 13103 [22]. Lastly, the obtained analytical

results should be verified by numerical calculations using FEM, which are successfully used for a long time in the research of phenomena related to wheel and rail [23, 24].

## 2 Strength Calculation in Accordance with EN 13103

The European standard EN 13103 prescribes authoritative loads for the strength calculation of axles of railway vehicles. The scheme of loads for calculation is given in Fig. 2. The forces of action on the axle journals are [22]:

$$P_1 = \left( 0.625 + 0.075 \frac{h_o}{b} \right) m_1 \cdot g \quad (1)$$

$$P_2 = \left( 0.625 - 0.075 \frac{h_o}{b} \right) m_1 \cdot g \quad (2)$$

$$H \approx Y_1 - Y_2 \quad (3)$$

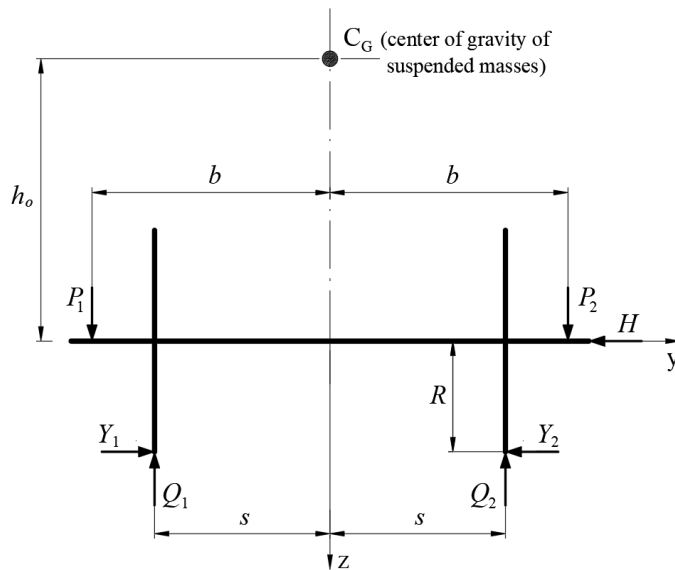


Figure 2

Scheme of loads for strength calculation of railway axles [22]

The reactive forces in the wheel-rail contacts are [22]:

$$Y_1 = 0.3 \cdot m_1 \cdot g \quad (4)$$

$$Y_2 = 0.15 \cdot m_1 \cdot g \quad (5)$$

$$Q_1 = \frac{1}{2s} [P_1(b+s) - P_2(b-s) + (Y_1 - Y_2) \cdot R] \quad (6)$$

$$Q_2 = \frac{1}{2s} [P_2(b+s) - P_1(b-s) - (Y_1 - Y_2) \cdot R] \quad (7)$$

In the previous expressions  $h_o$  is height of gravity center of suspended masses,  $b$  is half-distance between axle-box cases,  $s$  is half-distance between nominal rolling circles,  $R$  is wheel radius, and  $m_1$  is mass, which is defined as the difference between axle-load mass ( $m_{al}$ ) and wheelset mass ( $m_{ws}$ ):

$$m_1 = m_{al} - m_{ws} \quad (8)$$

The diagram of bending moments of the axle in the  $yz$  plane is given in Fig. 3.

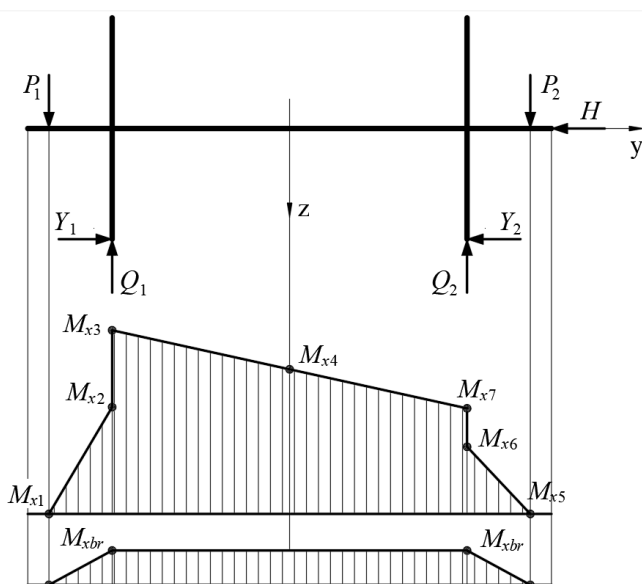


Figure 3

Diagram of bending moments of axle in  $yz$  plane

The bending moments in the plane  $yz$ , caused by the loads of axle defined in Fig. 1 are defined by the following expressions:

$$M_{x1} = 0 \quad (9)$$

$$M_{x2} = P_1(b-s) \quad (10)$$

$$M_{x3} = P_1(b-s) + Y_1 \cdot R \quad (11)$$

$$M_{x4} = P_1 \cdot b + Y_1 \cdot R - Q_1 \cdot s \quad (12)$$

$$M_{x5} = 0 \quad (13)$$

$$M_{x6} = P_2 (b - s) \quad (14)$$

$$M_{x7} = P_2 (b - s) + Y_2 \cdot R \quad (15)$$

The maximum bending moment in the plane yz, caused by the braking with shoe brake is defined by the following expression:

$$M_{xbr} = \mu \cdot 0.3 \cdot F_s (b - s) \quad (16)$$

where:  $\mu$  – friction coefficient between shoe and wheel,  $F_s = B_k \cdot P_w$  – braking force,  $B_k$  – braking coefficient,  $P_w = (m_1 + m_{ws}) \cdot g / 2$  – wheel static load.

The maximum bending moment in the plane xy (Fig. 4), caused by the braking is defined by the following expression:

$$M_{zbr} = 0.3 \cdot F_s (b - s) \quad (17)$$

The torsion moment of the axle (Fig. 4), caused by the braking is defined by the following expression:

$$M_{ybr} = 0.3 \cdot P_w \cdot R \quad (18)$$

In any axle cross-section, the equivalent stress  $\sigma_e$  must be less than or equal to permissible stress  $\sigma_{per}$ :

$$\sigma_e \leq \sigma_{per} \quad (19)$$

The equivalent stress is determined by the following expression:

$$\sigma_e = S_k \cdot \frac{32M_e}{\pi d^3} \quad (20)$$

where:

$$M_e = \sqrt{M_x^2 + M_y^2 + M_z^2} \text{ – equivalent moment in considered cross-section}$$

$d$  – axle diameter in considered cross-section

$S_k$  – stress concentration factor in considered cross-section

The stress concentration factor depends on the location of the considered cross-section and is defined by the expressions:

$$S_k = \frac{(4-Y)(Y-1)}{5 \cdot (10X)^{(2.5X+1.5-0.5Y)} + 1}; \quad X = \frac{r}{D}; \quad Y = \frac{D}{d} \quad (21)$$

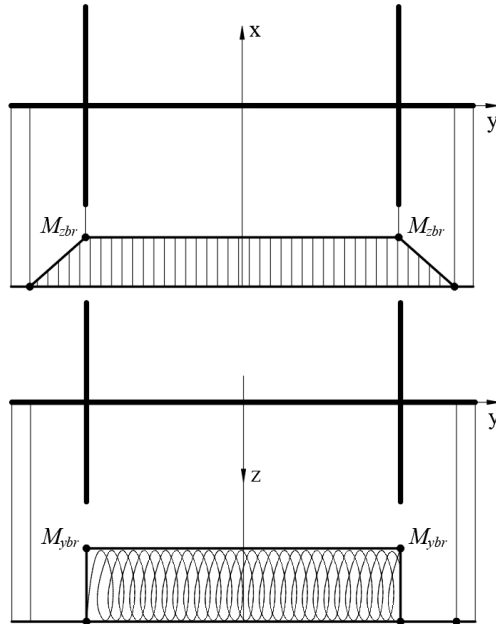


Figure 4

Diagram of bending moment of axle in xy plane and diagram of torsion moment of axle

The explication of parameters  $d$ ,  $D$  and  $r$  in expression (21) is given in Fig. 5.

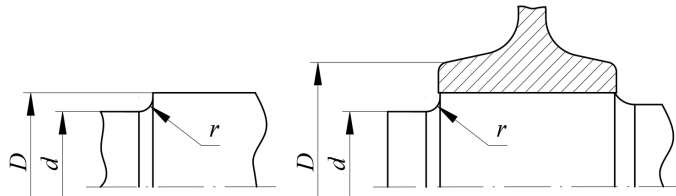


Figure 5

Explication of parameters  $d$ ,  $D$  and  $r$

The permissible stress is defined as the ratio between the endurance limit  $\sigma_N$  for a given axle material, and the safety factor  $s$ :

$$\sigma_{per} = \frac{\sigma_N}{s} \tag{22}$$

### 3 Analytical Identification of Critical Section

The subject of research is the standard axle of a freight wagon for an axle load of 22.5 tons, shown in Fig. 6. In order to perform analytical identification of critical section of the considered axle, five representative cross-sections S1-S5 for are selected for strength calculation. It is important to note that these cross-sections are selected in the places where pressed joints or transition radii between different diameters of the axle are present.

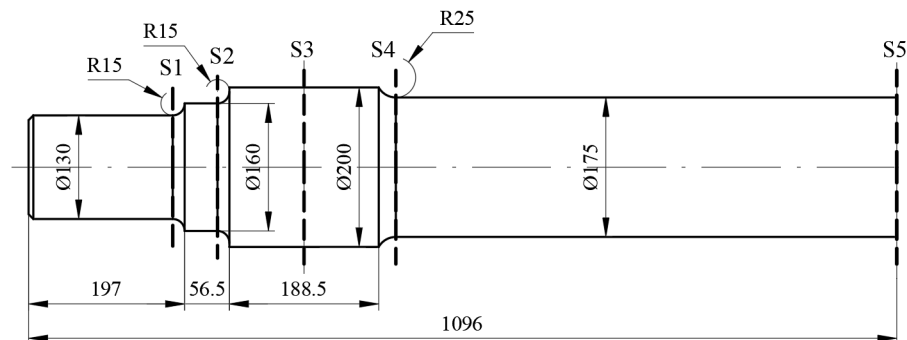


Figure 6

Subject of research – standard axle of a freight wagon for an axle load of 22.5 tons

The input parameters for the calculation of the strength of the considered axle are given in the Table 1.

Table 1  
Values of input parameters for calculation of strength of considered axle

$m_{al} = 22500$ kg	axle-load
$m_{ws} = 1074$ kg	wheelset mass
Axle material	EA1T
$h_o = 1900$ mm	height of center of gravity of suspended mass for loaded wagon
$2b = 2000$ mm	distance between axle-box cases
$2s = 1500$ mm	distance between nominal rolling circles
$D = 920$ mm	nominal wheel diameter

The obtained values of parameters for the determination of axle stresses, obtained on the basis of expressions given in the Chapter 2, are given in the Table 2.

The expressions for the determination of equivalent moments in considered cross-sections of the axle are:

$$M_{eS1} = \sqrt{\left(\frac{0.086 \cdot M_{x2} + 0.086 \cdot M_{xbr}}{0.252}\right)^2 + \left(\frac{0.086 \cdot M_{zbr}}{0.252}\right)^2} \quad (23)$$

$$M_{eS2} = \sqrt{\left(\frac{0.1425 \cdot M_{x2} + 0.1425 \cdot M_{xbr}}{0.252}\right)^2 + \left(\frac{0.1425 \cdot M_{zbr}}{0.252}\right)^2} \quad (24)$$

$$M_{eS3} = \sqrt{(M_{x3} + M_{xbr})^2 + M_{ybr}^2 + M_{zbr}^2} \quad (25)$$

$$M_{eS4} = \sqrt{\left(\frac{0.632 \cdot (M_{x3} - M_{x4})}{0.75} + M_{x4} + M_{xbr}\right)^2 + M_{ybr}^2 + M_{zbr}^2} \quad (26)$$

$$M_{eS5} = \sqrt{(M_{x4} + M_{xbr})^2 + M_{ybr}^2 + M_{zbr}^2} \quad (27)$$

Table 2

Obtained values of parameters for determination of axle stresses, obtained on basis of expressions given in Chapter 2

Parameter	Value	Parameter	Value	Parameter	Value
$m_1$ [kg]	21426	$M_{x1}$ [kNcm]	0	$B_k$	0.75
$P_1$ [kN]	161.32	$M_{x2}$ [kNcm]	4033	$F_s$ [kN]	82.77
$P_2$ [kN]	101.42	$M_{x3}$ [kNcm]	6933.76	$\mu$	0.1
$H$ [kN]	31.53	$M_{x4}$ [kNcm]	4009.63	$M_{xbr}$ [kNcm]	62.08
$Y_1$ [kN]	63.06	$M_{x5}$ [kNcm]	0	$M_{zbr}$ [kNcm]	620.78
$Y_2$ [kN]	31.53	$M_{x6}$ [kNcm]	2535.5	$M_{ybr}$ [kNcm]	1522.97
$Q_1$ [kN]	180.97	$M_{x7}$ [kNcm]	3985.88		
$Q_2$ [kN]	81.77	$P_w$ [kN]	110.36		

The obtained values of safety factors and equivalent moments in the considered axle cross-sections are given in the Table 3.

Table 3

Obtained values of safety factors and equivalent moments in considered axle cross-sections

Cross-section	Stress concentration factor $S_k$	Equivalent moment $M_e$ [kNcm]
S1	1.11	1413.49
S2	1.36	2342.13
S3	1.00	7186.56
S4	1.19	6739.52
S5	1.00	4391.32

Finally, the obtained values of equivalent stresses in considered axle cross-sections are given in the Table 4. The table also gives the values of endurance limits defined by [22] in considered axle cross-sections and safety factor as a ratio between endurance limit and equivalent stress.

The obtained results have shown that the most critical section of the considered axle is located in the zone of transition radius between the wheel-seat and the middle part of the axle (zone between cross-section S3 and S4 shown in Fig. 6).

Table 4

Obtained values of equivalent stresses, endurance limits and safety factors in considered axle cross-sections

Cross-section	Equivalent stress	Endurance limit	Safety factor
	$\sigma_e$ [kN/cm <sup>2</sup> ]	$\sigma_N$ [kN/cm <sup>2</sup> ]	$s$
S1	7.28	12	1.65
S2	7.93	12	1.51
S3	9.15	12	1.31
S4	15.25	20	1.31
S5	8.35	20	2.39

This result is in agreement with many cases of failures of railway axles that have occurred in the past, where the axles have fractured right in the identified zone [1, 25-27].

## 4 Verification of Analytical Results

The obtained analytical results were verified by FEM (finite element method) calculation in the ANSYS software package. The formed numerical model consists of the considered axle and a pair of wheels. The model is composed of 140359 finite elements and 233962 nodes (Fig. 7).

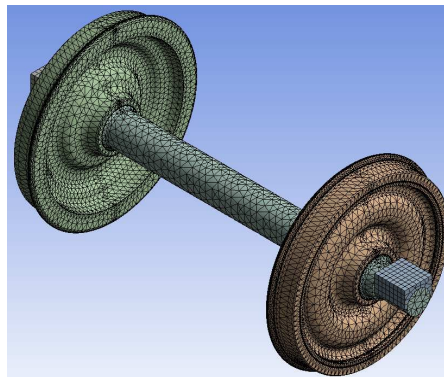


Figure 7

Numerical FEM model (140359 finite elements and 233962 nodes)

The obtained numerical results for the equivalent stresses of the axle in the considered cross-sections from Chapter 3 are shown in Fig. 8.

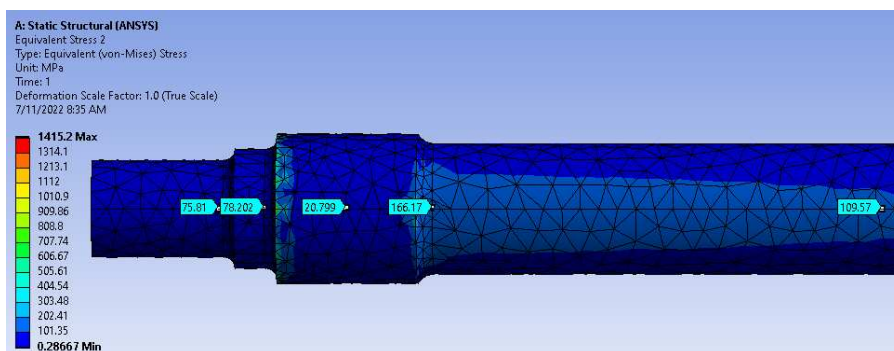


Figure 8

Obtained numerical results for equivalent stresses in considered cross-sections of axle

A comparative view of the equivalent stresses obtained by analytical and numerical way is given in Table 5.

Table 5

Comparative view of equivalent stresses obtained by analytical and numerical way

Cross-section	Analytical results $\sigma_e$ [kN/cm <sup>2</sup> ]	FEM results $\sigma_e$ [kN/cm <sup>2</sup> ]
S1	7.28	7.58
S2	7.93	7.82
S3	9.15	2.08
S4	15.25	16.6
S5	8.35	10.96

The obtained FEM results have shown good degree of agreement with the analytical results. There is only one exception in section S3, where the contact surface with the wheel is present in the numerical model. Therefore, a lower value of equivalent stress is obtained in this section. In general, it can be concluded that the analytical and numerical results are in agreement and that the analytically identified critical zone of the axle in chapter 3 is valid.

## Conclusions

The paper presents an analytical method for identifying the critical section of axle of a freight wagon. The method is based on the requirements of the European standard EN 13103 for axle strength. Analytical results for standard axle of freight wagons for an axle-load of 22.5 t have shown that the critical section is located in the zone of transition radius between the wheel-seat and the middle part of the axle. In this zone, the axle has the lowest safety factor of about 1.3, expressed as the ratio between the endurance limit and the equivalent stress. This result is in correspondence with many cases of failures of axles from exploitation that have broken just in the identified zone. The established analytical procedure was

verified by the results of FEM calculation, while the analytical and numerical results are in correspondence. The outcomes of the paper should be taken into account in the further design, optimization and standardization of axles of freight wagons.

### Acknowledgement

The authors wish to express their gratitude to Serbian Ministry of Education, Science and Technological Development for supporting this research (contract no. 451-03-68/2022-14/200108).

### References

- [1] Railway Investigation Report R04V0173: Main-track Train Derailment, Canadian Pacific, Train No. 823-957, Transportation Safety Board of Canada, 2004
- [2] S.D. Iwnicki: Handbook of Railway Vehicle Dynamics, Taylor & Francis, London, 2006
- [3] E. Andersson, M. Berg, S. Stichel: Rail Vehicle Dynamics. Railway Group KTH, Stockholm, 2007
- [4] D. Petrović, M. Bižić: Improvement of suspension system of Fbd wagons for coal transportation, Engineering Failure Analysis, 2012, 25, 89-96, doi:10.1016/j.engfailanal.2012.05.001
- [5] M. Bizic, D. Petrovic, Z. Djinovic, M. Tomic: Experimental Testing of Impact of Railway Wagons, Experimental Techniques, 2015, Volume 39, Issue 3, pp. 69-78, doi:10.1111/j.1747-1567.2012.00850.x
- [6] S. Fischer, D. Harangozó, D. Németh, B. Kocsis, M. Sysyn, D. Kurhan, A. Brautigam: Investigation of Heat-Affected Zones of Thermite Rail Weldings, Facta Universitatis, Series: Mechanical Engineering. 2023, doi: <https://doi.org/10.22190/FUME221217008F>
- [7] L. Kou, M. Sysyn, J. Liu: Influence of Crossing Wear on Rolling Contact Fatigue Damage of Frog Rail, Facta Universitatis, Series: Mechanical Engineering. 2022, doi: <https://doi.org/10.12700/APH.20.1.2023.20.15>
- [8] A. Németh, S. Fischer: Investigation of the glued insulated rail joints applied to CWR tracks, Facta Universitatis, Series: Mechanical Engineering, 2021, 19(4), 681-704, doi: <https://doi.org/10.22190/FUME210331040N>
- [9] C. Strzalka, M. Zehn: The influence of loading position in a priori high stress detection using mode superposition, Reports in Mechanical Engineering, 2020, 1(1), 93-102, doi: <https://doi.org/10.31181/rme200101093s>
- [10] S. Szalai, B. Eller, E. Juhász, M. R. Movahedi, A. Németh, D. Harrach, G. Baranyai, S. Fischer: Investigation of deformations of ballasted railway

- track during collapse using the Digital Image Correlation Method (DICM), *Reports in Mechanical Engineering*, 2022, 3(1), 168-191, doi: <https://doi.org/10.31181/rme20016032022s>
- [11] G. Miodragović, M. Bošković, R. Bulatović: The application of metaheuristic algorithms in multi-objective optimization of engineering problems, *Engineering Today*, 2022, Vol. 1, No. 3, doi: 10.5937/engtoday2203007M
- [12] J. Martínez-Casas, L. Mazzola, L. Baeza, S. Bruni: Numerical estimation of stresses in railway axles using a train–track interaction model, *International Journal of Fatigue*, 2013, 47:18-30, doi:10.1016/j.ijfatigue.2012.07.006
- [13] V. Nikolov: Influence of the traction force and the speed of movement on the strength characteristics of the locomotive axles, *IMK-14 – Research & Development in Heavy Machinery*, 2021, 27, 4, EN 125-133, doi:10.5937/IMK2104135S
- [14] S. Krishna Sudha, E. Raghavendra Yadav, S. D. V. V. S. B. Reddy: Design and harmonic analysis of locomotive wheel axle, *International Journal of Advance Research in Science and Engineering*, 2017, Volume 6, Issue 10, pp. 2595-2606
- [15] A.S. Xue, Y.X. Zhao, B.B. Du: Design reliability assessment on the railway wagon axle with 30 ton axle weight, *Advanced Materials Research*, 2013, 658:323-326 doi:10.4028/www.scientific.net/AMR.658.323
- [16] F. Dikmen, M. Bayraktar, R. Guclu: Railway Axle Analyses: Fatigue Damage and Life Analysis of Rail Vehicle Axle, *Strojniški vestnik – Journal of Mechanical Engineering* 58, 2012, 9, 545-552, doi:10.5545/sv-jme.2011.206
- [17] O. Yasniy, Y. Lapusta, Y. Pyndus, A. Sorochak, V. Yasniy: Assessment of lifetime of railway axle, *International Journal of Fatigue*, 2013, Volume 50, pp. 40-46, doi.org/10.1016/j.ijfatigue.2012.04.008
- [18] S. W. Han, S. W. Son, H. S. Jung: Weight reduction of an urban railway axle based on EN standard, *Transactions of the Korean Society of Mechanical Engineers*, 2012, A 36(5):579-590, doi:10.3795/KSME-A.2012.36.5.579
- [19] S. W. Son, H. S. Jung, S. Choi: Study on Design of Railway Hollow Axle, *Transactions of Korean Society of Automotive Engineers*, 2014, 22(4):46-54, doi:10.7467/KSAE.2014.22.4.046
- [20] S. Bruni, P. J. Mistry, M. S. Johnson, A. Bernasconi, M. Carboni, D. Formaggioni, G. Carra, S. Macchiavello, E. Ferrante, I. Kaiser, J. Viñolas, I. Marazzi: A vision for a lightweight railway wheelset of the future, *Proceedings of the Institution of Mechanical Engineers, Part F: Journal of Rail and Rapid Transit*, 2022, <https://doi.org/10.1177/09544097221080619>, in press

- [21] P. J. Mistry, M. S. Johnson, S. Li, S. Bruni, A. Bernasconi: Parametric sizing study for the design of a lightweight composite railway axle, *Composite Structures*, 2021, Volume 267, doi.org/10.1016/j.compstruct.2021.113851
- [22] EN 13103-1:2017+A1:2022 Railway applications - Wheelsets and bogies - Part 1: Design method for axles with external journals instead of EN 13103, *Railway applications – Wheelsets and bogies – Non-powered axles – Design method*, 2010
- [23] M. Milošević, A. Miltenović, M. Banić, M. Tomić: Determination of residual stress in the rail wheel during quenching process by FEM simulation, *Facta Universitatis - Series: Mechanical Engineering*, 2017, Vol. 15, No. 3, pp. 413-425, doi.org/10.22190/FUME170206029M
- [24] A. Miltenović, M. Banić, D. Stamenković, M. Milošević, M. Tomić, J. Bucha: Determination of friction heat generation in wheel-rail contact using FEM, *Facta Universitatis - Series: Mechanical Engineering*, 2015, Vol. 13, No 2, pp. 99-108
- [25] C. Klinger, D. Bettge, R. Häcker, T. Heckel, D. Gohlke, D. Klingbeil: Failure Analysis on a Broken ICE3 Railway Axle, Federal Institute for Materials Research and Testing, Working Group „Failure Analysis“, ESIS TC 24 Workshop, BAM Berlin, 11-12 October 2010
- [26] V. Grubisic, G. Fischer: Railway axle failures and durability validation, *Proceedings of the Institution of Mechanical Engineers, Part F: Journal of Rail and Rapid Transit*, 2012, Volume 226, Issue 5, pp. 518-529, doi.org/10.1177/0954409712442325
- [27] M. Bayraktar, N. Tahrali, R. Guclu: Reliability and fatigue life evaluation of railway axles, *Journal of Mechanical Science and Technology*, 2010, 24 (3), pp. 671-679, doi.10.1007/s12206-009-1219-1

## Nomenclature

Symbol	Meaning
$P_1, P_2$ [kN]	vertical forces on the axle journals
$H$ [kN]	lateral force on the axle journal
$Q_1, Q_2$ [kN]	vertical forces in the wheel-rail contacts
$Y_1, Y_2$ [kN]	lateral forces in the wheel-rail contacts
$h_o$ [cm]	height of gravity center of suspended masses
$b$ [cm]	half-distance between axle-box cases
$s$ [cm]	half-distance between nominal rolling circle
$R$ [cm]	wheel radius
$m_{al}$ [kg]	axle-load mass
$m_{ws}$ [kg]	wheelset mass
$M_x$ [kNcm]	bending moment in the plane yz
$M_{xbr}$ [kNcm]	bending moment in the plane yz caused by the braking

$\mu$	friction coefficient between shoe and wheel
$F_s$ [kN]	braking force
$B_k$	braking coefficient
$P_w$ [kN]	wheel static load
$M_{zbr}$ [kNcm]	bending moment in the plane xy caused by the braking
$M_{ybr}$ [kNcm]	torsion moment of the axle caused by the braking
$\sigma_e$ [kN/cm <sup>2</sup> ]	equivalent stress
$\sigma_{per}$ [kN/cm <sup>2</sup> ]	permissible stress
$M_e$ [kNcm]	equivalent moment
$d$ [cm]	axle diameter in considered cross-section
$S_k$	stress concentration factor
$\sigma_N$ [kN/cm <sup>2</sup> ]	endurance limit
$s$	safety factor

# Investigation of Empirical and Analytical Methods Accuracy for Surface Settlement Prediction in Train Tunnel Excavation Projects

**Ali Maroof<sup>1</sup>, Danial Mohammadzadeh S.<sup>2,3</sup>,  
Nader Karballaezadeh<sup>4\*</sup>, Kiarash Sabourian Bajgiran<sup>3</sup>,  
Amir Mosavi<sup>5\*</sup> and Imre Felde<sup>5</sup>**

<sup>1</sup> Faculty of Civil, Water, and Environmental, Shahid Beheshti University, 1983969411 Tehran, Iran; M\_marooof@sbu.ac.ir

<sup>2</sup> University of Applied Science and Technology, Education Center of Mashhad Worker's House, 9188945449 Mashhad, Iran; Danial.Mohammadzadehshadmehri@mail.um.ac.ir

<sup>3</sup> Department of Civil Engineering, Mashhad Branch, Islamic Azad University, 9187147578 Mashhad, Iran; D.mohammadzadeh.sh@mshdiau.ac.ir

<sup>4</sup> Faculty of Civil Engineering, Science and Research Branch of Islamic Azad University, 1477893855 Tehran, Iran; N.karballaezadeh@Shahroodut.ac.ir

<sup>5</sup> John von Neumann Faculty of Informatics, Óbuda University, Bécsi út 96/b, H-1034 Budapest, Hungary; Amir.mosavi@uni-obuda.hu, Felde@uni-obuda.hu

\* Corresponding Authors

---

*Abstract: Ground deformation, due to tunneling, is one of the most significant challenges in tunnel design in soft ground along with, the predicting the related effects of tunneling on nearby structures. One of the methods of predicting ground settlement in tunneling projects, is to use analytical and numerical methods. By measuring the amount of settlement with accurate instruments and back-analysis of behavioral measurement data, in addition to estimating the state of settlement of the ground and surrounding structures, it is possible to determine the geotechnical parameters of the soil and structure in the design of upcoming sections and future designs. In this study, an attempt has been made to verify the measured settlements caused by digging the tunnel of an urban train line, by using back analysis. For this purpose, comparisons with predictions obtained from empirical and analytical methods and the Geotechnical Engineering Finite Element Analysis software (PLAXIS) was used. The results show that often, the empirical methods obtain values more than the measured values, for ground settlement.*

*Keywords: Tunnel excavation; surface settlement; back analysis; PLAXIS; civil engineering; infrastructures; transportation; mobility*

---

# 1 Introduction

Displacements that occur in the ground, which are the result of tunneling activities in urban environments, is one of the most important challenges in digging shallow tunnels in soft ground that usually exists in urban areas is the problem of land settlement and its impact on the nearby urban structures and facilities [1]. Further, ground-borne vibrations from railway or tramway tracks can cause damage to nearby urban structures and facilities [2-6]. Reliable forecasting of the aforementioned displacements, to assess possible human-financial losses and consider protective measures to reduce the above risks, are very useful. The effects on nearby structures such as existing tunnels, deep foundations, and so on, depend on the extent of the surface settlement profile and its amount. The effects of this change of location on the surface and buried structures and their servicing should be checked and settlement should be prevented if necessary. Displacements resulting from tunnel excavation in the soft ground can be predicted by various methods, including experimental methods based on field measurements [7-10], empirical and semi-empirical methods [11-13], numerical models [1, 14, 15], and physical models [16]. In these relationships, parameters such as the tunnel properties and its depth, the ground conditions, and the amount of volume reduction or convergence caused by tunnel digging are effective. The amount of ground settlement, its direction, and location within the tunnel depend on geotechnical conditions, static stresses in the ground and loads on the surface, underground water conditions, tunnel excavation method, and the type of tunnel lining. The recorded data provides the possibility of comparing analytical methods with monitoring data and calibrating and validating the numerical methods [1].

One of the best methods for estimating the ground displacements in upcoming sections is the back analysis and numerical modeling of the monitoring values measured in similar conditions. Back analysis can approximate the cross-section of settlements with the Gaussian distribution curve [7], by fitting the monitoring data with the Gaussian curve parameters. In the present research, the observed settlements in the northern part of Mashhad city urban train line 2, are compared with the results of empirical and analytical relationships, as well as numerical modeling. Using the results of field measurements of ground settlements and back analysis, the required parameters for predicting the settlement in the next sections have been determined, and it will be possible to predict the settlement in similar future sections with a higher degree of confidence. This finding can provide new strategies for settlement prediction and deformation control methods.

## 2 Project Specifications

The Mashhad urban train line 2 has a length of 14.3 kilometers, a diameter of 9.4 meters, and a depth of between 10 and 23 meters. The soil layers are often fine-grained (*CL-ML*, USCS classification) up to a depth of 16 meters. From a depth of 16 to 25 meters, it is *SM* and the underground water level is in the depth is 22 meters, almost 3 meters below the lowest level of the tunnel. In Figure 1, the geometric situation of the tunnel placement in the ground layers, the dimensions of the tunnel, the type of the layers' material, and the underground water level are schematically shown [17]. In the first section of the tunnel excavation (northern part), nearly 300 meters long, more than 50 triple rows of settlement pins have been installed and measured. In this research, the settlement that occurred in this part was analyzed and compared with empirical relationships and numerical results.

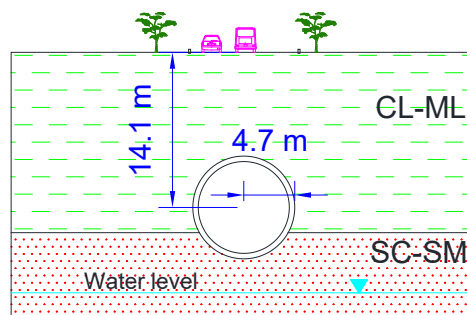


Figure 1

The cross-section of the ground profile and tunnel

## 3 Surface Ground Settlement Calculation

Reviewing the technical literature on the estimation of surface settlement resulting from tunnel excavation shows various analytical-empirical methods. In these methods, relationships have been presented that estimate the settlement profile at the surface and different depths of the ground. Although these methods are semi-empirical/semi-analytical and give an approximation of deformations, it must be noticed that these methods can be a quick and useful analysis for settlement approximation. In this part, the surface settlement and settlement parameters, including Gaussian curve inflection point, volume loss, and maximum settlement, were calculated using experimental relations and compared with the results obtained from the measured data in the subsequent section.

Peck showed that the ground settlement curve due to tunneling has a normal distribution curve [7]. The settlement profile is increased in depth and has the highest value on the central axis of the tunnel (Gaussian distribution curve) [18]. Based on the data obtained from the measurement of the ground surface settlement profile, the settlement is defined according to the following equation [7, 19].

$$S = S_{max} \times e^{\frac{-x^2}{2i^2}} \quad (1)$$

where  $S_{max}$  is the maximum settlement at the vertical tunnel centerline,  $x$  is the distance from the axis of the tunnel,  $i$  is the curvature point of the settlement curve. The trough width,  $i$ , is the distance from the center line of the tunnel to the inflection point of the curve. The total width of the settlement profile is approximately equal to  $5i$  [20].

The following empirical equation is also proposed by Attewell to estimate surface settlement [9]:

$$S = (V_s \times e^{\frac{-x^2}{2i^2}}) / \sqrt{2\pi} \quad (2)$$

In equation 2,  $V_s$  is equal to the total volume of ground surface settlement in one meter of tunnel length. The volume of the settlement curve per unit of tunnel length ( $V_s$ ) depends on the type of ground and the drilling method and is obtained from the integration of equation 1 [14]:

$$V_s = \sqrt{2\pi} i S_{max} \quad (3)$$

Another dimensionless parameter called volume loss or ground loss is defined, which is equivalent to the amount of contraction of the tunnel opening.  $V_L$  is the surplus volume (in terms of the theoretical volume of the excavated tunnel) of the dug ground and is calculated as the percentage of the volume of the settlement curve ( $V_s$ ) divided by the volume of the tunnel ( $V_t$ ) per unit length [14]:

$$V_L = \frac{V_s}{V_t} = \frac{\sqrt{2\pi} i S_{max}}{(\pi D^2 / 4)} \cong 0.319 K \left( \frac{Z_0}{D} \right) \left( \frac{S_{max}}{D} \right) \quad (4)$$

Where  $Z_0$  is the depth of the tunnel axis and  $D$  is the diameter of the tunnel. By combining the above equations and considering  $i = kZ_0$ , the following equation can be deduced, to obtain the  $S_{max}$  parameter:

$$S_{max} = \frac{0.313 V_L}{k Z_0} D^2 \quad (5)$$

In order to increase the accuracy of predicting settlements and deformations of the ground caused by tunneling, there is a need to choose the appropriate values of the mentioned parameters. Different methods of obtaining volume loss parameters ( $V_L$ ), the turning point of the settlement curve ( $i$ ), and maximum settlement ( $S_{max}$ ) are given in the following sections.

### 3.1 Determination of Ground Settlement Measurement Parameters

#### 3.1.1 Inflection Point Parameter ( $i$ )

The inflection point of the Gaussian curve,  $i$ , has been investigated by many researchers. O'Reilly and New proposed equation 6 to determine the inflection point ( $i$ ) in a tunnel with a depth of  $Z_0$  [8].

$$\begin{aligned} i &= 0.43Z_0 + 1.1 & 3 < Z_0 < 34 \text{ m} & \text{for cohesion soils} \\ i &= 0.28Z_0 - 0.1 & 6 < Z_0 < 10 \text{ m} & \text{for granular soils} \end{aligned} \quad (6)$$

Other equations presented by other researchers to determine the parameter  $i$  are given in Section 6.1.

#### 3.1.2 Volume Loss Parameter ( $V_L$ )

In addition to equation 4 which was presented to determine the volume loss, Loganathan and Poulos presented equation 7 to calculate volume loss in shield tunnels [10]. This equation is dependent on the free space parameter ( $g$ ) and it is obtained from the sum of three components related to the free space behind the tunnel cover resulting from the difference in the diameter of the tunnel cover and trail shield, the three-dimensional shape changes of the working chest and the quality of tunnel excavation.

$$\varepsilon_0 = V_L = \frac{\pi(R + 0.5g)^2 - \pi R^2}{\pi R^2} = \frac{4gR + g^2}{4R^2} \quad (7)$$

where  $\varepsilon_0$  and  $V_L$  are the volume loss value,  $R$  is the radius of the tunnel and  $g$  is the gap parameter, and it is obtained according to equation 8.

$$g = G_P + U_{3D}^* + \omega \quad (8)$$

where  $G_P$  is the free space outside the lining,  $U_{3D}^*$  is equivalent to the three-dimensional elastoplastic deformation of the tunnel face, and  $\omega$  is a value related to work skill. Due to the use of the EPB tunneling machine and the control of the deformations of the tunnel face,  $U_{3D}^*$  is assumed to be equal to zero. Also, the work skill parameter is assumed to be equal to zero. Regarding the injection of grout behind the tunnel lining with cement mortar,  $G_P$  is recommended to be assumed equal to 0.07 in the above formula [10].

Table 1 presents the result of volume loss calculations based on equations 7 and 8, taking into account the difference between the boring radius and the outer radius of the tunnel lining (without grout injection,  $\omega \cong 0.6G_P$ ) and the difference between the drilling radius and the lining radius (full injection) and also normal injection (7% space behind the segments).

Table 1  
Volume loss calculations based on the Loganathan and Poulos study

Conditions	$V_L(\%)$	$g(\text{m})$	$R(\text{m})$	$D(\text{m})$
No grout injection	3.66	0.17	4.55	9.1
Complete injection	0.18	0.01	4.55	9.1
Normal injection	0.25	0.01	4.55	9.1

### 3.1.3 Maximum Settlement ( $S_{\max}$ )

Assuming parameter  $i$  is equal to 6.75 meters and considering  $V_L$  equal to 0.5, 1, and 2%, the settlement curve is predicted using Peck's equation [7], and depicted in Figure 2.

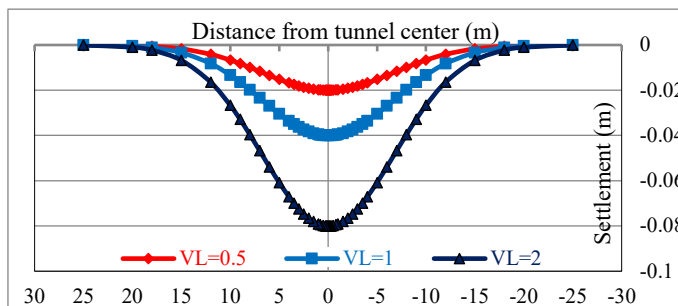


Figure 2  
Settlement curve based on Peck's equation

Further, Loganathan and Poulos proposed equation 9 to calculate ground settlement [10].

$$S_{z=0} = 4\varepsilon_0(1-\nu)R^2 \frac{H}{H^2 + y^2} e^{-\frac{1.38y^2}{(H+R)^2}} \quad (9)$$

where  $\varepsilon$  is the lost volume,  $\nu$  is Poisson's ratio of the soil above the tunnel,  $R$  is the radius of the tunnel,  $H$  is the depth of the tunnel, and  $y$  is the lateral distance from the tunnel axis. Using the volume loss calculated in section 3.1.2, equal to 0.018 by assuming full injection, and considering the tunnel axis, the maximum settlement is predicted according to Table 2.

Table 2  
Prediction of maximum settlement by Loganathan and Poulos's equation

$V_L$	$\nu$	$R(\text{m})$	$H(\text{m})$	$y(\text{m})$	$S_{z=0}(\text{m})$
0.02	0.35	4.55	14.1	0	0.068

Oteo and Moya also proposed equation 10 to estimate the top settlement of the tunnel (Sarch) [21].

$$S_{arch} = (\psi(0.85-v)\gamma D^2)/E \quad (10)$$

where  $\gamma$  is the density of the earth,  $D$  is the diameter of the tunnel,  $E$  is Young's modulus of the earth,  $v$  is Poisson's ratio, and  $\psi$  is a coefficient related to the activation speed of the support inside the tunnel (its values are generally between 0.25 and 0.5, but, for the case when there is no support in the tunnel face, it is equal to one), and  $S_{arch}$  is the settlement on the tunnel crest. The values of the maximum ground settlement based on equation 10 are presented in Table 3.

Table 3  
Prediction of maximum settlement by Oteo and Moya equation

NO.	$\psi$	$v$	$\gamma(\text{kN/m}^3)$	$D(\text{m})$	$E(\text{kN/m}^2)$	$S_{arch}(\text{m})$
1	0.25	0.35	18	9.4	35000	0.006
2	0.5	0.35	18	9.4	35000	0.011

Mair et al. proposed equation 11 to calculate ground settlement [20].

$$(\delta/a) = (s_u/2G)(a/r)e^{(N-1)} \quad (11)$$

where  $S_u$  is the undrained shear strength,  $G$  is the shear modulus,  $a$  is the inner radius of the tunnel,  $\delta$  is the radial displacement in radius  $r$ , and  $N$  is the stability ratio ( $\sigma_0 = S_u$ ). Using the above equation, the amount of vertical settlement on the ground surface in two saturated and unsaturated conditions is calculated and presented in Table 4.

Table 4  
Prediction of maximum settlement using Mair et al. equation

Conditions	$S_u(\text{kN/m}^2)$	$G(\text{kN/m}^2)$	$a(\text{m})$	$r(\text{m})$	$N$	$\delta/a$	$\delta(\text{m})$
Saturation	70	13000	4.2	14.1	3.6	0.011	0.045
non-saturated	100	22000	4.2	14.1	2.54	0.003	0.013

Gonzalez and Sagaseta proposed equation 12 relations for soils with cohesion and internal friction angle [22].

$$\varepsilon = \frac{1}{2}\varepsilon_s = \begin{cases} N_c/2I_t & \text{if } N_q < N_{qc} \text{ (elastic)} \\ (N_{cc}/2I_t)[(N_q/N_{qc})^{(1-\sin\phi\sin\theta)}/(\sin\phi(1-\sin\theta))] & \text{if } N_q > N_{qc} \text{ (elastic-plastic)} \end{cases} \quad (12)$$

where in:

$$N_{qc} = \frac{1}{1-\sin\phi}, N_{cc} = \frac{\cos\phi}{1-\sin\phi}, I_r = \frac{G}{(c + p_i \tan\phi)}, N_q = \frac{p_0 + c \cot\phi}{p_i + c \cot\phi}, N_c = (N_q - 1) \cot\phi$$

$p_0$  is the all-around stress of the earth (vertical and horizontal stress equal),  $p_i$  is the tunnel face pressure,  $c$  is the cohesion,  $\phi$  is the angle of internal friction,  $G$  is the shear modulus, and  $I_r$  is the hardness index. Using soil unsaturated parameters,  $N_{qc}$  is equal to 0.73 and in the case of applying a working chest pressure of more than 0.73 bar, it should be considered as the elastic state, and in the working face pressure less than 0.7 bar it should be used the elastoplastic relationship. The amount of

ground displacement has been calculated in two cases of tunnel face pressure equivalent to 1.8 bar (average working chest pressure during tunnel excavation) and without applying tunnel face pressure during machine failure and work stoppage (Table 5).

Table 5  
Prediction of maximum settlement by Gonzalez and Sagaseta equation

Excavator conditions	Soil conditions	$P_0$ (kN/m <sup>2</sup> )	$P_i$ (kN/m <sup>2</sup> )	$G$ (kN/m <sup>2</sup> )	$C$ (kN/m <sup>2</sup> )	$\phi$ (°)	$v$
With working chest pressure	non-saturated	273	180	22000	100	25	–
No chest pressure work	non-saturated	273	0	22000	100	25	0
Excavator conditions	Soil conditions	$N_c$	$N_{ce}$	$I_r$	$N_q$	$N_{qe}$	$\varepsilon$ (mm)
With working chest pressure	non-saturated	0.51	–	120	1.24	1.73	2
No chest pressure work	non-saturated	2.73	1.57	220	2.27	1.73	7

Chow also presented equation 13 to calculate vertical settlement [23].

$$S = -(\gamma D^2 Z_0^2) / 4G(y^2 + Z_0^2) \quad (13)$$

where  $\gamma$  is the density of the ground,  $D$  is the diameter of the tunnel,  $G$  is the shear modulus,  $Z_0$  is the depth of the tunnel and  $y$  is the distance from the tunnel axis. By using this equation, the settlement curve can be obtained at different distances from the tunnel axis. The maximum settlement on the crest of the tunnel is 18.13 mm according to Chow's relationship.

## 4 Field Measurement of Settlements

### 4.1 Observed Ground Surface Settlement

To measure and monitor the deformation of the earth's surface, a leveling method with an accuracy of one millimeter has been used. For this purpose, pins with a depth of about 120 cm in three rows with a longitudinal distance of 10 meters (5 meters in more sensitive sections) and a transverse distance (perpendicular to the path) of 5 meters, before the arrival of the drilling machine, were installed inside the ground and zero reading of their height has been done as a reference point. The position of the surface settlement gauge pins and the tunnel are shown in Figure 3 [24]. To prevent the influence of the surface layer of the earth, the mentioned pins are fastened upon the earth only in their lower 40 cm. In addition to these points,

the surface settlement near the existing structures around the tunnel (distance of 20 meters from the tunnel axis) has also been measured. The settlement recorded at these points was often zero.

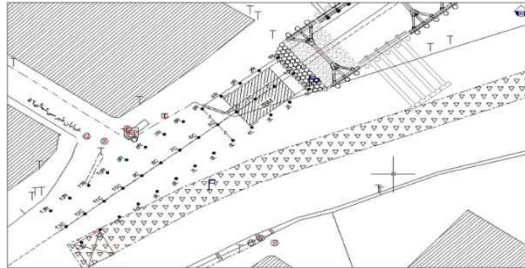


Figure 3

The position of the surface settlement gauge pins (L, C, R), tunnel route axis (a), street (b), residential area (d), and tunnel entrance (e)

All the information used in this paper is the result of reading the above mapping points. The results of the ground surface settlement in the center, left and right sides of the tunnel axis are presented in the diagram of Figure 4. This figure was extracted from [24] report. The settlement of the ground in the center of the tunnel is more than the points on the right and left sides of the tunnel, and the settlement in the points on the left and right sides is almost the same. Also, the settlement of the points, follows virtually the same process.

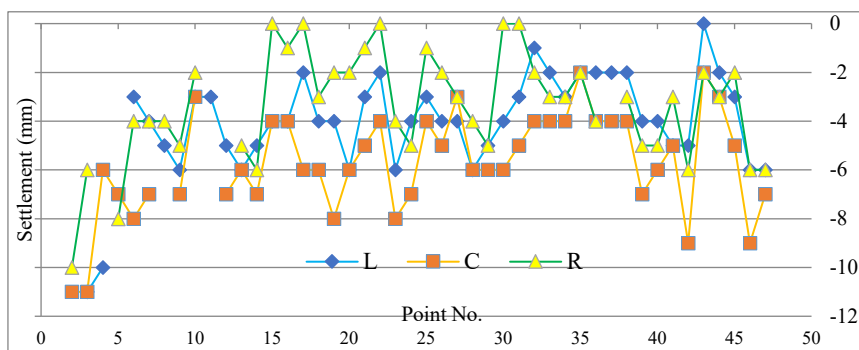


Figure 4

The measured settlement of the ground surface in the center, left, and right sides of the tunnel axis

## 4.2 Distribution of Settlement in the Longitudinal Section

In shield tunneling, the total ground settlement is caused by the following four stages [25]. Changing the shape of the front and top of the work front due to the release of tension (10 to 20%). This component will be a smaller amount in the case

of machines with the ability to apply pressure to the working face, such as EPB machines. Inductive displacements behind the shield (40 to 50%). These displacements are the result of additional drilling (the difference between the drilling diameter and the diameter of the shield), which is designed to reduce the friction between the shield and the ground, as well as the ease of angling and rotating the shield in curves. Settlement due to the space behind the segments resulting from the difference in the diameter of the tunnel cover and the tail skin (30 to 40%). These displacements can be reduced by grout injecting. Settlement over time caused by tunnel lining deformation and soil creep or consolidation (5 to 10%). The settlement distribution in the longitudinal profile for the excavated path is shown in Figure 5 extracted from [26]. About 12% of the settlement occurred before the arrival of the cutter head, 48% during the excavation, and 40% during the lining and subsequently.

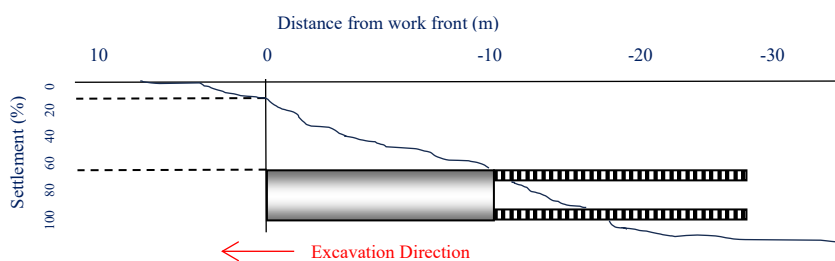


Figure 5

The distribution of the average settlement of the ground surface during tunnel excavation, with an earth pressure balanced shield (EPB)

### 4.3 The Settlement in the Cross-Section

Due to the presence of three surface settlement control pins, perpendicular to the longitudinal axis, in each row, the approximate transverse profile of the settlement curve can be drawn. The settlement curve of the ground surface for each row of pins is drawn in Figure 6.a, and in Figure 6.b. Further, the average settlement measured in cross-sections, the best adapted Gaussian distribution curve is shown. The ground settlement curve due to the tunnel excavation is in good agreement with the Gaussian curve (Equation 1).

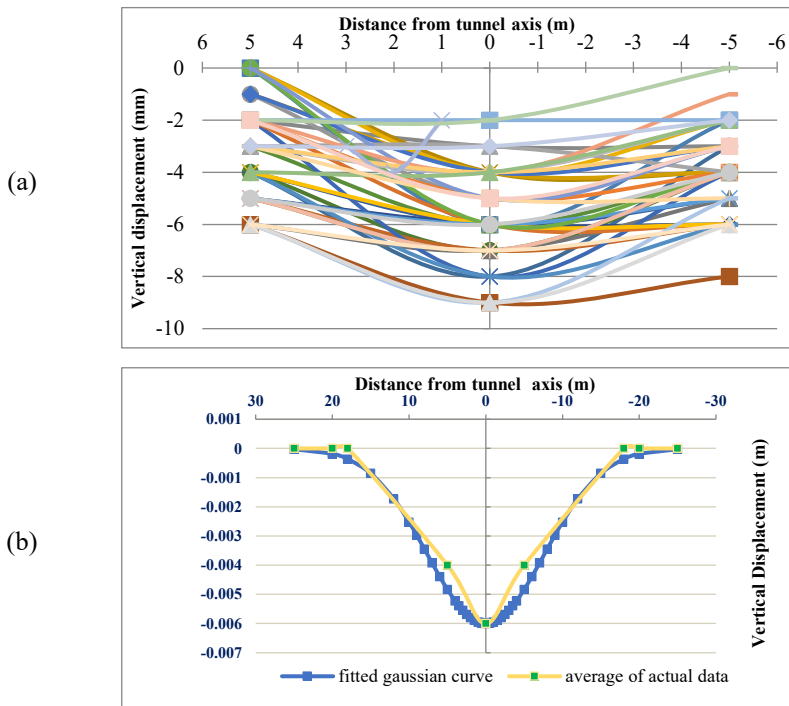


Figure 6

(a) Measured profiles of transverse surface settlement, (b) the average settlement of the ground surface in the cross-section, and the best-fitted Gaussian distribution curve

## 5 Back Analysis of the Settlement Parameters

Considering that the cross-section of settlements related to tunnel direction can be approximated by the Gaussian distribution curve (Equation 1). It is possible to use the equations related to the Gaussian curve to predict and back analysis of the settlement profile, using data obtained from field measurement. For this purpose, the inflection point of the Gaussian curve ( $i$ ) can be obtained with the second derivative of equation 1 and the volume loss parameter ( $V_L$ ) from equation 4. The maximum settlement ( $S_{max}$ ) using the measured data and the ratio of the inflection point to the tunnel depth,  $K$ , are obtained from the equation  $K = \frac{i}{z}$ . The graphs related to the back analysis of the inflection point parameters of the Gaussian curve ( $i$ ), volume loss ( $V_L$ ), maximum settlement ( $S_{max}$ ), and parameter  $K$  obtained by fitting the data with the Gaussian curve (equation 1) are shown in Figure 7. The average of these results is summarized in Table 6.

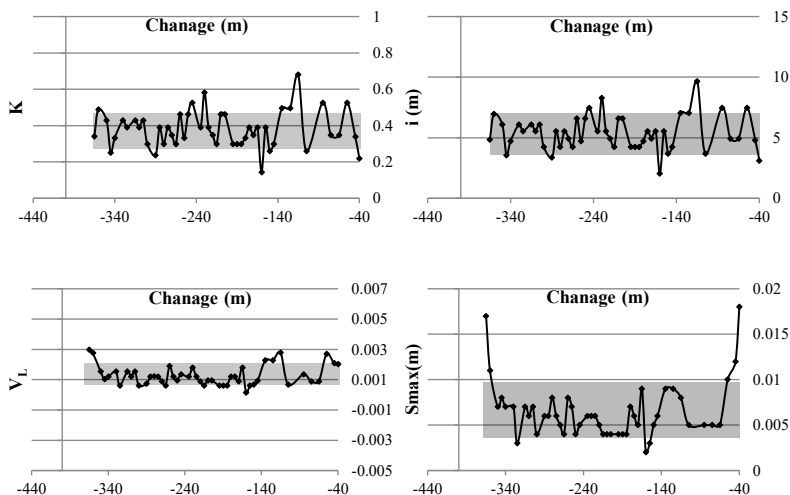


Figure 7

The parameters resulting from the back analysis of the Gaussian surface settlement curve

Table 6

The average results of the back analysis by adopting the Gaussian curve to the measured data

Component	$i$ (m)	$K$	$V_L$ (%)	$S_{max}$ (mm)
Value	5.4	0.39	0.1	6

## 6 Comparing the Analytical and Predicted Values

Now, according to the results obtained from the prediction of the various parameters of the settlement curve and compared with the values obtained from the analysis of the measured data, it is possible to predict the settlement of similar sections of the project. The comparison of the measured values of Gaussian curve inflection point parameters, maximum settlement and volume loss parameters with the values obtained from the experimental relations is given in the following sections.

### 6.1 Gaussian Curve Inflection Point ( $i$ )

The presented methods and the calculation values of parameter  $i$ , considering the tunnel depth ( $Z_0$ ) of 14.1 m and the tunnel radius ( $R$ ) of 4.7 m, based on the suggestions of different researchers are presented in Table 7. The parameter  $i$  is calculated by averaging the calculation values, equation 14 [1], whose value is suggested to be equal to 5.75.

$$i_{ave} = \frac{(\sum_{i=1}^n i)}{n} = 5.75 \quad (14)$$

Table 7  
Various equations for predicting the inflection point,  $i$

Equation	K	$i$ (m)	Reference
$(i/R) = (Z_0/2R)^n$ ( $n = 0.8$ to $1$ )	-	6.7 ~ 5	Peck (1969) [7]
$i = 0.43Z_0 + 1.1$	-	7.16	O'Reilly and New [8]
$(i/R) = (Z_0/2R)^{0.8}$	-	6.5	Clough & Schmidt [27]
According to the diagram	-	4.8 ~ 7.2	Boscardin and Cording [28]
$i = 0.25(1.5Z_0 + 0.5R)$	-	5.87	Atkinson & Potts [29]
$i = (0.4$ to $0.5)Z_0$	0 ~ 4.5	5.7 ~ 6	Mair & Taylor [20]
$i = 0.5Z_0$	0.5	7	Mair et al. [30]
$(i/R) = (Z_0/2R)^{0.8}$ ( $n = 1$ )	0.5	7	Attwell & Farmer [31]

According to the different methods for calculating the inflection point of the settlement curve in Table 7, the equations presented by Mair & Taylor (1993) and Atkinson & Potts (1997) have better agreement with the measured values.

## 6.2 Volume Loss Parameter ( $V_L$ )

The volume loss parameter,  $V_L$ , is calculated on the basis of the methods provided in Section 3.1.2, and the results are presented in Table 8.

Table 8  
Comparison of the volume loss suggested by different researchers with the measured value

Researcher(s)	Proposed $V_L$ (%)	Measured $V_L$ (%)
O'Reilly and New (1982) [8]	1-2	
Mair & Taylor (1993) [20]	1-2	
Mair (2008) [32]	>1	
Lunardi (2008) [33]	0.3	0.1
Loganathan and Poulos (1998) [10]	0.25	
Macklin (1999) [15]	0.4	

According to Table 8, the equations proposed by Lunardi (2008) and Loganathan and Poulos (1998) have a better fit than others.

## 6.3 Maximum Ground Settlement ( $S_{max}$ )

The results of calculating the maximum settlement with the methods presented in Section 3.1.3 are also presented in Table 9.

Table 9

Comparison of the maximum sitting suggested by different people with the observed value

Researcher(s)	Proposed $S_{max}$ (mm)	Real $S_{max}$ (mm)
Peck (1969) [7] - $V_L = 0.5$ %	20	
Oteo and Moya (1979) [21]	6	
Mair et al. (1993) [20]	13	6
Gonzalez and Sagaseta (2001) [22]	2	(2 ~ 10)
Loganathan and Poulos (1998) [10]	68	
Chow (1994)	18	

The equations proposed by Oteo and Moya (1979) and Mair et al. (1993) are closer to the average measured values.

## 7 Numerical Studies

Numerical Finite Element (FE) modeling is a useful tool for simulation and prediction of ground-induced deformation by tunneling. Using numerical methods, it is possible to calculate the distribution of stress and strain in the ground adjacent to the tunnel space due to the complex interaction between excavation and tunnel construction methods and the initial stress distribution, which often indicates inhomogeneous behavior. It is also possible to effectively consider the non-linear behavior depending on time or multi-stage construction.

### 7.1 Numerical Modeling

A numerical analysis of the tunnel construction was conducted to compare the measured tunneling-induced settlements with the calculated deformation of numerical modeling. According to geotechnical studies, the earth's materials are often lean clay with silt and silty sand. The input parameters to the model for the specifications of the equivalent soil layers and tunnel lining parameters are presented in Tables 10 and 11. A traffic and surcharge load is also equal to  $20 \frac{\text{kN}}{\text{m}^2}$  as a distributed load applied in the model.

Table 10

Engineering parameters of soil layers

Layer depth (m)	Soil	$\gamma_d$ (kN/m <sup>3</sup> )	Moisture (%)	Cohesion (kN/m <sup>2</sup> )	Internal friction	Elasticity modulus (kN/m <sup>2</sup> )	$\nu$	Undrained shear strength
0 ~ 16	CL-ML	15.5	20	35	25°	36000	0.35	100 kN/m <sup>2</sup>
16 ~ 25	SM	19	27	1	35°	64000	0.33	-

Table 11  
Specifications of the concrete segment of the tunnel lining

Description	$E$ (kN/m <sup>2</sup> )	$EA$ (kN/m)	$EI$ (kNm <sup>2</sup> /m)	$\nu$	$W$ (kN/m/m)
Concrete cover (segment)	35000000	12250000	125000	0.15	8.4

In this study, two-dimensional Plaxis software was used. Among the advantages of the mentioned software is the possibility of multi-stage construction and the use of various constitutive models [34]. The boundaries of the model in the horizontal direction from the center of the tunnel are considered to be five times the radius of the tunnel and in the vertical direction, two and a half times the radius of the tunnel. Deformation outside this range can be ignored. For the meshing of the model, the 15-node element was used as the basic element type, and according to the concentration of stress around the tunnel, the mesh was refined in these areas. Considering that during the two phases of digging and tunnel construction, the soil around the tunnel is loaded and the hardening soil model differentiates between pristine loading and loading-reloading, this behavior model can be used for tunnel modeling [35, 36]. Staged construction analysis is done according to the existing stresses, maintenance of the tunnel face during drilling with a shield, installation of the final segment, injection of the space behind the lining, and contraction to the tunnel cover. The initial stage is to model the initial equilibrium, and after the model reaches the equilibrium, the settlement becomes zero. The settlement in the next stages is measured relative to the initial stage. In the second stage, the tunnel is modeled by the machine, and the tunnel is uncovered. At this stage, the drilling machine has endured some load and  $\sum Mstage$  can be considered to be about 0.5 [35]. In the next step, the installation of the tunnel lining is modeled. The injection behind the segments can be modeled by applying a large load equivalent to the injection pressure (between 1.5 and 2 bar in the present study). The reduced volume is caused by the deformation of the tunnel lining, additional soil excavation (space behind the tunnel lining), and water drainage. In this study, the value of volume loss ( $V_L$ ) was determined based on the real data obtained from the surface settlement control ( $V_L = 0.1\%$ ) and applied in the numerical model.

## 7.2 Results

Calculation of the settlement with the numerical model shows that the maximum vertical settlement of the tunnel on the tunnel centerline and corresponding to the tunnel crest is equal to 9 mm and the settlement of the ground surface is 6 mm. The settlement curves of the ground are presented in Figure 8.

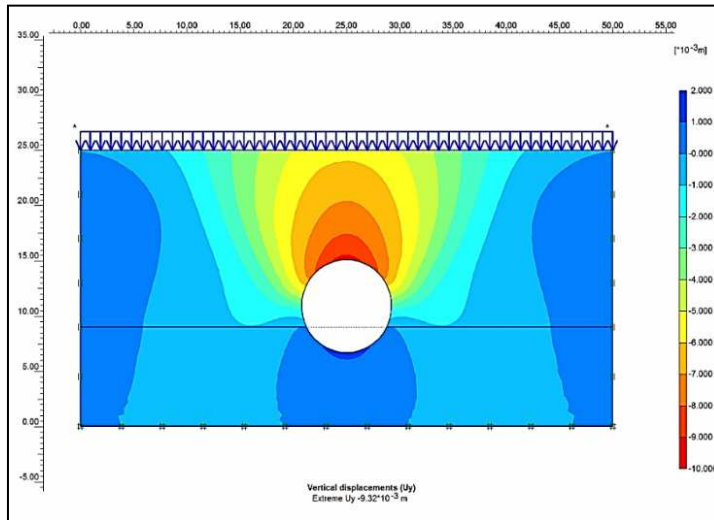


Figure 8  
Curves of vertical settlement of the soil mass

The ground surface settlement curve above the tunnel axis is close to the average real measured deformations, next to the fitted Gaussian curve to the measured data, and the curve resulting from the numerical models, are presented in Figure 9. The broader curve from the numerical model is a little wider than the Gaussian curve, that is, in this case, the trough width or distance from the center line of the tunnel to the inflection point of the curve (*i*) is greater. Although the total width of the settlement profile is often considered to be approximately equal to  $5i$ , in this study the total width of the settlement profile is about  $6i$  for numerical studies and about  $6.5i$  for the experimental equations and measured values.

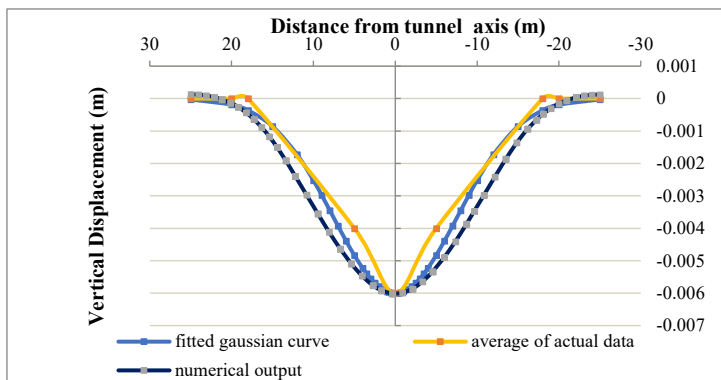


Figure 9  
Surface settlement curve obtained from measured values, results of the numerical model, and Gaussian distribution curve

## Conclusions

Among the many existing methods, through detailed comparison with the measured values, the most appropriate experimental and analytical relationships have been identified, for the prediction of the settlement parameters  $S_{\max}$ ,  $i$ ,  $V_L$ , etc. of the ground. The conclusions can be summarized as follows:

- The average maximum surface settlement that usually occurs on the ground above the tunnel centerline is equal to 6 mm.
- The average horizontal distance of the turning point of the settlement curve with the axis of the tunnel (parameter  $i$ ) is estimated to be about 5.4 meters. Therefore, the settlements of the tunnel in the transverse direction become insignificant at a distance of 15 meters (equivalent to  $3i$ ) and the structures outside it can be assumed to be safe.
- The average volume loss parameter ( $V_L$ ) has been calculated to be about 0.1% of the tunnel volume, which is less than the usual world experiences for soft ground.
- The back analysis with the numerical model shows that the trough width of the settlement curve obtained from the numerical studies is about 1 meter (20%) larger than the experimental curve (Gaussian curve fitted to the real data).
- By using the calibrated numerical model, it is possible to more accurately predict ground subsidence.

## Acknowledgment

This research was partially funded by the 2020-1.1.2-PIACI-KFI-2020-00129 project.

## References

- [1] Chakeri, H., Y. Ozcelik, and B. Unver, *Effects of important factors on surface settlement prediction for metro tunnel excavated by EPB*. Tunnelling and Underground Space Technology, 2013. **36**: p. 14-23
- [2] Kazemian, M., et al., *Effects of Wheel Surface Defects on Ground Borne Vibration*. Acta Polytech. Hung, 2022. **19**: p. 129-141
- [3] Fischer, S., *Geogrid reinforcement of ballasted railway superstructure for stabilization of the railway track geometry—A case study*. Geotextiles and geomembranes, 2022. **50**(5): p. 1036-1051
- [4] Jóvér, V., et al., *Investigation of the Geometrical Deterioration of Paved Superstructure Tramway Tracks in Budapest (Hungary)*. Infrastructures, 2023. **8**(8): p. 126
- [5] Jóvér, V., et al., *Investigation of “Open” Superstructure Tramway Tracks in Budapest*. Infrastructures, 2023. **8**(2): p. 33

- 
- [6] Fischer, S. and S.K. Szürke, *Detection process of energy loss in electric railway vehicles*. Facta Universitatis, Series: Mechanical Engineering, 2023. **21**(1): p. 081-099
- [7] Peck, R.B., *Deep excavations and tunneling in soft ground*. Proc. 7th ICSMFE, 1969, 1969: p. 225-290
- [8] O'REILLY, M.P. and B. New, *Settlements above tunnels in the United Kingdom-their magnitude and prediction*. 1982
- [9] Attewell, P., *Predicting the dynamics of ground settlement and its derivatives caused by tunnelling in soil*. Ground engineering, 1982. **15**(8): p. 13-22
- [10] Loganathan, N. and H. Poulos, *Analytical prediction for tunneling-induced ground movements in clays*. Journal of Geotechnical and geoenvironmental engineering, 1998. **124**(9): p. 846-856
- [11] Chou, W.-I. and A. Bobet, *Predictions of ground deformations in shallow tunnels in clay*. Tunnelling and underground space technology, 2002. **17**(1): p. 3-19
- [12] Pinto, F. and A.J. Whittle, *Ground movements due to shallow tunnels in soft ground. I: analytical solutions*. 2014
- [13] McCabe, B., et al., *Settlement trough parameters for tunnels in Irish glacial tills*. Tunnelling and underground space technology, 2012. **27**(1): p. 1-12
- [14] Wang, Z., et al., *Finite element analysis of long-term surface settlement above a shallow tunnel in soft ground*. Tunnelling and underground space technology, 2012. **30**: p. 85-92
- [15] Macklin, S., *The prediction of volume loss due to tunnelling in overconsolidated clay based on heading geometry and stability number*. Ground engineering, 1999. **32**(4): p. 30-33
- [16] Jiang, M. and Z.-Y. Yin, *Influence of soil conditioning on ground deformation during longitudinal tunneling*. Comptes Rendus Mecanique, 2014. **342**(3): p. 189-197
- [17] Mir Mehrabi, h.a.M., M. A., *Prediction and investigation of settlement caused by tunnel excavation by numerical method and comparison with measured values (In Persian)*, in *The 2nd Iran Dam and Tunnel Conference*. 2013: Tehran, Iran
- [18] Ter-Martirosyan, A.Z., et al., *Surface Settlement during Tunneling: Field Observation Analysis*. Applied Sciences, 2022. **12**(19): p. 9963
- [19] Ding, Z., et al., *Theoretical analysis on the deformation of existing tunnel caused by under-crossing of large-diameter slurry shield considering construction factors*. Tunnelling and Underground Space Technology, 2023. **133**: p. 104913

- [20] Mair, R., R. Taylor, and A. Bracegirdle, *Subsurface settlement profiles above tunnels in clays*. Geotechnique, 1993. **43**(2): p. 315-320
- [21] Oteo, C. and J. Moya. *Evaluación de parámetros del suelo de Madrid con relación a la construcción de túneles*. in *Proceedings of the 7th European Conference on Soil Mechanics and Foundation Engineering, Brighton*. 1979
- [22] González, C. and C. Sagaseta, *Patterns of soil deformations around tunnels. Application to the extension of Madrid Metro*. Computers and Geotechnics, 2001. **28**(6-7): p. 445-468
- [23] Chow, L., *The prediction of surface settlements due to tunnelling in soft ground*. M. Sc, 1994
- [24] Organization, M.S.L.T., *Analysis of Ground Settlements between North Shaft and Station A2 (in Persian)*. 2012
- [25] Leca, E. and B. New, *Settlements induced by tunneling in soft ground*. Tunnelling and Underground Space Technology, 2007. **22**(2): p. 119-149
- [26] Mirmehrabi, H., Maroof, A., *Prediction of surface subsidence of Mashhad city train line 2 tunnel: analytical methods and comparing with monitoring results (in Persian)*. Retrofit. Rehabil. Ind., 2014. **11**: p. 30-39
- [27] Clough, G.W. and B. Schmidt, *Design and performance of excavations and tunnels in soft clay*. 1981
- [28] Boscardin, M.D. and E.J. Cording, *Building response to excavation-induced settlement*. Journal of Geotechnical Engineering, 1989. **115**(1): p. 1-21
- [29] Atkinson, J. and D. Potts, *Subsidence above shallow circular tunnels in soft ground*. Journal of the Geotechnical Engineering Division, 1977. **103**(4)
- [30] Mair, R., M. Gunn, and M. O'reilly, *Ground movement around shallow tunnels in soft clay*. Tunnels & Tunnelling International, 1982. **14**(5)
- [31] Attewell, P. and I. Farmer, *Ground deformations resulting from shield tunnelling in London Clay*. Canadian Geotechnical Journal, 1974. **11**(3): p. 380-395
- [32] Mair, R. *Research on tunnelling-induced ground movements and their effects on buildings—lessons from the Jubilee Line Extension. Keynote Lecture*. in *Proceedings of International Conference on Response of Buildings to Excavation-induced Ground Movements, held at Imperial College, London, UK*. 2001
- [33] Lunardi, P., *Design and construction of tunnels: Analysis of Controlled Deformations in Rock and Soils (ADECO-RS)*. 2008: Springer Science & Business Media
- [34] Mohammadzadeh, D., et al. *Urban train soil-structure interaction modeling and analysis*. in *Engineering for Sustainable Future: Selected papers of the*

*18<sup>th</sup> International Conference on Global Research and Education Inter-Academia–2019 18*. 2020. Springer

- [35] Brinkgreve, R., et al., *2D–Version 8*. Delft, Delft University of Tehnology & PLAXIS bv, 2004. **18**
- [36] Mohammadzadeh, D., et al., *Three-Dimensional Modeling and Analysis of Mechanized Excavation for Tunnel Boring Machines*. Acta Polytech. Hung, 2021. **18**: p. 213-230

# Impact Assessment of Railway Bridge Construction Schedule, based on 3D Geotechnical Finite Element Modeling

**Edina Koch and Richard P. Ray**

Széchenyi István University, Department of Structural and Geotechnical Engineering, Egyetem tér 1, 9026 Győr, Hungary  
e-mail: koche@sze.hu, ray@sze.hu

---

*Abstract: The increasing demand for high-speed railways has risen, to solve the "age-old" problem of bridge abutments, the step between the backfill and the bridge deck. Examples prove that inadequate technical solutions can generate damage that may require long-term speed restrictions or lead to short maintenance cycles, significantly increasing the total cost of ownership. The problems associated with the transition zones require complex analysis. The complex interaction of structural elements with different stiffnesses and different dynamic behavior varies over time due to the time-dependent behavior of the soil, and in addition, a bridge deck and its connecting elements can be constructed in several sequences. This study investigated a typical single-span railway bridge and its soil environment using PLAXIS 3D geotechnical finite element software. Different constitutive soil models were used to approximate the behavior of the bridge and the connecting elements. To model the soil behavior, the HS-small constitutive model was implemented. Loads of the structure are transferred onto the subsoil by 60 cm diameter piles modeled as embedded piles. Six different construction schedules were analyzed using time-domain analyses. The importance of high-speed railways was highlighted, and a 250 km/h train speed was applied, using dynamic analysis. The study focuses on the effect of different construction schedules on settlement, consolidation time, the behavior of the transition, and the substructure movements. The results of this study show that geotechnical approaches by themselves are not enough to solve the problem of the transition zone, highlighting the collaboration of geotechnical, structural and railway engineers.*

*Keywords: numerical modeling; railway bridge; time effect; transition zone*

---

## 1 Introduction

Track or railway transitions are locations along the track characterized by an abrupt variation of their stiffness, such as rail tracks changing from stiff to soft structures or vice versa [1]. This abrupt change generates differential settlements and increased dynamic loading that expedites track degradation through the

progressive deterioration of track geometry and materials [2] [3]. The typical railway transition zone is the bridge approach that experiences sudden changes in track stiffness. Track structures on the embankment and bridge sides reveal different layer geometries and properties. Additionally, differential settlement of the foundation and unsupported ties have been found near bridge abutments [4]. These conditions significantly impact rider comfort and operational safety during operation. Railroaders have recognized that track geometry issues and differential movement at railway transitions present a significant challenge to track profile maintenance [5] [6]. The bump problem at the transition between the embankment and the bridge is an important concern for railways and highways. These bumps can lead to a rough riding surface, creating high-speed discomfort and high maintenance costs [7] [8]. Transitions should provide a gradual stiffness variation.

At the bridge abutments, the stiffness of the rail support suddenly changes, causing vertical accelerations in the passing vehicle and additional stresses on the rail. Even after a short period, the sum of these stresses leads to residual deformations in the substructure that degrade the track geometry [9].

According to the European Rail Research Institute [10], the factors that affect the behavior of the track in transition zones can be separated into four groups: (1) external to the track (axle loads, weather conditions, speed, and vibrations), (2) geotechnical issues (sub-grade and soil conditions), (3) structural conditions (bending stiffness, lateral movements and interaction between track and bridge) or (4) related to the track design and layout (stiffness, location of track dilation devices or presence of continuous welded rail).

Several different solutions for transition zones have been proposed and applied. These transitions smooth the stiffness variation between the "flexible" approach section and the "rigid" section over the structure. Transitions based on smoothing the stiffness variation on the "flexible" side include:

- Using oversized sleepers or changing their spacing
- Installing underlayments of hot-mix-asphalt, geotextiles, or soil-cement
- Adding rails, approach slabs, and others [5] [11]

Transitions based on lowering the stiffness on the "rigid" section include:

- Placing soft rail pads under sleeper pads
- Installing plastic sleepers
- Laying down ballast mats [12] [13]

According to Li and Davis [5], transition zones must address the specific stiffness issues of the track discontinuities to be effective. The behavior of the railway track and infrastructure under the combination of high speed and repetitive axle loadings evolves due to a complex soil-structure interaction problem that challenges geotechnical and structural R&D [14].

Many numerical studies have focused on the influence of the vertical stiffness variation on this problem [15-17]. However, few have addressed a more critical aspect: Differential settlement's impact and long-term development [18] [19]. Intrinsically, the complex interaction of structural elements with different stiffnesses and different dynamic behavior varies over time due to the time-dependent behavior of the soil. In addition, a bridge abutment and its approaching elements can be constructed in different sequences, and therefore the nature and direction of the interactions can vary. Time is perhaps the most critical factor in analyzing the interactions between abutments and bridges [20].

In current practice, bridge designers calculate the internal forces of the superstructure with structural finite element software. This technique usually separates the analyses of the superstructure, substructure, and specific aspects of the foundation. Generally, the superstructure software models the foundation and the soil environment by linear springs and replaces the backfill with an external load [21]. Such a model only crudely approximates the actual soil-structure interaction behavior. Moreover, superstructure designers usually ignore the effects of the construction sequence and time-dependent processes such as soil consolidation [22]. Modern three-dimensional geotechnical FEM packages can model the behavior of the soil more realistically by applying advanced constitutive models. They can consider drainage, initial stress conditions, unloading-reloading phases, and soil-structure interaction. For dynamic behavior, linear or non-linear time history analyses allow investigating wave propagation phenomena in the subsoil and their effects on the structure [23].

This paper presents a model and simulation results of a typical single-track railway bridge and its soil environment. This research investigated the effect of different construction schedules, focusing on the settlement, consolidation time, transition behavior, and substructure movements.

## **2 Methodology of Modeling**

### **2.1 The Bridge and its' Soil-Environment**

The basic model of the bridge and connecting longitudinal section of the open track appear in Figure 1. The typical soil environment generates a time-critical analysis for the construction schedule. A 10 m thick soft, medium plasticity clay layer overlays a 10 m thick saturated sand layer. The groundwater level lies at the surface of the upper layer. The dense sand embankment measures 5.3 m high with a 1:1.5 slope. The 15 m long backfill on the crest, lying behind the bridge abutments, was "built-up" from very dense sand. The effective thickness of the embedded ballast is 0.35 m.

The height of the bridge abutments aligns with the embankment, and parallel wing walls connect to them. Piles support the abutments, arranged in 2 rows of 3 piles, each with a center-center separation of 2.4 m. The piles measure 0.6 m-diameter and 11.2 m long. The software models the piles as embedded beam elements, typical for this problem [22]. Data from load tests and past performance determine the values of soil skin friction and toe resistance. The pile caps, bridge abutments, wing walls, and superstructure consist of concrete solid elements with a Young's modulus of  $E=30$  GPa. The superstructure was constructed with steel support and railway bedding, with an opening of 15.6 m. To model the soil-structure interaction, interface elements were placed behind the abutment and the wingwalls,  $R_{inter}=0.8$  were applied for the backfill. Based on several numerical modeling of pile load test,  $R_{inter}=0.95$  was used for subsoil [22]. The model represented an integral bridge with rigid connections between the abutment and superstructure [24] [25]. The monolithic assembly of integral bridges eliminates the need for expansion joints and bearings [26].

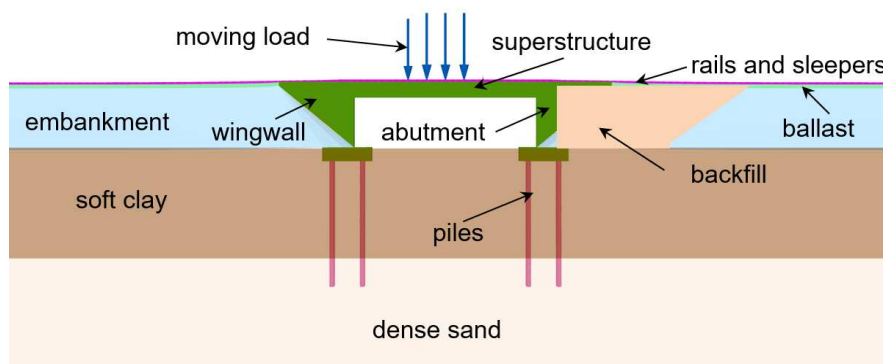


Figure 1

PLAXIS 3D model of the bridge and its soil environment

Beam elements represent rails with flexural and tensile rigidity based on their cross-section (60E1). The prestressed reinforced concrete sleepers (B70 type) are also modeled as beam elements with an adequate moment of inertia and cross-section. Table 1 lists input properties for the rails and sleepers. The sleepers were positioned in the model with a spacing of 60 cm intervals.

To analyze the effect of the model depth, 15 m, 20 m, and 25 m was investigated. For the selection of the applied model, the applied criteria for the incremental displacement was 1.0 mm. After the analysis, the overall model dimensions measure 96 m long, 75 m wide, and 20 m deep. The model contained 38466 elements and 62482 nodes with a mesh size of 2 m. Standard fixities and energy-absorbing boundaries reduced wave reflections in the domain.

The Hardening Soil model with small strain stiffness (HS-small) constitutive model was used to describe the soil behavior [27]. The input parameters for the medium-dense embankment and the dense backfill were determined based on [28]. Previous research provided properties of typical Hungarian soft clay [29] [30]. The ballast layer was modeled as elasto-plastic with Mohr-Coulomb yield parameters [31]; the reinforced concrete elements (pile cap, wing wall, bridge abutment) used a Linear Elastic model. The Poisson's ratio was  $\nu = 0.2$  for all layers, as recommended by PLAXIS [23]. Similar to [31], static E moduli were applied for the different soil types. The geotechnical properties of soil layers appear in Table 2.

Table 1  
Input parameters of rail and sleeper

Parameter	Sleeper B70	Rail 60E1
$A$ (m <sup>2</sup> )	0.0513	0.0077
$\square$ (kN/m <sup>3</sup> )	25	78
$E$ (GPa)	36	200
$I_3$ (m <sup>4</sup> )	0.0253	0.00003
$I_2$ (m <sup>4</sup> )	0.00024	0.00000513

Table 2  
Geotechnical properties of the layers

Parameter		Subsoil	Subsoil	Embankment	Backfill	Ballast
		Dense sand	Soft clay	Medium dense sand	Dense sand	Gravel
Model		HS-small	HS-small	HS-small	HS-small	MC
$E$	MPa					100.00
$E_{50}^{\text{ref}}$	MPa	51.00	6.00	36.00	48.00	
$E_{\text{oed}}^{\text{ref}}$	MPa	51.00	4.80	36.00	48.00	
$E_{\text{ur}}^{\text{ref}}$	MPa	153.00	24.00	108.00	144.00	
$G_0^{\text{ref}}$	MPa	117.80	40.00	100.00	114.40	
$m$	-	0.43	0.80	0.51	0.45	
$\square_{d,7}$	-	1.15E-4	2.5E-4	1.4E-4	1.2E-4	
$c'_{\text{ref}}$	kPa	1.00	30.00	1.00	1.00	10.00
$\square'_{\text{ref}}$	deg	39.00	25.00	35.50	38.00	40.00
$\psi$	deg	9.00		5.50	8.00	10.00
$k$	m/day	2.00	2E-4	1.00	2.00	10.00

## 2.2 The Construction and Load Phases

As mentioned, a bridge construction process could have various construction and loading phases due to different constraints or goals. The variants may have advantages and disadvantages regarding the construction time, the costs, and the displacements threatening the structure. Six different construction methods and schedule variants were chosen for analysis from many different options. In all variants, five construction stages were identical but occurred in different sequences for each variant:

1. Pile and abutment installation (also with deep mixing or vertical drains) duration of 10 days, always preceded Bridge Superstructure.
2. Bridge Superstructure 10 days.
3. Lower Embankment (0.0-2.6 m) 10 days, sometimes followed by consolidation time to 90% pore pressure reduction.
4. Upper Embankment (2.6-5.3 m) 10 days, sometimes immediately after Lower Embankment, always followed by consolidation time to 95% pore pressure reduction.
5. Ballast 10 days, Sleepers and Rails 10 days, Train Loading (always the final three stages in sequence).

Note that the consolidation stages were not precisely the same duration since the embankment sequence occurred at different times, either consecutively, or with other activities scheduled between the placement of the lower and upper portions. The consolidation stages' duration depended entirely on the average pore pressure reduction within the soil.

Each variant uses a slightly different sequence of construction in order to study their effect on the settlement and performance of the embankment and bridge. The six variants are listed below:

- Variant 1. Piles and Abutment, Bridge Superstructure Lower Embankment, 90% Consolidation, Upper Embankment, 95% Consolidation, Ballast, Sleepers and Rails, Train
- Variant 2. Piles and Abutment, Lower Embankment, 90% Consolidation, Upper Embankment, 95% Consolidation, Bridge Superstructure, Ballast, Sleepers and Rails, Train
- Variant 3. Lower Embankment, Rest Period of 60 days, Upper Embankment, Piles and Abutment, Bridge Superstructure, Backfill, 95% Consolidation, Ballast, Sleepers and Rails, Train

- Variant 4. Piles and Abutment, Lower Embankment, 90% Consolidation, Bridge Superstructure, Upper Embankment, 95% Consolidation, Ballast, Sleepers and Rails, Train
- Variant 5. Deep Soil Mixing, Piles and Abutment, Bridge Superstructure, Lower Embankment, Upper Embankment, 95% Consolidation, Ballast, Sleepers and Rails, Train
- Variant 6. Vertical Drains, Piles and Abutment, Bridge Superstructure, Lower Embankment, Upper Embankment, 95% Consolidation, Ballast, Sleepers and Rails, Train

Variants 5 and 6 require less consolidation time since the soft clays are stabilized by deep mixing or dissipate pore pressure more efficiently with vertical drains.

The consolidation stages use typical time-dependent behavior with coupled stress and pore pressure changes. The final train loading stage is a dynamic calculation.

The deep-mixing ground improvement was modeled as such: the improved material was regarded as a Linear Elastic model with  $E=30$  MPa young modulus and much higher permeability,  $k=8.6 \cdot 10^{-2}$  m/day. It can result from a cement or lime treatment carried out approximately in a  $3.0 \times 3.0$  m, 60 cm diameter raster and 10 m length column [32]. The raster of the vertical drains is  $2.0 \times 2.0$  m, and the length is bedded 1.0 m into the lower sand.

Figure 3 presents sketches showing the sequence of placement for the main components of the bridge and its soil environment.

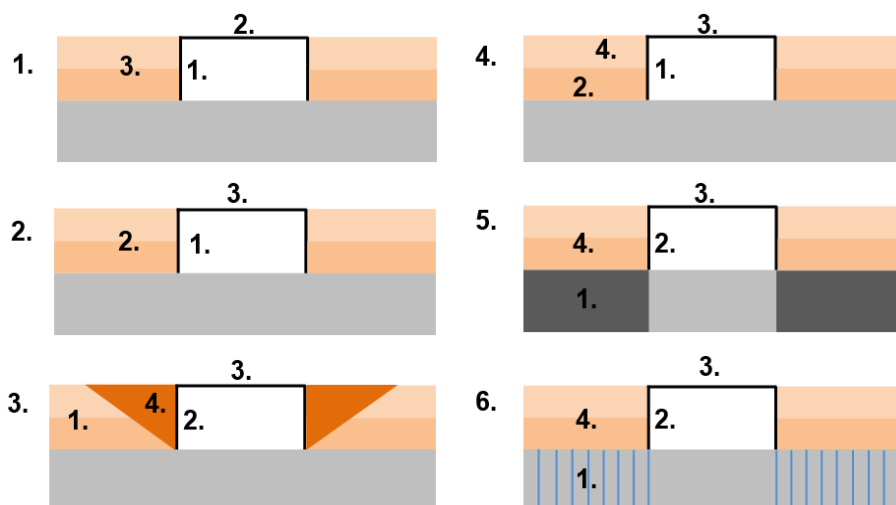


Figure 3

Schematic drawings of the investigated variants

The LM71 Eurocode load model represented the moving train with eight dynamic point loads of 125 kN vertical force [33]. PLAXIS 3D characterizes dynamic loads using a time-force signal. In the model, every dynamic point load has its multiplier, which turns the loads on and off, simulating the effects of the rolling vehicle. The dynamic time step must be changed to simulate different travel velocities while the distance between dynamic point loads is constant [31]. For analyzing the effect of the construction phases of a bridge construction, the vehicle's speed was set to 250 km/h. A train with 250 km/h speed passes 1.6 m in 0.023 sec; hence the time interval must be chosen 0.023 sec for the fixed dynamic point loads. The total elapsed time between the first and the last load was 1.3824 sec. An additional time of 0.6176 sec was considered to allow complete dissipation of the waves induced by the passing train.

### 3 Results Related to the Settlements

The final settlements of variant 1 are shown in Figures 4 and 5. These refer to the loading situation where the train reaches the middle of the bridge. The settlement behavior was similar for the other variants because the construction phases barely affected the final settlements, except for the ground improvement (variant 5). The essential settlement data are summarized in Table 3. The following conclusions can be made according to the Figures and the Table.

The open track has the most significant settlement, ~24 cm, which is obviously less in case of a ground improvement. Much less displacement can be seen behind the abutments, and directly behind the abutment, the settlement of the backfill is ~10-15% of the settlement of the open track. It is because the embankment fill is much smaller here because of the abutment and the sloped embankment, and the bridge abutment "supports" some of the embankment fill. Therefore, it can be stated that the settlement prognosis, based on the conventional calculation of settlement caused by the load due to the trapezoidal cross-section of the embankment, overestimates the settlements around the bridge abutment. The settlements behind the bridge abutment increase rapidly, at a distance of 3.5 m, generally about 60 mm, except variant 5, the applied ground improvement. Figure 5 shows that out of the ~24 cm of the open track's settlement, ~2.0 cm is the compression of the embankment, and ~1 cm is the subsidence of the sandy soil layer. The compression of the backfill is less than 1 cm. The bridge abutment and the superstructure exhibit negligible magnitudes of settlement (13-16 mm), which roughly corresponds to the settlement measurements of the abutments resting on a pile foundation.

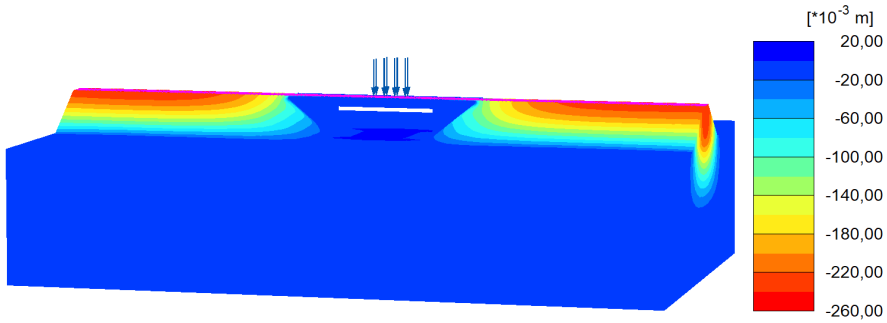


Figure 4  
Vertical settlements for the construction schedule variant 1

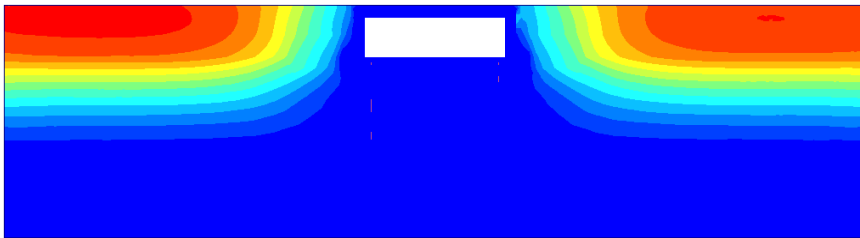


Figure 5  
Longitudinal section of the bridge and its surroundings for the construction variant 1  
(with the same scale of colors as Figure 3)

Table 3  
The settlement of the track axis depending on the construction variants

Construction variants	Open track	Backfill from the bridge abutment		Bridge abutment
		to 4.0 m	to 0.5 m	
mm				
1.	248.0	97.0	39.0	12.0
2.	249.0	96.0	30.0	13.3
3.	269.0	84.0	24.0	9.6
4.	246.0	95.0	28.0	9.6
5.	40.0	30.0	12.0	7.2
6.	257.0	102.0	38.0	11.4

## 4 Results of the Consolidation

Time may not play such an essential role in the case of a structure as the bridge abutment. Due to today's enforced construction time, there is no time to wait for the entire consolidation in most cases. Moreover, the project managers want an accurate prediction, which is difficult and impossible to produce. Poor predictions related to consolidation may cause problems with differential settlement in the bridge abutment and the backfill and generate negative skin friction within the piles.

The consolidation curves of the six different construction variants are shown in Figure 6. In order to be transparent, only those curves are shown, which were determined on the embankment surface, 20 m from the bridge abutment below the open track. The vertical displacement of the backfill zone, measured on the ground surface directly behind the abutment, is less than 2 cm; therefore, it is not shown in the figure. The full consolidation time of construction schedule variants 1, 2, and 4 is approximately 550 days; it is not significantly affected by the sequence of the superstructure's construction.

The immediate settlement is ~5 cm, followed by ~6 cm consolidation settlement due to the "consolidating time" of the lower embankment. These require about ~300 days. The second phase of the consolidation settlement due to the upper embankment is ~10 cm, and 200-250 days are necessary to reach a 95% degree of consolidation. The duration of the construction is approximately six months less in the case of variant 3 (the embankment of the open track is built before); however, the total consolidation settlement is 2 cm more. In the case of installing vertical drains into the subsoil (variant 6), the consolidation time is reduced by one-third, the embankment can be built in one phase, and the total consolidation settlement is ~25 cm. Following the expectations, the settlement and the consolidation time are drastically reduced in case of ground improvement (variant 5), and the embankment can be built in one phase.

Figure 6 also shows that the railway superstructure's construction induces further 5-8 mm incremental settlements after the complete consolidation. The settlement due to the train load, usually around 8 mm, is not presented in the figure but will be discussed separately later.

If the consolidation time exceeds 2-3 months, the settlement measurements are taken, and the construction phases can be set based on their results. According to Hungarian practice, the consolidation is considered to be "finished" if the settlement rate is below 1 cm/month. Figure 7 indicates the settlement rate of the same surface point as it was investigated regarding the settlement. Note that this rule's origin is unknown, but it can still be recognized in the geotechnical report of the bridge construction.

The figure clearly shows that the settlement rate suddenly increases when a new step of construction, e.g., the fill or sleepers' construction, starts. During the consolidation, the settlement rate decreases over time.

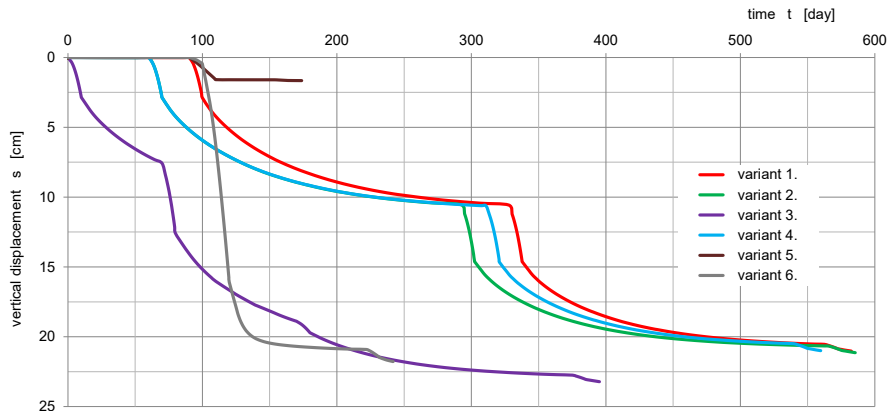


Figure 6

The consolidation of the open track concerning the construction variants

Variant 1 shows the slowest reduction of the settlement rate. After constructing the upper part of the embankment, the shape of the curves is similar in the case of variants 2 and 4, but variant 2 shows a slightly faster reduction. The sudden reduction can be observed in the case of variants 5 and 6 due to the prior ground improvement (deep mixing and vertical drains). For variant 3, the settlement rate reduction is relatively fast after the superstructure placement due to the early embankment construction.

The figure also shows that the settlements are still increasing even after the total (95% degree of consolidation) consolidation. Partly because it was not "full", partly as the railway superstructure also induces consolidation settlements, and partly due to the presence of the train load. The figure clearly confirms the false practice of the 1 cm/month rule; the expected incremental settlement is around 5 cm after reaching the given value.

This analysis aimed to show that the construction time can be optimized based on the total final settlement and the prediction of the settlement rate if the subsoil can be correctly parametrized. It could only happen in the case of a good soil analysis; however, such a prediction should also be based on the settlement measurements of the first construction phases.

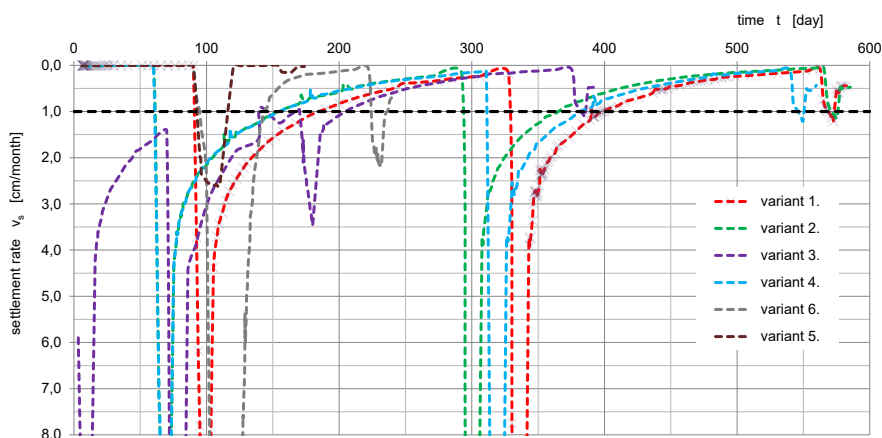


Figure 7

The settlement rate concerning the construction variants

## 5 Results Related to the Transition Zone

Analyzing the behavior of the transition zone was another goal of this study. Figure 8 shows the effect of the train load on the open track section (20 m from the abutment) and the backfill zone (0.5 m from the abutment). The selected points are located on the upper layer of the ballast. According to Figure 8, the train load produces twice the settlement on the open track (9-10 mm) when compared to settlement in the backfill (5 mm). The train induces permanent deformation (7-8 mm) remains after the train passes. In the case of variants 3, 5 and 6, the remaining settlement is slightly lower on the open track section than for variants 1, 2 and 4. In the backfill zone, the permanent settlement is around 2 mm.

The vertical settlements due to the train load are shown in the longitudinal profile in Figure 9. They have a lower magnitude near the bridge abutment and rapidly change directly behind it. It is because the bridge abutment barely settles under the train load. The effect of the train load is the smallest in the case of variant 3, likely due to the early construction of the embankment. In the case of ground improvement, the train load has the most considerable effect, likely due to the stiff subsoil. The curves are actually overlapping directly  $\sim 5$  m behind the bridge abutment and show a settlement of  $\sim 7$  mm. The deflection of the superstructure is around 3 mm; there is no significant difference in the case of the different variants.

Based on the results, it seems that the correct behavior of the last section in front of the bridge abutments cannot be solved only by applying geotechnical design.

In this case, according to the new Hungarian Railway Regulation, Volume 6 [34], a deck slab, such as a variation of the thickness of a high quality-balancing layer, as well as the reinforcement of the superstructure, e.g., additional rails or oversized sleepers, could help.

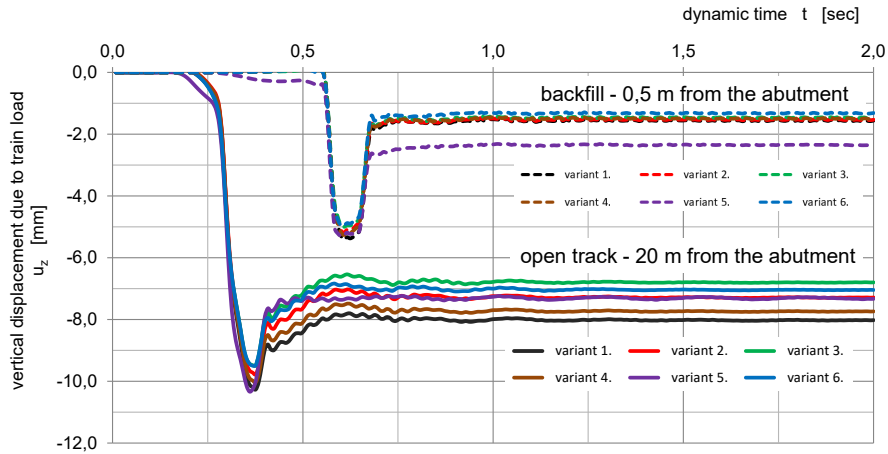


Figure 8

Vertical displacement due to the train load

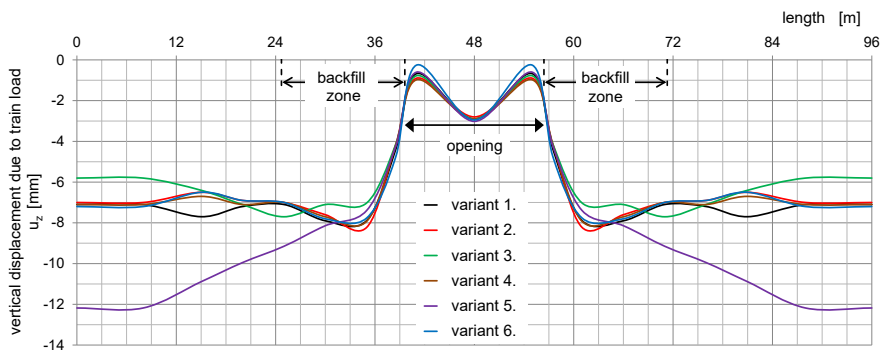


Figure 9

Vertical displacements due to the train load in each variant

## 6 Results Concerning the Substructure

Figure 10 illustrates the horizontal displacement of the bridge abutment before constructing the railway superstructure according to variant 1. In the figure, only the concrete pile cap, the bridge abutment, and the wing wall are visible for better

evaluation of displacements. The figure shows that the bottom of the wall moves towards the opening about 2 mm, while the top moves towards the embankment approximately 3.5 mm. Based on the middle part of the figure, it can be noted that the displacement of the bridge abutment is small, under 5 mm.

The horizontal displacements of the bridge abutment for the relevant construction phases are shown in Figure 11, related to variant 1. After constructing the superstructure, a horizontal displacement of approximately 2 mm can be seen, and the bridge abutment moves towards the embankment. Following the construction of the first step of the embankment, the top of the bridge abutment still moves towards the embankment, while the bottom moves towards the bridge. It can be observed that such a displacement is getting more significant in the following construction phases, and later, due to the trainload, the bridge abutment tilts towards the opening.

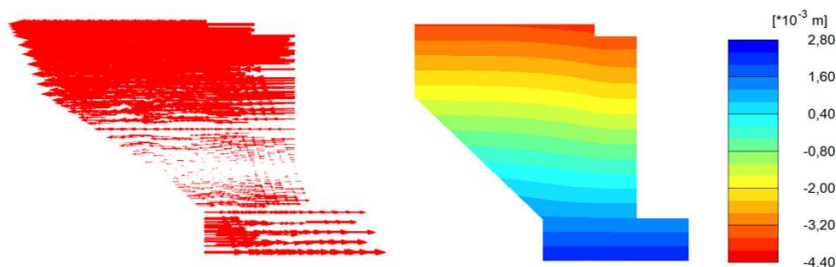


Figure 10

Horizontal displacement of the bridge abutment before constructing the beam

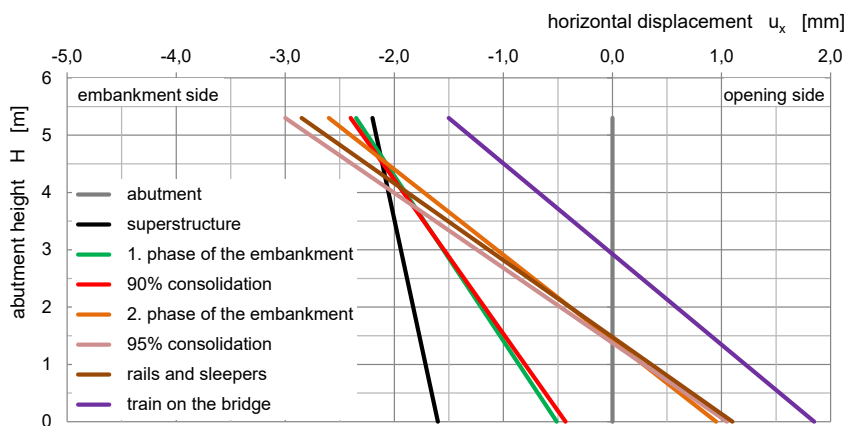


Figure 11

Horizontal movement of the bridge abutment concerning the construction phases (variant 1)

Figure 12 shows, according to the construction phases, the horizontal displacements of the bridge abutment relating to the state when the train load is above the abutment. Except for versions 2 and 4, the horizontal displacement of the bridge abutment seems to be quite similar; the extent of the displacement stays under 5 mm due to the early support. These displacements are about 0.1% of the height of the wall. The largest displacement, 20 mm, can be seen by variant 2; the bridge abutment wall moves totally towards the embankment, which induces a passive state in the backfill, and the wall gets strong support from it. The reason behind this is that the construction of the superstructure, together with the support of the abutments, begins after the consolidation; till then, the settlement of the embankment is dominant. The differential settlement induced by embankment consolidation near the base of the abutment causes its top to rotate into the embankment. Actually, the abutment fits into the bowl-shaped settlement depression. Construction phase variant 4 shows similar results, although the displacement is less because the support was created after constructing half of the embankment.

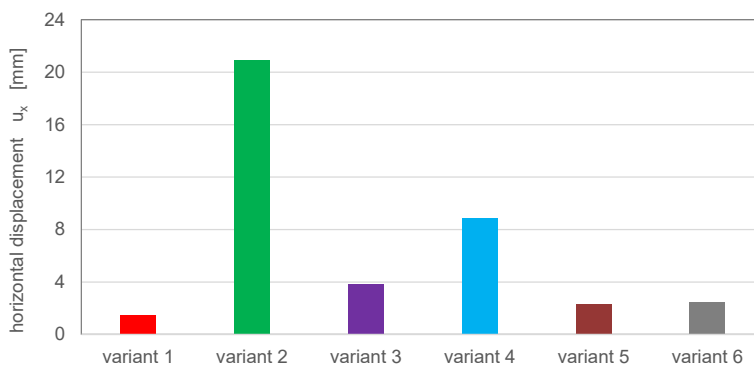


Figure 12

The displacement of the bridge abutment concerning the investigated variants

## Conclusions

This study investigated a typical railway bridge and the related soil environment, focusing on the effect of different construction schedules. According to the analysis, several benefits and practical consequences could be concluded:

- Plaxis 3D software, applying the HS-small constitutive model and modeling the moving train, provides a realistic analysis of the current problem. It describes the global behavior of the railway bridge and its soil environment.
- Due to the spatial effects and a more realistic loading condition, the results of the settlements around the bridge abutment are more favorable, than the results derived from conventional analysis or 2D modeling.

- c) This type of modeling could allow for optimization of the construction process, the best sequence of construction phases, or the earliest date of construction of the railway superstructure.
- d) Due to the complex behavior of the bridge and its surroundings, we should not rely on simple design methods to provide a solution to the problem. The analysis presented here indicates the trends of soil and structural displacements, as well as the time required for adequate consolidation.
- e) The results showed that ground improvement could be a suitable technology to reduce construction time, but it is more costly. Using construction variant 1, 2, and 4 require the most time. Moreover, in the case of variant 2, horizontal displacement of the bridge abutment is might be greater than allowed; it may result in higher forces within the piles.
- f) Construction variant 3, reduces construction time and the cost is modest. The results related to the settlement, consolidation time, and horizontal movements of the bridge abutment are within reason.
- g) The results clearly show that geotechnical approaches, by themselves, are not sufficient to solve the problem of the transition zone. A holistic approach, combining geotechnical and railway superstructure tools, would produce a better transition between the bridge and the connecting embankment.

## References

- [1] Varandas JN. *et al.* Three-dimensional non-linear modelling of railway tracks application to transition zones. INSERTZ, International Seminar on Rail Track Substructures and Transition Zones, Lisbon, Portugal, 2014
- [2] Indraratna B, Sajjad M. B, Ngo T, Correia A. G, Kelly R. Improved performance of ballasted tracks at transition zones: A review of experimental and modelling approaches, *Transportation Geotechnics*, Volume 21, December 2019, 100260, p. 25
- [3] Fischer S. Geogrid reinforcement of ballasted railway superstructure for stabilization of the railway track geometry – A case study. *Geotextiles and Geomembranes*, Volume 50, Issue 5, 2022, pp. 1036-1051
- [4] Sañudo R, Dell'Olio L, Casado J. A, Carrascal I. A, Diego S. Track transitions in railways: A review. *Construction and Building Materials* 112. 2016, pp. 140-157
- [5] Li D, Davis D. Transition of railroad bridge approaches. *Journal of Geotechnical and Geoenvironmental Engineering*. 2005, 131, pp. 1392-1398
- [6] Banimahd M, Woodward P. K, Kennedy J, Medero G. M. Behavior of train-track interaction in stiffness transitions. In *Proceedings of the Institution of Civil Engineers-Transport*; Thomas Telford Ltd.: London, UK, 2012, Volume 165, pp. 205-214

- [7] Briaud J. L, Tafti S. R. High Speed Trains Geotechnics: What is a Tolerable Bump?, *Procedia Engineering*, Volume 189, 2017, pp. 186-192
- [8] Li W, Hou W, Mishra D, Tutumluer E. Modeling the Dynamic Behavior of Track Transitions Along Shared Track Corridors. *Frontiers in Built Environment*, 7:693744, 2021, p. 16
- [9] Zhang X, Zhao C, Zhai W, Shi C, Feng Y. Investigation of track settlement and ballast degradation in the high-speed railway using a full-scale laboratory test. *Proceedings of the Institution of Mechanical Engineers, Part F: Journal of Rail and Rapid Transit*. 2019, 233(8), pp. 869-881
- [10] European Rail Research Institute. Utrecht. ERRI D 230.1/RP 3. "Bridge ends" "Embankment Structure Transition" State of the Art Report, Nov. 1999
- [11] Kerr A. D, Moroney B. E. Track transition problems and remedies. Paper presented at the the American Railway Engineering Association, Washington, USA, 1993
- [12] Sasaoka C. D, Davis D. Implementing track transition solutions for heavy axle load service. Paper presented at the AREMA 2005 Annual Conference, AREMA, 2005
- [13] Li D, Otter D, Carr G. Railway bridge approaches under heavy axle load traffic: problems, causes, and remedies. Paper presented at the Institution of Mechanical Engineers, Part F: *Journal of Rail and Rapid Transit*, 2010, <https://doi.org/10.1243/09544097JRRT345>
- [14] Correia A. G, Cunha J, Marcelino J. L. Caldeira J. Varandas Z. Dimitrovová A. A, Silva M. G. d, Dynamic analysis of rail track for high speed trains. 2D approach. 5<sup>th</sup> Intl Worksop on Application of Computational Mechanics on Geotechnical Engineering, Portugal, 2007, p. 14
- [15] Banimahd M, Woodward P. K, Kennedy J, Medero G. Behaviour of train-track interaction in stiffness transitions. *Proc. Inst. Civil Eng. Transport* 165, pp. 205-214, doi:10.1680/tran.10.00030); 2012
- [16] Costa D. A, Sofia E. A, Potvin R, Laurans E, Funfschilling C. Railway transitional zones: a case history from ballasted to ballastless track. *Int. J. Railway Tech.* 3 (1), 2014. pp. 37-61, doi:10.4203/ijrt.3.1.2)
- [17] Paixão A, Varandas J. N, Fortunato E, Calçada R. Numerical simulations to improve the use of under sleeper pads at transition zones to railway bridges. *Eng. Structures* 164, 2018, pp. 169-182, doi: 10.1016/j.engstruct.2018.03.005
- [18] Paixão A, Fortunato E, Calçada R. A numerical study on the influence of backfill settlements in the train/track interaction at transition zones to

- railway bridges. *Proc. Inst. Mech. Eng. Part F J. Rail. Rapid Transit.* 230 (3), 2016, pp. 866-878, doi:10.1177/0954409715573289
- [19] Stark T. D, Wilk S. T. Root cause of differential movement at bridge transition zones. *Proc. Inst. Mech. Eng. Part F J. Rail. Rapid Transit.* 230 (4), 2016, pp. 1257-1269, doi:10.1177/0954409715589620
- [20] Szepesházi R. Development of bridge substructure design, 50. Bridge Engineering Conference, Siófok, 2009. pp. 429-470
- [21] Laufer I. Soil-structure interaction at bridge abutment, 5<sup>th</sup> Kézdi Árpád Conference, Budapest, 2017, pp. 143-163
- [22] Koch E, Hudacsek P, Wolf Á. Validated 3D FEM analysis of the geotechnical performance of a semi-integral bridge In: Rahman, Mizanur; Jaksa, Mark Proceedings of the 20<sup>th</sup> International Conference on Soil Mechanics and Geotechnical Engineering. Sydney, Ausztrália: Australian Geomechanics Society (2022) 5, 302 p. pp. 763-768
- [23] Brinkgreve R. B. J, Vermeer P. A. PLAXIS-Finite element code for soil and rock analyses, *Plaxis 3D Manuals*, 2010, Delft University of Technology & Plaxis bv, The Netherlands
- [24] Ahmed A, Naggari H. N. Soil-structure interaction of integral abutments. *Transportation Geotechnics* 38, 2023: 100900. p. 15
- [25] Kong B, Cai CS, Zhang Y. Parametric study of an Integral abutment bridge supported by prestressed precast concrete piles. *Eng Struct* 2016;120:37-48
- [26] Civjan SA, Bonczar C, Brežna SF, DeJong J, Crovo D. Integral Abutment Bridge Behavior: Parametric Analysis of a Massachusetts Bridge. *J Bridge Eng* 2007;12(1) 64-71
- [27] Schanz T, Vermeer P. A, Bonnier P. G. The hardening soil model: formulation and verification. *Beyond 2000 in computational geotechnics*, 1999, pp. 281-296
- [28] Brinkgreve R, Engin E, Engin H. K. Validation of empirical formulas to derive model parameters for sands. 2010, 10.1201/b10551-25
- [29] Koch E. Modeling of embankment foundation, PhD dissertation, Széchenyi István University, Győr, 2013
- [30] Fischer S. Investigation of the horizontal track geometry regarding geogrid reinforcement under ballast. *Acta Polytechnica Hungarica*, 19(3), 2022, pp. 89-101, doi: <https://doi.org/10.12700/APH.19.3.2022.3.8>
- [31] Shahraki M, Sadaghiani M. R. S, Witt K. J, Meier T. 3D modelling of train induced moving loads on an embankment. *Plaxis Bulletin*, 36, 2014, pp. 10-15
- [32] Koch E, Szepesházi R, Bene K. Laboratory tests and numerical modeling for embankment foundation on weak soils using deep-mixing. In: Monika,

Sulovska (ed.) 11<sup>th</sup> Slovak Conference on Geotechnical Engineering: Effect of water on geotechnical structures, Bratislava, Szlovákia: Slovenská technická univerzita v Bratislave, 2013, pp. 257-267

- [33] EN 1991-2: Eurocode 1: Actions on structures - Part 2: Traffic loads on bridges. Authority: The European Union Per Regulation 305/2011, Directive 98/34/EC, Directive 2004/18/EC. 2003
- [34] H.1. Railway bridge regulation, H.1.2. Directive, General design specification of railway bridge and other structures, MAÚT, Budapest, 2019

# Innovative Approaches to Railway Track Alignment Optimization, in Curved Sections

**Mykola Kurhan, Dmytro Kurhan and Nelya Hmelevska**

Department of Transport Infrastructure, Ukrainian State University of Science and Technologies, Lazaryan St. 2, 49010 Dnipro, Ukraine  
{m.b.kurhan, d.m.kurhan, n.p.hmelevska}@ust.edu.ua

---

*Abstract: The efficient advancement of railway transportation is impossible without the integration of cutting-edge innovations. This study places emphasis on the application of computer modeling for railway track alignment, enabling the determination of an optimal strategy for rectifying curves within the plan. This approach ensures enhanced accuracy and effectiveness in curve realignment efforts. The calculations involved in plan correction are not only essential for addressing track deviations but also for solving a set of challenges associated with increasing permissible travel speeds. Particular significance is attributed to the reconstruction of track alignment, especially for international routes transitioning from wide (1520 mm) to standard European gauge (1435 mm). The incorporation of innovative technologies for railway curve correction, along with line plan optimization across multiple track sections, facilitates the realization of maximum stipulated velocities while ensuring safety, smoothness of motion, and passenger comfort. The investigation results detailed in this paper were conducted with support from a grant provided by The National Research Foundation of Ukraine under the project, "Scientific Justification of the Introduction of the European Track on the Territory of Ukraine in the Post-War Period".*

*Keywords: railway; innovative activity; innovative technologies; railway curves, transport corridor*

---

## 1 Introduction

Global experience attests that effective railway transport development is unattainable without the implementation of innovations. Ukraine, akin to other European nations, is embracing various innovative technologies in the reconstruction of railway alignments. Noteworthy, among these innovative technologies, are the following:

- GPS navigation for ensuring precise railway track construction, thereby reducing deviations from the designated route and enhancing train travel safety

- Employment of automated process control systems during railway construction and reconstruction, allowing the maintenance of required line plan parameters and reducing deviations from specified standards
- Laser scanning of railway tracks, enabling accurate measurement of track parameters, including radius, leading to the creation of a precise track plan and identification of areas necessitating curve rectification
- Utilization of modern geodetic techniques, facilitating accurate measurement of railway track geometry and ensuring more precise curve realignment within the plan
- Deployment of autonomous machinery for plan-wise curve correction, substantially reducing the time and cost required for such adjustments
- Utilization of computer modeling for railway track alignment, allowing the determination of optimal strategies for curve rectification.

These advancements collectively contribute to a more precise and efficient approach to railway track alignment, aligning with the contemporary standards and expectations for modern rail systems.

Each innovation has its specific sphere of application. In 2020, the Strategic Research and Innovation Program for European Rail Transport was published by the European Rail Research Advisory Council (ERRAC). Its endeavors are geared towards furnishing innovative solutions that assist the railway sector in becoming more efficient, safer, and environmentally sustainable [1]. The seamless operation of railway transport hinges on the technical condition of rolling stock, railway track, and its alignment within the plan [2-5]. Consequently, for modern railways, the implementation of innovative methods in track repairs and ongoing maintenance on sections equipped with high-precision coordinate systems, ensuring track alignment with the designated position, becomes practically indispensable.

## **2 Statement of the Problem**

Calculations for track alignment rectification typically occur in cases of track deviations, which can result from various factors [6-10]. Such calculations are also required for adjusting plan parameters (curve radius, length of transition curve, superelevation) when addressing the complex challenge of increasing permissible travel speeds along a given route [11-14]. Additionally, the reconstruction of track alignment is necessary for substantial changes in its parameters, such as transitioning to a different gauge. The latter is particularly pertinent today for international routes traversing Ukraine, where a transition from the broad (1520 mm) to the standard European (1435 mm) gauge is planned [15] [16].

Accurate information about railway track alignment is linked to measurements of quantities defining track geometry, which can be classified into global and local categories. Global measurements determine the position of elements within the global system of geographic coordinates, while local measurements establish the position of elements relative to other elements (e.g., elevation of the outer rail at a specific kilometer of the track) or temporary deviations of parameters from their design values (e.g., various track deformations). Depending on the measurement method applied, global or local parameters are determined, or both simultaneously. For instance, an innovative method for determining the position of the track axis using Global Navigation Satellite System (GNSS) receivers was proposed in the study [17].

If the actual characteristics of the track alignment deviate from the design parameters, this can lead to either speed limitations or exceeding the norms, which, in turn, would result in decreased levels of safety and travel comfort, as well as increased forces of interaction between the train wheels and the elements of the track superstructure. These increased forces contribute to the wear of rails, as well as other components of the track superstructure, and the wheels and elements of the rolling stock [18].

Scientific research aimed at improving curve parameters, minimizing wear in curves, and realigning curves to enhance speed continues. In the paper [19], problematic issues regarding the selection of horizontal radius and length of transition curves are discussed in detail, including an analysis of radius diagrams and angular diagrams. Various types of transition curves are assessed considering the presence of obstacles. The influence of track irregularities on the optimal length of transition curves and the level of maximum speed is demonstrated indirectly.

In the dissertation [20], a scientific approach is presented that considers the cost difference between constructing new tracks or reconstructing railways, involving the elimination of obstacles related to connections: transition curve - circular curve - transition curve. Curvature plots and angle-turn diagrams were utilized to determine when individual curves should be replaced with compound curves. The definition of the most suitable length for transition curves is provided, allowing for the realization of the highest permissible speed.

In order to enhance accuracy and calculation speed, a methodology for curve survey calculation has been proposed based on the coordinate method and the least squares method [21]. When minimizing shifts during curve realignment, the radius of the circular curve, coordinates of the circle center, lengths of transition curves, and coordinates of characteristic points of the curve are computed.

An analysis of curves on Indian railways [22] has revealed that over time, curves can deviate from their initial position due to the following reasons. Firstly, unbalanced loading on both the inner and outer rails caused by exceeding the elevation of the outer rail at low speeds or a deficiency of elevation at high speeds, instead of the equilibrium speed for which the elevation was intended. The second

reason involves the influence of significant horizontal forces exerted on the rails by trains. These horizontal forces alter the curvature profile, reducing or increasing curvature at specific locations, thereby altering radial acceleration and consequently disrupting the smoothness of train movement. Hence, to restore smooth vehicle movement on these curves, curve realignment and adjustment of its parameters become necessary.

Currently, the issue of reconstructing railway tracks within the global reference system is of great relevance. Its essence lies in determining the position of railway track axes within a Cartesian or local coordinate system [23]. To achieve such representation of the track's centerline, many countries have developed methods primarily utilizing the Global Navigation Satellite System (GNSS). The accuracy of this type of measurement can reach one centimeter under favorable conditions. The authors have previously described the methodology they developed, and this article presents a method for determining corrections to measured horizontal GNSS coordinates that account for the presence of the superelevation in curves.

A technical system enabling the resolution of tasks related to optimal reconstruction of curved tracks to increase train speed with minimal investment has been proposed by the authors in their work [24]. Consideration is given to providing passenger comfort while increasing speed on curved track sections.

In the study [25], the question of determining the horizontal radius of the railway track is addressed. The method is based on altering the incline angles of the moving chord in the Cartesian coordinate system. By assessing the influence of chord length on obtained radius values, it has been established that chord length does not play a significant role in radius determination and does not limit the application of this method. Simultaneously, attention is drawn to the accuracy of radius determination and its relevance to transition curve sections.

The initial data significantly impact the results of permissible train speeds. In the work [26], the utilization of modern geodetic technologies for determining track geometry is proposed. The author in [27] considers the issue of determining the horizontal radius of the railway track's axis to obtain unknown geometric characteristics of the track as not definitively resolved. This is explained by the fact that geometric characteristics were determined using approximate methods. Hence, a new concept for determining track radius through altering the slope angle of the moving chord has been introduced. To employ this method, the coordinates of points in a Cartesian system are required for a given railway section.

Numerous scientific studies have been dedicated to justifying the form of transition curves for the introduction of high-speed train travel. For instance, in [28], a new form of transition curve adapted to operational requirements imposed on the railway is presented. Parameters of two types of transition curves used in Hungary and Austria are defined in the paper [29]. It is demonstrated that the convenience of using transition curves in the form of the clothoid is unjustifiably limited in Hungarian regulations for speeds up to 120 km/h.

In the scientific study [30], the authors examined the change in track gauge width on curves for various secondary and main railway lines in Hungary with low and high transport volumes. The analyzed curves encompassed transition curves and circular curves. The variation of the gauge width parameter as a function of elapsed time was investigated by calculating distribution functions.

The pursuit of novel methods for surveying line plans and calculating curve realignment to place them in their design positions continues. In the study [31], a reconstruction method for existing railways with constrained optimization based on point cloud data is presented. Drawing from the theory of intelligent algorithms, the concept of the Particle Swarm Optimization (PSO) algorithm is introduced, along with the method of directed search. After obtaining point cloud data of the track's alignment, a target function with constraint conditions was established and integrated with railway surveying technology. The complexity and reconstruction time for solitary and continuous curves containing multiple basic curve units are analyzed. Utilizing measurement data, design data, and synthetic data as inputs, this research demonstrated the suitability, reliability, and practicality of its application.

A review of scientific works reveals that methods proposed by various authors are valuable for the reconstruction of existing railways, but their effectiveness may be contingent on specific operational conditions. Numerous studies have been dedicated to optimizing individual or constituent curves, adjusting their parameters (radius, transition curves, superelevation, etc.), yet the optimization of the entire track plan for a section or multiple sections remains underexplored.

This paper places emphasis on the application of computer modeling for railway track alignment, enabling the determination of an optimal strategy for rectifying curves within the plan. This approach ensures enhanced accuracy and effectiveness in curve realignment efforts, not only for local sections but also across the entire track section.

### 3 Methods

To explore the aforementioned phenomena, the software tool RWPlan, developed at the Ukrainian State University of Science and Technologies, was utilized in the course of this study. The foundation of this development was laid by I. Korzhenevich [32]. The calculations of speed limits and the construction of curve profiles are performed within the program using the algorithm by D. Kurhan, while computations concerning the elevation of the outer rail in curves for train flows and the consideration of speed constraints are carried out by N. Hmelevska. The innovative approach within the RWPlan software lies in its capability to employ various surveying methods for line plans, utilized both within railway administration and project organizations. The software also allows for the analysis

of not just individual curves, but also track sections or multiple sections, optimizing the project plan according to various criteria while ensuring the attainment of the maximum permissible speed [14].

For existing plan design methods, a clear system of criteria for optimal positioning of the project curve has not yet been established. The task is formulated as follows: it is necessary to determine the position of the project curve that ensures the minimum amount of realignment work for track correction within the main earthwork platform, taking into account specified constraints (fixed points, shift directions, etc.). Clearly, with the aim of enhancing design quality and reducing construction costs, this criterion should indeed be considered during calculations. However, there are certain circumstances that must be taken into account in the optimization process.

It is often believed that the minimum realignment work would be achieved when the algebraic sum of alignment deviations equals zero. Previous studies have indicated that such a condition holds true when the length of the circular curve between the ends of the transitions constitutes no less than  $2/3$  of the total curve length. For short curves, primarily composed of two transition parts and a circular section amounting to less than  $1/3$  of the total length, an algebraic sum of deviations equating to zero does not yield the minimum realignment work, especially if the track is severely misaligned within the transition curves. The minimum realignment work can be achieved when the entire curved section results in the minimum sum of absolute values of shifts.

In this study, the authors have applied the proposed methodology for optimizing the project plan, taking into account various criteria, namely: minimum sum of absolute shift values, minimum sum of squared shift values, minimum sum of curve realignment costs. This approach allows for the incorporation of the aforementioned observations.

Hence, the sequence of calculations in the optimization of lengthy track sections consists of the following steps:

1. Coordinate survey is established based on the curve parameters. Segmentation of the long track section is achieved using angle diagrams and the radius of the segment.
2. Optimization of each curve is carried out in either the involute or coordinate models, employing one of the four optimization criteria: minimum sum of squared shifts, absolute shifts, absolute root shifts, or minimum costs.
3. Upon calculating each fragment, model parameters are gradually revealed and the survey of individual fragments is amalgamated for the entire section. When integrating interdependent curves, the maximum curvature difference between these elements is controlled. If the difference exceeds the predetermined limit, the program adjusts the radius values to satisfy

this restriction. Throughout the optimization process, the potential elevation adjustment of the outer rail within the transition curve is monitored.

4. Calculation and evaluation of the shift magnitudes for the entire section are executed. The limitation magnitude and the prescribed shift at the end of the section are taken into account in all cases, while other restrictions are incorporated during the optimization process. It is possible to incorporate shift magnitude constraints for specific segments.
5. The maximum permissible travel speeds for the proposed design are computed, followed by an analysis of the outcomes using the pre-established criterion.

## 4 Results and Discussion

Let us consider an example of calculations using the algorithm presented above for the Kyiv-Hrebinka-Poltava-Lozova route (Ukraine), Fig. 1. The positional layout of the track plan was determined under the condition of route modernization, aiming to achieve the highest possible speed while remaining within the existing embankment. The maximum allowable horizontal displacements of the track (alignment corrections) depend on various factors, such as the track's construction, its condition [33] [34], the presence of infrastructure devices, including power supply systems, signaling systems, etc. [35-40]. Following a thorough terrain analysis, it was stipulated that permissible shifts in the range of 0-250 mm would be acceptable in this scenario.



Figure 1  
Railway section Kyiv - Lozova

As a result of the track plan and traction calculations, data were obtained for the following variants:

1. Without section reconstruction.
2. Station reconstruction is carried out to enhance travel speeds, with no alteration to the track plan.
3. In addition to station reconstruction, modifications are made to the elevation of the outer rail in curves, ensuring maximum speeds with minimal rail wear. In this case, the track's positional layout, radii, and lengths of transition curves remain unchanged.
4. Alongside station reconstruction, the track is placed in a new design position, guaranteeing maximum feasible speeds while maintaining the track within the existing embankment.

Trains of various types operate on this section. The calculations are presented for trains of the Hyundai type, which are designed for high-speed travel. The travel time of trains does not significantly differ between directions; therefore Table 1 provides the time only for the direct direction.

As evident from the results, on the Hrebinka-Poltava section, station reconstruction yields a significant effect (16 minutes). The implementation of outer rail superelevation calculated according to regulations allows for an additional saving of 4 minutes. Laying the track in the projected position results in a time saving of 10 minutes compared to the 2nd variant. On the Poltava-Lozova section, station reconstruction has a relatively modest effect (7 minutes). However, by adjusting the outer rail superelevation, an additional 18 minutes can be saved. Furthermore, aligning the track in the projected position leads to a substantial reduction in time (26 minutes) compared to the 2nd variant.

Table 1  
Train travel time for Hyundai trains in the forward direction by variants

Direction	Distance, km	Train travel time by variants, minutes			
		1	2	3	4
Kyiv - Hrebinka	148	67	59	55	51
Hrebinka - Poltava	186	134	118	114	108
Poltava - Krasnohrad	81	68	64	51	48
Krasnohrad - Lozova	95	70	61	56	51
<b>Poltava - Lozova</b>	<b>176</b>	<b>138</b>	<b>125</b>	<b>107</b>	<b>99</b>
<b>Hrebinka - Lozova</b>	<b>362</b>	<b>272</b>	<b>243</b>	<b>221</b>	<b>207</b>

When calculating the design variant for each curve, the feasibility and potential for speed enhancement were considered. Variants that require adjustments within the range of up to 250 mm were explored, avoiding significant realignments. Graphical

fragments depicting radius, superelevation, and maximum permissible train speeds on the Poltava-Krasnohrad section for the design variant are presented in Figs. 2 and 3.

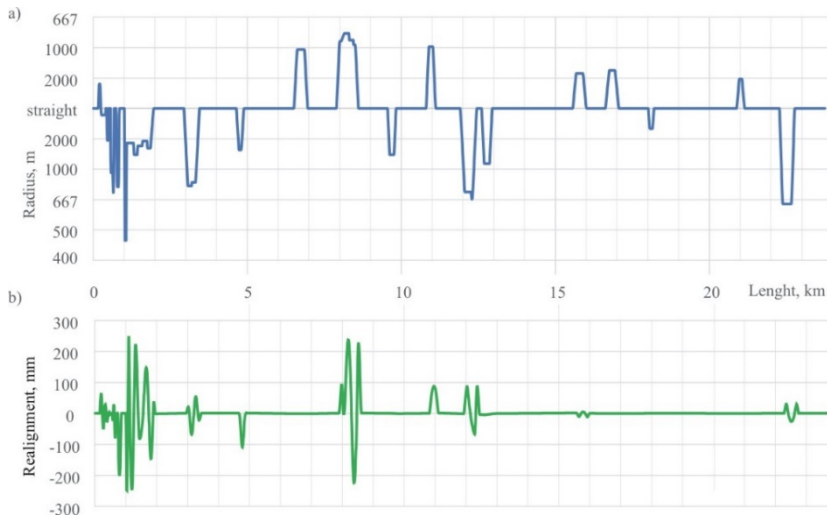


Figure 2

Segment of the Poltava – Krasnohrad section: a) track plan; b) track alignment

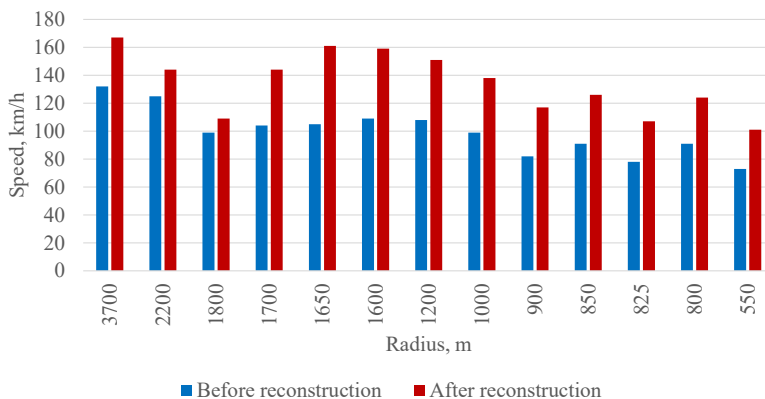


Figure 3

Permissible movement speeds on the Poltava – Krasnohrad section

By optimizing the outer rail superelevation while considering the maximum permissible speed and rail wear, an optimal solution has been achieved. In all variants, the acceleration of passenger trains does not exceed  $0.7 \text{ m/s}^2$ , while for freight trains, it remains within  $\pm 0.3 \text{ m/s}^2$ .

## Conclusions

Based on both theoretical and experimental research, it has been determined that the implementation of innovative technologies, for railway curve alignment in the plan, will allow establishing plan parameters and optimal train speeds. This will result in reduced wear of rails and train wheels, decreased track maintenance efforts, minimized energy or fuel consumption for freight and passenger transportation and contribute to enhancing safety, smoothness, and passenger comfort.

The analysis of technical and technological challenges arising from the incompatibility of standards between Ukrainian and European railway infrastructures has demonstrated that the proposed algorithm for the sequential alignment of the track plan during the optimization of long sections can be applied, including during the transition from the broad (1520 mm) to the standard European (1435 mm) gauge.

The calculation results and the developed methodology can be used for, theoretically, justifying maximum permissible train speeds, while simultaneously ensuring the standards of strength, stability, durability and the reliability of railway track and rolling stock components. This theoretical groundwork also serves as a basis for implementing European standard railway curve alignment technologies, for the facilitation of high-speed train travel.

## Acknowledgement

The investigation results detailed in this paper were conducted with support from a grant provided by The National Research Foundation of Ukraine under the project "Scientific Justification of the Introduction of the European Track on the Territory of Ukraine in the Post-War Period" (project registration number 2022.01/0021), which was obtained through the "Science for the Recovery of Ukraine in the War and Post-War Periods" competition.

## References

- [1] Rail Strategic. Research & Innovation Agenda. SRIA. [https://rail-research.europa.eu/wp-content/uploads/2020/12/RAIL-Strategic-Research-and-Innovation-Agenda-2020-\\_FINAL\\_dec2020.pdf](https://rail-research.europa.eu/wp-content/uploads/2020/12/RAIL-Strategic-Research-and-Innovation-Agenda-2020-_FINAL_dec2020.pdf) [online, last visited on: 2023.08.09]
- [2] A. Shvets. Influence of the instability form on the traffic safety indicator of freightrolling stock. *Engineering Applications*, Vol. 2(3), 2023, pp. 206-217
- [3] L. Muradian, I. Pitsenko, V. Shaposhnyk, A. Shvets, A. Shvets. Predictive model of risks in railroad transport when diagnosing axle boxes of freight wagons. *Proceedings of the Institution of Mechanical Engineers, Part F: Journal of Rail and Rapid Transit*, Vol. 237(4), 2023, pp. 528-532, <https://doi.org/10.1177/09544097221122043>

- [4] G. Kún and T. Wühl, "Classification of Communication Interfaces in Railway Systems," 2023 IEEE 17<sup>th</sup> International Symposium on Applied Computational Intelligence and Informatics (SACI), Timisoara, Romania, 2023, pp. 000749-000754, <https://doi.org/10.1109/SACI58269.2023.10158659>
- [5] E. Ambriško, J. Šaderová, R. Antal. Evaluation of Railway Vehicle Reliability Parameters. *Acta Polytechnica Hungarica*, Vol. 20(4), 2023, pp. 27-43, <https://doi.org/10.12700/APH.20.4.2023.4.2>
- [6] S. Fischer, N. Liegner, P. Bocz, Á. Vinkó, G. Terdik. Investigation of Track Gauge and Alignment Parameters of Ballasted Railway Tracks Based on Real Measurements Using Signal Processing Techniques. *Infrastructures*. Vol. 8(2), 2023, 26, <https://doi.org/10.3390/infrastructures8020026>
- [7] O. Nabochenko, M. Sysyn, V. Kovalchuk, Y. Kovalchuk, A. Pentsak, S. Braichenko, Studying the railroad track geometry deterioration as a result of an uneven subsidence of the ballast layer. *Eastern-European Journal of Enterprise Technologies*, Vol. 1(97), 2019, pp. 50–59, <https://doi.org/10.15587/1729-4061.2019.154864>
- [8] V. Jóvér, M. Sysyn, J. Liu, S. Fischer. Geometry variation of ballasted railway tracks due to weather conditions. *Naukovyi Visnyk Natsionalnoho Hirnychoho Universytetu*, Vol. 1, 2023, pp. 74-79, <https://doi.org/10.33271/nvngu/2023-1/074>
- [9] M. Sysyn, M. Przybylowicz, O. Nabochenko, J. Liu. Mechanism of Sleeper–Ballast Dynamic Impact and Residual Settlements Accumulation in Zones with Unsupported Sleepers. *Sustainability*, Vol. 13(14), 2021, 7740, <https://doi.org/10.3390/su13147740>
- [10] A. Kampczyk, K. Rombalska. Configuration of the Geometric State of Railway Tracks in the Sustainability Development of Electrified Traction Systems. *Sensors*, Vol. 23(5), 2023, 2817, <https://doi.org/10.3390/s23052817>
- [11] M. Kurhan, D. Kurhan, N. Hmelevska. Development of the High-Speed Running of Trains in Ukraine for Integration with the International Railway Network. *Acta Polytechnica Hungarica*, Vol. 19(3), 2022, pp. 207-218, <https://doi.org/10.12700/APH.19.3.2022.3.16>
- [12] O. Hubar, R. Markul, O. Tiutkin, V. Andrieiev, M. Arbuzov, O. Kovalchuk. Study of the interaction of the railway track and the rolling stock under conditions of accelerated movement. *IOP Conf. Ser.: Mater. Sci. Eng.*, Vol. 985, 2020, 012007, <https://doi.org/10.1088/1757-899X/985/1/012007>
- [13] D. Potapov, V. Vitolberg, A. Malishevskaya, V. Novikov, P. Plis. Estimation of stress state of rails under traffic speeds over 160 Km/H. *AIP Conference Proceedings* 2684, 2023, 020013, <https://doi.org/10.1063/5.0120023>

- [14] M. Kurhan, D. Kurhan, M. Husak, N. Hmelevska. Innovative Technologies for the Introduction of High-Speed Train Operation (on the Example of Track Maintenance in the Plan). *Transport Means*, 2022, 372-377
- [15] M. Kurhan, D. Kurhan. The effectiveness evaluation of international railway transportation in the direction of “Ukraine – European Union”, *Transport Means*, 2018, pp. 145-150
- [16] M. Kurhan, S. Fischer, D. Kurhan. The Prospect of Using the Dual Gauge Line for the Ukraine–Hungary Railway Connection. *Periodica Polytechnica Transportation Engineering*, Vol. 51(1), 2023, pp. 70-78, <https://doi.org/10.3311/PPtr.20572>
- [17] A. Wilk, W. Koc, C. Specht and etc. Innovative mobile method to determine railway track axis position in global coordinate system using position measurements performed with GNSS and fixed base of the measuring vehicle. *Measurement*, Vol. 175, 2021, 109016, <https://doi.org/10.1016/j.measurement.2021.109016>
- [18] M. Kurhan, D. Kurhan, R. Novik, S. Baydak, N. Hmelevska, N. Improvement of the railway track efficiency by minimizing the rail wear in curves. *IOP Conf. Ser.: Materials Science and Engineering*, Vol. 985, 2020, 165475, <https://doi.org/10.1088/1757-899X/985/1/012001>
- [19] B. Kufver. Mathematical description of railway alignments and some preliminary comparative studies. <http://www.diva-portal.org/smash/get/diva2:675179/FULLTEXT01.pdf> [online, last visited on: 2023.08.09]
- [20] B. Kufver. Optimisation of horizontal alignments for railways: Procedures involving evaluation of dynamic vehicle response. Doctoral thesis, 2000
- [21] H. Y. Li, Z. Y. Cheng, X. Cheng and etc. Calculation method for curve–surveying of the existing railway line. *China Railway Science*, Vol. 30, 2009, pp. 18-22
- [22] Transition Curves (for Railway Cant). <https://forums.autodesk.com/t5/civil-3d-forum/transition-curves-for-railway-cant/td-p/7785193> [online, last visited on: 2023.08.09]
- [23] W. Koc, C. Specht, J. Szmaglinski, P. Chrostowski. Method for Determination and Compensation of a Cant Influence in a Track Centerline Identification Using GNSS Methods and Inertial Measurement. *Appl. Sci.* Vol. 9, 2019, 4347, <https://doi.org/10.3390/app9204347>
- [24] I. Lebid, I. Kravchenya, T. Dubrovskaya, N. Luzhanska, M. Berezovyi, Y. Demchenko. Identification of the railway reconstruction parameters at imposition of high speed traffic on the existing lines. *MATEC Web Conf.*, Vol. 294, 2019, 05003, <https://doi.org/10.1051/mateconf/201929405003>

- [25] W. Koc. Analysis of the Effectiveness of Determining the Horizontal Curvature of a Track Axis Using a Moving Chord. *Problemy Kolejnictwa - Railway Reports*, Vol. 65(190), 2021, pp. 77-86, <https://doi.org/10.36137/1902E>
- [26] M. Jamka, S. Lisowski, M. Strach. Zastosowanie współczesnych technologii geodezyjnych w określaniu geometrii toru w aspekcie dopuszczalnych prędkości pociągów. *Research and Technical Papers of Polish Association for Transportation Engineers in Cracow*, Vol. 91(149), 2009, pp. 567-581
- [27] W. Koc. The Method of Determining Horizontal Curvature in Geometrical Layouts of Railway Track with the Use of Moving Chord. *Archives of Civil Engineering*, Vol. 66(4), 2020, pp. 579-591, <https://doi.org/10.24425/ace.2020.135238>
- [28] W. Koc. New Transition Curve Adapted to Railway Operational Requirements. *Journal of Surveying Engineering*, Vol. 145(3), 2019, [https://doi.org/10.1061/\(ASCE\)SU.1943-5428.0000284](https://doi.org/10.1061/(ASCE)SU.1943-5428.0000284)
- [29] S. Fischer. Comparison of railway track transition curves. *Pollack Periodica*, Vol. 4(3), 2009, pp. 99-110, <https://doi.org/10.1556/pollack.4.2009.3.9>
- [30] S. Fischer, D. Németh, H. Horváth. Investigation of the Track Gauge in Curved Sections, Considering Hungarian Railway Lines. *Infrastructures*, Vol. 8(4), 2023, 69, <https://doi.org/10.3390/infrastructures8040069>
- [31] F. Li, X. Ren, W. Luo, X. Chen. Methodology for Existing Railway Reconstruction with Constrained Optimization Based on Point Cloud Data. *Applied Sciences*, Vol. 8(10), 2018, 1782, <https://doi.org/10.3390/app8101782>
- [32] Brain Rail Systeem. RWPlan. [https://brailsys.com/RWPlan\\_0.htm](https://brailsys.com/RWPlan_0.htm) [online, last visited on: 2023.08.09]
- [33] M. Sysyn, O. Nabochenko, V. Kovalchuk, M. Przybyłowicz, S. Fischer. Investigation of interlocking effect of crushed stone ballast during dynamic loading. *Reports in Mechanical Engineering*, Vol. 2(1), 2021, pp. 65-76, <https://doi.org/10.31181/rme200102065s>
- [34] S. Szalai, B. Eller, E. Juhász, M. Movahedi Rad, A. Németh, D. Harrach, G. Baranyai, S. Fischer. Investigation of deformations of ballasted railway track during collapse using the Digital Image Correlation Method (DICM). *Reports in Mechanical Engineering*, Vol. 3(1), 2022, pp. 168-191, <https://doi.org/10.31181/rme20016032022s>
- [35] V. Havryliuk. Detecting of Signal Distortions in Cab Signalling System Using ANFIS and WPESE. *IEEE 4<sup>th</sup> International Conference on Intelligent Energy and Power Systems (IEPS)*, Istanbul, Turkey, 2020, pp. 231-236, <https://doi.org/10.1109/IEPS51250.2020.9263165>

- [36] V. Havryliuk. Model of Propagation of Traction Current Harmonics from Trains to a Track Circuit Receiver. Asia-Pacific International Symposium on Electromagnetic Compatibility (APEMC), Nusa Dua - Bali, Indonesia, 2021, pp. 1-4, <https://doi.org/10.1109/APEMC49932.2021.9597152>
- [37] S. Fischer, S. Szalai. Detection Process of Energy Loss in Electric Railway Vehicles. *Facta Universitatis, Series: Mechanical Engineering*, Vol. 21(1), 2023, pp. 81-99, <https://doi.org/10.22190/FUME221104046F>
- [38] S. Fischer, D. Harangozó, D. Németh, B. Kocsis, M. Sysyn, D. Kurhan, A. Brautigam. Investigation of Heat-Affected Zones of Thermite Rail Weldings. *Facta Universitatis, Series: Mechanical Engineering*, 2023, DOI: <https://doi.org/10.22190/FUME221217008F>
- [39] A. Németh, S. Fischer. Investigation of the Glued Insulated Rail Joints Applied to CWR Tracks, *Facta Universitatis, Series: Mechanical Engineering*. Vol. 19(4), 2021, pp. 681-704, <https://doi.org/10.22190/FUME210331040N>
- [40] S. Szalai, S. Kocsis Szürke, D. Harangozó, S. Fischer. Investigation of Deformations of a Lithium Polymer Cell Using the Digital Image Correlation Method (DICM). *Reports in Mechanical Engineering*, Vol. 3(1), 2022, pp. 116-134, <https://doi.org/10.31181/rme20008022022s>

# Optimum Train Weighing in Motion using Inertial Sensors

**Milad Kazemian<sup>1</sup>, Majid Movahedi Rad<sup>2</sup>, Morad Shadfar<sup>3</sup>,  
Ahmad Mohammadi Doost<sup>3</sup>, Ebrahim Hadizadeh Raisi<sup>4</sup>,  
Szabolcs Fischer<sup>2</sup>**

<sup>1</sup>Faculty of Civil Engineering, Islamic Azad University Science and Research Branch, Hesarak 1477893855, Tehran, Iran, e-mail: milad.kazemian@srbiau.ac.ir

<sup>2</sup>Department of Structural and Geotechnical Engineering, Széchenyi István University, Egyetem tér 1, Győr 9026, Hungary, e-mail: {majidmr,fischersz}@sze.hu

<sup>3</sup>Department of Railway Rolling Stock Engineering, School of Railway Engineering, Iran University of Science and Technology, Narmak 13114-16846, Tehran, Iran, e-mail: st\_r\_maher@azad.ac.ir, m\_amirhosssein@modares.ac.ir

<sup>4</sup>Research and Education Department of Technical and Infrastructure Deputy, General Administration of Khorasan Railway, Kamyab Boulevard 91735-173, Mashhad, Iran, e-mail: hadizadeh\_e@rai.ir

Corresponding author e-mail: fischersz@sze.hu

---

*Abstract: Continuous monitoring with advanced equipment and innovative scientific techniques is essential for timely and perfect maintenance. The interaction and dynamic force between wheel and rail is one of the most widely monitored issues. In this paper's case study of ballasted railway tracks in Iran, a set consisting of two separate strain gauge arrays and three different positions for installing accelerometers were designed according to the conditions. After installation, the system was calibrated with a predetermined passing axle load. The dependency of the arrays' and the equipment's installation location with the velocity of the passing axle load was examined as part of the field study after repeated investigation and comparisons of the setups' results. In order to gather data with the least error and the highest level of accuracy, it was decided on the more appropriate array with less dependence and a better installation position.*

*Keywords: Railway monitoring; Maintenance; Measurement; Strain gauges; Accelerometer*

---

# 1 Introduction

In today's world, a country's infrastructure is viewed as its capital and national wealth since its capacity to develop and progress is determined by how effectively its infrastructure performs. The rail transport industry, which significantly influences people's everyday lives and the environment, is an essential measure of a country's growth. As a result, a condition monitoring system must be established to detect any defects that may appear as safety issues. Consequently, precise information may be acquired by designing novel equipment or integrating cutting-edge technology into a complete monitoring system [1, 2, 3]. Both experimental and numerical studies have the potential to produce big advances. When monitoring railway tracks, many researchers in this field are interested in the interactions and dynamic forces between wheels and rails. However, little experimental research has been conducted on the dynamic effect of heavier freight trains on railway tracks. Strain gauges and accelerometers are two monitoring-related technologies that, based on their functional capacity and sensitivity, should be employed in ideal conditions and an ideal combination, requiring a scientifically intelligent design. Keith *et al.* [4]. In one research, experimental field tests were conducted to investigate how heavy loads induced by large axle loads influenced the dynamic behavior of the railway track. It is demonstrated that when various speed and axle load changes are applied to the wheel-rail dynamic force, dynamic deformation of the track structure, and track vibration behavior, some of the indicators reflecting the dynamic behavior of the railway track increase roughly linearly with train running speed and axle load, while others are barely influenced. Zhiyong *et al.* [5]. The project created a wheel load detector based on a strain gauge for monitoring wheel-rail contact forces at insulated rail joints (IRJs). The laboratory and field testing results showed that the design followed generally recognized theoretical assumptions. Field data vividly depicted the wheel-rail impact force produced across the joint gap, demonstrating its use in recognizing the wheel-rail contact-impact force signature at IRJs. Manicka *et al.* [6]. The necessary fusion technique and the outlined theoretical relationships between the samples gathered by various sensors demonstrated in a comprehensive analysis that the features of the wheel defects used in the data generation step were entirely represented in the defect signals reconstructed by the suggested method. Consequently, the proposed technique enables early defect detection and identification, including small and long-wave flaws. The number of sensors, the effective zone size, and the wheel's circumference, which acts as the defect signal's basic period, all impact the fusion process. Alemi *et al.* [7]. Wheel flaws on railroad wagons have been discovered as a substantial cause of damage to the railroad's infrastructure and rolling equipment, in addition to creating costly noise and vibration emissions. A sensor network is being created for permanent installation on the railway network. Shelling, flat areas, and a lack of roundness are all issues. It outperforms current defect identification approaches for flat spots and predicts the other two kinds of defects. The neural network technique explicitly simulates the multisensory structure of the measurement system via numerous instances, learning, and shift invariant networks to increase performance on wheels with flat areas and non-roundness. Gabriel *et al.*

[8]. Vertical overloads may cause track degradation and safety breaches, but wheel-rail lateral contact forces are more directly connected to running safety. According to the computational and experimental data, the size of the lateral force may be estimated using an independent coefficient obtained from the applied loads. Bruner *et al.* [9]. The curvature of the wheel profile impacts a train's performance in various ways. In a field test, the station monitors the lateral and vertical wheel/rail forces at the point of contact in a 484-meter-radius curve at speeds up to 100 km/h. In a bogie, the four-wheel positions have markedly distinct force signatures. While the strength of the three other high rails increases with distance, the leading high rail has strong forces unaffected by the change in running distance. Palo *et al.* [10]. The issue's placement and sensor needs were investigated in a study on the static and dynamic behavior of ballasted railway tracks. It could be helpful to estimate stress transfer from the train passage to the track using predictive computational models. Georges *et al.* [11]. Weighing in motion systems would assist in solving the shortcomings of conventional static weighing, such as costs and traffic management. Weigh-in-motion systems, however, do not allow direct measurement of the static load since the dynamic interaction between the train and the track results in dynamic loads added to the static ones. Investigating the effect of track unevenness and train speed on the weights measured by the weigh-in-motion system. A rigorous statistical investigation based on multiple computations was done to achieve that purpose. In order to estimate the static load, a technique to rectify the direct result supplied by the weigh in motion system is presented. This strategy is based on the results and patterns discovered throughout the extensive parametric investigation. Mosleh *et al.* [12]. The successful operation of a field test system methodology and the system's optimization should be thoroughly evaluated with regard to various types of trains. This is influenced by the type of sensors and where they are set up. Mosleh *et al.* [13]. The installation of sensors along a railway track's entire length will allow real-time monitoring of the states of its technical components, and the proposal of a diagnostic sensor system based on railway track stress-strain analysis. Avsievich *et al.* [14]. The initial stage in data processing is to determine the speed of a passing train after identifying it (time, date, and direction). For the purpose of calculating train speeds, each peak of a vertical acceleration signal represents the passage of a train axle above the considered accelerometer. Blanc *et al.* [15]. The ability to predict failure of track infrastructure components can be improved through maintenance prioritization and procedures, thereby enhancing the safety of railway operations. Edwards *et al.* [16]. It may be helpful to use an alternative model-based method based on the local response function method that can forecast accurate stress results in particular locations without the need for direct measurement data at those locations. Menghini *et al.* [17]. The degree of fit between actual and estimated track forces and irregularities is demonstrated through point-by-point graphs of actual and estimated values, and indicators of the accuracy of estimates are generated using R-Squared values, which represent the percentage by which the variance of mistakes is less than the variance of actual values. Gadhav *et al.* [18]. When performing calibration and the primary test according to the desired plan, it is crucial to take into account the impact that imbalanced vertical loads have on the data recorded in the monitoring system. Silva *et al.* [19]. A signal analysis approach

based on the analytical domain and monitoring equipment suitable for conditions in the environment will be productive in providing a suitable instrument for studying experimental non-stationary vibration signals comprising shock. Salehi *et al.* [20]. Physical calibrations are crucial in the strain recovery process, in addition to placing the strain gauges optimally to reduce uncertainty in the simulation model. Nieminen *et al.* [21]. The installation of sensors should take into account the best site for installation, and the layout of the sensors really offers a platform for simple installation and a more accurate data recording system. Jing *et al.* [22]. The smart rail pad demonstrated excellent signal response to fluctuations in loading, with an average percent error of 6%. It can be used for load sensing and as an axle counter to measure wheel loads. Schalkwyk *et al.* [23]. In order to track the structural performance of the track and to identify changes in traffic volumes and loading circumstances, analyzing rail pads—a crucial component of railway structural design—that are fitted with various types of sensors is very beneficial. Sol-Sánchez *et al.* [24]. A simulation study is conducted as part of the additional analysis of the findings to establish the precise location of the sensors based on the rail's fatigue life, the likelihood of mistakes and redundancy, and various railway traffic situations. Pillai *et al.* [25]. Comparison of the distributed acoustic sensor (DAS) results with point location measurements made using a conventional strain gauge and deflections determined via imaging and digital image correlation (DIC), provides accurate distributed strain measurements with the capability for continuous spatial and temporal coverage across substantial tracts of track. These measurements translate to estimates of track deflection and load. Milne *et al.* [26]. When a sizable high number of strain gauge pair installations are made in the track, a realistic assessment of the static load may be made. Therefore, a statistical correlation must be taken into account when calculating the static load from weigh-in-motion (WIM) systems with fewer sensors. This means that the estimation of the static load interval should take a certain level of confidence into account for each of the vehicle wheelsets. Pintão *et al.* [27]. Shear strain data at specific locations has been used to develop mechanics-based algorithms to estimate the speed and wheel loads of trains passing over a bridge under study. The speed estimation algorithm uses shear strain at quarter span and takes the train's speed variation into account. For wheel load estimation, two algorithms are studied. The shear strain algorithm only makes use of the peak value of the shear strain measured at an axial location close to the bridge. [28]. With the advancement of the transportation industry and the demand, the settlement and wear of the ballast caused by dynamic stresses at high frequencies is still an important issue on high-speed tracks, leading to high maintenance costs. Khairallah *et al.* [29]. A more thorough, real-time, and current understanding of the railway track condition would be made possible by predictive maintenance operations carried out with cutting-edge monitoring systems. As a result, maintenance expenses would go down because interventions would only be made when they were truly necessary. In-depth discussion will also be given on monitoring systems that keep track of temperature, stresses, displacements, strain measurements, train speed, mass, and position, axle counts, wheel flaws, rail settlements, wear and tear, and the condition of railroad bridges and tunnels [30, 31]. A field investigation Two stiff common crossings were the

subject of experimental observations under the dynamic stress of a high-speed train. According to the findings, the maximum displacements within a specific velocity range increased by 2.5 times. Due to the relative displacement measurements between the rail and the sleeper, the different dynamic impact loading for the wing rail, and the lack of a difference in displacements between the trailing and facing travel directions, measured maximal strains are not as explicit as the displacement results. Kovalchuk *et al.* [32]. Ingenious methods and routine inspections are two of the key factors that influence the cost of railway maintenance, according to both laboratory and numerical studies. Modern monitoring techniques, prognostics, and health management strategies provide a wealth of opportunities for improving inspection and maintenance procedures. [33, 34].

However, there are still lots of required optimization for different stages of measuring wheel-rail force from software and hardware points of view. Most research are presented with a fixed arrays of sensors, which is one of the major challenge in correct data acquisition. It also needs to consider track maintenance issues. The challenge of correct data acquisition mainly lies in sensor array and arrangement design, which determines quality of the signal. In this paper, different arrays and locations of the strain gauges and accelerometers are studied for data collection. The results are analysed and discussed and sensitivity against velocity are also considered.

## 2 Field test

### 2.1 Scope of Study



Figure 1

The test site and its location relative to Mashhad railway station

The location of the study area which is between the Chaman and Sarkhes bridges and 2,392 meters away from the Mashhad railway station, is shown in more detail in Figure 1, along with its position in relation to the Mashhad railway station. The aforementioned location has two input and output lines that are connected to the Chaman concrete deck bridge on the west side and the railway switches on the east side, respectively. The passing train speed is approximately 80 km/h, and test equipment was installed on tangent railroad part in the exit line.

## 2.2 Railway Track System

Figure 2 depicts the layout of a ballasted railroad track. The sleepers are attached to two rails (there is an elastic pad between the rail and the sleepers). This set is situated on a ballast layer, allowing for the safe and easy passage of trains. The characteristics of the ballast layer, rails, and rail pads affect the track's dynamic performance. To keep track performance, maintenance actions are needed which are mainly focused on the area between two sleepers. The tamping machine is used to keep the ballast layer quality in check which uses rail web on the area between sleepers and support. There are also some actions required for bolt tightening. Considering all of this, the rail web in the area on the sleeper would be the safest place for sensor installation. The sensor must be able to provide accurate data on this location, too. The following is a quick list of the test site pavement's technical specifications:

- Rail type: UIC60 heavy, rail weight is 60.34 kg/m
- Sleeper type: Mono block concrete sleeper, total weight of the sleeper is 260 kg
- Fastening type: Weslo type spring fastener, its weight is 503 gr
- Ballast type: Mostly made of porphyry and metamorphic rocks

As mentioned in the Introduction, accelerometers can measure track dynamic performance, whereas strain gauges are typically less sensitive to track dynamics and track structure failures. As a result, both kinds of sensors should be used to measure all static and dynamic components of a contact force measurement.



Figure 2  
Railway components details

### 2.3 Test Equipment

As previously mentioned, the instruments were installed on a tangent part of the railroad so the operation conditions, such as speed and bogie normal function, would be under control, and any abnormality within the bogie and wheels would be monitored with higher accuracy. Specifications for used strain gauges, accelerometers, and data logger can be found in Tables 1 to 3.

Table 1  
Strain gauge technical specification used for field test (detailed)

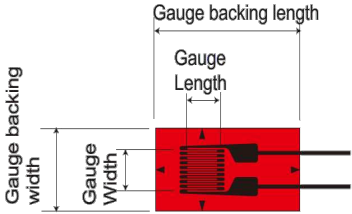
	<table border="0"> <tr> <td>Applicable specimen</td> <td>Metal, Glass, Ceramics</td> </tr> <tr> <td>Backing</td> <td>Special plastics</td> </tr> <tr> <td>Element</td> <td>Cu-Ni</td> </tr> </table>	Applicable specimen	Metal, Glass, Ceramics	Backing	Special plastics	Element	Cu-Ni														
Applicable specimen	Metal, Glass, Ceramics																				
Backing	Special plastics																				
Element	Cu-Ni																				
<table border="0"> <tr> <td>Operational temperature (°C)</td> <td>-196 ~ +150°C</td> <td>Temperature compensation range (°C)</td> <td>+10 ~ +100°C</td> </tr> <tr> <td>Strain limit</td> <td>5% (<math>50000 \times 10^{-6}</math> strain)</td> <td>Applicable adhesive</td> <td>CN, P-2, EB-2</td> </tr> <tr> <td>Fatigue life at room temperature</td> <td><math>1 \times 10^6</math> (<math>\pm 1500 \times 10^{-6}</math> strain)</td> <td>Gauge length (mm)</td> <td>0.5</td> </tr> <tr> <td>Gauge width (mm)</td> <td>1.2</td> <td>Backing length (mm)</td> <td>5</td> </tr> <tr> <td>Backing width (mm)</td> <td>2.2</td> <td>Resistance (<math>\Omega</math>)</td> <td>120</td> </tr> </table>	Operational temperature (°C)	-196 ~ +150°C	Temperature compensation range (°C)	+10 ~ +100°C	Strain limit	5% ( $50000 \times 10^{-6}$ strain)	Applicable adhesive	CN, P-2, EB-2	Fatigue life at room temperature	$1 \times 10^6$ ( $\pm 1500 \times 10^{-6}$ strain)	Gauge length (mm)	0.5	Gauge width (mm)	1.2	Backing length (mm)	5	Backing width (mm)	2.2	Resistance ( $\Omega$ )	120	
Operational temperature (°C)	-196 ~ +150°C	Temperature compensation range (°C)	+10 ~ +100°C																		
Strain limit	5% ( $50000 \times 10^{-6}$ strain)	Applicable adhesive	CN, P-2, EB-2																		
Fatigue life at room temperature	$1 \times 10^6$ ( $\pm 1500 \times 10^{-6}$ strain)	Gauge length (mm)	0.5																		
Gauge width (mm)	1.2	Backing length (mm)	5																		
Backing width (mm)	2.2	Resistance ( $\Omega$ )	120																		

Table 2  
 Technical specification of the wired accelerometer used in field test

AC102-1A				
	Sensitivity ( $\pm 10\%$ )	100 mV/g	Spectral Noise @ 10 Hz	14 $\mu\text{g}/\sqrt{\text{Hz}}$
	Frequency Response ( $\pm 3\text{dB}$ )	0,5-15000 Hz	Spectral Noise @ 100 Hz	2.3 $\mu\text{g}/\sqrt{\text{Hz}}$
	Frequency Response ( $\pm 10\%$ )	2,0-10000 Hz	Spectral Noise @ 1000 Hz	2 $\mu\text{g}/\sqrt{\text{Hz}}$
	Dynamic Range	$\pm 50$ g, peak	Output Impedance	<100 ohm
	Settling Time	<2.5 seconds	Bias Output Voltage	10-14 VDC
	Voltage Source	18-30 VDC	Case Isolation	>10 <sup>8</sup> ohm
	Constant Current Excitation	2-10 mA		

Table 3  
 Technical specification of data logger used in field test

Analog inputs	8 ch voltage, IEPE, current (with ext. Shunt)
ADC type	16 bit SAR with 100 kHz 5th order analog AAF filter or bypass (500 kHz)
Sampling rate	Simultaneous 1 MS/s
Ranges	$\pm 10$ V, $\pm 5$ V, $\pm 1$ V, $\pm 0.2$ V
Typ. SNR @ 100 kHz	89 dB
Input coupling	DC or AC (1 Hz)
Input impedance	1 M $\Omega$
IEPE mode	4 or 8 mA excitation; Sensor detection (Short: <4 V; Open: > 19 V)
TEDS	Supported in IEPE mode
Overvoltage protection	50 V continuous; 200 V peak (10 msec)
Typical power consumption (max.)	15 (22 W)

## 2.4 Tested Rail Fleet

The fleet used in this project includes Siemens locomotives and passenger wagons made in Germany, whose pictures are shown in Figure 3 and their technical specifications are in Tables 4 and 5.



Figure 3

Passing locomotive and wagons used in the test program

Table 4

General specification of Locomotive used in field test

Fleet	Loco type	Made in	Min speed (km/h)	Max speed (km/h)	Ax-to-Ax distance of two bogies (mm)	Ax-to-Ax distance of two axles in a bogie (mm)	Wheel diameter (mm)	Axle load (tonne)
Locomotive	ER24PC BO-BO	Germany 2011- 2016	39.4	160	10362	2700	1100	20

Table 5

General specification of Wagons used in field test

Fleet	wagon type	Made in	Min speed (km/h)	Max speed (km/h)	Wagon weight - empty (tonne)	Wagon weight - full (tonne)	Bogie type of wagon	Axle load (tonne)
Wagon	RL11	Germany	-	140	45	50	MD36	11.25

### 3 Test Plan

The following key factors should be taken into account when measuring the wheel-rail contact force:

- Repeatability of measurements, taking train wheel radius and speed into account.
- Installation time should be minimized; the instruments should not interfere with maintenance vehicles if long-term measurement is required.
- To be able to avoid the need for expensive speed detectors, the vehicle's speed should be calculated with the highest degree of accuracy.
- The force calculation method should be able to analyze all data as quickly and accurately as possible and report the results.
- The configuration should be safe and not require routine manual calibration and maintenance.

The sensor formation was designed with the previously mentioned issues in mind. Figure 4 shows a schematic representation of the rail web with the installed equipment and sensor configuration. All the accelerometers are in vertical direction and strain gauges are installed as half-bridge circuit. The strain gauge arrays in this paper come in two varieties: "V" and "<". In comparison, the "<"-shaped array is concentrated on the bending strain, and the "V"-shaped arrays deal with shear strain when there is a wheel passage. Normally, calculation of wheel vertical force focuses on bending strain, which has an interference with maintenance issues. The V array is introduced to cover this shortcoming.

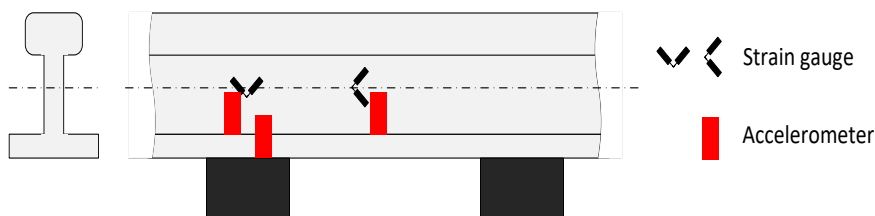


Figure 4

Configuration of strain gauges and accelerometers on the rail web

To make sure that no data is missing, it is necessary to measure in a complete round. So, for every passage, the whole wheel surface is scanned. The designed sensor arrangement and localization are done to ensure the mentioned condition is met. This arrangement is also able to analyze the wheel multiple times with the help of different combinations of installed sensors, so the error would reduce noticeably. It means a higher calculation volume with no change in the response time of the device. With the configuration shown in Figure 5, one side of the passing train is completely covered, allowing for accurate comparisons. Accelerometers are very sensitive to the track structure's defects, in contrast to strain gauges, whose results are essentially independent of such defects. So keeping track's quality high in the

instrumented area is crucial. The accelerometers' installation position can also help determine the wheel's dynamic component. In order to investigate the dynamic component of the vertical forces of the wheels, three different accelerometer positions are taken into account: 1) on the rail foot in the rail's position on the sleeper, 2) on the sleeper, and 3) on the rail foot, between the sleepers.

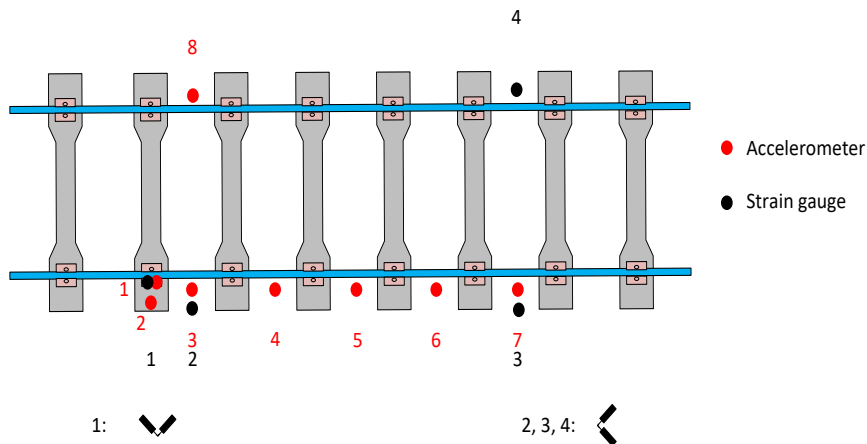


Figure 5

Locations of sensors and their types

In order to control operation conditions like speed and bogie normal function and to more accurately monitor any abnormalities within the bogie and wheels, the instruments were installed on a tangent track, as it is shown in Figure 6.



Figure 6  
Instrumentation location on tangent track



Figure 7  
The drezin used for system calibration

As shown in Figure 7, the system was initially calibrated using a drezin (a light rail vehicle) with known axle load. Table 6 describes the calibration procedure, which also includes load and speed. Using locomotives from passing trains with axle loads of 19.75 tons, the main calibration is carried out (9.875 tons per wheel).

Table 6  
Calibration condition for drezin

Test condition	Number of tests
V=5 km/h	2
V=10 km/h	2
V=20 km/h	2
V=40 km/h	2

## 4 Result

### 4.1 Strain Gauge Results

Results of recorded data caused by drezin passage is illustrated in Figures 8 for strain channels. The sudden jump in the diagram is caused by shear strain, which is proportional to the axle load and velocity as the wheel passes over the sensor. These quantities can be found and measured to determine the wheel load. By calculating the phase difference between these sensors, velocity can also be determined.

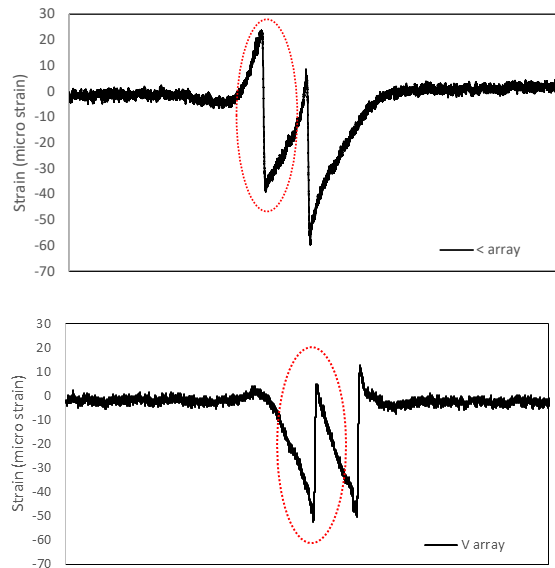
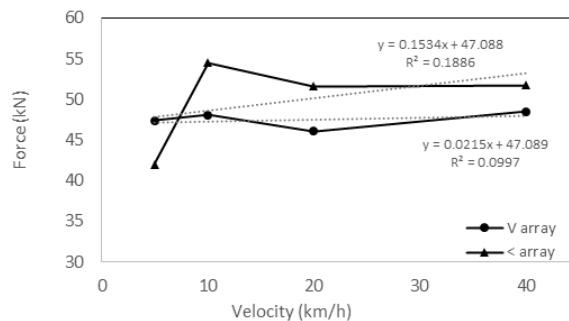


Figure 8

Measured strain for "<" array (up) and "V" array (down)

The drezin used for primary calibration weighs 4.8 tons and has a wheelbase of 2.7 meters. By plotting the shear strain mentioned in Figures 8 in terms of velocity, Figure 9 is obtained. The value shown for each speed is the average of all channels and passages. The dependency of the two mentioned arrays on velocity is relatively low and linear. It should also be noted that the proposed "V" arrangement has a lower dependency on velocity compared to the "<" arrangement. These would enable measuring the static components of the signal with higher accuracy due to the probable error in the velocity calculation. Additionally, the mean squared error for "V" array is lower than the conventional "<" array.



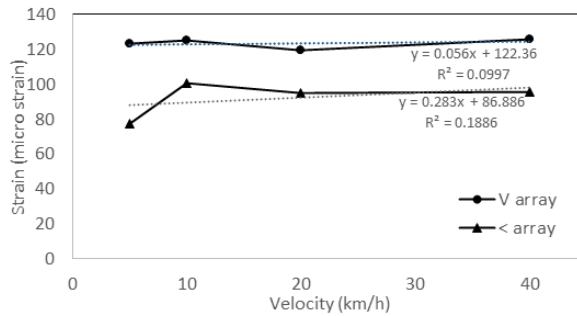


Figure 9

Linear pattern for velocity – drezin passage results, Force (up) and Strain (down)

The results of the entire passage for a passenger train pulling a locomotive weighing 79 tons are shown in Figure 10. The values in Figure 10-top are for Channel 1 in Figure 5 with the "V" arrangement, and the rest are for Channels 2–4 with the "<" arrangement, respectively. The train passages are completely recorded by both passages, which display the same pattern. Therefore, the "V"-shaped array can be considered an alternative to the "<"-shaped array, which conflicts with track maintenance activities.

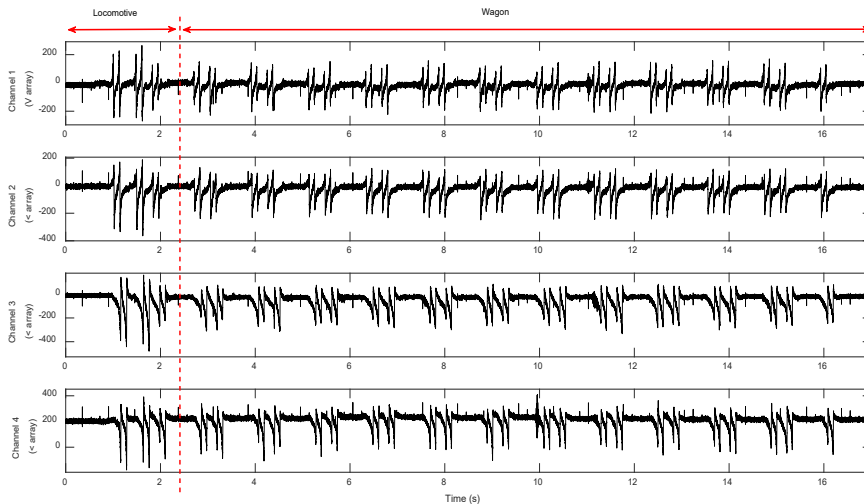


Figure 10

Strain results for a passenger train

Figure 11 displays the strain results proportional to vertical loads for a locomotive (79 tons in weight) for various passages. Higher speeds and axle loads can produce the same patterns and outcomes (compared to primary calibration). Despite the different velocity dependencies, the pattern is still linear. While this parameter has increased for the "<"-shaped array from 0.283 to 0.4833, it has decreased from

0.056 to 0.0326 for the "V"-shaped array. So calibration is required for various speed ranges. These findings demonstrate the benefits of a "V"-shaped array's lower dependence on speed when needed. It should be noted that more research should be done to determine how sensitive this arrangement is to track failures. Similar to the drezin test, as it is shown in figure 11, values for error is lower in "V" array.

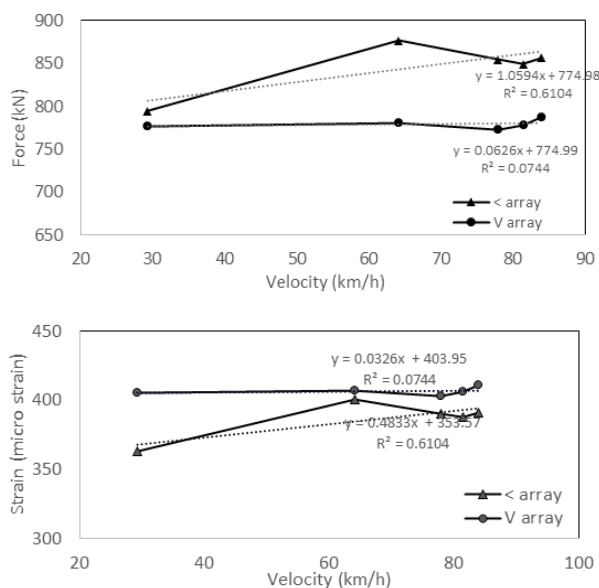


Figure 11

Linear pattern for velocity in vertical load calculation – Locomotive passage results, Force (up) and Strain (down)

## 4.2 Acceleration Results

As earlier described, accelerometers are much more sensitive than strain gauges to the track structure's defects, the results of which are essentially independent of them. So keeping track's quality high in the instrumented area is crucial. The accelerometers' installation position can also help determine the wheel's dynamic component. In this research, the authors installed accelerometers at three different positions: on the rail foot in the position of the rail on the sleeper, on the sleeper, and the rail foot in the distance between sleepers, to investigate the dynamic component of the vertical forces of the wheel and rail (see Figures 4 and 5). Figure 12 shows the three positions' time domain and Short Time Fourier Transform (STFT) [35] values. This transformation has a 1024-point window with a 1000-point overlap. The window type is Gaussian, and the sampling frequency is 10 kHz.

The wheel passage is clearly shown in Figure 12-b. In other words, the rail and rail pad had a low-pass filtration influence on the acceleration signal as it passed

through them. There is also much noise in Figures 12-a and 12-c. This illustration emphasizes the importance of signal filtering in order to identify various failures. The characteristics of the track superstructure have a significant impact on the accelerometer's response as well. In summary, it can be said that moving the accelerometer from between the sleepers (channel 3) to the sleepers (channel 1) has no detrimental impact on the precision of the measured signal. But results from channel 2 can be used with minimum pre-processing.

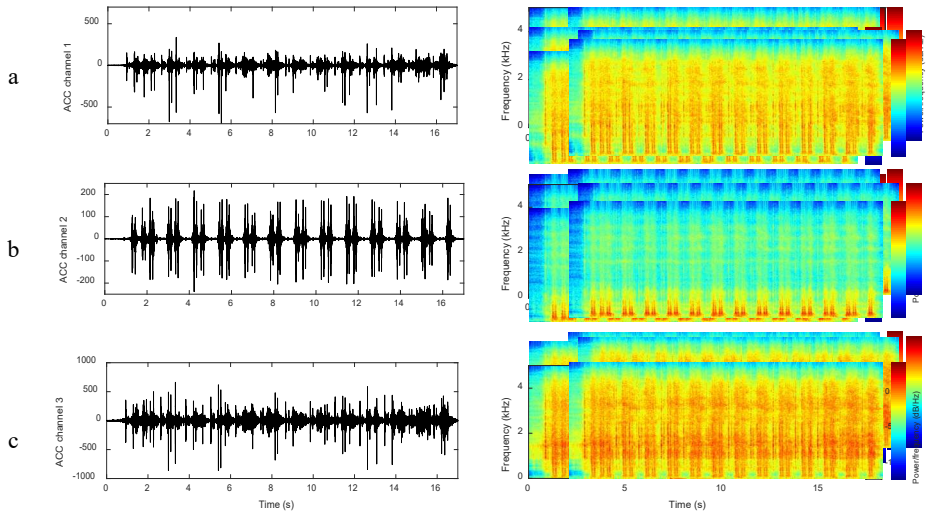
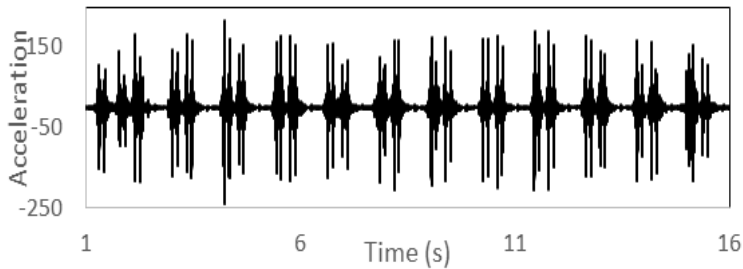


Figure 12

Acceleration results for a passenger train

So, the strain gauges V-array and sleeper mounted acceleration can accurately measure static and dynamic forces of wheel-rail system. Combining results from these two sensors would results to figure 13. The region 1~3 is healthy wheel (or monitor state), 3~4 stands for maintenance schedule, 4~5 is maintenance priority and >5 is immediate action. Te presented array and setup could provide condition monitoring of rail fleet to increase safety and reduce maintenance costs.



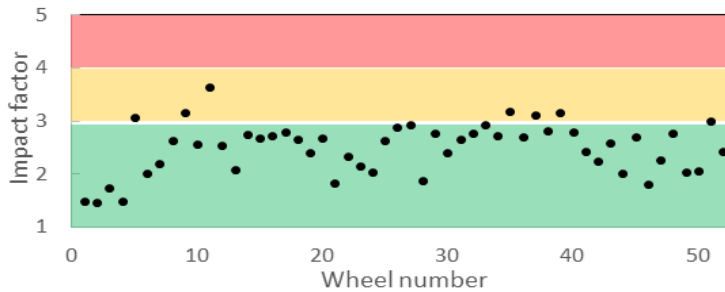


Figure 13

Converted results in impact factor (acceleration's unit is  $m/s^2$ , hence wheel number's is piece)

## Conclusions

In this study, with the help of a field test, the results of two different strain gauge arrangements and accelerometer installation positions and their differences in measuring the dynamic force between the wheel and the rail were investigated and compared. In Iran's Mashhad railway station, the railroad track was instrumented for a field test, and the results were analyzed in two steps: 1) a light rail vehicle (drezin) with low weight and speed, and 2) a passenger train with relatively high axle load and speed. The results are summarized as follows:

"V" and "<" arrays were put to the test as half bridges for strain gauges. When there are only minor velocity changes, the "V" arrangement is practically velocity-independent.

The "V"-arrangement has an advantage because of its installation location, which causes less interference with track maintenance operations.

The "V" array showed lower error compared to the "<" array.

The results must be calibrated for various speed ranges. In contrast to the "<" array, the "V" array also demonstrated a decrease in velocity dependence with increasing velocity. Further research is required into the "V" array's dependence on the state and caliber of the track.

For the acceleration, the installed accelerometer on the sleeper showed lower noise and dependency to track dynamics, which will require less data preparation. The reason is the filtering phenomenon of the passing signal through rail pad and sleeper.

The presented arrays can be used for optimum condition monitoring of wheel-rail system.

## References

- [1] S Weston, P. F., Goodman, C. J., Li, P., Goodall, R. M., Ling, C. S., Roberts, C., Track and Vehicle Condition Monitoring During Normal Operation

- Using Reduced Sensor Sets, HKIE Transactions, Special Issue on Railway Development in the 21<sup>st</sup> Century, March, 2006, pp. 47-53
- [2] S Ho, S. L. and Lee, K. K. and Lee, K. Y. and Tam, H. Y. and Chung, W. H. and Liu, S. Y. and Yip, C. M. and Ho, T. K., A comprehensive condition monitoring of modern railway. In: Proceedings of The Institution of Engineering and Technology International Conference on Railway Condition Monitoring, 2006, 29-30 November 2006, Birmingham
- [3] H Lee, K. Y., Lee, K. K., Ho, S. L., Exploration of Using FBG Sensor for Axle Counter in Railway Engineering, WSEAS Transactions on Systems, Issue 6, Vol. 3, August, 2004, pp. 2440-2447
- [4] Keith Bladon & Philip Beck., monitoring rolling stock wheel condition. Teknis Electronics, IRSE - Adelaide - July 1996
- [5] Shi, Z., Wang, K., Zhang, D., Chen, Z., Zhai, G., & Huang, D. (2019) Experimental investigation on dynamic behavior of heavy-haul railway track induced by heavy axle load. *Transport*, 34(3), 351-362
- [6] Manicka Dhanasekar, Hossein Askarinejad., Determining wheel–rail vertical contact force at insulated rail joints. CRC for Rail Innovation, 23 May 2011
- [7] Alireza Alemi, Francesco Corman, Yusong Pang, Gabriel Lodewijks., Reconstruction of an informative railway wheel defect signal from wheel–rail contact signals measured by multiple wayside sensors. *Journal of Rail and Rapid Transit*, July 2018
- [8] Gabriel Krummenacher, Cheng Soon Ong, Stefan Koller, Seijin Kobayashi, Joachim M. Buhmann, Senior Member., Wheel Defect Detection With Machine Learning. *IEEE transaction on intelligent transportation system*, VOL. 19, NO. 4, APRIL 2018
- [9] M. Bruner, M. Catena, D. Cortis, G. Malavasi, S. Rossi, M. Testa., Estimation of the wheel-rail lateral contact force through the analysis of the rail web bending strains. *Elsevier, Measurement* 99 (2017) 23-35
- [10] Mikael Palo, Håkan Schunnesson, Uday Kumar., Condition monitoring of rolling stock using wheel/rail forces. *The Ninth International Conference on Condition Monitoring and Machinery Failure Prevention Technologies*, 2012
- [11] Georges Kouroussis, Christophe Caucheteur, Damien Kinet, Georgios Alexandrou, Olivier Verlinden, Véronique Moeyaert., Review of Trackside Monitoring Solutions. From Strain Gages to Optical Fibre Sensors, 2015, 15, 20115-20139
- [12] Mosleh , Pedro Alves Costa, Rui Calc,ada., A new strategy to estimate static loads for the dynamic weighing in motion of railway vehicles. *Proc IMechE Part F: J Rail and Rapid Transit*, 24 February 2019

- [13] Mosleh A, Montenegro PA, Costa PA, Caçada R. Railway vehicle wheel flat detection with multiple records using spectral kurtosis analysis. *Applied Sciences*. 2021 Apr 28;11(9):4002
- [14] Avsievich A, Avsievich V, Avsievich N, Ovchinnikov D, Ivaschenko A. Railway Track Stress–Strain Analysis Using High-Precision Accelerometers. *Applied Sciences*. 2021 Dec 14;11(24):11908
- [15] Blanc J, Khairallah D, Ramirez D, Chupin O, Pouget S, Ta QA, Duval A, Hornych P, Benoist S. Monitoring of railway structures with bituminous and granular sub-layers: Assessment after four years of use. *Construction and Building Materials*. 2022 Jun 20;336:127515
- [16] Edwards JR, Mechitov KA, Germoglio Barbosa I, de O. Lima A, Spencer Jr BF, Tutumluer E, Dersch MS. A Roadmap for Sustainable Smart Track—Wireless Continuous Monitoring of Railway Track Condition. *Sustainability*. 2021 Jul 3;13(13):7456
- [17] Menghini A, Leander J, Castiglioni CA. A local response function approach for the stress investigation of a centenarian steel railway bridge. *Engineering Structures*. 2023 Jul 1;286:116116
- [18] Gadhav R, Vyas NS. Rail-wheel contact forces and track irregularity estimation from on-board accelerometer data. *Vehicle System Dynamics*. 2022 Jun 3;60(6):2145-66
- [19] Silva R, Guedes A, Ribeiro D, Vale C, Meixedo A, Mosleh A, Montenegro P. Early Identification of Unbalanced Freight Traffic Loads Based on Wayside Monitoring and Artificial Intelligence. *Sensors*. 2023 Jan 31;23(3):1544
- [20] Salehi M, Bagherzadeh SA, Fakhari M. Experimental detection of train wheel defects using wayside vibration signal processing. *Structural Health Monitoring*. 2023:14759217221149614
- [21] Nieminen V, Tuohineva A, Autio M. Wheel load reconstruction using strain gauge measurements on the bogie frame for strain prediction and fatigue assessment. *International Journal of Fatigue*. 2023 Jan 20:107533
- [22] Jing G, Siahkouhi M, Qian K, Wang S. Development of a field condition monitoring system in high speed railway turnout. *Measurement*. 2021 Feb 1;169:108358
- [23] van Schalkwyk MH, Gräbe PJ. Condition monitoring of train wheels using a cost-effective smart rail pad. *Engineering Research Express*. 2022 Sep 5;4(3):035045
- [24] Sol-Sánchez M, Castillo-Mingorance JM, Moreno-Navarro F, Rubio-Gómez MC. Smart rail pads for the continuous monitoring of sensed railway tracks: Sensors analysis. *Automation in Construction*. 2021 Dec 1;132:103950

- 
- [25] Pillai N, Shih JY, Roberts C. Sensor Selection and Placement for Track Switch Condition Monitoring through Validated Structural Digital Twin Models of Train–Track Interactions. *Engineering Proceedings*. 2021 Nov 1;10(1):49
- [26] Milne D, Masoudi A, Ferro E, Watson G, Le Pen L. An analysis of railway track behaviour based on distributed optical fibre acoustic sensing. *Mechanical Systems and Signal Processing*. 2020 Aug 1;142:106769
- [27] Pintão B, Mosleh A, Vale C, Montenegro P, Costa P. Development and validation of a weigh-in-motion methodology for railway tracks. *Sensors*. 2022 Mar 3;22(5):1976
- [28] Deepthi TM, Saravanan U, Meher Prasad A. Algorithms to determine wheel loads and speed of trains using strains measured on bridge girders. *Structural Control and Health Monitoring*. 2019 Jan;26(1):e2282
- [29] Khairallah D, Chupin O, Blanc J, Hornych P, Piau JM, Ramirez Cardona D, Ducreau A, Savin F. Monitoring and modeling railway structures on high-speed lines with asphalt concrete underlay: A study on the Bretagne–Pays de la Loire line. *Transportation Research Record*. 2020 Dec;2674(12):600-7
- [30] Castillo-Mingorance JM, Sol-Sánchez M, Moreno-Navarro F, Rubio-Gómez MC. A critical review of sensors for the continuous monitoring of smart and sustainable railway infrastructures. *Sustainability*. 2020 Nov 12;12(22):9428
- [31] Du C, Dutta S, Kurup P, Yu T, Wang X. A review of railway infrastructure monitoring using fiber optic sensors. *Sensors and Actuators A: Physical*. 2020 Mar 1;303:111728
- [32] Kovalchuk V, Sysyn M, Gerber U, Nabochenko O, Zarour J, Dehne S. Experimental investigation of the influence of train velocity and travel direction on the dynamic behavior of stiff common crossings. *Facta Universitatis, Series: Mechanical Engineering*. 2019 Nov 29;17(3):345-56
- [33] Szalai S, Eller B, Juhász E, Movahedi MR, Németh A, Harrach D, Baranyai G, Fischer S. Investigation of deformations of ballasted railway track during collapse using the Digital Image Correlation Method (DICM) Reports in *Mechanical Engineering*. 2022 Mar 16;3(1):168-91
- [34] Sysyn M, Nabochenko O, Kovalchuk V, Gruen D, Pentsak A. Improvement of inspection system for common crossings by track side monitoring and prognostics. *Struct. Monit. Maint*. 2019 Sep;6(3):219-35
- [35] Cohen L. (1995) "Time-Frequency Analysis: Theory and Applications" Prentice-Hall, Inc., Upper Saddle River, NJ, USA

# Performance Analysis and Related Data Utilization of Rapid Crack Inspection Technology for Railway Tunnel Lining Surface

**Qiankuan Feng<sup>1</sup>, Yan Huang<sup>2</sup>, Guohua Song<sup>1</sup>, Zhaoning Wang<sup>1</sup>,  
Yan Gao<sup>1\*</sup>, Shilei Wang<sup>1</sup>**

<sup>1</sup>Infrastructure Inspection Research Institute, China Academy of Railway Sciences Corporation Limited, NO. 2 Daliushu Road, Haidian District, Beijing, China 100081

<sup>2</sup>Track Maintenance Department, China Railway Nanning Bureau Group Corporation Limited, NO. 21 Foziling Road, Qingxiu District, Nanning City, Guangxi China, 530022

e-mail: fqk@rails.cn, jcsqsb@rails.cn, songguohua@rails.cn,  
wangzhning@rails.cn, gaoyan@rails.cn, wangshilei@rails.cn)

---

*Abstract: As an important means, the vehicle-mounted imaging technology is usually used to acquire the status data of cracks on lining surfaces of large-scale railway tunnels in operation. Taking a 4 km railway tunnel as a test sample, this paper firstly verified the performance of a vehicle-mounted lining crack inspection system, and analyzed the key performance parameters such as crack inspection rate, length recognition accuracy, mileage positioning error, etc. After its effectiveness was verified, the inspection system was used to inspect the lining cracks of operation railway tunnels with total length of 55 km. The test results show that 60% of cracks with the width of less than 0.3 mm could be inspected, while the figure for the cracks with the width of more than 0.3 mm was 93%. At the confidence level of 90%, the errors in crack mileage and longitudinal crack length are  $\pm 0.8$  m and  $\pm 0.7$  m respectively. There exists splicing redundancy between circumferential cracks, and the error is proportional to the number of channels spanned by the cracks. The statistics of lining cracks of operation railway tunnels with total length of 55 km show that circumferential cracks, longitudinal cracks, oblique cracks and water seepage cracks accounted for 55%, 23.1%, 16.9%, and 1.5% of the total, respectively. According to the lining crack state assessment criteria, single-inspected cracks are classified as those that need "focus" and "attention" respectively. In consideration of the impact of crack shapes on the lining structure safety, data utilization strategies for different types of cracks are proposed in this paper.*

*Keywords: operation railway tunnel; lining; surface crack; rapid inspection; inspection data utilization*

---

## 1 Introduction

As in 2021, the operating mileage of railway tunnels in China had totaled up to 19,000 km. The tunnels put into operation in the past 10 years and 20 years accounted for 64% and 81% of the total tunnels, respectively [1].

Due to differences in construction periods, uncertainties in construction quality, and complexity in geological and hydrological conditions, the tunnels in operation have various types of defects and diseases. After a long-term evolution, most of tunnel linings are subject to damages mainly including cracking, water seepage, deformation, etc. Shear cracks are the main diseases that affect the overall performance of lining. Concrete shear failure is a premature, brittle failure that leads to the progressive collapse of the entire structure. In most cases, severe cracking emerges, and propagation takes place immediately [2]. Therefore, tunnel lining conditions are related to diseases' development rate and impact, and need to be observed for a long-term [3].

At present, the diseases of tunnel lining are mainly inspected manually. However, the inspection accuracy is limited due to the restriction in skylight time, lighting condition, inspection distance, etc., thereby resulting in the increasingly prominent contradiction between the inspection technology and the scale of operating tunnels [4]. Digital Image Correlation Method (DICM) is a new technique that can be used to detect the pattern of cracks in concrete [5] [6]. Károlyfi *et al.* [7] [8] studied the correspondences between formwork geometry and concrete composition in the case of fair-faced concrete elements, and proposed an evaluation method for discoloration of the fair-faced concrete surfaces using digital image processing techniques. Now the apparent imaging inspection system based on the mobile platform can be used to obtain the data on the distribution of apparent lining diseases such as cracking and water seepage [9] [10]. The development of machine learning technology has made it possible to conduct the large-scale periodic inspection of tunnels via the apparent imaging technology. In this regard, a lot of studies and practices have been carried out at home and abroad [11] [12]. The inspection speed of the equipment used in these studies is mostly 5~10 km/h, and relatively few fast detection equipment with detection speed above 20 km/h. In 2013, the Spanish company Euroconsult developed a rail-road tunnel inspection vehicle with an inspection speed of up to 30 km/h [13]; In 2020, JR East launched the fourth-generation tunnel lining inspection system (TuLIS) equipped with 12 sensors (lasers + cameras). With a inspection speed of 20 km/h, it is mainly used to inspect lining surface conditions and 3D shapes of tunnel section [14]. In 2018, China Academy of Railway Sciences developed an inspection vehicle for high-speed railway tunnels [15] to inspect the defects behind the lining, and surface diseases. This inspection vehicle features a geological radar inspection speed of 3 km/h, an imaging inspection speed of 50 km/h, and a crack recognition accuracy of 0.5 mm.

Digital tunnel inspection has received extensive attention because it is conducive to more efficient, objective and scientific analysis and management of tunnel

conditions. In 2016, VRVIS Research Center and Vienna University of Technology in Austria jointly developed an integrated geometric view-based system for visual analysis of tunnel lining damage data on the basis of using the visual analysis tool Visplore and the 3D real-time rendering engine Ardvark [16]. The digital management software developed by German company SPACETEC for the purpose of tunnel inspection is mainly composed of Tunnel-Info, Tu-View, Tunnel-Inspector, Tu-Drive and other modules [17].

## 2 Lining Surface Inspection System (LSI system)

This paper introduces a system for rapid inspection of cracks on the railway tunnel lining surface. This system is used to quickly capture high-definition images of lining surface and automatically identify lining surface defects.

### 2.1 Integrated System Hardware

The LSI system mounted on the wheel-track tunnel inspection vehicle comprises a high-definition acquisition module, a mileage positioning module, and a data processing module (Figure 1). Among them, the high-definition acquisition module consists of 8 CCD line-scan cameras, lighting units, and synchronization control units. The 8 cameras with a laser-assisted illumination instrument are controlled by the synchronization unit, which can ensure the data collected via each channel are related to the same lining section. The mileage positioning module is used to obtain the pulse count of the encoder mounted on the axle, calculate the real-time mileage and speed, and realize the longitudinal mileage positioning of images. This system supports a maximum inspection speed of 80 km/h.

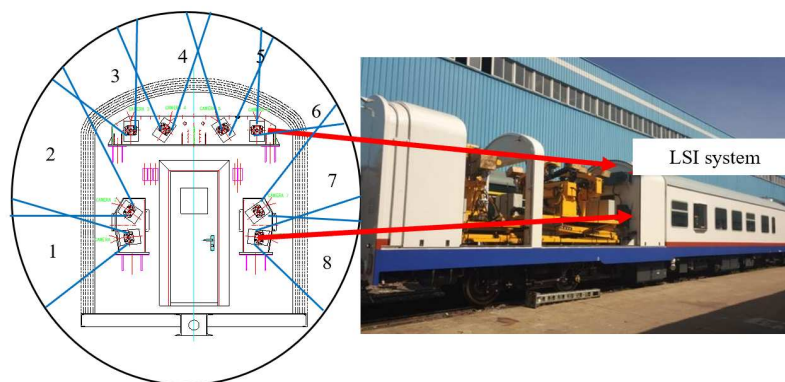


Figure 1  
Lining surface inspection system

## 2.2 Data Processing and Crack Recognition

Lining surface cracks are identified mainly through automatic recognition and manual verification. Automatic recognition is based on the optimized Simple Linear Iterative Clustering (SLIC) algorithm as a gradient-based super-pixel segmentation algorithm, and the lining crack dataset CLS-CRACK is constructed. In addition, the ResNet18 network architecture and Caffe deep learning framework are used for crack recognition, and the DeepLabv3 framework is used to extract crack data through the segmentation network. Through automatic recognition, the images indicating the existence of cracks will be preliminarily screened out, and abnormal areas of the image with suspected cracks will be marked. After the mistakes of automatic recognition are corrected through manual verification, it is possible to confirm the cracks and calculate their lengths, widths, areas and other characteristics parameters.

## 3 Performance Analysis of Lining Surface Inspection System

In order to verify the performance of the LSI system, the data on actual distribution of lining cracks of a 4 km railway tunnel in operation were obtained via site survey and Amberg imaging equipment. Then, those data were compared with the results of LSI system under the condition of 50 km/h, to assess key performance parameters such as crack inspection rate, length measurement error, mileage positioning error, etc.

### 3.1 Site Survey

The 4 km site survey area of railway operation tunnel was tested (2 km inward from the large and small mileage entrance of tunnel), covering the plain concrete section and reinforced concrete section (Figure 2). The scope of site survey covers the left and right side walls of lining, namely an area 3 m upward the sidewalk slab.

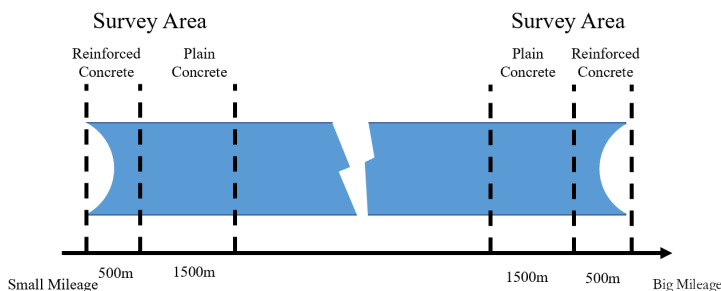


Figure 2  
Schematic diagram of the distribution of site survey sections

Site survey of the tunnel includes the measurement of crack number, mileage, width and length. Specifically, the width was measured using a crack width meter (Figure 3a), and the measurement accuracy was 0.01 mm, with details shown in Figure 3c. In addition, the crack length was measured based on the expanded view of the lining section (Figure 3f) obtained by an Amberg laser scanner (Figure 3d, Figure 3e).

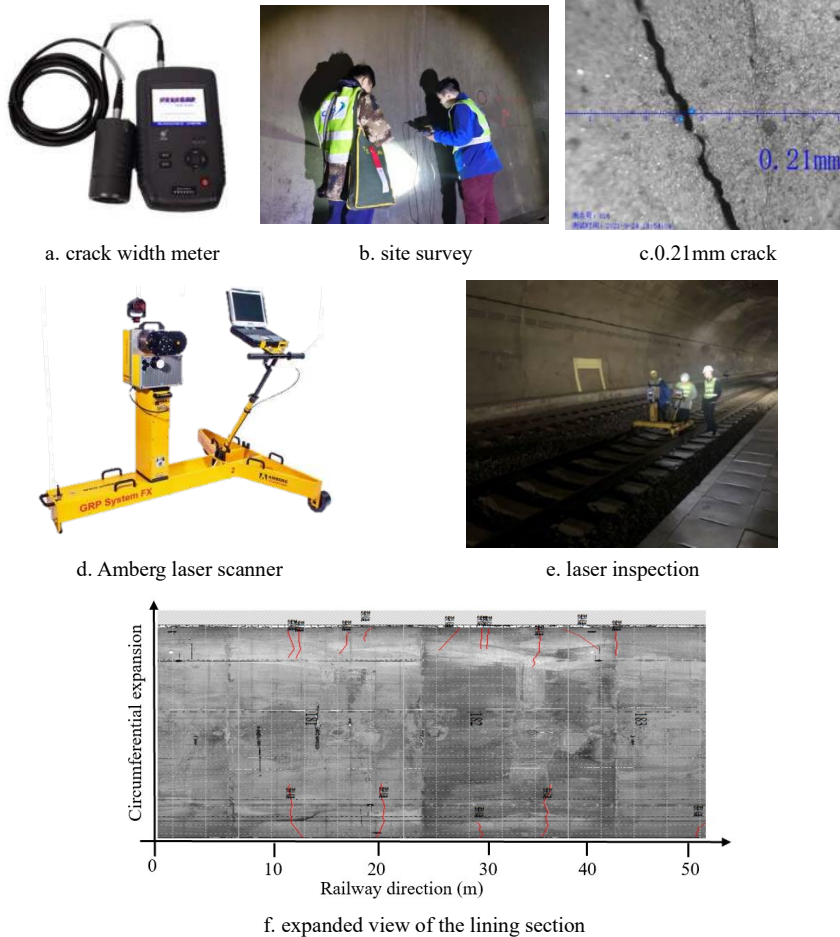


Figure 3  
Inspection devices for site survey, and effects of field application

Table 1  
Statistics of cracks with different states

Statistics	Circumferential cracks	Longitudinal cracks	Total
Repaired cracks	251	6	257
Unrepaired cracks	216	0	216
Total	467	6	473

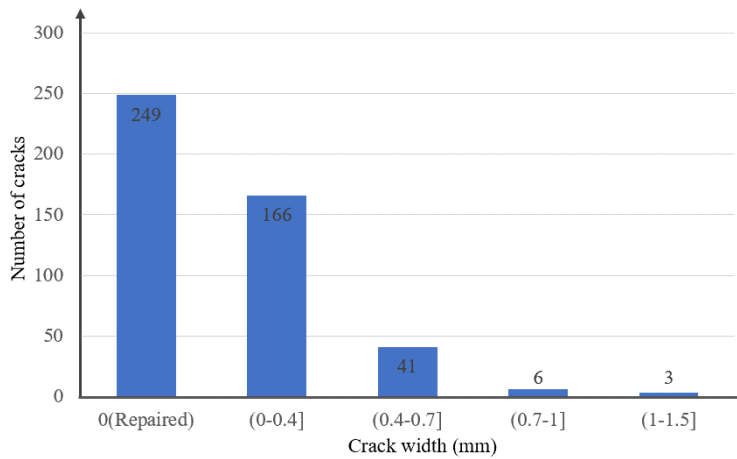


Figure 4  
Distribution of cracks by width

Through the site survey, a total of 465 cracks on the left and right lining walls of the 4 km survey area were found and recorded, including 459 circumferential cracks and 6 longitudinal cracks (Table 1). So far, 249 of 465 cracks have been repaired by epoxy mortar (Figure 5b), indicating the remaining 216 ones need to be repaired (Figure 5a). The widths of measurement positions of the 216 ones range from 0.1 mm to 1.5 mm. The distribution of cracks by width is shown in Figure 4.

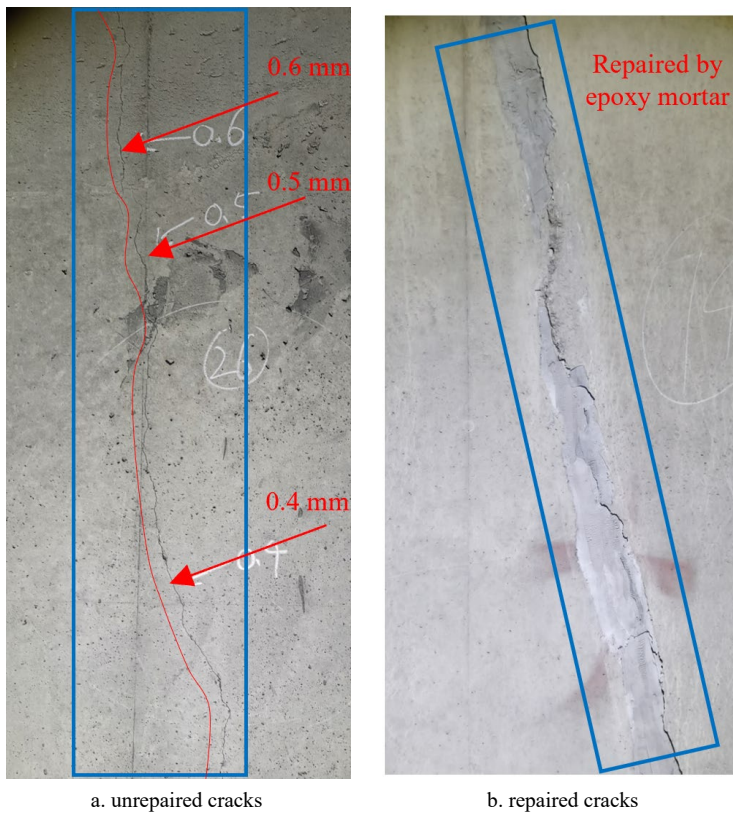


Figure 5

Comparison of cracks with different states

### 3.2 Crack Inspection Rate Analysis

As shown in Figure 5, the cracks' characteristics are significantly different before and after repair. Therefore, the repaired cracks were not selected to analyze the inspection rate. As the samples, 216 unrepaired cracks mentioned above were used for inspection rate analysis. Analysis results shown in Figure 6 and Table 2. Crack inspection through the LSI system is based on the neural network and manual intervention.

After training, the caffe-based neural network algorithm can be used to effectively identify the abnormal area of an image, but is unable to directly screen out the cracks. In other words, manual intervention is required to ultimately identify the cracks. However, manual intervention was affected by subjective factors such as personal experience and operational standardization, thereby making the final crack inspection rate be lower than the system prompt rate. Such a decreasing trend

became increasingly apparent with a decrease in crack width. For example, the crack inspection rate was 92.6% when the width was greater than 0.3 mm, but reduced to 60% when the width was less than 0.3 mm (Figure 6).

Table 2  
Analysis of crack inspection rates through the LSI system

Crack width	Site survey	System prompt rate	System + manual inspection rate
(0, 0.3] mm	148	81.8%	60.1%
Above 0.3 mm	68	98.5%	92.6%
Total	216	87.0%	70.4%

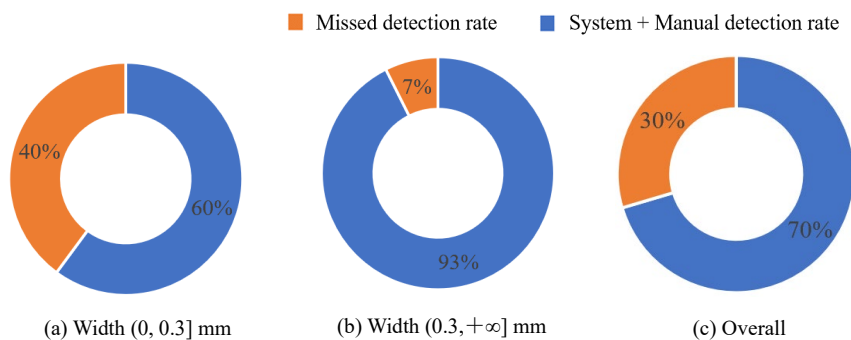


Figure 6

Analysis of crack inspection rates through the LSI system

### 3.3 Error Analysis

#### 3.3.1 Mileage Error Analysis

In order to ensure the consistency of analysis samples, 251 circumferential repaired cracks with obvious characteristics were selected for mileage error analysis. According to the crack morphology and location, the LSI system inspected cracks correspond to the site survey results one by one, and then the mileage difference of the starting point of the lowest circumferential crack is calculated.

Results show that mileage errors of the LSI system are normally distributed, with an error mean of 0.2 m, a standard deviation of 0.42, and a mileage deviation between  $-0.8$  m and 0.9 m when the confidence level is 90% (Figure 7).

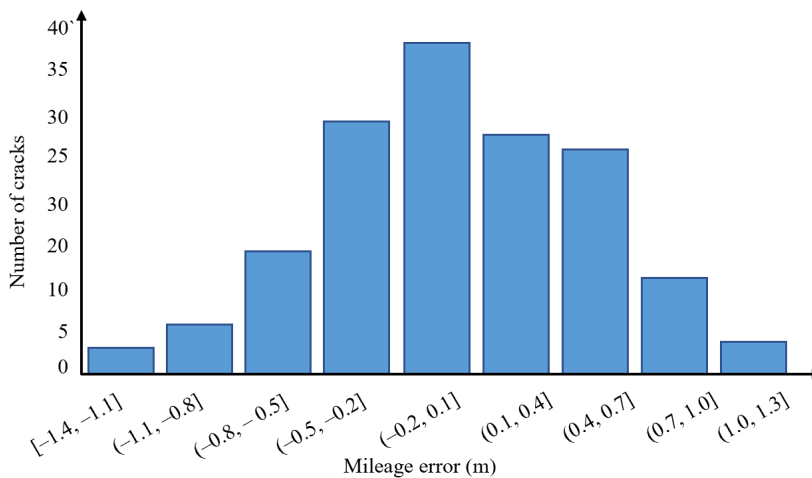


Figure 7

Statistical analysis of mileage errors in repaired cracks

### 3.3.2 Length Error Analysis

Laser scanning makes it possible to accurately obtain the geometrical shape of a lining section. In addition, image distortion can be avoided by projecting pixel points along the lining section, so as to ensure the measurement accuracy. As the samples, 115 repaired circumferential cracks whose starting points could be clearly identified through laser imaging were analyzed, to extract the data of crack length. The regression analysis of crack lengths determined through laser imaging and LSI system is itemized in Figure 8. As shown in the graph, the crack length identified by the LSI system is systematically enlarged by about 27% than the actual crack length determined through site survey. In addition, the upper and lower bounds of the 90% confidence interval are also indicated. It can be seen that on the basis of systematic amplification, the crack length identified by the LSI system has a dispersion of  $-0.4\sim 1$  m.

The crack lengths identified through the LSI system were further analyzed for staged fitting. Figure 9 shows that the system had an error of 5%, and measurement results changed by step significantly with an increase in crack length. When the crack length covered one channel, two channels and three channels, the measurement errors were about 0.5 m, 1.2 m, and 1.8 m, respectively. Analysis results show that the LSI system is based on the data acquired through multiple cameras, thus resulting in a strong correlation between the measurement error and crack length.

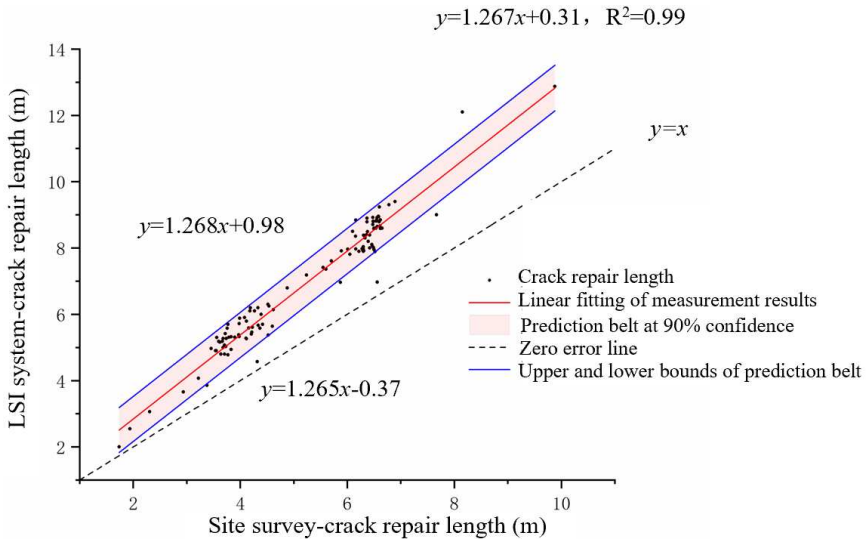


Figure 8

Regression analysis of circumferential crack length

Moreover, 5 repaired longitudinal cracks whose starting points could be clearly identified through laser imaging were analyzed. The regression analysis of crack lengths determined through laser imaging and LSI system was made (Figure 10). The longitudinal crack length obtained by lining scan imaging is highly correlated to that identified through the LSI system. The upper and lower bounds of the 90% confidence interval are indicated and the crack length identified through the LSI system had a dispersion of  $\pm 0.7$  m. Longitudinal cracks are distributed along the line direction, and generally located in single channels of the LSI system. The results of comparing the lengths errors of circumferential cracks and longitudinal cracks further show that the length error of circumferential cracks is caused by the redundancy of image stitching.

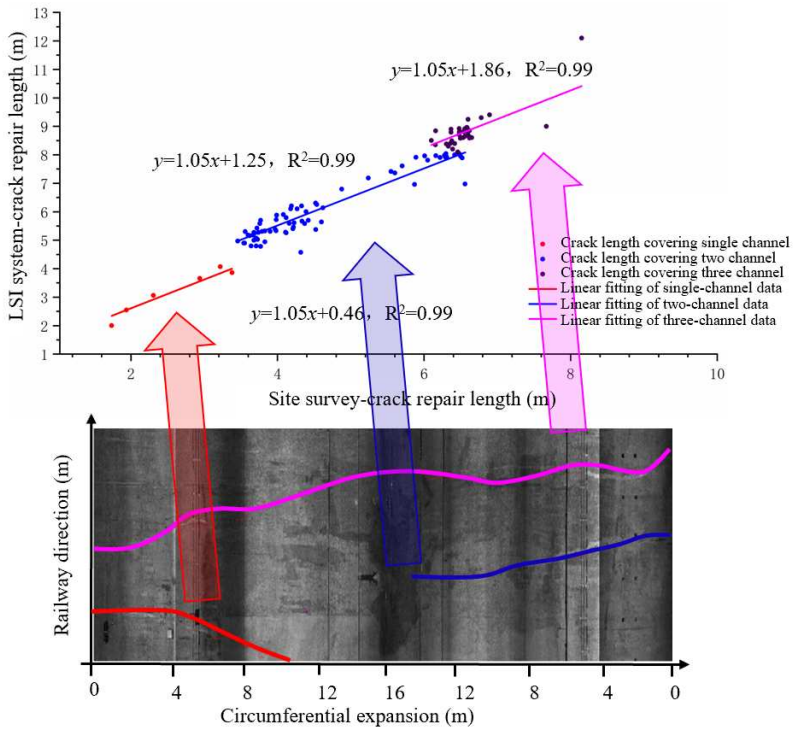


Figure 9  
Staged fitting results of circumferential crack length

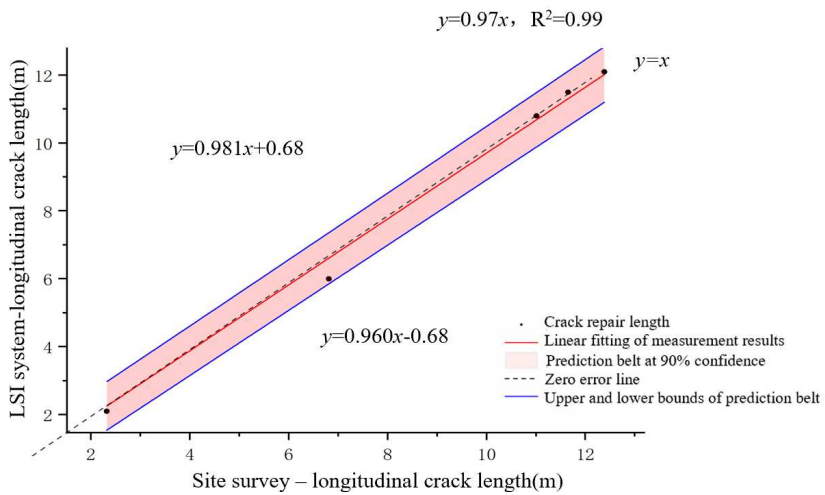


Figure 10  
Regression analysis of longitudinal crack length

### 3.4 Summary

According to the application results of LSI system in 4 km test tunnel, key performance parameters such as crack inspection rate, mileage, length, and measurement error were studied in this section. The results show:

- (1) 60% of cracks with a width of less than 0.3 mm could be inspected through the LSI system, while the figure for the cracks with a width of more than 0.3 mm was 93%.
- (2) The mileage deviation ranged from  $-0.8$  m to 0.9 m.
- (3) The systematic length error of circumferential cracks caused by the redundancy of image stitching was 27%. The circumferential crack length had a dispersion of  $-0.4\sim 1$  m within the 90% confidence interval.
- (4) Also, the longitudinal crack length had a dispersion of  $\pm 0.7$  m within the 90% confidence interval.

After automatic recognition and manual verification of the lining surface images collected at an inspection speed of 50 km/h, it was found that the inspection system could meet the requirements for fast railway tunnel lining crack inspection. In view of a large error in circumferential crack length recognition, a priority will be given to the research on the technology of multi-channel image stitching with little redundancy, to improve the accuracy of circumferential crack length recognition.

## 4 Tunnel Lining Apparent Inspection Data Utilization Strategy

### 4.1 Characteristics of Apparent Cracks in Operating Tunnel Lining

Through the LSI system, a total of 6,629 lining cracks were inspected along the 55 km railway tunnel. Specifically, circumferential cracks, longitudinal cracks, oblique cracks, massive cracks and water seepage cracks accounted for 55%, 23.1%, 16.9%, 4.9%, and 1.5% of the total, respectively. There were 8.3 cracks per 100 meters on average (Table 3, Figure 11).

Table 3  
Lining crack inspection results of the 55 km operation railway tunnel

	Crack type	Quantity	Density (Quantity/100 m)	Proportion
Crack	Circumferential crack	3598	6.5	54.3%
	Longitudinal crack	1498	2.7	22.6%
	Oblique crack	1101	2	16.6%

	Massive crack	327	0.6	4.9%
Water seepage crack	Circumferential crack	49	0.1	0.7%
	Longitudinal crack	36	0.1	0.5%
	Oblique crack	20	0	0.3%
Total		6629	8.3	100.0%

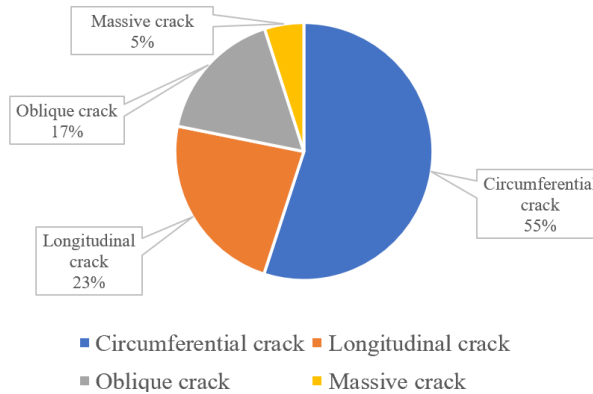


Figure 11

Distribution of apparent lining cracks in operating tunnels

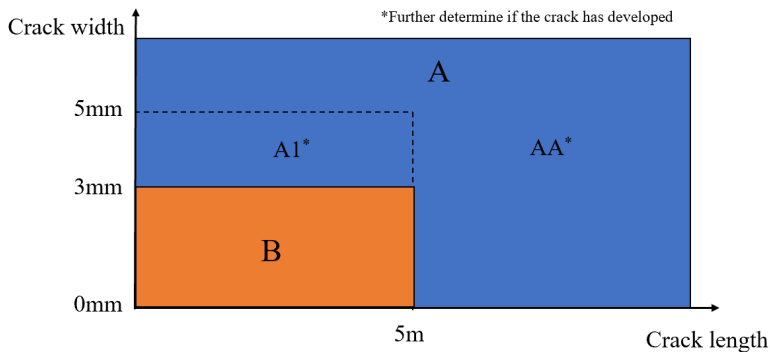


Figure 12

Evaluation standard for crack inspection grade of Railway tunnel in China

Crack ratings AA, A1, and B are specified in Assessment standard for structure deterioration of railway bridge and tunnel Part 2: Tunnel (Q/CR 405.2–2019). The specific rating standards and disposal measures are shown in Figure 12. Only the cracks under development can be rated as A. Single inspection is not enough to ascertain whether the cracks continue to develop. Therefore, the single-inspected cracks are classified as those that need "focus" and "attention" respectively. The state assessment criteria are itemized in Table 4. According to such criteria, the A-grade cracks along the 55 km railway tunnel were further distinguished.

In addition, crack grades and disposal urgency were optimized to a certain extent. After such optimization, there were 1,919 cracks worthy of focus, accounting for 28.9% of the total (Table 5). As a result, it significantly reduced the workload of routine inspection by the maintenance unit.

Table 4  
Lining surface crack rating criteria

Crack type	Action proposal
Crack length: $L > 12$ m	<b>Focus</b> , rated as AA if monitoring results show the sign of development
Crack width: $\delta > 5$ mm	<b>Focus</b> , rated as AA if monitoring results show the sign of development
Crack length: $5 \text{ m} \leq L < 12$ m	<b>Attention</b> , rated as AA if monitoring results show the sign of development
Crack length: $L < 5$ m, and Crack width: $5 \text{ mm} \geq \delta \geq 3$ mm	<b>Attention</b> , rated as A1 if monitoring results show the sign of development

Table 5  
"Focus" and "Attention" cracks

Crack type		Focus	Attention	Total	Proportion of focus
Crack	Circumferential crack	930	2668	3598	25.8%
	Longitudinal crack	397	1101	1498	26.5%
	Oblique crack	218	883	1101	19.8%
	Massive crack	327	0	327	100.0%
Water seepage crack	Circumferential crack	20	29	49	40.8%
	Longitudinal crack	16	20	36	44.4%
	Oblique crack	11	9	20	55.0%
Total		1919	4710	6629	28.9%

## 4.2 Data Utilization Strategy

Inspection results show that there might be thousands of cracks in a single tunnel due to the environmental effects, construction defects and external forces, thus posing some challenges to the analysis and management of lining conditions. Moreover, the development of cracks is neither continuous, nor certain. Cracks will not continue to develop unless they are affected by external forces or in case of significant changes in environmental conditions. Therefore, it is suggested to inspect the tunnel lining conditions through the LSI system once every six months, so as to understand the service status of lining in a timely manner.

In consideration of LSI system performance verification results, and the impact of crack shapes on the lining structure safety, data utilization strategies for different types of cracks are proposed based on the mechanism for periodic inspection of lining surface conditions (Table 6).

- (1) The cracks with a width of less than 0.3 mm are fine cracks having little impact on lining safety. Thus, it is suggested that only the cracks with a width of 0.3 mm and above are worthy of attention in the disease recognition process.
- (2) In consideration of systematic errors, the longitudinal cracks with a length increment of no more than 0.7 m, and the circumferential cracks with a length increment of no more than 1.2 m shall be deemed as normal cracks in case of periodic inspection.
- (3) Circumferential cracks occupy a large proportion but have a low impact on structural safety, it is suggested to conduct the comparative analysis once every two years, to effectively reduce the workload of the maintenance unit.
- (4) Longitudinal cracks and oblique cracks are mostly stress cracks. Particularly when longitudinal cracks penetrate through the lining surface, the overall performance of lining under stress will decline, with a huge local stress. After the inspection each time, it is necessary to focus on analyzing the development trend of such cracks, assess them according to the criteria listed in Table 4, and put forward the disposal measures in a timely manner.
- (5) Water seepage indicates that the cracks have been penetrated through by the water source behind the lining. Therefore, it is suggested to strengthen manual inspections before and after rainfall or during the freezing and thawing period, and to place emphasis on the crack development and local deformation of surrounding lining.
- (6) Most massive cracks are near construction joints, and are likely to fall off. Thus, it is suggested to take corrective measures in time.

Table 6  
Comparative analysis cycles for different types of cracks

Crack type	LSI system survey	Comparative analysis cycle	Check items/Actions
Circumferential crack	Once half a year	Once every two years	Crack length
Longitudinal crack and Oblique crack		Once half a year	Deformation and crack width
Water seepage crack		strengthen manual inspections before and after rainfall or during the freezing and thawing period	Water seepage and local deformation
Massive crack		Take corrective measures in time.	Chisel or anchor reinforcement

## Conclusions

- (1) After automatic recognition and manual verification of the lining surface images collected at an inspection speed of 50 km/h, it was found that the inspection system

could meet the requirements of the maintenance unit. Results show that the inspection rate of the cracks with a width of more than 0.3 mm, longitudinal crack length error, systematic length error of circumferential cracks, and dispersion are 93%,  $\pm 0.7$  m, 27% and  $-0.4\sim 1$  m, respectively. The analysis of crack length errors will facilitate the subsequent identification of crack development conditions.

(2) The statistics about the 55 km railway tunnel show that there were 8 cracks per 100 meters on average. In addition, circumferential cracks accounted for 55% of the total, while oblique and longitudinal cracks took up only 40%. Based on the existing criteria, new criteria of crack classification for aperiodic inspection were proposed. According to the new criteria, the cracks are classified as those that need "focus" and "attention" respectively. After such optimization, there were 1,919 cracks worthy of focus, accounting for 28.9% of the total. As a result, it significantly reduced the workload of routine inspection by the maintenance unit.

(3) Based on the periodic inspection mechanism, this paper proposes corresponding analysis cycles for different types of cracks, to ensure the timely analysis of the cracks affecting the lining structure safety, and to reduce the workload of the maintenance unit busy dealing with excessive circumferential cracks.

(4) Tunnel lining defects are characterized by a complexity in types, a large number, and a large difference in the impact on lining safety. In the process of risk investigation, cancellation confirmation, and follow-up observation, it is necessary to develop a system for digital management of inspection results, and build a closed-loop digital management model integrating inspection data display, integrated analysis, disease database construction, site review, and track monitoring.

### Acknowledgement

This research was funded by Science and Technology Research and Development Program of China State Railway Group Co., Ltd. [J2023G013]: Research on comprehensive lining evaluation technology of high-speed railway tunnel in operation, and Research and Development project of China Academy of Railway Science Co., Ltd. [2022YJ180]: Study on lining image-form symbiosis technology of high-speed railway tunnel in operation.

### References

- [1] S. Wang, Y. Gao, F. Qi, Z. Ke, H. Li, Y. Lei, Z. Peng: Review on Inspection Technology of Railway Operation Tunnels. *Journal of Traffic and Transportation Engineering*, Vol. 20, 2020, No.5, pp. 41–57
- [2] Al-Rousan R. Z., Alnemrawi B. R. Prediction of Interface Shear Strength of Heat Damaged Shear-keys using Nonlinear Finite Element Analysis, *J. Appl. Comput. Mech.*, 04(1), 2023, 1-16, <https://doi.org/10.22055/jacm.2023.42998.4000>

- [3] Q. Feng, S. Wang, Y. Gao, G. Song, F. Qi: Comparative Study on Monitoring System and State Assessment of High-Speed Railway Bridge Tunnel Inspection. *Railway Engineering*, Vol. 61, 2021, No. 1, pp. 140–146
- [4] Q. Feng, S. Wang, F. Qi, Y. Gao, G. Song: Research on Framework of the Inspection and Monitoring System about Railway Bridge and Tunnel. *Railway Technology Innovation*, 2021, No. 6, pp. 44–49
- [5] Major, Z., Ibrahim, S.K., Movahedi Rad, M., Németh, A., Harrach, D., Herczeg, G., Szalai, S., Kocsis Szürke, s., Harangozó, D., Sysyn, M., Kurhan, D., Baranyai, G., Gáspár, L., Fischer, s. Numerical Investigation of Pre-Stressed Reinforced Concrete Railway Sleeper for High-Speed Application. *Infrastructures*, 2023, 8(3), 41. doi: <https://doi.org/10.3390/infrastructures8030041>
- [6] Szalai, S., Eller, B., Juhász, E., Movahedi, M. R., Németh, A., Harrach, D., Baranyai, G., Fischer, S. Investigation of deformations of ballasted railway track during collapse using the Digital Image Correlation Method (DICM). *Reports in Mechanical Engineering*, 2022, 3(1), 168–191, doi: <https://doi.org/10.31181/rme20016032022s>
- [7] Károlyfi, K. A., Horváth, A. Papp, F. Digital image processing method for evaluation of discoloration on fair-faced concrete surfaces *Építőanyag-Journal of Silicate Based and Composite Materials*, Vol. 74, 2022, No. 02, pp. 67–70, <https://doi.org/10.14382/epitoanyag-jsbcm.2022.11>
- [8] Károlyfi, K., Papp, F. The correspondences between formwork geometry and concrete composition in the case of fair-faced concrete elements. *Pollack Periodica An International Journal for Engineering and Information Sciences* Vol. 13, 2018, No. 02, pp. 43–54. <https://doi.org/10.1556/606.2018.13.2.5>
- [9] W. Qiu, Y. Cheng: High-Resolution DEM Generation of Railway Tunnel Surface Using Terrestrial Laser Scanning Data for Clearance Inspection. *Journal of Computing in Civil Engineering*, 2017, Vol. 31, No. 1, pp. 4016045
- [10] Z. Huang, H. Fu, X. Fan, J. Meng, W. Chen, X. Zheng, F. Wang, J. Zhang: Rapid Surface Damage Detection Equipment for Subway Tunnels Based on Machine Vision System. *Journal of Infrastructure Systems*, Vol. 27, 2021, No. 1, pp. 04020047
- [11] S. Stent, R. Gherardi, B. Stenger, *et al*: Visual Change Inspection on Tunnel Linings. *Machine Vision and Applications*, Vol. 27, 2016, No. 3, pp. 319–330
- [12] R. Montero, G. Victoresj, S. Martinez, *et al*: Past, Present and Future of Robotic Tunnel Inspection. *Automation in Construction*, Vol. 59, 2015, pp. 99–112

- [13] J. Laurent, F. Dominguez: Use of 3D Scanning Technology for Automated Inspection of Tunnels. Proceedings of the World Tunnel Congress, 2014, pp. 1–10
- [14] Y. Fujino, D. Siringoringo: Recent Research and Development Programs for Infrastructures Maintenance, Renovation and Management in Japan. Structure and Infrastructure Engineering, Vol. 16, 2020, No. 1, pp. 3–25
- [15] X. Chai, X. Zhu, J. LI, *et al.*: Tunnel Lining Crack Identification Algorithm Based on Deep Convolutional Neural Network. Railway Engineering, Vol.58, 2018, No.6, pp. 60–65
- [16] T. Ortner, J. Sorger, H. Piringer, *et al.*: Visual Analytics and Rendering for Tunnel Crack Analysis. Ieee Transactions on Visualization and Computer Graphics, Vol. 32, 2016, pp. 859–869
- [17] K. Tabrizi, M. Celaya, B. Miller, *et al.*: Damage Assessment of Tunnel Lining by Mobile Laser Scanning: Pittsburgh, Pennsylvania, Implementation Phase of FHWA SHRP 2 R06G Project. Transportation Research Record, Vol. 2642, 2017, No.1, pp. 166–179

# Review of Railway Operation Tunnel Inspection System and Condition Assessment Method

**Guohua Song<sup>1</sup>, Yan Huang<sup>2</sup>, Zhaoning Wang<sup>1</sup>, Qiankuan Feng<sup>1</sup>, Feiyu Jia<sup>1</sup>, Shilei Wang<sup>1\*</sup>**

<sup>1</sup>Infrastructure Inspection Research Institute, China Academy of Railway Sciences Group Co. Ltd., No. 2 Daliushulu, Haidian District, Beijing, China, 100081

<sup>2</sup>Track Maintenance Department, China Railway Nanning Bureau Group Corporation Limited, NO. 21 Foziling Road, Qingxiu District, Nanning City, Guangxi China, 530022

e-mail: songguohua@rails.cn, jcsqsb@rails.cn, wangzhning@rails.cn, fqk@rails.cn, jiafy@rails.cn, wangshilei@rails.cn

---

*Abstract: Currently, the expanding scale of railway tunnels in operation raises higher requirements for effective management thereof so as to ensure their safe operation. Just in this context, this paper compares and analyzes the tunnel inspection systems, condition assessment methods and technical equipment prevailing in many countries including Japan, European countries, the United States and China. Study results show that in terms of tunnel inspection systems, various countries have set their respective tunnel inspection cycles according to the tunnel integrity, service duration, service status, speed level and other factors. In particular, Japan and Europe have designed the tunnel inspection procedures, putting forward requirements for the professional competence of inspectors. In terms of condition assessment, Japanese standards are more hierarchical and systematic in the integrated application related to lining crack, deformation and defect, but are insufficient in the assessment of serious internal lining defects. In contrast, European standards focus on the impact of diseases on the overall performance of the tunnel structure. In addition, Chinese standards highlight the single-indicator assessment, but ignore the correction of assessment results in case of multiple deterioration types. It's worth noting that Japan and China have respectively developed their own rail-mounted tunnel inspection devices to replace manual inspection. Based on a comprehensive comparison of tunnel inspection systems and condition assessment methods of different countries, according to the scale, inspection device technical level and service characteristics of China's railway tunnels, this paper proposes a framework of railway tunnel inspection regulation, while optimizing and supplementing the contents and requirements of relevant tunnel inspection regulation.*

*Keywords: Railway Tunnel; Inspection System; Inspection Device; Condition Assessment Method*

---

## Introduction

By the end of 2020, the total mileage of China's railways in operation reached 145,000 km. Over the same period, a total of 16,798 railway tunnels and 3,631 high-speed railway tunnels had been put into operation, with a total length of about 19,630 km and 6,003 km, respectively. All these indicate that China has become the country with the largest scale of railway tunnels in operation in the world [1, 2]. In China with a vast territory, environments along railway lines are complex and changeable in climatic, geological and hydrological conditions. Similarly, tunneling is vulnerable to many complex factors such as corrosion, freeze thawing, etc. Due to differences in construction periods, construction standards, and uncertainties in construction quality, railway tunnels in operation are exposed to various types of defects and diseases [3]. In fact, any minor defect or disease of tunnel lining might affect the safe operation of a railway in operation [4].

The railway infrastructure inspection system is vital for and of great significance to the safe operation of railways in China, as well as scientific and rational guidance in maintenance and repair [5]. After analyzing the service characteristics and maintenance modes of Chinese bridges and tunnels, Lu Chunfang [4] pointed out that preventive maintenance is a trend of maintenance and repair of high-speed railway bridges and tunnels in China. In addition, Chen Qi [6] *et al.* proposed to optimize the technical rules and procedures of infrastructure maintenance to better achieve the safety management, monitoring and inspection, application of machinery and devices, and production organization, etc. Also, Chen Dongsheng [7] proposed several management modes for high-speed railway maintenance in China according to the foreign experience in this regard. Ma Weibin [8] summarized the existing technologies for railway tunnel inspection, monitoring, assessment and disease treatment in China, and then proposed a technical system for disease treatment of railway tunnels in operation.

Despite the constant progress in tunnel damage identification technology and quality inspection method [9-14], currently tunnel condition data are acquired mainly through manual inspection, and there still exists a certain gap to achieve targeted maintenance and preventive maintenance of railway infrastructure due to the deficiencies in inspection method efficiency, and accuracy. Furthermore, as the railway maintenance management units face increasingly pressures in reducing production costs and improving the efficiency of maintenance and repair, it is found that conventional inspection systems, devices and condition assessment methods are becoming hard to meet the requirements with the scale development of tunnels. In view of this, it is necessary to optimize the inspection systems and improve the condition assessment standards on the basis of comparing and analyzing the railway tunnel inspection situations of different countries. Specifically, it is required to study and establish a scientific and efficient inspection system in line with the scale of railway tunnels, so as to timely identify

railway transportation safety risks, objectively understand the law of tunnel structure performance evolution, and provide a reasonable guidance in the targeted maintenance of tunnels.

## 1 Tunnel Inspection Systems

In order to ensure the safe and efficient operation of railways, many countries including Japan, Europe, the United States and China have established different tunnel infrastructure inspection systems. In particular, along with the development of inspection technologies and devices, they have successively updated their respective professional inspection standards and systems since the beginning of the 21<sup>st</sup> Century.

### 1.1 Japanese Tunnel Inspection System

Upon entrustment by the Railway Bureau of the Ministry of Land, Infrastructure, Transport and Tourism of Japan, Railway Technical Research Institute (RTRI) founded the Research Committee on Maintenance Management of Railway Civil Engineering Structures and the Research Committee on Track Maintenance Management in 2000, initiating the research on identifying the inspection cycles and integrity of civil engineering structures and tracks. In January 2007, the said Railway Bureau promulgated the Standards for the Maintenance Management of Railway Structures [15, 16] (hereinafter referred to as the "Standards"). Focusing on the safety, usability and restorability of structures, the Standards clarify the railway structures maintenance management system and procedures, including the basic concepts, inspection methods, integrity assessment criteria, maintenance management measures and records, etc. The required performance, performance item and judgment criterion of the tunnel structure are detailed in Table 1.

Table 1  
Required performance, performance item and judgment criterion of the tunnel structure

Required performance	Performance items	Judgment criterion
Safety	Stability of tunnel structure	No risk of tunnel collapse
	Structure boundary	No invasion into the boundary
	Line stability	No uplift, subsidence and movement of railway subgrade that might affect the safe operation of trains
	Spalling stability	No spalling of concrete, maintenance materials and so on that might affect the safe operation of trains
	Safety in case of water	No phenomenon of water seepage or freezing

	seepage and freezing	that might affect the safe operation of trains
Usability	Usability in case of water seepage or freezing	No phenomenon of water seepage or freezing that might affect the functions of devices in the tunnel
	Dirt on the surface	No dirt that would seriously hinder the normal inspection
	Impact on surrounding environment	No impact on surrounding environment
Restorability	Post-disaster recovery	Easiness in post-disaster repair of damaged tunnels

Tunnel inspection falls into several categories, i.e., preliminary inspection, comprehensive inspection, individual inspection and random inspection. Among them, comprehensive inspection can be divided into comprehensive inspection and special comprehensive inspection. Specifically, a preliminary inspection is required before any railway structures newly-built, renovated or expanded is put in to use. The comprehensive inspection is conducted regularly, to identify the integrity of the entire structure, and the necessity of individual inspection, while the special comprehensive inspection aims to improve the accuracy of integrity identification. In contrast, an individual inspection is conducted in the course of any comprehensive inspection or random inspection, and is specific to a railway structure with an integrity rating of A or any other railway structure for which such inspection is deemed necessary. In addition, random inspection aims to find out exceptions arising from the occurrence of a natural disaster. For example, a random inspection is required if concrete spalling might seriously affect the safety of any third party or adjacent engineering might affect the target structure.

The cycles of preliminary inspection and comprehensive inspection are detailed in Figure 1. Specifically, a comprehensive inspection is generally conducted once every two years, and the first special comprehensive inspection is conducted within 10 years after the railway structure is put into operation. If the results of special comprehensive inspection show the target structure has the required performance, the comprehensive inspection cycle may be extended accordingly. The process of tunnel inspection and maintenance is shown in Figure 2.

In accordance with Japanese standards, qualified tunnel inspectors with rich experience accumulated through receiving training over years shall be able to identify tunnel risks comprehensively according to various factors, and particularly have the skills of special comprehensive inspection conducted to extend the comprehensive inspection cycle.

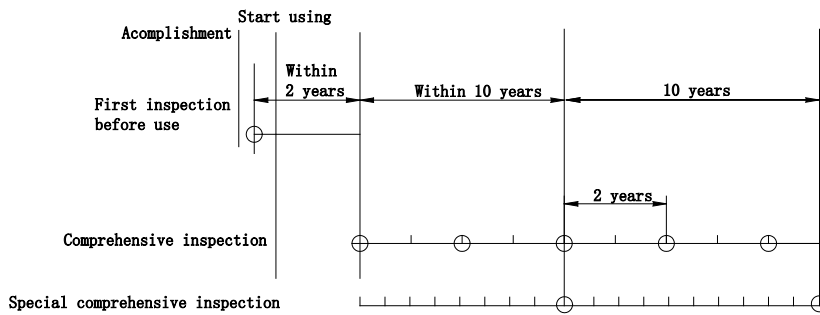


Figure 1

Schematic diagram of preliminary inspection and comprehensive inspection cycles

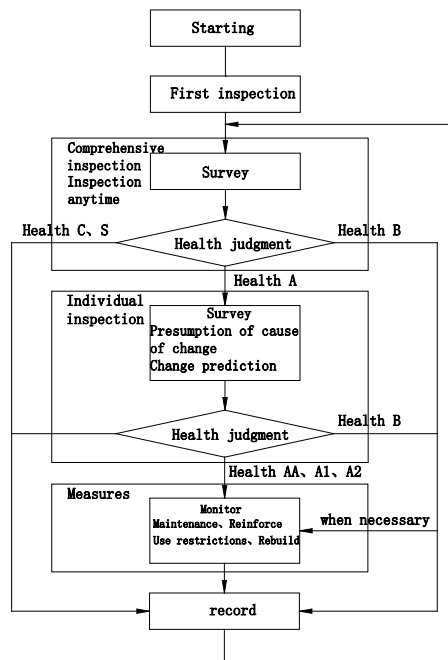


Figure 2

Process of Japanese structure inspection and maintenance

## 1.2 European Tunnel Inspection System

Although their tunnel maintenance systems vary to a certain extent, European countries generally follow the principle of moderate separation of "management, inspection, and maintenance", and actively promote the business outsourcing [17]. Whereas EU standards and International Union of Railways (UIC) standards are integrated, the tunnel inspection systems of European countries are generally

consistent with the tunnel inspection requirements raised by UIC. The Code for Management and Maintenance of Tunnels in Service ( “the Code” for short) [18] (UIC Code 779-10) specifies the contents of management, maintenance, performance improvement, and operation of tunnels in operation. Inspection constitutes an important part of tunnel maintenance. According to the Code, the inspection work is composed of planned monitoring and unplanned monitoring. Further, planned monitoring consists of routine monitoring, annual monitoring, detailed inspection, and special monitoring. The content, personnel and period of each inspection are shown in Table 2. If it is hard to identify the tunnel conditions after the conventional condition assessment, some geotechnical and geological professionals and experts shall be organized to conduct the supplementary inspection and theoretical analysis.

Table 2  
Types of European tunnel inspection

Inspection type		Duties	Implementer	Cycle
Planned monitoring	Routine monitoring	General inspection of tunnels in combination with line inspection	Lineman	Line inspection
	Annual monitoring	Reviewing various inspection results in the detailed inspection report, and making supplementary explanations	Tunnel inspector	1 year
	Detailed inspection	Issuing a detailed inspection report, updating and distributing the disease records to all the parties of maintenance management, and clarifying the maintenance work recommendations and their urgency in the report	Professional engineers, assisted by experts if necessary	4-6 years
	Special monitoring	Inspecting the sensitive areas (such as the areas featuring the rapid disease development or marked “unstable” in the inspection report) more frequently, taking corresponding safety measures (such as train speed limitation) if necessary, before disposal (generally accompanied by the measurement of geometry such as convergence, crack)	/	/
Unplanned monitoring		Carrying out any special inspection, or any meticulous	External experts or	/

	inspection of structures or parts thereof in unforeseen circumstances (such as occurrence of a natural disaster or sudden appearance of some special problems)	specialized firms, with assistance needed if necessary	
--	--	--	--

### 1.3 American Tunnel Inspection System

In 2005, the Federal Highway Administration of the U.S. Department of Transportation and the Federal Transit Administration jointly promulgated the Highway and Rail Transit Tunnel Inspection Manual ( “the Manual” for short) [19]. In the Manual, tunnel inspection was expounded from the perspectives of structure, machinery, electrical engineering and others, and the inspectors, responsibilities, devices, preparations, and safety measures were introduced. According to structural requirements, new tunnels shall be inspected once every 5 years, while old tunnels shall be subject to the short-distance inspection once every 2 years. In addition, old tunnels shall be inspected on a daily, weekly and monthly basis.

In 2008, American Railway Engineering and Maintenance-of-Way Association (AREMA) published the Railway Bridge Inspection Manual [20], recommending some methods for the inspection of railway bridges and tunnels (including tunnel structures). The Manual mainly introduces the general concepts of bridge and tunnel inspection, and different types of inspections for specific structures.

Unlike the railways in Japan, Europe, and China, American railways are owned by private companies. Thus, for their own sake, such private companies would minimize the maintenance costs. Specially, annual maintenance costs of bridges and tunnels only account for about 10% of the overall costs. In addition because American railways are privately owned, and the official tunnel structure rating methods issued by the U.S. railway authority involve the potential liability issues, currently there are no uniform rating methods for railway tunnel structures. Thus, various railway companies in the United States usually establish their own procedures for the inspection, maintenance, rating and safety management of tunnel structures in accordance with general guidelines released by the federal government as well as their internal management rules.

### 1.4 Chinese Tunnel Inspection System

In China, railway bridges and tunnels are maintained and repaired based on the speed grades, namely high-speed and normal speed. In addition, types and frequencies of tunnel inspection are specified. The tunnel inspections for both high-speed trains and normal-speed trains are basically the same, including periodic inspection, temporary inspection, and special inspection. In accordance

with the Rules for Maintenance and Repair of Bridges and Tunnels for Normal-speed Railways (TG/GW 103-2018) [21], important tunnel devices shall be inspected once every six months. In addition, each tunnel shall be comprehensively inspected during the comprehensive maintenance period. However, the inspection cycle may be appropriately extended if a line only allows the passing of freight vehicles and the annual transport volume is less than 5 million tons. In accordance with the Rules for Maintenance and Repair of Bridges and Tunnels for High-speed Railways (Trial) (TG/GW 114-2011) [22], important tunnel devices shall be inspected once every quarter, while the inspection frequency for others depends on the structural position. For example, tunnel entrances and exits shall be inspected once every six months, while tunnels and surroundings shall be inspected once a year. In contrast, with normal-speed rail tunnels, high-speed rail tunnels are inspected more frequently, and the inspection cycle for each part of the tunnel structure is clarified. However, the requirements for temporary inspection and special inspection are the same for both normal-speed rail tunnels and high-speed rail tunnels, depending on the environmental conditions and service time thereof.

## 1.5 Comparison of Different Inspection Systems

In accordance with Japanese tunnel inspection standards, comprehensive inspection cycle shall be 2 years, and a special comprehensive inspection shall be conducted in not less than 10 years. In addition, the comprehensive inspection cycle may be extended if conditions permit after the special comprehensive inspection, and basic qualifications and skills of relevant inspection personnel are specified. Throughout the inspection process, inspection personnel focus on implying and predicting the causes of changes in tunnel performance.

In accordance with European tunnel inspection standards, mainly the tunnel diseases specified in the detailed inspection report shall be reviewed, and the detailed inspection cycle shall be 4-6 years. The process of condition assessment based on conventional condition assessment, supplementary inspection and theoretical analysis is proposed, and the responsibilities and roles of different positions are specified.

In accordance with American tunnel inspection standards, the short-distance inspection cycle shall be 2-5 years, depending on the service time of tunnels. However, because American railways are privately owned, currently there are no uniform rating methods for railway tunnel structures.

In accordance with Chinese tunnel inspection standards, inspection cycles for high-speed railway tunnels and normal-speed railway tunnels shall vary to some extent. Specifically, the comprehensive inspection cycle of high-speed railway tunnels shall be one year, while the inspection cycles of normal-speed railway tunnels shall depend on the time of comprehensive maintenance.

## 2 Tunnel Condition Assessment

### 2.1 Japanese Tunnel Condition Assessment

In Japan, the structure integrity is identified according to the inspection results, change causes and prediction results. The integrity ratings include A, B, C, and S. Among them, A is further divided into AA, A1, and A2. The tunnel integrity identification criteria and corresponding maintenance measures are itemized in Table 3.

In accordance with Japanese standards, mountain tunnels and urban tunnels shall be inspected and assessed separately. The integrity of mountain tunnels is affected by external factors and environmental effects. Specifically, there are 9 types of external actions, mainly including surrounding rock pressure, landslide, water pressure, frost heave and adjacent construction. Also, there are 7 kinds of environmental effects, mainly including concrete carbonization and harmful water erosion. In addition, tunnel conditions can be identified according to the deterioration forms under typical external actions such as rock mass bias, landslide, unbalanced water pressure, and frost heave. Based on the analysis of change causes, the tunnel integrity can be further assessed.

Table 3  
Criteria for assessing the tunnel integrity

Integrity	Tunnel conditions	Maintenance measures
A	AA Threatening the safety of passengers and masses, affecting the normal operation of trains and having other possible dangers	Taking emergency measures
	A1 Performance reducing due to ongoing changes, or performance losing due to heavy rain, water seepage, earthquake, etc.	Taking prompt actions
	A2 Performance reducing in the future due to possible changes	Taking measures when necessary
B	Changes that might lead to integrity A	Taking measures such as monitoring as necessary
C	Minor changes	Prioritizing the inspection thereof next time
S	Fine integrity	N/A

In accordance with Japanese tunnel inspection standards, if the tunnel lining integrity is rated as A, individual inspection shall be carried out in the process of comprehensive inspection once every two years, to achieve the itemized assessment of integrity (AA, A1, A2).

Crack is a common tunnel disease, and the criteria for assessing the degree of crack deterioration are shown in Figure 3. The integrity assessment of mountain

tunnels with cracks is detailed in Table 4. The development status depends on the ratio between the lining deformation  $u$  and the development time  $t$ . In case of  $10 \text{ mm/year} < u/t$  or  $2 \text{ mm/month} < u/t$ , it is deemed as very fast development; in case of  $3 \text{ mm/year} < u/t < 10 \text{ mm/year}$ , it is regarded as fast development; in case of  $1 \text{ mm/year} < u/t < 3 \text{ mm/year}$ , it is determined as slow development.

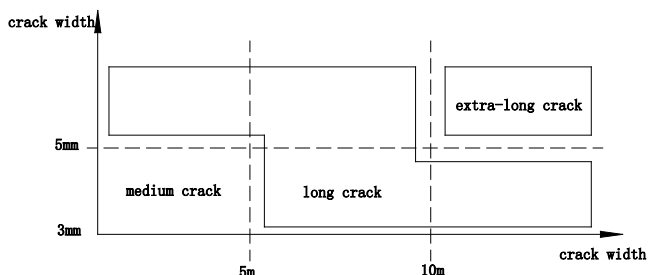


Figure 3  
Criteria for distinguishing extra-long cracks, long cracks and medium cracks

Table 4  
Integrity assessment of mountain tunnels with cracks

Degree of deterioration	Development status	Deterioration prediction	Integrity
Extra-long cracks, or shear cracks, serious crushing	Yes	Instability of current tunnel	AA
	No	Being unable to identify its stability before next inspection	A1
Long cracks, crushing	Very fast development	Instability of current tunnel	AA
	Fast	Being unable to identify its stability before next inspection	A1
Medium cracks	Very fast development	Instability of current tunnel	AA
	Fast	Being unable to identify its stability before next inspection	A1
	Slow development	High possibility of reduced stability before next inspection	A2
No obvious cracks	Very fast development	Instability of current tunnel	AA
	Fast	Being unable to identify its stability before next inspection	A1
	Slow development	High possibility of reduced stability before next inspection	A2
	No	Stability of current tunnel	B~C

The deterioration location, initial defect, and structural form shall also be taken into account for the purpose of integrity rating. In addition, assessment results shall be corrected if necessary. In the case of vertical pressure, landslide and other

circumstances caused by any mountain movement, the integrity rating will be reduced by one grade. If the depth of cracks in a masonry tunnel made of bricks or concrete blocks exceeds 100 mm, the tunnel lining thickness, location and scope, and deterioration degree shall be taken into account, and the integrity may be reduced accordingly by one grade. If the tunnel lining has initial defects such as material deterioration and insufficient thickness, the bearing capacity of lining will be undermined. In this case, the integrity will be assessed based on the effective thickness (the thickness with an intensity greater than 15 MPa), and assessment results can be appropriately corrected, as shown in Table 5.

Table 5  
Correction of assessment results for initial defects of lining

Effective thickness $\gamma$ , effective thickness $t_s$	Correction of assessment results
$\gamma < 1/3$ , or effective thickness $t_s < 250\text{mm}$	Integrity reducing by 2 grades
$1/3 \leq \gamma < 2/3$	Integrity reducing by 1 grade

Note: Effective thickness  $\gamma = t_s / \text{design thickness}$ ;  
 $t_s$  = thickness with an intensity greater than 15 MPa

## 2.2 European Tunnel Condition Assessment

In some European countries, tunnel conditions are assessed by I-IV grades. The overall conditions of and corresponding repair measures for each grade of tunnels are shown in Table 6.

Table 6  
Tunnel condition rating and repair measures

Grade	Overall condition	Description	Repair measures
<b>I</b>	Favorable	No problem, or insignificant problem	Maintaining the current conditions
<b>II</b>	Reasonable	Existence of some non-structural problems (diseases)	Minor maintenance to avoid deterioration
<b>III</b>	Poor	Structural diseases, serious or massive deformation or cracking, large-scale water seepage	Repair required within 5 years
<b>IV</b>	Very poor	Severe structural diseases, risks of collapse in important structure areas	Dealing with as soon as possible to stabilize the conditions within one year, with regular special inspection required for special monitoring of hazardous areas

### 2.3 Chinese Tunnel Condition Assessment

In accordance with the Assessment Standard for Structure Deterioration of Railway Bridges and Tunnels [23] (Q/CR405.2-2019), tunnel deterioration can be rated as A, B, C, and D according to the impact on structural functions and traffic safety, and grade A can be further divided into AA and A1. Different repair measures for different tunnel deterioration grades are shown in Table 7, and the deterioration rating depends on the highest deterioration level of a single disease. In accordance with the Interim Regulations on the Safety Rating of Railway Tunnel Linings [24] (TYH [2004] No. 174), lining defects and diseases shall be quantitatively graded. In particular, the severity of lining defects and diseases of segmented tunnels shall depend on the highest level of single quantitative indicators. In addition, the lining safety level shall rest with surrounding rock level, groundwater condition, impact on traffic safety, and other factors. The safety level of tunnel lining shall depend on the safety level of the tunnel segment with most severe diseases.

Table 7  
Tunnel deterioration rating and repair measures

Deterioration grade		Impact on structural functions and traffic safety	Measures
A	AA (very severe)	Serious deterioration, endangering traffic safety	Taking measures immediately
	A1 (Severe)	Serious deterioration, which might endanger traffic safety	Taking measures as soon as possible
B (relatively severe)		Possibility to become very severe	Strengthening monitoring and taking measures if necessary
C (moderate)		Minor impact	Strengthening inspection, keeping normal maintenance
D (minor)		No impact	Normal maintenance and inspection

### 2.4 Comparison of Tunnel Condition Assessment Standards

Japanese tunnel condition assessment standards focus on implying and predicting the causes of changes in tunnel performance. Tunnel integrity assessment is based on the severity of tunnel diseases, deterioration degree, development status, and impact on structural stability. In addition, the deterioration location, initial defect, and structural form shall also be taken into account to correct assessment results. Japanese standards are more hierarchical and systematic in the integrated application related to lining damages, deformations and defects, but are insufficient in the assessment of serious internal lining defects. In contrast, European standards focus on the impact of diseases on the overall performance of the tunnel structure. In addition, convenient Chinese standards highlight the single-indicator assessment, but ignore the correction of assessment results in case of multiple deterioration types.

### 3 Tunnel Inspection Devices

With the growing scale of tunnels in operation, traditional inspection modes gradually become outdated due to their high subjectivity, low efficiency, and certain risks. Just in this context, Japan and China respectively developed special rail-mounted tunnel lining inspection devices.

#### 3.1 Japanese Tunnel Inspection Devices

In 2001, East Japan Railway Company (JR East) [25] and Mitsui Engineering & Shipbuilding (MES) jointly developed a self-powered tunnel lining inspection vehicle installed with radar antennas. Relying on two radar antennas on the crank arm, and one radar antenna on the straight arm, the inspection device can detect the lining within a range above the arched line, having the function of three-dimensional inspection of lining cavity within a range of 40 cm [26, 27]. The working condition of inspection is shown in Figure 4.



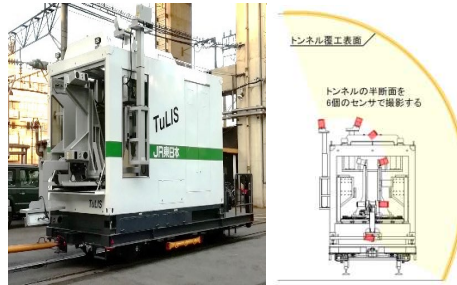
Figure4

Working condition of JR East's geological radar inspection vehicle

In order to realize the fine inspection of surface conditions of normal-speed railway tunnels, JR East introduced the vehicle for detecting surface conditions of lining using the laser scanner (1# vehicle) in 1999. In 2010, JR East successively introduced the 2# and 3# inspection vehicles. Currently, the three inspection vehicles are still used to detect the surface conditions of normal-speed railway tunnel lining at a speed of 8.5 km/h. The general view of the inspection vehicles is shown in Figure 5 (a). In order to detect the JR East upgraded the original tunnel inspection system used for nearly 20 years in 2020. The upgraded version of inspection vehicle is equipped with 12 sensors (lasers + cameras), which can realize the continuous inspection of surface conditions and 3D shapes of linings at a speed of up to 20 km/h. Currently, new inspection vehicles were put in to use for the Shinkansen tunnels in February 2020 [28]. A inspection vehicle for Shinkansen tunnels is shown in Figure 5 (b).



(a) A inspection vehicle for normal-speed railway tunnels



(b) A inspection vehicle for Shinkansen tunnels put into use in 2020

Figure 5

Japanese vehicles for detecting surface conditions of railway tunnel linings

### 3.2 Chinese Tunnel Inspection Devices

In 2012, China Academy of Railway Sciences developed a inspection vehicle for normal-speed railway tunnels [29, 30]. This vehicle with the 25T passenger train body is equipped with 5 sets of medium-and-high-frequency geological radar antennas. With a maximum antenna inspection depth of 1.5 m, and a inspection speed of 3~5 km/h, it is used to detect normal-speed railway tunnels. An inspection vehicle for normal-speed railway tunnels is shown in Figure 6.

Based on the inspection technology for normal-speed railway tunnels, China Academy of Railway Sciences developed a inspection vehicle for high-speed railway tunnels in 2018 [31, 32]. This vehicle is equipped with 9 sets of high-and-low-frequency radar antennas, and a CCD imaging system. With 8 industrial cameras, the CCD imaging system achieves a crack recognition accuracy of 1mm. In addition, its geological radar inspection speed is 3 km/h, and its imaging inspection speed is 50 km/h [33]. Figure 7 shows the general view of a inspection vehicle for high-speed railway tunnels, as well as the distribution of imaging systems.



Figure 6

An inspection vehicle for normal-speed railway tunnels

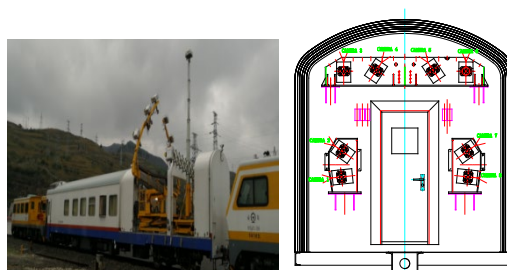


Figure 7

An inspection vehicle for high-speed railway tunnels

### **3.3 Comparison of Inspection Devices**

Japanese tunnel inspection vehicles are all self-powered, with geological radars and cameras mounted on different vehicles. In contrast, Chinese tunnel inspection vehicles refitted from the 25 T passenger train body are not self-powered, but are towed by other vehicles. In addition, geological radars and cameras are mounted on the same vehicle. It's worth noting that in terms of the imaging inspection speed, Chinese vehicles for detecting surface conditions of tunnel linings are superior to Japanese ones.

## **4 Suggestions on Improvement of Railway Tunnel Inspection System**

It is important to effectively detect and conduct quantitative and scientific assessment of railway tunnel defects and diseases developing constantly. However, the current railway tunnel inspection system is hard to meet such needs. In consideration of the actual conditions, scale and development law of China's railway tunnels, China should establish a sound system of railway tunnel inspection throughout the process of management.

### **4.1 Establishing a Railway Tunnel Inspection System**

The overall framework of the railway tunnel inspection system composed of four modules (inspection items, inspection system, inspection technology and devices, data analysis and evaluation) is shown in Figure 8.

### **4.2 Establishing a System of Railway Tunnel Inspection Throughout the Process of Management**

With reference to foreign railway tunnel inspection systems, relevant tunnel inspection systems should be further optimized based on existing tunnel inspection systems according to the scale of China's railway tunnels and the actual conditions in application of new technology and devices, so as to realize the whole-process management of tunnel diseases. Tunnel inspections mainly include routine inspection, cyclic inspection, temporary inspection, special inspection, and key tunnel calibration and monitoring. Different types of inspections vary greatly in the inspection objects, frequency, operation requirements, data accuracy, personnel (organization), etc. Details are shown in Table 8.

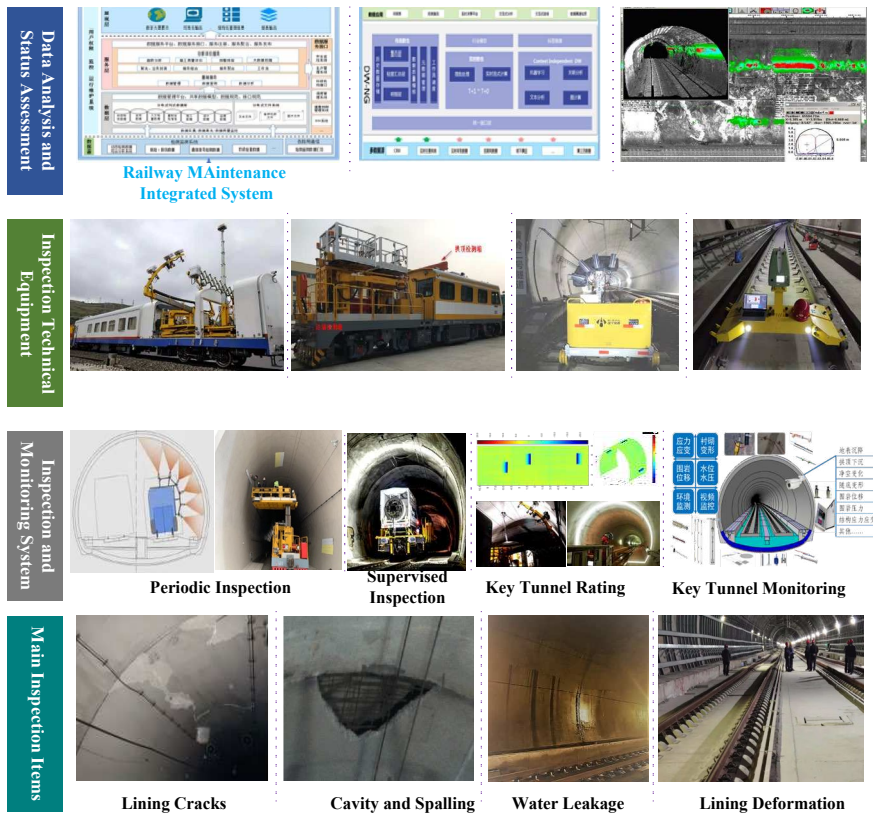


Figure 8 Framework of railway tunnel inspection system

Table 8 Attributes of different inspections

Inspection type	Object	Frequency	Operation requirement	Personnel/or ganization
Routine inspection	Surrounding environment; Overall condition seen visually; Diseases that need special attention;	Daily	Simple tools	Trackwalker
Cyclic inspection	Full contact	Cyclic (4~6 years)	Professional auxiliary inspection devices	Inspector
Temporary inspection	Key parts	After a natural disaster;	Professional auxiliary	Inspection engineer

		Adjacent engineering; Affecting third-party safety	inspection devices	
Special inspection	Uncertain defects and diseases	As required	Professional technology or devices	Inspection engineer Testing agency
	External environment\ tunnel boundaries	As required		
Key calibration and monitoring	Complex geological tunnel; Rapid disease development; Occurrence of geological disasters	Cycle ( $\leq 10$ years) or real-time online	Professional technology and devices	Inspection engineer Analytical engineer Testing agency

**Routine inspection** shall refer to the ordinary inspection of accessible parts along the ground or rail surface in the visual manner or by using simple tools without the help of professional auxiliary facilities. The objects of routine inspection mainly include the surrounding environment, overall tunnel condition in a visual range, and diseases that need special attention as indicated in the cyclic inspection list.

**Cyclic inspection** shall refer to a comprehensive and detailed contact inspection of tunnels according to the inspection plan. It is necessary to issue a detailed inspection report, update and distribute the disease records to all the parties of maintenance management, and clarify the maintenance work recommendations and their urgency in the report.

**Temporary inspection** shall refer to the inspection of exceptions after the occurrence of any natural disaster. A random inspection is required if concrete spalling might seriously affect the safety of any third party or adjacent engineering might affect the target structure.

**Special inspection** shall refer to the special inspection of structural condition, material performance, defects and diseases, and external environment of a tunnel in operation with the help of professional technology or devices. The inspection objects include the safety condition of tunnel lining, and tunnel boundaries. A special inspection is required if the distribution and impact of defects and diseases are uncertain. Supervisory tunnel inspection belongs to the scope of special inspection.

**Calibration and monitoring of important tunnels** shall refer to the comprehensive calibration and assessment of surrounding environments of complex geological tunnels, to assess their safety levels. If the diseases develop rapidly and geological disasters may affect the traffic safety, the monitoring system is required for real-time monitoring, forecasting and warning.

## Conclusions

This paper compares and analyzes the status quo and practical experience of Japan, Europe, the United States, and China in terms of railway tunnel inspection. Results show that Japanese tunnel condition assessment standards focus on implying and predicting the causes of changes in tunnel performance. In addition, they are more hierarchical and systematic in the integrated application related to lining damages, deformations and defects, but are insufficient in the assessment of serious internal lining defects. In contrast, European standards focus on the impacts of diseases on the overall performance of the tunnel structure, and the review of discovered diseases, regarding inspection as an important part of tunnel maintenance. In accordance with American standards, the inspection cycle shall depend on the service time of the tunnel in operation. Because American railways are privately owned, currently there are no uniform rating methods for railway tunnel structures. In accordance with Chinese standards, the inspection cycle shall depend on the operating speed of the railway in operation. Chinese standards highlight the single-indicator assessment, but ignore the correction of assessment results in case of multiple deterioration types. To overcome the deficiencies of manual inspection, Japan and China have respectively developed their own rail-mounted tunnel inspection devices.

In consideration of the operation characteristics, scale and development law of China's railway tunnels, this paper proposes to optimize the railway tunnel inspection system. The framework of a sound system of railway tunnel inspection throughout the process of management has been established. The railway tunnel inspection system is composed of four modules, namely inspection items, inspection system, inspection technology and devices, data analysis and evaluation. Railway tunnel inspections throughout the process of management mainly include routine inspection, cyclic inspection, temporary inspection, special inspection, and key tunnel calibration and monitoring. Different types of inspections vary greatly in the inspection objects, frequency, operation requirements, data accuracy, personnel (organization), etc.

## Acknowledgement

This research was funded by Science and Technology Research and Development Program of China State Railway Group Co., Ltd. [J2023G013]: Research on comprehensive lining evaluation technology of high-speed railway tunnel in operation, and Research and Development project of China Academy of Railway Science Co., Ltd. [2022YJ180]: Study on lining image-form symbiosis technology of high-speed railway tunnel in operation.

## References

- [1] S. TIAN, W. Wang, C. YANG, et al, "Development and prospect of railway tunnels in China in recent 40 years," *Tunnel Construction*, 41(11):1903-1930, 2021

- 
- [2] S. WANG, Y. GAO, F. QI, Z. KE, H. LI, L. LEI, Z. PENG, "Review on inspection technology of railway operation tunnels," *Journal of Traffic and Transportation Engineering*, 20(2):1-16, 2020
- [3] Transportation Bureau of China Railway Corporation. Current situation of railway tunnel. *Tunnel Construction*, 2015 ( 6): 534
- [4] C. LU, "Maintenance and repair mode and technologies for highspeed railway bridges and tunnels," *Chinese Railways*, 2017(7):1-8
- [5] D. NIU, "Technology and development of railway infrastructure lifetime inspection," *Railway Engineering*, 60(4): 5-8, 16, 2020
- [6] Q. CHEN, Y. WANG, H. KANG et al, "Research on Evaluation Model Construction of Technical Regulations and Rules on Comprehensive Maintenance of Railway Infrastructure," *Railway Freight Transport*, 40(1):29-35, 2022
- [7] D. CHEN, J. QU, X. Tian, et al. "Research on maintenance management mode of China high-speed railway," *Railway Engineering*, 2012(5):129-135
- [8] W. MA, J. CHAI, "Development status of disease inspection, monitoring, evaluation and treatment technology of railway tunnels in operation," *Tunnel Construction*, 39(10):1553-1562, 2019
- [9] Heidary, R., Esmacili, M., & Nik, M. G. (2023) Experimental and Numerical Analysis of Vibrations Induced by a Twin Tunnel, Underground Railway. *Acta Polytechnica Hungarica*, 20(1), pp. 187-198
- [10] Peng, Z., Yang, X., Liu, W., & Rad, M. M. (2023) Research on Risk Control Parameters of a Shielded Tunnel-enlarged Station, based on Bearing Capacity of Pre-removed Segment. *Acta Polytechnica Hungarica*, 20(1), pp. 213-229
- [11] Y. JIANG, J. WU, Y. MA et al, "Application of Impact Echo Acoustic Method in Quality Testing of Railway Tunnel Lining," *Railway Engineering*, 60(5):6-10, 2020
- [12] C. GAO, P. WANG, Z. HAN et al, "Development and Application of Tunnel Lining Quality Inspection Vehicle for Newly-built High Speed Railway," *Railway Engineering*, 60(7):69-72, 2020
- [13] WIMSATT A, WHITEJ, LEUNG C et al. "Mapping voids, debonding, delamination, moisture, and other defects behind or within tunnel linings," Washington DC:Transportation Research Board, 2013
- [14] KURAHASHI, MIKAMI K, KITAMURA T et al, "Demonstration of 25 Hz inspection speed laser remote sensing for internal concrete defects, " *Journal of Applied Remote Sensing*, 12(1):1-11, 2018
- [15] Japan Ministry of Land, Infrastructure, Transport and Tourism, Railway Technical Research Institute. Standard for maintenance and management of

- railway structures,commentary(tunnel). Tokyo:Maruzen Publishing Co. Ltd., 2007
- [16] Japan Ministry of Land,Infrastructure,Transport and Tourism,Railway Technical Research Institute.Standard for maintenance and management of railway structures,commentary (concrete structures). Tokyo:Maruzen Publishing Co. Ltd., 2007
- [17] Malva R. The inspection monitoring and diagnosis of tunnels.Proceedings of the World Tunnel Congress 2014-Tunnels for a better Life. 2014
- [18] UIC Code 779-10R: Management and maintenance principles for existing tunnels. Paris: UIC.2011
- [19] U.S. Department of Transportation, Federal Highway Administration. Highway and Rail Transit Tunnel Inspection Manual. Washington, DC: FHWA, 2005EMA, 2008
- [20] American Railway Engineering and Maintenance of Way Association. AREMA bridge inspection handbook, Lanhanm, AR
- [21] China Railway. Rules for Maintenance and Repair of Bridges and Tunnels for Normal-speed Railways (TG/GW 103-2018) . Beijing:China Railway Publishing House, 2018
- [22] China Railway.Maintenance rules for high-speed railway bridge and tunnel buildings ( Trial ) ( TG/GW114-2011 ) . Beijing:China Railway Publishing House, 2011
- [23] China Railway.Assessment Standard for Structure Deterioration of Railway Bridges and Tunnels ( Q/CR 405.2-2019 ) . Beijing: China Railway Publishing House, 2011
- [24] Ministry of Railways of the People’s Republic of China. Official letter from transportation Bureau of MOR(TYH2004, No. 174). Beijing:China Railway Publishing House, 2014
- [25] NOZAWA S, “Maintenance management of railway structures,”Construction Industry Research Commitee, 180:53, 2019
- [26] MATSUNUMA M, SUZUKIT, “Verification of tunnel lining inspection car using electromagnetic radar,”*Construction Project*, 2011(736):34-38
- [27] Niitu T, “Maintenance and Management of JR East Civil Engineering Structures,” *Japan Railway and Transport Review*, No. 2014, 63:26-33
- [28] Masataka KAGO, Koichiro MIZUNO, Masahiko TOMORI, et al,“ Development of maintenance management technique based on engineer’s evaluation for railway tunnel,” *Journal of Infrastructure Maintenance*, Vol. 1, No. 1 (514-520), 2022

- 
- [29] F. QI, G. LI, B. JIANG, "Development and application of railway tunnel state inspection vehicle," *Chinese Railways*, 2013(9):75-77, 99
- [30] C. ZhANG, "Research Manufacture and application of inspection vehicle for detecting railway tunnel lining condition," *Railway Engineering*, 2015(4):40-43
- [31] Y. LEI, T. TIAN. "The vibration characteristic and impact analysis of the tunnel lining inspection device based on arc rotating multi-section mechanism," *Advances in Mechanical Engineering*, 12(4), 2020
- [32] Y. LEI, Y. ZOU, T. TIAN, et al, "Analysis on vibration characteristics and suppression strategy of vehicle mounted GPR inspection device for tunnel lining," *Machines*, 2021
- [33] J. LI, C. ZHANG, X. CHAI, et al, "Research on crack inspection system of tunnel lining based on image recognition technology," *Railway Engineering*, 58(1):20-24, 2018